Evolution of Galaxies in Clusters

Dissertation der Fakultät für Physik
der
Ludwig-Maximilians-Universität München

vorgelegt von Gabriella De Lucia
aus Avellino, Italien

München, den 30. Januar 2004

Ai miei genitori

Contents

Contents

Contents

Zusammenfassung

In dieser Doktorarbeit studiere ich die Entstehung und Entwicklung von Galaxien in Galaxienhaufen sowohl theoretisch als auch unter Einbeziehung von Beobachtungsdaten. Galaxienhaufen stellen die größten gravitativ gebundenen Strukturen im Universum dar. Durch ihr Studium erhält man eine Fülle von Informationen, zum einen, indem man die Dynamik individueller Objekte erforscht und zum anderen aus ihrer Eigenschaft als Indikatoren der großräumigen Struktur im Universum. Diese Doktorarbeit gliedert sich in zwei Teile: Einem theoretischen Teil schließt sich eine Datenanalyse an.

Im ersten Kapitel beschreibe ich warum Galaxienhaufen wichtig sind, erkläre die Motivation und Zielsetzung der in dieser Arbeit verwendeten Analyse und erläutere den dafür nötigen theoretischen Hintergrund als auch den Hintergrund für die Beobachtungen.

Zuerst untersuche ich die Vorhersagen des hierarchischen *Modells der kalten dunklen Materie* für die beobachteten Eigenschaften der Population von Galaxien in Galaxienhaufen und für ihre Entwicklung als Funktion der kosmischen Rotverschiebung. Ich verwende eine große Anzahl von hochaufgelösten numerischen Simulationen von Galaxienhaufen zusammen mit einer hochaufgelösten Simulation einer "typischen" Region des Universums. Die große Auflösung der verwendeten Simulationen ermöglicht es mir, die Entwicklung der Zentren der dunklen Materiehalos zu verfolgen, welche mit größeren Strukturen zusammenwachsen. Dies erlaubt eine eindeutige Identifizierung leuchtender Galaxien in den Haufen und Substrukturen der dunklen Materie. Ich studiere sowohl die Verteilung der Substrukturen aus dunkler Materie im Raum und in ihrer Masse als auch ihre Akkretions- und Verschmelzungsgeschichte als Funktion der Halomasse und als Funktion der Umgebung. Dabei zeige ich, daß die Massenverteilung der Substrukturen fast unabhängig von der Masse des Stammhalos ist, in welchem sich die Substrukturen befinden. Halos mit der Größe von Galaxien sind deshalb einfach maßstabsgerecht verkleinerte Abbilder von Halos der Größe von Galaxienhaufen. Ein Teil der Masse derjenigen Substrukturen, welche von größeren Systemen akkretiert wurden, wird innerhalb von kurzer Zeit abgestreift und ihre Verschmelzungsraten sind unterdrückt aufgrund der großen Geschwindigkeitsdispersion des Stammsystems. Im folgenden zeige ich, daß ein signifikanter Bruchteil der Substrukturen bei relativ kleiner Rotverschiebung akkretiert wurde. Dies impliziert, daß ein signifikanter Bruchteil der Galaxien, welche sich zum gegenwärtigen Zeitpunkt

in Galaxienhaufen befinden, zu Rotverschiebungen $\gtrsim 1$ immer noch aktive Sternentwicklung zeigten. Diese Analyse ist Bestandteil des zweiten Kapitels.

Um eine enge Verbindung zwischen den theoretische Vorhersagen und den Beobachtungen zu ziehen, entwickle ich ein semi-analytisches Programm, welches selbstkonsistent die photometrische und chemische Entwicklung der Galaxien in den Haufen, als auch die chemische Geschichte des Gases innerhalb der Haufen und innerhalb der Galaxien verfolgt. Dabei modelliere ich den Transport von Masse und Metallen zwischen den Sternen, das kalte Gas in Galaxien, das heiße Gas in dunklen Materiehalos, und das intergalaktische Gas außerhalb der virialisierten Halos. Außerdem modelliere ich die Effekte von Staub auf die emittierte Strahlung von Galaxien. Ich experimentiere mit drei verschiedenen Rückkopplungsmodellen und zeige, daß es in allen Szenarien möglich ist, die Modellparameter so einzustellen, daß die resultierenden Eigenschaften und Verteilungen in guter Übereinstimmung mit Beobachtungen der Galaxien in den Haufen im lokalen Universum sind. Das dritte Kapitel beschreibt das semi-analytische Modell im Detail und zeigt einen Vergleich mit einer Anzahl von Beobachtungsergebnissen für Galaxien aus nahen Haufen.

Im folgenden verwende ich dieses Modell, um die Anreicherung des intergalaktischen Mediums und des Gases innerhalb der Galaxienhaufen mit den chemischen Elementen als Funktion der Zeit zu studieren. Dabei untersuche ich, zu welchem Zeitpunkt der Großteil der Anreicherung stattfand und welche Galaxien den größten Beitrag lieferten. Als Ergebnis finde ich, daß in allen drei Rückkopplungsmodellen die Anreicherung bei großen Rotverschiebungen stattfand (60-80 Prozent der Metalle wurden bei Rotverschiebung größer als eins ausgestoßen) und daß massive Galaxien einen wichtigen Beitrag zum Metallhaushalt der Galaxienhaufen liefern. Im weiteren Verlauf analysiere ich die beobachtbaren Merkmale der verschiedenen Modelle der Rückkopplungsmechanismen. Dabei zeige ich, daß die beobachtete Abnahme des baryonischen Massenanteils von Galaxienhaufen zu Gruppen nur in einem "extremen" Modell reproduziert werden kann, in welchem das wiederausgestoßene Material auf einer Zeitskala wiederaufgenommen wird, die vergleichbar mit der Hubblezeit ist. Die Resultate dieser Untersuchungen werden in Kapitel 4 präsentiert.

Der zweite Teil meiner Doktorarbeit handelt von der Interpretation von Daten des *ESO Distant Cluster Surveys* (EDisCS). Dieses *ESO Large Program* hat das Ziel, die Entwicklung der Galaxien in Galaxienhaufen über mehr als 50 Prozent der kosmischen Zeit zu studieren. Es verbindet die photometrische und spektroskopische Information einer großen Auswahl von Galaxienhaufen bei Rotverschiebungen um 0.5 und 0.8. Ich führe eine detaillierte dynamische und strukturelle Analyse einer Untermenge der EDisCS Galaxienhaufen durch, für welche vollständige photometrische und spektroskopische Daten vorhanden sind. Meine Untersuchungen konzentrieren sich auf die Analyse der Galaxienhaufenstruktur. Im besonderen entwickle ich eine Methode, um Substruktur zu quantifizieren, welche der projizierten räumlichen Verteilung als auch der Geschwindigkeitsverteilung Rechnung trägt. Die Ergebnisse

werden dann detailiert mit Resultaten der numerischen Simulation verglichen. Alle beobachteten Haufen besitzen eine komplexe dynamische Struktur und die Menge an Substruktur ist mit derjenigen aus den numerischen Simulationen vergleichbar. Im Kapitel 5 diskutiere ich, wie die Erweiterung der Methode auf den gesamten EDisCS Datensatz wichtige Einschränkungen auf die relative Bedeutung der verschiedenen physikalischen Prozesse liefern wird, die Galaxienentwicklung in dichten Umgebungen beeinflussen.

Zum Schluß analysiere ich die Farb-Helligkeits-Beziehung einer Untermenge der EDisCS Galaxienhaufen bei großen Rotverschiebungen. Dabei vergleiche ich die erhaltenen Resultate der hochrotverschobenen Galaxienhaufen mit denjenigen des nahen Coma Galaxienhaufens und zeige, daß die hochrotverschobenen Galaxienhaufen ein Defizit an leuchtschwachen Galaxien der roten Sequenz im Vergleich zu denjenigen bei kleiner Rotverschiebung aufweisen. Dies deutet an, daß ein großer Bruchteil der leuchtschwachen passiven Galaxien in Galaxienhaufen zum gegenwärtigen Zeitpunkt bei großen Rotverschiebungen aktive Sternentstehung aufgewiesen haben könnten. Diese Aussage stimmt qualitativ mit den Vorhersagen des hierarchischen Modells überein. Diese Analyse wird in Kapitel 6 präsentiert.

Summary

In this thesis I study the formation and the evolution of galaxies in clusters, both from a theoretical and an observational point of view. Clusters of galaxies represent the largest gravitationally bound structures in the Universe and a wealth of information may be obtained from their study both as individual dynamical units and as tracers of the large scale structure of the Universe. The thesis is divided into two parts: a theoretical part and a data analysis part.

In Chapter 1, I describe the importance of clusters of galaxies, explain the motivation and the objectives of the analysis presented in this thesis, and review the necessary theoretical and observational background.

First, I explore the predictions of hierarchical cold dark matter models for the observed properties of the cluster galaxy population and their evolution as a function of redshift. I use a large set of high-resolution numerical simulations of clusters together with a high resolution simulation of a 'typical' region of the Universe. The high resolution of the simulations used in this thesis permits me to track the evolution of the cores of dark matter haloes that fall into larger structures. This allows me to make a one-to-one identification between luminous cluster galaxies and dark matter substructures. I study the spatial and mass distribution of dark matter substructures and their accretion and merger histories as a function of halo mass and as a function of environment. I show that the mass distribution of substructures is almost independent of the mass of the parent halo. Galaxy–sized haloes are thus simply 'scaled' versions of cluster–sized haloes. Substructures accreted onto larger systems undergo significant stripping on short time–scales and their merger rates are suppressed because of the large velocity dispersion of the parent system. I show that a significant fraction of substructures are accreted at relatively low redshift, implying that a significant fraction of galaxies in clusters today were still actively forming stars at redshifts $\gtrsim 1$. This analysis represents the subject of Chapter 2.

In order to make a close link between theoretical predictions and observations, I also develop a semi–analytic code that follows the photometric and chemical evolution of cluster galaxies, as well as the chemical history of the intra-cluster and intergalactic medium in a self–consistent way. I model the transport of mass and metals between the stars, the cold gas in galaxies, the hot gas in dark matter haloes, and the intergalactic gas outside virialized haloes. I also model the effects of dust on the radiation emitted by galaxies. I experiment with three different feedback models

and show that, in all cases, it is possible to tune the model parameters in order to obtain a good agreement with observations of cluster galaxies in the nearby Universe. Chapter 3 describes the semi–analytic model in detail, and presents a comparison with a number of observational results for galaxies in nearby clusters.

I then use the model to study the chemical enrichment history of the intra–cluster and intergalactic medium. I investigate when the bulk of the enrichment occurred and which galaxies were responsible for it. I find that, for all three feedback models, the chemical enrichment occurs at high redshift (60–80 per cent of the metals are ejected at redshifts larger than 1) and that massive galaxies provide an important contribution to the metal budget of the clusters. I then analyse the observational signatures of the different feedback prescriptions and show that the observed decline in the baryon fraction from clusters to groups can only be reproduced in an 'extreme' model where ejected material is re–incorporated on a time–scale comparable to the Hubble time. I present the results of these investigations in Chapter 4.

The second part of my thesis deals with the interpretation of data from the ESO Distant Cluster Survey (EDisCS). This is an ESO Large Programme aimed at the study of the evolution of cluster population over more that 50 per cent of cosmic time. It combines photometric and spectroscopic information for a large sample of clusters at redshifts ~ 0.5 and 0.8. I perform a detailed dynamical and structural analysis of a subset of the EDisCS cluster sample for which we have complete photometric and spectroscopic data available. My investigation is focused on the analysis of cluster structure. In particular, I develop a new method of measuring substructure that takes into account both the projected spatial distribution of galaxies and the velocity information. I then carry–out a detailed comparison with results from numerical simulations. All the observed clusters have a complex dynamical structure and the amount of substructure is comparable to the one I find in the numerical simulations. In Chapter 5 I discuss how the extension of the method to the whole EDisCS dataset will provide important constraints on the relative importance of different physical processes that drive galaxy evolution in dense systems.

Finally, I analyse the colour–magnitude relation of a subset of the EDisCS clusters at high redshift. I compare the results obtained for the high–redshift clusters with the nearby Coma cluster and show that high redshift clusters exhibit a deficit of low–luminosity galaxies on the red–sequence, in comparison to the low–redshift clusters. This suggests that a large fraction of low–luminosity passive galaxies in clusters today might have been actively forming stars at higher redshifts. This is in qualitative agreement with the predictions of hierarchical models. This analysis is presented in Chapter 6.

–Quello che lei non sa è il vero scopo del nostro lavoro [. . .]. È perchè tutto non sia stato inutile, per trasmettere tutto quello che sappiamo ad altri che non sappiamo chi sono nè cosa sanno.

Italo Calvino, La memoria del mondo

1
Thesis objectives and framework

Abstract

I explain the motivation and the objectives of the analysis presented in this thesis and I review the needed theoretical and observational background. The importance of clusters of galaxies, which represent the main subject of this thesis, is emphasised, both as tracers of the large scale structure of the Universe and as an ideal laboratory for the study of galaxy evolution. In the first part of the chapter, I review the basics of the current favoured cosmological model, developing the basic formalism of the linear theory of perturbations and illustrating the results of the spherical collapse model. I review recent progress in numerical simulations and introduce the concept of semi–analytic models. In the second part of the chapter, I will present basic observational results on clusters of galaxies and evolution of galaxies in clusters. Given the broad range of this thesis, this chapter only provides a limited account of the field.

1.1 Motivation

With their rich variety of shapes and their fascinating spiral patterns, galaxies represent the most stunning phenomenon of the night sky. We know that these striking features of the Universe represent complex systems made up of different components – dust, gas, stars – held together by their mutual gravitational attraction and covering a wide range in mass, from 10^{12} $M_\odot$[1] for the giant ellipticals to 10^6–10^8 $M_\odot$ for dwarf galaxies and with typical sizes of the order of 1 kpc[2] for dwarfs and 10 kpc for

---

[1] 1 $M_\odot = 1.989 \cdot 10^{33} g$.
[2] 1 pc $= 3.0857 \cdot 10^{16}$ m.

giants.

The distribution of galaxies in the sky does not appear to be uniform: galaxies tend to gather in associations that are characterised by a variety of forms and may contain a handful of galaxies or thousands. These associations are called *groups* and *clusters of galaxies.*

Clusters represent the largest gravitationally bound structures in the Universe and their study may yield a wealth of information both as individual dynamical units and as tracers of the large scale structure of the Universe. On large scales, clusters provide a powerful cosmological diagnostic through the study of their statistical properties as a function of redshift. The number density of clusters of a given mass at varying redshifts ($N(M, z)$) is strongly dependent on the cosmological parameter $\Omega_{\rm M}$, the matter density of the Universe, and on σ_8, the amplitude of density perturbations on 8–Mpc scales (see Sec. 1.3.1).

As individual units, clusters of galaxies constitute an ideal laboratory for the study of galaxy formation and evolution and of the environmental influence on galaxy evolutionary processes. This is due mainly to three reasons:

- evolutionary processes are faster in high–density regions;

- some particular classes of objects are only found within large virialized systems. For example, cD galaxies (large luminous ellipticals whose stellar envelope can extent out to 1 Mpc) are only found in the cores or rich regular clusters. Ellipticals and lenticulars represent a conspicuous fraction of the cluster galaxy population;

- since clusters contain high density of galaxies, they are relatively luminous at many wavelengths and are therefore 'easy' to recognise and observe up to high redshift. They thus allow us to extend our studies of galaxy evolution over a long base line in cosmic time.

However, clusters of galaxies do have an important drawback: they are 'rare' objects that lie on the tail of the mass distribution (see Sec. 1.3.4); for a standard ΛCDM cosmology (see Sec. 1.3.1) the space density of haloes with mass larger than $10^{14}\,{\rm M_\odot}$ is only $7 \times 10^{-5}\,(h^{-1}\,{\rm Mpc})^{-3}$. This means that, even if clusters of galaxies contain on average $\sim 100\,{\rm L_*}$[3] galaxies, only about 10 per cent of the cosmic galaxy population resides in these massive systems at the present day, and even a lower fraction at high redshift. As explained above, however, the possibility to identify such systems over a wide range in redshift provides a unique opportunity to study the evolution of particular classes of objects and to investigate the influence of environment on the properties of galaxy population and their evolution.

---

[3]The parameter $\rm L_*$ represents a characteristic luminosity of cluster galaxies corresponding to a turn–over between a power–law behaviour and an exponential cut–off in the cluster luminosity function, i.e. the distribution in luminosity of the cluster galaxies.

In addition, clusters of galaxies represent very complex systems, involving a variety of interacting components – galaxies, X–ray emitting gas, and dark matter (see Sec. 1.6.1). They thus offer a unique opportunity to link many aspects of astrophysics and cosmology and, in particular, to clarify the interplay between dark and baryonic component.

In recent years, our knowledge of galaxy clusters has greatly improved thanks to multi–wavelength studies that allow complementary information to be obtained about these complex systems: optical imaging and spectroscopy provide information on the luminosities, the spatial distribution and kinematical properties of cluster galaxies. X–ray observations of clusters at different redshifts provide an unique tool to study the cosmological history of baryons. Recently, it has also been suggested that the presence of radio haloes and relics in clusters is indicative of a cluster merger. Merger shocks, with velocities larger than $10^3 \, \mathrm{km \, s^{-1}}$, convert a fraction of the shock energy into acceleration of pre-existing relativistic particles and provide the large amount of energy necessary for magnetic field amplification (Feretti 2002). Radio observations can then provide important information on eventual mergers allowing for example to give a further probe of the relative velocity of the structures and of the gas flows.

1.2 Historical context and thesis objectives

The startling beauty of the night sky has always intrigued people, leading to the birth of myths and legends that have sometimes had a strong influence on cultures, religions and also on everyday life. The very name given to our own Galaxy represents a memory of one of these legends: the ancient Greeks described this swathe of light, visible on a dark night from horizon to horizon, with a river of milk flowing from the breast of Hera, wife of Zeus – the word 'galaxy' comes from the Greek word for milk. We also know that ancient Greeks developed a surprisingly advanced understanding of astronomy: still today we use the magnitude system to quantify the brightness of an astrophysical object.

In spite of the early interest in this fascinating world, astronomy as a scientific discipline still had to wait some time to be born. It was only in the XVII century that Galileo discovered that this stream of light was not made up of some sort of 'celestial fluid' but was instead composed of myriads of unresolved stars. More and more 'patches of light' started to be observed – *nebulae* or *Island Universes*, using the definition given by Immanuel Kant. A famous 'comet hunter' – Charles Messier[4]– and a musician – Wilhelm Herschel – independently produced the first catalogues of nebulae.

---

[4]Charles Messier was nicknamed "le furet des comètes" by Louis XV. His interest in the nebulae was only marginal: he started cataloguing these objects in order not to misidentify them with comets.

Despite a *Great Debate* held in 1920 to establish the nature of these objects, it was only Hubble in 1923 to provide the definitive demonstration of their extra–galactic nature, measuring the periods of the Cepheids[5] in M31.

In this respect, the history of clusters of galaxies is as old as the history of nebulae: Hershel had already noted a *"remarkable collection of many hundreds of nebulae which are to be seen in what I have called the nebulous stratum of Coma Berenices"* (Herschel 1785). However, only in the late 30s (Smith 1936; Zwicky 1937) were these objects recognised as very large conglomerations of galaxies at great distances. The first dynamical analysis of clusters also showed that there must exist much more gravitational material than indicated by the stellar content of the galaxies in clusters. This was the first discovery of the preponderance of *dark matter* in the Universe (see Sec. 1.3.2).

In the early 60s, cluster research developed along the lines of measuring the numbers, sizes, luminosities, spatial and velocity distribution of cluster galaxies. The development of the first large catalogue of clusters (Abell 1958), based on a visual estimate of the number density of galaxies, represented one of the major milestones in the field. Extensive optical and spectroscopic follow–up studies were more time–consuming and it was not until more than one decade later (Rood 1974) that the first cluster mass estimates were obtained from measurements of the velocity distribution of cluster galaxies using the virial theorem. Then it became clear that clusters of galaxies were dominated by dark matter, with galaxies representing less than 5 per cent of the total mass. The astronomical community was finally oriented towards a paradigm in favour of dark matter; the time was ripe for the first pioneering works that started out the modern picture of hierarchical galaxy formation (Rees & Ostriker 1977; White & Rees 1978).

In the following decades, progress in the field has been so rapid that a complete overview would easily fill several hundreds pages. The development of new technologies and instrumentation and, at the same time, rapid progress on the theoretical side, have allowed astronomers to gather an incredible amount and variety of information. It is interesting and important to note that observational and theoretical progress have always proceeded side by side: often theoretical efforts have received formidable acceleration from observational results, as in the case of the discovery of the Butcher–Oemler effect, i.e. the observation that distant clusters tend to have 'bluer' galaxies than low–redshift clusters. This study, in fact, represented the first strong evidence that the properties of galaxies and/or clusters have evolved rapidly with time, thus addressing the difficult question of which physical mechanisms are responsible for this evolution – a question that remains largely unanswered. Very often

---

[5]Cepheids are pulsating stars that obey a very well–defined relation between the pulsation period and the luminosity. Such a relation can be used to infer the relative distance of two Cepheids and, once calibrated using nearby stars, the absolute distance of such a star.

observers have tuned their studies in order to distinguish between different possible physical mechanisms proposed by theorists. This is very much still the case and the present decade represents a very exciting moment for this field. In the last two decades, satellite missions like IRAS, COBE, WMAP have revolutionised the field, giving tighter and tighter constraints on the cosmological parameters; the Hubble Space Telescope has allowed to have a deep look at the high redshift Universe and a new class of 8–10 meter telescopes are producing a wealth of observational data. At the same time, rapid advances in computer technology and in the theoretical understanding of the physical mechanisms driving galaxy evolution, have allowed the development of more complex and complete models. It is likely that making a close link between the observations and theory will allow us to obtain strong constraints on the physical mechanisms driving galaxy formation and evolution.

This thesis represents an attempt in this direction. I will use the state–of–art numerical simulations of the formation of structure (see Sec. 1.4) in order to explore the predictions of the current favoured model for the observed properties of the cluster galaxy population and their evolution as a function of redshift. As I will explain later, numerical simulations of gravitational clustering of dark matter represent an indispensable tool for investigating the non-linear growth of structures in its full geometrical complexity (see Sec. 1.3.3). In addition, there is conspicuous observational evidence for a significant fraction of dark matter even in the very inner regions of galaxies (see Sec. 1.3.2 and Chapter 2). If observed galaxies have large fractions of dark matter, then N–body simulations can be used to predict the distribution of their dark matter components, to associate the dark matter substructures with galaxies and to predict properties such as their spatial and mass distributions that can be directly compared to observational results. Such comparison can provide important hints for the physics that needs to be included in viable models of galaxy formation and evolution. This analysis, that represents the subject of Chapter 2, has been accepted for publication in MNRAS (De Lucia et al. 2003a).

Dark matter alone, however, does not provide any direct information about the baryonic component that is the direct observable. In order to make a close link between the theoretical predictions and the observations, I will, as a second step, develop a semi–analytic model (see Sec. 1.5) that follows the photometric and chemical evolution of galaxies, as well as the chemical history of the intra–cluster and intergalactic medium, in a self–consistent way. I will build mock catalogues that contain not only galaxy properties such as luminosity, colour and bulge-to-disc ratio, but also spatial and kinematic information about galaxies inside dense clusters. I will compare the model predictions with a variety of observational data for galaxy clusters showing that this kind of analysis can provide important constraints on different physical mechanisms driving galaxy formation and evolution. The model developed permits also to study the chemical enrichment history of the intra–cluster and intergalactic medium. Clusters of galaxies can be considered as good *archives* of their past star

formation and metal production histories (Renzini 1997). Numerical simulations, in fact, predict that the baryon fraction in clusters does not change appreciably during their evolution. This implies that direct observations of elemental abundances in the intra–cluster medium can provide important information on the past star formation in clusters and eventually on the mechanisms that were responsible for the transport of metals from galaxies into the intra–cluster medium. This analysis, that represents the subject of Chapters 3 and 4, has been accepted for publication in MNRAS (De Lucia et al. 2003b).

In the second part of my thesis, the analysis will be related to the interpretation of data from the ESO Distant Cluster Survey (EDisCS). This is an ESO Large Programme aimed at the study of the evolution of cluster population over more that 50 per cent of cosmic time by combining photometric and spectroscopic information on a large sample of clusters at redshift ~ 0.5 and 0.8. The homogeneity of quality data and the large sample of clusters permit to analyse the properties of the galaxy population, as well as their cluster–to–cluster variations. I will use the model developed as a part of this thesis to generate mock catalogues from the simulations for direct comparison with the data. My analysis will be related, in particular, to the quantification of the amount of substructure in observed and simulated clusters. I will develop a new method to quantify the importance of substructures, that combines the spatial distribution of galaxies on the plane of the sky with the radial velocity information. I will show that the detail of the simulation permits to carry–out on the simulated data the same analysis conducted on the observed clusters. Extending the analysis to the complete EDisCS sample, it will be possible to gain some insight into how different physical processes affect galaxies in clusters. This analysis represents the subject of Chapter 5.

My analysis on EDisCS clusters will also be related to the study of the colour–magnitude relation of a subset of our high redshift clusters. I will show, by means of an accurate comparison with passive galaxy population in nearby clusters, that the high redshift clusters exhibit a clear deficit of low–luminosity red sequence galaxies. These results have important consequences on models for the formation and evolution of early–type galaxies in clusters. This analysis represents the subject of Chapter 6

In order to provide both a theoretical and observational framework for the analysis presented in this thesis, I have divided this chapter in two parts. In the first part I review the basics of the current favoured cosmological model, illustrating the results of the linear theory of perturbations and of the spherical collapse model. I review recent progress in numerical simulations and introduce the concept of semi–analytic models. In the second part of the chapter I present basic observational results on clusters of galaxies and the evolution of galaxies in clusters.

1.3 Formation and evolution of the structure in the Universe

The basic picture of modern cosmology (Weinberg 1972; Peebles 1993; Padmanabhan 1993; Peacock 1999) is that of a Universe that began from a hot and homogeneous state. Density fluctuations in the early Universe were exponentially amplified during a phase of *inflation* (Guth 1981), a theory that eliminates many of the problems of the so–called *standard model*. How the inflation started and eventually stopped and, most importantly, which of the many proposed theories are viable, is still a matter of debate. The expansion of the perturbations eventually stopped because of self–gravity, and the perturbations *turned around* collapsing into bound structures. In the current favoured model, smaller structures collapse first and are later incorporated in larger collapsing structures in a *bottom–up* scenario that provides a natural explanation for the formation of galaxies, clusters, filaments and superclusters. Modern cosmology is founded on Einstein's theory of General Relativity and merely represents a very simple application of this theory.

1.3.1 The homogeneous Universe

The study of structure formation and evolution requires a spacetime framework that allows a physical connection between phenomena occurring at different cosmic epochs. For the very special case of a homogeneous and isotropic Universe the metric turns out to be quite simple and is given by the Robertson–Walker metric (Peacock 1999):

$$dl^2 = c^2dt^2 - a^2(t)\left(\frac{dr^2}{1 - kr^2} + r^2(d\theta^2 + \sin^2\theta\ d\phi^2)\right)$$

where r, θ and ϕ represent the spherical coordinates and k is the curvature of the Universe whose value can be < 0 (for an open Universe), 0 (for a flat Universe) and > 0 (for a close Universe). $a(t)$ represents the scale–factor of the Universe (which is a measure of its size) and its form depends on the material the Universe is made of.

Using the Robertson–Walker metric, Einstein's field equations simplify into the Friedmann equations:

$$\frac{\ddot{a}}{a} = -\frac{4\pi G}{3}\left(\rho + \frac{3p}{c^2}\right) + \frac{\Lambda c^2}{3} \tag{1.1}$$

and

$$\left(\frac{\dot{a}}{a}\right)^2 = \frac{8\pi G}{3} - \frac{kc^2}{a^2} + \frac{\Lambda c^2}{3} \tag{1.2}$$

where ρ represents the matter density, p the pressure and Λ the cosmological constant, corresponding to an energy density of the vacuum:

$$\rho_v c^2 = \frac{\Lambda c^4}{8\pi G}$$

The Hubble parameter, that represents the expansion rate of the Universe, is related to the scale–factor by the equation:

$$H(a) = \frac{\dot{a}}{a}$$

In order to solve the above equations, one needs to specify the time dependence of ρ and p, i.e. to specify an equation of state, that obviously depends on the form of energy/matter. In the early Universe the energy density is dominated by relativistic particles and radiation; the equation of state is $p = \rho/3$ and the density scales as a^{-4}. As the Universe expands, the energy density of radiation decays and the Universe enters a matter–dominated phase. Non relativistic matter is assumed to be pressureless and its energy density scales as a^{-3}.

It is useful to define the following density parameters:

$$\Omega_{\mathrm{M}} = \frac{\rho}{\rho_c}, \qquad \Omega_{\Lambda} = \frac{\Lambda c^2}{3H_0^2}, \qquad \Omega_c = -\frac{kc^2}{a_0^2 H_0^2} \qquad (1.3)$$

where $\rho_c = 3H_0^2/8\pi G$ represents the matter content of the Universe. Note that these definitions refer to the values of the corresponding quantities at the present time. With these definitions Eq. 1.1 becomes $q_0 = \frac{1}{2}\Omega_{\mathrm{M}} - \Omega_{\Lambda}$ and Eq. 1.2 becomes $\Omega_{\mathrm{M}} + \Omega_c + \Omega_{\Lambda} = 1$, at the present time. In the previous equation, q_0 is defined as $q_0 = -(\ddot{a}a/\dot{a}^2)_{t_0}$ and represents the rate at which expansion of the Universe is accelerating.

Different methods have been used and are currently used to measure the cosmological parameters. In Sec. 1.1, we have explained that clusters of galaxies provide a powerful diagnostic for the measurement of Ω_{M} (the matter density of the Universe) and σ_8, that parametrises the normalisation of the power spectrum (see Sec. 1.3.3). Supernovae of type Ia (SNIa) are considered as excellent *standard candles* because of the constancy of their *luminosity at maximum brightness*. Since SNIa are relatively luminous objects, they can be observed out to high redshift, thus providing a powerful tool for the determination of the geometry and matter content of the Universe.

The perhaps most elegant method for the measurement of the cosmological parameters is based on measurements of temperature fluctuations in the microwave background radiation. Decomposing the temperature fluctuations in spherical harmonics, it is possible to recover the underlying fluctuation spectrum (see Sec. 1.3.3).

The most recent and incredibly tight results have been obtained from the WMAP team (Spergel et al. 2003). Fig. 1.1[6] shows the constraints from BOOMERANG data from de Bernardis et al. (2002) overlaid with the contours from the Supernova Cosmology Project (Perlmutter et al. 1999) and 2dF data (Verde & Heavens 2001). In

---

[6]The figure is taken from http://www.physics.upenn.edu/~lverde/cosmmodel.html
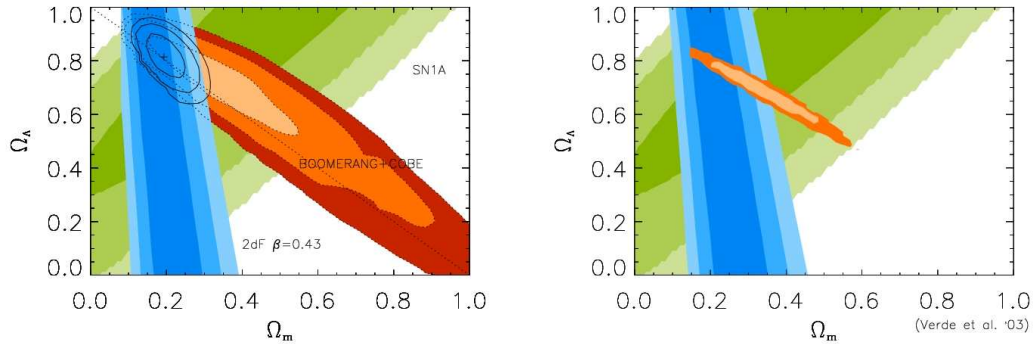
Figure 1.1: Cosmological parameters measurements before (left panel) and after (right panel) WMAP.

the right panel the orange likelihood surface shows the new results from WMAP. Observational data seem to converge towards a *concordance* cosmological model with a low–density ($\Omega_\mathrm{M} = 0.3$) and vacuum dominated ($\Omega_\Lambda = 0.7$) Universe. WMAP data also provide an accurate estimate of the Hubble constant at the present time (H_0), that is found to have a value of $72 \pm 5\,\mathrm{km\,s^{-1}\,Mpc^{-1}}$. Although the present estimate of the Hubble constant is extremely accurate, it is still common to introduce a dimensionless parameter (h), that was originally introduced to parametrise the uncertainty on the value of the Hubble constant: $H_0 = 100h\,\mathrm{km\,s^{-1}\,Mpc^{-1}}$.

The redshift z of an object is the fractional Doppler shift of its emitted light resulting from radial motion:

$$z = \frac{\nu_e}{\nu_o} - 1 = \frac{\lambda_o}{\lambda_e} - 1$$

where the subscripts 'e' and 'o' are used for 'emitted' and 'observed'. In terms of cosmography, the cosmological redshift is directly related to the scale factor $a(t)$. If one neglects peculiar motions:

$$1 + z = \frac{a(t_0)}{a(t_e)}$$

For small distance d one obtains:

$$z \approx \frac{v}{c} = \frac{d}{D_\mathrm{H}}$$

where v is the radial velocity of the object and $D_\mathrm{H} = c/H_0 = 3000\,h^{-1}\,\mathrm{Mpc}$ represents the *Hubble distance*. Redshift is directly measurable from the spectra and is related

to both the distance of the objects and the epoch of emission of the light, and thus often represents a convenient time variable.

Introducing the definitions given in Eqs. 1.3 in the second Friedmann equation (Eq. 1.2), one obtains:

$$H(z) = \frac{\dot{a}}{a} = H_0 E(z)$$

where

$$E(z) = \sqrt{\Omega_{\mathrm{M}}(1+z)^3 + (1 - \Omega_{\mathrm{M}} - \Omega_\Lambda)(1+z)^2 + \Omega_\Lambda}$$

This last equation is very useful to obtain the definition of distances that are commonly used in cosmology (Hogg 1999). In fact, since $dz = da$, $dz/E(z)$ is proportional to the time-of-flight of a photon travelling across the redshift interval dz divided by the scale factor at that time. Since the speed of light is constant, this is a proper distance divided by the scale factor, which is the definition of a comoving distance. The total line-of-sight comoving distance is obtained integrating these contributions (Hogg 1999):

$$D_{\mathrm{C}} = D_{\mathrm{H}} \int_0^z \frac{dz'}{E(z')}$$

1.3.2 Dark matter

There is now conspicuous observational evidence that the majority of the mass in the Universe consists of a unspecified *dark matter* component (see also Sec. 2.1).

The observational evidence of a *missing mass* problem actually dates back to the 30's, when Zwicky estimated that the speeds of galaxies in rich clusters are too large to keep the system gravitationally bound, unless the dynamical mass is at least 100 times larger than the mass contained in galaxies. The reality of the missing mass problem, however, gained a hold upon the astronomical community only in the early 70's, through the work of Freeman (1970) and others who demonstrated that the rotation curve of spiral galaxies is either flat or rising at the optical edge of the galaxies, contrary to the expectation of a Keplerian fall off in rotational velocity as a function of radial distance.

Baryons as candidate for dark matter are ruled out by the theory of primordial nucleosynthesis (Cavaliere et al. 1998). Non-baryonic candidates are classified as *hot* and *cold* dark matter (also an intermediate state, called *warm* dark matter has been proposed), depending on their kinematical state in the early universe at the time of decoupling of light and matter. Hot dark matter candidates would have been relativistic, cold dark matter ones non-relativistic. This categorisation has important ramifications for structure formation, and there is a chance of determining whether the dark matter is hot or cold from studies of galaxy formation.

So far, hot dark matter is ruled out because it gives rise to coherent structures which are too large to be consistent with the observed galaxy distribution (Hut & White

1984) because of the strong damping on small scales due to free streaming[7]. Warm dark matter seems to be still a viable possibility. At present, the best agreement with observational studies is given by cold dark matter, in the form of Weakly Interacting Massive Particles (WIMPS), which naturally arise in supersymmetric extensions of the standard model.

Dark matter is assumed to behave as a collisionless fluid for most of the history of the Universe. Since the number of particles is believed to be large, two–body interactions can be neglected and the system can be described by a distribution function in the phase–space whose evolution is given by the collisionless Boltzmann equation (also called Vlasov equation):

$$\frac{df}{dt} = \frac{\partial f}{\partial t} + \mathbf{v}\frac{df}{d\mathbf{r}} - \frac{d\Phi}{d\mathbf{r}}\frac{df}{d\mathbf{v}} = 0 \qquad (1.4)$$

where the potential is given by the Poisson equation:

$$\Delta^2 \Phi(\mathbf{r}, t) = 4\pi G \rho(\mathbf{r}, t)$$

1.3.3 The linear growth of perturbation

We have already pointed out that the observed Universe is far from being homogeneous, with a variety of structures ranging from dwarf galaxies to groups and clusters of galaxies, to huge superclusters. Nevertheless, the assumption of homogeneity still holds when the Universe is smoothed on large scales (somewhat larger than 100 Mpc). The currently favoured theories of structure formation assume that structure grows out of primordial quantum fluctuations that get amplified during a phase of rapid ($\Delta t \approx 10^{-33}$ s) expansion that is called inflation (Guth 1981).

The statistical properties of the density field $\delta(\mathbf{x}, t)$, at a given time, are usually characterised through the Fourier transform of its two–point correlation function[8], that is called *power spectrum*:

$$P(\mathbf{k}, t) = \left\langle |\delta(\mathbf{k}, t)|^2 \right\rangle$$

with

$$\delta(\mathbf{k}, t) = \frac{1}{(2\pi)^2} \int d\mathbf{x}\,\delta(\mathbf{x}, t)e^{-i\mathbf{k}\mathbf{x}}$$

and

$$\delta(\mathbf{x}, t) = \frac{\rho(\mathbf{x}, t) - \bar{\rho}}{\bar{\rho}}$$

---

[7]At the time of decoupling of light and matter, hot dark matter particles are still relativistic and therefore 'stream' from high density to low density regions, resulting in a damping of the fluctuations. The exact scale this occurs on depends on the mass and velocity of the particles involved.

[8]The two–point correlation function describes the probability, in excess of Poisson probability, to find two galaxies at a given relative distance.

where $\bar{\rho}$ is the background density.

The latest results from WMAP are consistent with a random Gaussian scale free Harrison-Zeldovich initial fluctuation spectrum, i.e. $P_{\text{initial}}(k) \propto k^n$ with $n = 1$.

Physical processes that depend critically on the particle content of the Universe, have modified the initial power spectrum producing a non–power law spectrum by the present day. The cumulative effect of these processes is represented through the so–called *transfer function*, that can be computed using publicly available codes (Seljak & Zaldarriaga 1996) or analytic approximations (Bardeen et al. 1986). If the Universe is dominated by cold dark matter, as is suggested by observational results (see Sec. 1.3.2), perturbations in the dark matter component begin to grow right after the epoch of *decoupling*, that marks the transition from a radiation dominated Universe to a matter dominated Universe (see Sec. 1.3.1). Amplification of these seeds will then produce density fluctuations which can accrete baryonic material after recombination, i.e. the epoch when the Universe became cool enough for the protons to capture electrons. As material continues to flow into the density fluctuation, it continues to grow in size thus sweeping up more material in the vicinity. Eventually galaxy–size objects are made via this gravitational coalescence of subunits and then clusters of galaxies are made later in the Universe via the continuation of this gravitational clustering hierarchy. In this model then, large systems like galaxy clusters are formed via hierarchical merging of smaller structures in a 'bottom-up' fashion.

After the recombination epoch, density fluctuations grow simply by self–gravitation and, as long as these inhomogeneities are small, their evolution can be followed using the linear perturbation theory. If the mean free path of the particles is small, matter can be treated as an ideal fluid. Using the equation of motion (Euler's equation), the continuity equation (that describes the conservation of mass) and the Poisson equation, it is possible to show with some algebraic manipulation that, in the linear regime, the growth of the perturbations is described by the following equation:

$$\ddot{\delta} + 2\frac{\dot{a}}{a}\dot{\delta} = 4\pi G\bar{\rho}\delta \tag{1.5}$$

The equation has, in general, two solutions: a decaying mode and a growing mode, that is the only one relevant for the structure formation. The above linear equation is usually transferred into the Fourier space, which is convenient because, so long fluctuations remain in the linear regime, all modes are decoupled and evolve independently from each other.

Note also that in the linear regime the initial spectrum of the perturbation remains unchanged, except that the amplitude of the fluctuations will grow according to the growing mode (as the system evolves the decaying mode simply damps away). So the power spectrum at some time can be written as:

$$P(k, t) = P(k, t_0)T^2(k)\frac{D_g(t)}{D_g(t_0)}$$

where $T(k)$ is the transfer function discussed earlier and $D_g(t)$ is the growing mode of Eq. 1.5.

1.3.4 Object formation

The observed isotropy of the microwave background radiation guarantees that the density contrast must have been quite small at epochs $t \gtrsim t_{\rm dec}$, i.e. at the decoupling epoch. At some later time, the density contrast corresponding to a spatial scale $\lambda = 2\pi/k$ will become comparable to unity and the linear perturbation theory will be no longer a valid approximation. Moreover, there will be no specific advantage to use the Fourier description, as the evolution of the density contrast becomes non–linear.

Let us consider a density contrast $\delta(\mathbf{x}, t)$ at some time t_i. The Universe can be divided in overdense ($\delta > 0$) and underdense ($\delta < 0$) regions. It is reasonable to expect that the self–gravity in an overdense region will work *against* the expansion of the Universe so that this region will start expanding at a slower rate compared to the background Universe. This will increase the density contrast and eventually the overdense region will collapse under its own self–gravity, forming a bound system.

Under the assumption of spherical symmetry with homogeneous density (*spherical collapse model*), it is possible to show that the perturbation breaks away from the general expansion and collapses when it reaches a critical overdensity of:

$$\delta_{\rm coll} = \frac{9\pi^2}{16} \approx 5.55$$

The linearly extrapolated density contrast at the collapse time is approximatively 1.686.

The above results are valid for a flat Universe with a zero cosmological constant (Einstein–de Sitter Universe), but can be extended to other cosmological model (Peebles 1993; Lacey & Cole 1993). Once the perturbation has *turned–around*, it starts collapsing. During the collapse there are large fluctuations in the gravitational potential, on time–scale of the order of the free–fall collapse time ($t_{\rm dyn} \simeq (G\rho)^{-1/2}$). Because of these fluctuations, particles do not follow orbits that conserve energy. This rapid and mass–independent process is named *violent relaxation*. Lynden-Bell (1967) computed that the equilibrium state this violent process leads to, reduces, for the appropriate number densities in clusters, to a Maxwell–Boltzmann distribution with a phase space density that produces a Gaussian velocity distribution and an isothermal spatial distribution of galaxies, which is roughly consistent with the observed distributions in the inner parts of clusters. The overdensity at virialization can be computed using the virial theorem that gives:

$$\delta_{\rm vir} = 18\pi^2 \simeq 178$$

The number of objects collapsed at a given redshift depends on the underlying initial Gaussian random density field. Press & Schechter (1974, PS) realized that, although the small–scale modes have become non linear, large scale modes may still follow the linear theory. Therefore, filtering the linearly evolving density field with filters of different sizes (that correspond to different masses), it is possible to determine if a given region of the space belongs to a collapsed object (it does belong to a collapsed object if it has reached the linearly extrapolated critical density $\simeq 1.686$). The PS formalism can then be used to determine the *mass function*, i.e. the fraction of mass in objects of mass M–$M+dM$:

$$n(M)dM = -\left(\frac{2}{\pi}\right)^{1/2} \frac{\bar{\rho}}{M} \frac{\delta_c}{\sigma^2} \frac{d\sigma}{dM} exp\left(-\frac{\delta_c^2}{2\sigma^2}\right) dM$$

where σ^2 is the variance of the linear density field smoothed over a mass scale M.

The PS formalism has been substantially extended in more recent years (Bond et al. 1991) and is often used to follow the evolution of the underlying dark matter component in the context of semi–analytic models (see Sec. 1.5 and Chapter 3)

1.4 N–body simulations

Although the linear theory represents an extremely useful tool to describe the early growth of structure and the growth on scales that are so large to be still in the linear regime, it obviously cannot provide a complete description of the highly asymmetric processes occurring in hierarchical galaxy formation. In that case, numerical simulations are usually employed. In N–body simulations the phase–space distribution function $f(\mathbf{r}, \mathbf{v})$ is replaced by a set of N particles that are subsequently evolved under their self–gravity. Each particle can essentially be viewed as a delta–function in the phase–space. Therefore, if the number of particles is large enough, the system provides a fair approximation of the phase–space distribution function.

N-body numerical simulations have nowadays evolved into a widely used tool in cosmology thanks to the rapidly growing computer performance and, at the same time, to the development of more sophisticated numerical algorithms.

Early simulations of structure formation (White 1976; Aarseth et al. 1979; Miller 1983) employed a direct summation method for the computation of the gravitational force. This method requires $O(N^2)$ operations for N particles and is therefore prohibitive when the number of particles increases. Different techniques have been subsequently developed, that substantially reduce the computational time (see Sellwood 1987, for an excellent, although out–of–date, review of the topic). In the so–called PM (Particle Mesh) codes, for example, the density field produced by the particles is computed on a Cartesian grid and the Poisson equation is solved on the grid points. This can be done within relatively short computational time using Fast

Fourier Transform Techniques (FFT), that provide directly the values of the gravitational potential on the grid. It is possible to show that the computational effort of the method is $O(N_{\mathrm{grid}}log(N_{\mathrm{grid}}))$. Further refinements of the PM code are given by the P^{3}M (Particle–Particle–Particle–Mesh) and APM (Adaptive Particle Mesh) codes. In these, the force computation is supplemented with a direct summation on scales below the mesh size (P^{3}M), or mesh refinements are placed on highly clustered regions (APM).

Substantial progress in the field has arisen from the introduction of so–called *treecodes*, where particles are arranged in a hierarchy of groups and the gravitational field at each point is computed by a summation over the multipole expansion of the gravitational field of these groups.

The simulations I will use in this thesis have been carried out using the treecode GADGET (Springel et al. 2001b), that is publicly available, and a particular re–simulation technique that is usually referred to as *mass refinement* or *zoom* technique (Tormen et al. 1997; Katz & White 1993). First, a cosmological simulation of a large region is used to select a suitable target cluster. The particles in the final cluster and its surroundings (usually all the particles within two times the virial radius of the selected halo) are then traced back to their initial Lagrangian region and are replaced by a larger number of lower mass particles. These are perturbed using the same fluctuation distribution as in the parent simulation, but now extended to smaller scales to account for the increase in resolution. This resampling of the initial conditions of the Lagrangian region of the cluster thus allows a localised increase in mass and force resolution. Outside the *high-resolution* region, particles of variable mass, increasing with distance, are used so that the computational effort is concentrated on the cluster of interest, while still maintaining a faithful representation of the large-scale density and velocity field of the parent simulation.

In the 'boundary region' a spherical grid is used, whose spacing grows with distance from the high–resolution region and that extends to the box size of the parent simulation. Outside the boundary region, vacuum boundary conditions are used, i.e. a vanishing density fluctuation field.

The effect of increasing mass resolution in the high–resolution region, at the centre of the re–simulation box, is clearly visible in Fig. 1.2 that shows a zoom–in on the dark matter distribution for a 'typical' region of the Universe at redshift zero. The maps represent slices of 10 Mpc along the z–direction and the dimensions of the box decrease going from the top left to the bottom right panel.

Note that direct numerical simulations of a set of N particles represent a challenging technical problem also for other reasons. Despite the significant improvement achieved in the last years, N–body simulations still usually employ a number of particles that is significantly smaller than the actual number of particles in the real system that is being modelled. In order to prevent excessive two–body relaxation, one is forced to use a numerical trick that is called *softening* of the gravitational
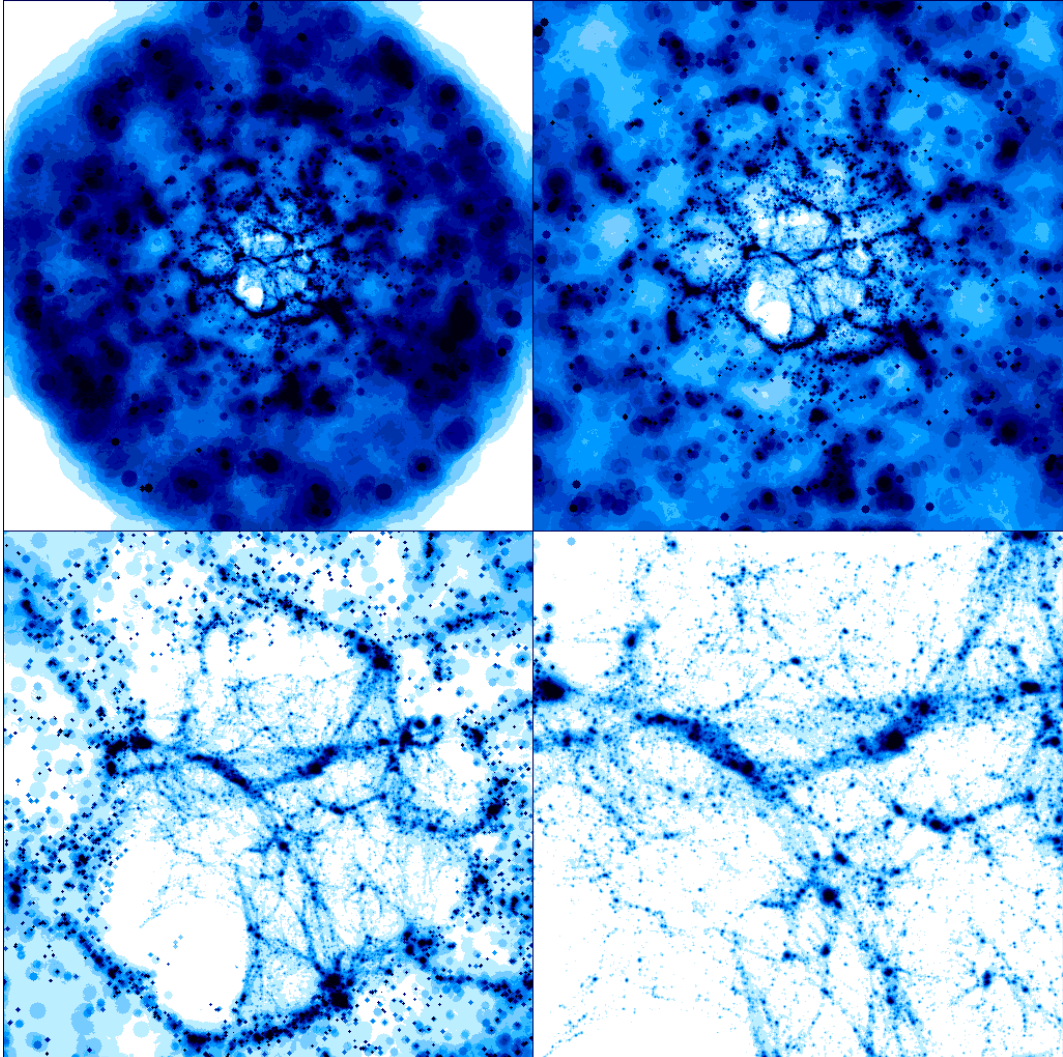
Figure 1.2: A zoom–in on the dark matter distribution for a 'typical' region of the Universe at redshift zero. The maps represent slices of 10 Mpc along the z–direction and the size of the box varies from 479 (top left), 380 (top right), 95 (bottom left) to 52 Mpc (bottom right). The figure clearly shows the increasing mass resolution in the high–resolution region at the centre of the re–simulation box.

force, i.e. at small separation the gravitational force is reduced below the Newtonian value in some smooth way.

A nice historical review of the increase rate of N in N-body simulations over the last thirty years can be found in Moore (2000). An important achievement of
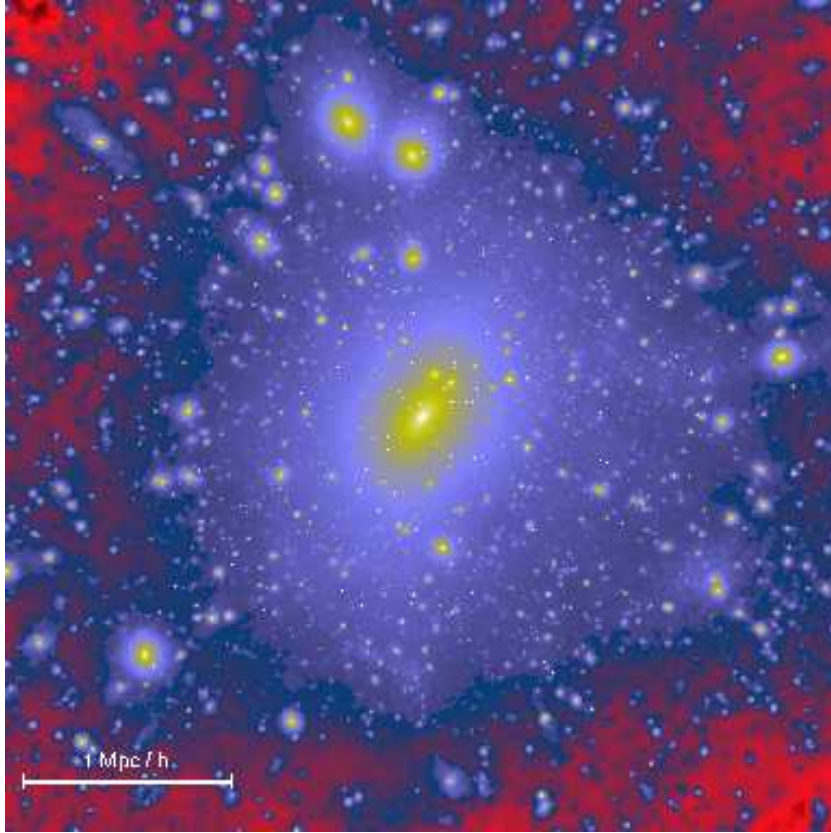
Figure 1.3: Density map of a high resolution cluster re–simulation at redshift zero. From Springel et al. (2001a). The cluster has a virial mass of $8.4 \times 10^{14} \, h^{-1} \, \mathrm{M}_\odot$. The high resolution region of the simulation contains 66 million particles.

the latest numerical simulations has been the solution of the 'overmerging problem' (Klypin et al. 1999a, see also Chapter 2), i.e. the possibility to resolve self-bound substructures in the smooth dark matter background of simulated haloes. This allows closer link to be made between simulated data and observational results.

As an example of the performance achieved by numerical N–body simulations in the last years, I reproduce in Fig. 1.3 the density map of one of the highest resolution simulations of a cluster carried–out so far (Springel et al. 2001a). The progress is impressive when compared to the state–of–art of numerical simulations of only two decades ago, which is reproduced in Fig. 1.4.
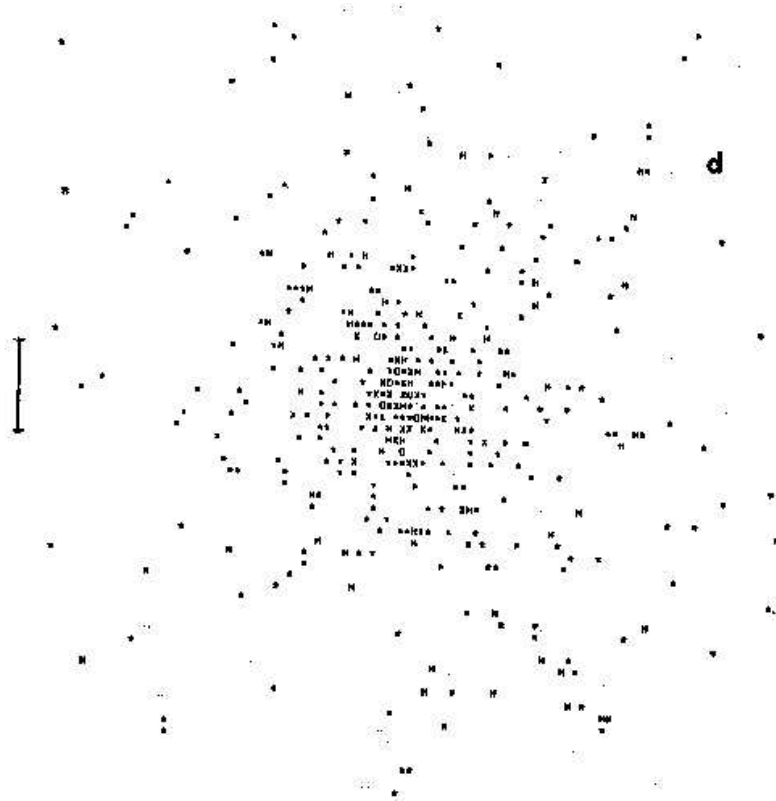
Figure 1.4: Projected distribution of a 700–body system with mass comparable to the virial mass of the Coma cluster. From White (1976).

1.5 The physics of galaxy formation

Modern N–body simulations are able to follow the formation and the evolution of dark matter haloes from scales typical of clusters of galaxies, down to scales typical of dwarf galaxies. Dark matter alone, however, does not provide any information about the baryonic component that is the direct observable. In order to make a close link between the theoretical predictions and the observations, it is then necessary to include the evolution of the baryonic component explicitely.

This can be achieved in two ways: the evolution of the baryonic component can be modelled 'directly', through the use of hydrodynamical methods that directly follow the gas–dynamics, or modelled making use of simplified 'recipes', physically motivated and supported by observational results.

Perhaps the most straightforward technique for adding hydrodynamics to a particle

code is Smoothed Particle Hydrodynamics (SPH)[9]. In SPH simulations, gas particles, carrying gas properties like temperature, composition and eventually stars, are associated to the dark matter particles. The gas component is gravitationally coupled to the dark matter but, unlike collisionless material, it also feels hydrodynamical forces arising from its thermal pressure. Radiative heating and cooling processes can be taken into account. These processes play a major role in the formation of galaxies: first, dark matter forms virialized systems during a process of violent relaxation (see Sec. 1.3.4); then the baryons sink to the centre of these haloes because of energy dissipation by emitting radiation. Note that atomic physics provides an accurate description of most of the heating and radiative processes, although some astrophysical situations require a quite high degree of complexity.

In the simple case of a collisionally ionised mix of hydrogen and helium, and also in the case of a 'polluted' gas, it is technically not extremely difficult to introduce a proper implementation of the cooling process in simulations. However, the inclusion of the cooling process is not enough for a complete description of the galaxy formation and leads to an *overcooling problem*, i.e. too much gas cools and form knots of cold and extremely dense gas if other processes like the star formation and the feedback are not implemented (see also Chapter 3).

The actual formation of galaxies include multiple processes that are strongly non linear and strongly interconnected. Moreover, the observational and physical understanding of these processes and also their dependence on environment are far from complete. For these reasons, the implementation of these processes requires some *ad hoc* prescriptions. Full cosmological hydrodynamical simulations, including star formation and feedback processes, have been carried out with some success in the last years (Springel & Hernquist 2003). Nevertheless it is important to note that the computational times are still highly prohibitive. This also means that this is not a 'convenient' method if one wants to explore the parameters space in order to investigate, for example, the influence of different physical prescriptions on different observational results.

A more powerful technique, in this respect, is provided by the so–called semi–analytic models (SAMs) in which the baryonic physics is approximated using simple yet physically and observationally motivated prescriptions. The SAMs find their seeds in the pioneering work by White & Rees (1978) and have been substantially extended and refined in the last years by a number of different groups (White & Frenk 1991; Lacey & Silk 1991; Kauffmann et al. 1993; Baugh et al. 1996; Kauffmann et al. 1999; Somerville & Primack 1999; Cole et al. 2000). These models have evolved, in

---

[9]More recently a number of alternative schemes have been imported into cosmological codes. In particular Eulerian codes, where the hydrodynamic equations are solved on a grid which is *fixed in time*, have become popular. These offer a number of potential advantages over SPH, for example easily allowing the addition of magneto–hydrodynamics and radiation fields. However, in order to follow the large density contrast that arises, adaptive mesh refinements techniques are essential.

the last years, into an important tool for interpreting observational data: with a low number of parameters the SAMs have been successful in providing a unified and coherent interpretation of a variety of observational properties of galaxies on different scales. These include the luminosity function (but see below), the Tully–Fisher and the Faber–Jackson relation, star formation histories, morphology, and colour distributions. Note however that these models are not without their problems. A well–known problem, for example, is the fact that these models usually predict too many galaxies both at the faint and at the bright end of the luminosity function, resulting in a shape that is not *curved enough* to be in good agreement with observational results (Kauffmann et al. 1999; Cole et al. 2000, see also Chapter 3). These models also have problems in reproducing the observed number of lenticular galaxies (S0) in galaxy clusters (Springel et al. 2001a; Diaferio et al. 2001), suggesting that additional mechanisms, besides those usually included, should be considered in order to understand the S0 population.

The field has in particular greatly benefited from recent work that has coupled the SAMs with N–body simulations (Kauffmann et al. 1997, 1999; Mathis et al. 2002; Diaferio et al. 2001; Benson et al. 2000a, 2001; Springel et al. 2001a, see also Chapter 3). In this way it is possible to obtain full spatial and kinematic distributions not only for the galaxy population at redshift zero but also for their progenitors at any earlier time, as for galaxies in real redshift surveys.

1.6 Observational results

In the following sections I will try to summarise some of the most important results on galaxy clusters and evolution of galaxies in clusters, that have been gathered in the last decades from observational data. The observational investigation of clusters of galaxies is by no means shorter than the history of the theoretical studies related to this topic. I will thus limit myself to a brief overview, referring to many existing reviews for a more extensive presentation of this topic (Biviano 2000; Bower & Balogh 2003; Poggianti 2003, and references therein).

1.6.1 Cluster components

Clusters of galaxies represent the largest quasi–virialized systems in the Universe. They typically contain 10^2–10^3 galaxies in a region of about 1–3 Mpc, with a total mass of $\sim 10^{14}\,\mathrm{M_\odot}$ for *rich groups* to $\sim 10^{15}\,\mathrm{M_\odot}$ for *rich clusters*. First observations showed that these structures are associated with deep gravitational potential wells containing galaxies with a typical velocity dispersion along the line–of–sight of $\sigma_v \sim 10^3\,\mathrm{km\,s^{-1}}$. The crossing time for a cluster of size R can be defined as:

$$t_{cr} = \frac{R}{\sigma_v} = 1 \left(\frac{R}{1\,\mathrm{Mpc}} \right) \left(\frac{\sigma_v}{10^3\,\mathrm{km\,s^{-1}}} \right)^{-1}\,\mathrm{Gyr}$$

Therefore, in a Hubble time ($\approx 10\,h^{-1}\,\mathrm{Gyr}$), the system has enough time in its internal region ($\lesssim 1\,h^{-1}\,\mathrm{Mpc}$) to dynamically relax. This condition cannot be attained in the surrounding environment. Assuming virial equilibrium, the typical cluster mass is:

$$M \simeq \frac{R\sigma_v^2}{G} \simeq \left(\frac{R}{1\,h^{-1}\,\mathrm{Mpc}} \right) \left(\frac{\sigma_v}{10^3\,\mathrm{km\,s^{-1}}} \right)^2 10^{15}\,h^{-1}\,\mathrm{M_\odot}$$

A number of different cluster properties have been traditionally used in order to construct a morphological classification of these systems. The Bautz & Morgan (1970) system, for example, is based on the degree to which the cluster is dominated by the brightest galaxies within it. In a similar manner, but with a finer classification, Rood & Sastry (1971) introduce a classification system that is based on the nature and distribution of the ten brightest cluster galaxies. Another commonly used classification system was first introduced by Oemler (1974), who simply classified clusters on the basis of their morphological content. Specifically, he defined a cluster as *spiral rich* if the spirals represent the dominant population, as *spiral poor* if the fraction of lenticulars is higher than the corresponding fraction of spirals, and as a *cD* cluster if it is dominated by a central cD galaxy with ellipticals representing the majority of the population.

Somewhat surprisingly, these different classifications appear to be highly correlated, with the result that clusters can be represented very crudely using a one–dimensional sequence from *regular* to *irregular*. Regular cluster are highly symmetric in shape with a high concentration of galaxies towards the centre. Moreover subclustering, is absent or weak in regular clusters. In contrast, irregular clusters have little symmetry or central concentration and usually show significant subclustering.

It is important to note that there is no one–to–one correspondence between the regularity of a cluster and its richness, related to the number of galaxies associated with that cluster. Regular clusters are usually rich, while irregular clusters may be either rich or sparse.

In Fig. 1.5, I show our two closest clusters: the Coma cluster (on the top), a rich cluster with mass $\sim 10^{15} \mathrm{M_\odot}$ containing thousands of galaxies, and Virgo (on the bottom), a relatively sparse and irregular cluster with mass $\sim 10^{14} \mathrm{M_\odot}$.

The galaxy population in clusters exhibits a remarkable *morphology–density* relation (Dressler 1980; Whitmore et al. 1993), with an increasing space density of early type galaxies towards the cluster centre. Which physical processes are responsible for establishing the observed morphological mix is still a matter of debate and it is possible that both global cluster properties and the local density environment may play a role.

Galaxies in clusters also exhibit a *luminosity segregation* (with more luminous galaxies being more centrally concentrated). This is however limited to only the very bright galaxies (Stein 1997; Biviano et al. 2002). Cluster galaxies also exhibit a

Figure 1.5: The Coma cluster (top panel) and the Virgo cluster (bottom panel).

kinematical segregation (Adami et al. 1998), with late type galaxies having a higher velocity dispersion than early type galaxies.

Many observational results suggest that the stellar population of galaxies in cluster cores are generally old, with most of the stars formed at redshifts larger than 2. These conclusions usually rely on the argument that recent episodes of star formation would produce an excessive scatter in observed colour–magnitude relation or the fundamen-
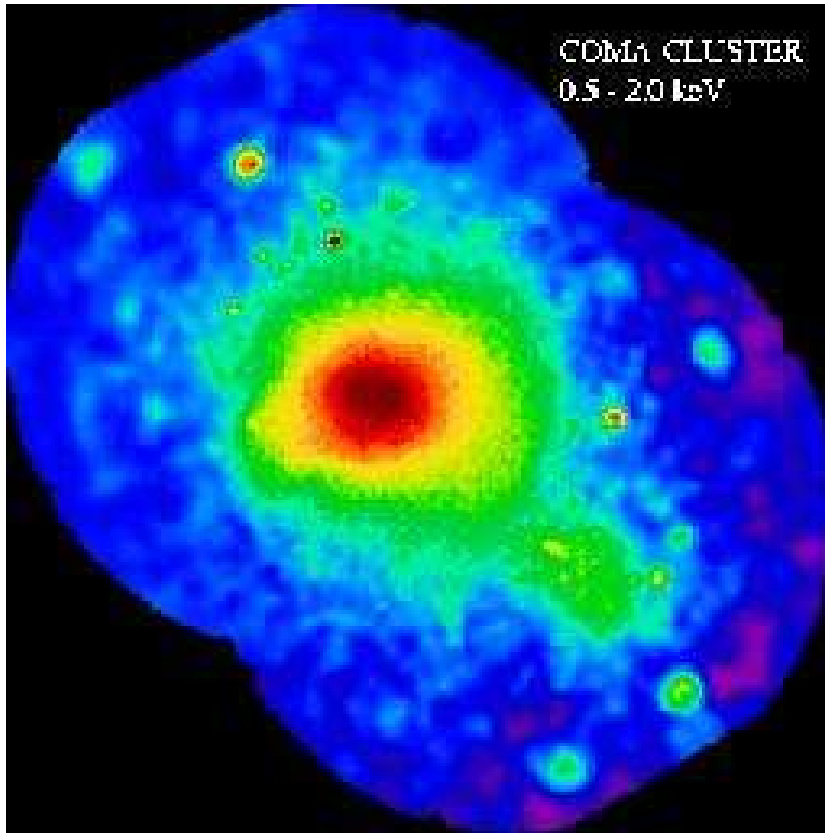
Figure 1.6: ROSAT image of the Coma cluster.

tal plane of elliptical galaxies, which are both very tight (van Dokkum & Franx 1996; Kodama et al. 1998). I will come back to this topic in Chapter 6, where I will study the colour magnitude relation in clusters at redshift ~ 0.8.

Early X–ray observations (Meekins et al. 1971; Gursky et al. 1971) showed that clusters of galaxies contain a hot plasma, with a typical temperature of 2–14 keV and a central density of $\sim 10^{-3}$ electrons cm^{-3}. The hot plasma detected through the luminous X-ray emission, is produced by thermal bremsstrahlung radiation and has a net luminosity of $\sim 10^{43-45}$ erg sec^{-1}. Fig. 1.6 shows the X–ray map of the Coma cluster taken with ROSAT.

The total mass of the hot gas in a cluster is generally larger than the total mass in stars, suggesting that at least part of this gas has a cosmological origin. On the other hand, the detection of line emission from iron suggests that a substantial portion of this gas must have been ejected from galaxies into the intra–cluster medium,

although the relative importance of different physical mechanisms that can provide viable explanations for this transfer of mass (and metals), is still a matter of debate (see Chapter 4).

1.6.2 Cluster surveys

The first extensive and statistically complete survey of clusters dates back to the work by Abell (1958). Clusters were identified as enhancements in the galaxy surface density on the Palomar Observatory Sky Survey (POSS) plates. Abell's criteria for the definition of galaxy overdensities were quite subjective: he required that at least 50 galaxies were contained within a metric radius $R_{\mathrm{A}} = 3\,h_{50}^{-1}$ in a given magnitude range. Abell also showed that there is a wide distribution of cluster richness, that broadly relates to the cluster mass. An important breakthrough in the search for galaxy clusters was provided by the advent of charge coupled device (CCD) imaging. In the last two decades a variety of different techniques have been used to identify galaxy clusters, the two most common being optical searches for projected galaxy overdensities and X–ray searches for extended thermal bremsstrahlung emission. Modern optically–selected cluster surveys include:

- the *Palomar Distant Cluster Survey* (Postman et al. 1996), a two band survey of 5 square degrees that used both positional and photometric data in order to enhance the contrast of galaxies overdensities. The survey has provided a catalogue of 79 clusters covering the redshift range 0.2–1.2.

- The *Red–Sequence Cluster Survey* (Barrientos et al. 2003), an ongoing project designed to provide a large sample of clusters over the redshift range 0.1–1.4. It uses the red sequence of early type galaxies as a direct cluster indicator.

- The *Las Campanas Distant Cluster Survey* that provides a sample of ~ 1000 cluster candidates over 130 square degrees. The cluster–finding algorithm employed in this case was suggested by Dalcanton (1996) and is based on an old idea of Shectman (1973) that the optical background light can be used to obtain information about the underlying distribution of galaxies (I will explain in more detail the algorithm in Chapter 5).

In the last twenty years, X–ray surveys have provided an efficient way of constructing samples of galaxy clusters out to high redshift. The ROSAT All–Sky Survey (Truemper 1993) and subsequent pointed observations have provided a large sample of X–ray selected clusters both in the Northern (NORAS, Böhringer et al. 2000) and in the Southern (REFLEX, Böhringer et al. 2001) hemisphere.

In the last years, optical and X–ray surveys of clusters have been complemented by other techniques such as the search for galaxy overdensities around high redshift

X–ray surveys	Optical/NIR surveys
ICM detection is an unambiguous indication of a real cluster	Possibility to survey large areas relatively quickly
High contrast ($L_{\mathrm{X}} \propto n_e^2$)	Noisy relation optical richness–cluster mass
Negligible background	Significant background
Low (~ 10 per cent) spurious rate	High (~ 30 per cent) spurious rate
Limited telescope access	Many telescopes available
Require optical/NIR follow–up for redshift	Many algorithms provide an estimate of the cluster redshift

Table 1.1: Advantages and drawbacks of X–ray and optical cluster surveys.

active galaxies (Dickinson 1997), or the measurement of the distortion of the cosmic microwave background due to the hot intra–cluster medium (Carlstrom 2002).

It is important to realize that different cluster–finding algorithms and different wavelengths find *different types of clusters*. The X–ray wavelength detects the hot intra–cluster medium, that is an indicator of a cluster in an advanced dynamical state. In the optical, one searches for overdensities of galaxies. Optical surveys are therefore able to identify younger systems with lower masses than X–ray surveys. On the other hand, the optical techniques suffer from strong limitations due to projection effects: filamentary structures or aligned small groups can easily mimic a rich cluster when projected on the plane of the sky. The various advantages and drawbacks of X–ray and optical surveys are listed in Table 1.1, adapted from Postman (2002).

It is therefore extremely important to keep under control the selection biases due to the particular selection method used, an objective that can be achieved, for example, by using multi–wavelength data.

1.6.3 Galaxy evolution in clusters

There is strong observational evidence that high density environments can significantly affect many galaxy properties. In particular the star formation rate, gas content and morphologies are strongly dependent on density (Moss & Whittle 2000; Balogh et al. 2000; Kodama et al. 2001; Balogh et al. 2002).

Theoretically, there are many mechanisms that can drive evolution in overdense

environments. These can be broadly grouped into three categories:

- *ram–pressure stripping*: galaxies travelling through a dense intra–cluster medium suffer a strong ram–pressure stripping effect that sweeps cold gas out of the stellar disc (Gunn & Gott 1972; Abadi et al. 1999; Quilis et al. 2000). Although the gas is tenuous, the rapid motion of the galaxy causes a large pressure front to build up in front of the galaxy. Depending on the binding energy of the gas in the galaxy, the intra-cluster gas will either be forced to flow around the galaxy or will blow through the galaxy removing some of the diffuse interstellar medium. Related mechanisms are thermal evaporation (Cowie & Songaila 1977) and viscous stripping of galaxy discs (Nulsen 1982), that occur when ram–pressure is not effective: turbulence in the gas flowing around the galaxy entrains the interstellar medium resulting in its depletion.

- *Collisions, mergings and harassment*: early simulations (Roos & Norman 1979; Barnes 1992) demonstrated that a merger between two spiral galaxies results almost always in a galaxy with structural parameters resembling those of elliptical galaxies. Simulations have also shown that collisions and close encounters can have strong effects on the star formation rates of galaxies. The tidal forces generated during the encounter funnel the gas towards the centre of the galaxy and possibly this gas ignites a star burst with subsequent ejection of a large fraction of the material (Barnes 1992; Mihos 2003). At the same time, the gas in the outer parts of the galaxy is drawn out of the system. The cumulative effect of many weak encounters (*harassment*) can also completely destroy galaxy discs (Moore et al. 1996b).

- *Strangulation*: current theories of galaxy formation suggest that when a galaxy is accreted onto a larger structure, the gas supply can no longer be replenished by cooling that is suppressed (Larson et al. 1980; Cole et al. 2000, see also Chapter 3).

The relative importance of different physical processes on the observable galaxy properties is still a matter of debate. It is clear that ram–pressure stripping can represent an effective mechanism only towards the centre of massive clusters because the ram–pressure force is proportional to v^2 (Gunn & Gott 1972). Individual collisions are expected to be most effective in groups since the velocity of the encounters is similar to the orbital timescale within the galaxy but, as mentioned above, Moore et al. (1996b) have demonstrated that the cumulative effect of many weak encounters can also be important in clusters of galaxies. In particular, this mechanism can be effective at destroying small galaxy discs, but its effect on the star formation rate of the galaxy is unclear.

Observational results indicate that star formation rates are quite low even in low mass clusters (Balogh et al. 2002). This suggests that the phenomenon of star for-

mation suppression is not driven by extreme processes like ram–pressure. Rather it is something that operates in more commonplace environments, possibly groups in the cluster infall region (Zabludoff & Mulchaey 1998; Kodama et al. 2001).

The population gradients observed in rich clusters seem to agree well with models of strangulation (Balogh et al. 2000; Diaferio et al. 2001), which also provide a natural explanation for the origin of the morphology density relation and agree with the apparent preference of blue galaxies for the outer regions of clusters.

As explained in Sec. 1.1, one of the most important advantages of studying clusters of galaxies is the fact that they are easy to observe up to high redshift, thus allowing one to follow the evolution of a particular class of objects as a function of time.

The first observational evidence of evolution of galaxies in clusters dates back to the work of Butcher & Oemler (1978), who showed a remarkable increase in the number of blue galaxies in clusters at $z > 0.2$. In a later work (Butcher & Oemler 1984), the reality of the effect was confirmed. In this paper Butcher & Oemler addressed a number of concerns about systematic effects in their analysis procedure and they broadened the sample of clusters both in number and in redshift. The fraction of blue galaxies in clusters at $z \sim 0.4$ was later demonstrated to be qualitatively similar to the excess of lenticular galaxies (S0) observed in nearby clusters, suggesting that S0 may be the result of morphological transformation of spirals, driven by the cluster environment (Dressler et al. 1997). As explained above, how exactly this transformation occurs and on which time–scales, is still a matter of debate. Moreover the reality itself of the Butcher–Oemler effect has been criticised by many authors (Andreon & Ettori 1999; Fairley et al. 2002; De Propris et al. 2003b). This criticism arises from the observation that the Butcher–Oemler sample does not provide a homogeneous sample of clusters over the studied redshift range, being primarily constituted by optically selected clusters. This selection, in fact, naturally favours the inclusion of clusters with a significant blue fraction at high redshift, thus mimicking a trend as a function of redshift.

The observation of clusters at high redshift has also indicated, somewhat surprisingly, that relations between elliptical galaxy properties observed in nearby clusters like the colour–magnitude relation and the fundamental plane, preserve an incredibly small scatter, thus supporting the idea that elliptical galaxies are passively evolving systems with stellar populations formed at $z > 2$–3. Old stellar ages in early type galaxies are confirmed also by their spectroscopic features. It is important, in this respect, to remember that the population of early type observed in high redshift clusters does not necessarily comprises all the early type galaxies existing at redshift zero. In the last years, in fact, evidence is accumulating for a large fraction of early–type galaxies in clusters being only recently transformed from other galaxy types. Dressler et al. (1997), for example, have shown that clusters in the redshift range 0.3–0.5 are characterised by a large fraction of spiral galaxies. These galaxies are nearly absent in nearby rich clusters (Dressler 1980), thus suggesting that many

of them could have transformed into early–type galaxies between $z = 0.5$ and $z = 0$. Recent studies (van Dokkum et al. 1999) also find evidence for a high merger fraction in high redshift clusters – events that most likely result in the formation of elliptical galaxies at later times.

More and more data are becoming available for clusters at high redshift. The emerging picture is that there may be a population of galaxies which were formed very early in the history of the cluster and that dominate the cluster cores. Subsequent generations of infalling field galaxies have had their star formation disrupted possibly with an associated starburst. As this transformation progresses, these galaxies may be identified as normal spirals, then galaxies with strong Balmer absorption spectra (k+a galaxies) and finally as S0 galaxies (Dressler et al. 1997).

A particular mention goes here to two projects that have significatively improved our knowledge on the evolution of galaxies in clusters in the last years: the Canadian Network for Observational Cosmology (CNOC, Yee et al. 1996), a study of 15 X–ray selected clusters over the redshift range 0.18–0.55, and the MORPHS collaboration (Smail et al. 1997; Dressler et al. 1999), a study of 10 clusters, primarily optically selected, over the redshift range 0.37–0.56. These two studies also provide the best example of how cluster selection may affect the scientific conclusions. The CNOC team reports a low k+a galaxy fraction (few per cent) while the MORPHS survey finds a significant larger fraction of these objects ($\sim$ 20 per cent). This could, at least in part, be due to the fact that X–ray luminous clusters at $z \lesssim 0.5$ tend to be dynamically older systems than the corresponding optically selected counterparts.

Although the long history of the scientific investigation of clusters of galaxies, many questions still remain unanswered: which physical processes, acting in which environments, are responsible for establishing the morphological mix of galaxy population? Which physical mechanisms are responsible for the transfer of metals from the galaxies into the ICM? Is the Butcher–Oemler effect real? Is the colour–magnitude relation made up of a boring collection of passively evolving objects? Or is it composed of a variegated population of galaxies that had a variety of star formation histories? I will address some of these questions in this thesis.

– Doctor Robert was silent for a moment, then he
started: "[. . .] Because here, between the cloudy
sky and the see below, suddenly visible, I read
their luminous secrets, and mine"
"And the secret, I assume, is this empty space. . . "

Aldous Huxley, The Island

2

Substructures in Cold Dark Matter Haloes

Abstract

In this chapter I present an extensive analysis of the properties of substructures within dark matter haloes (subhalos) using a set of high–resolution numerical simulations of the formation of structure in a ΛCDM Universe. There is now conspicuous evidence for significant fractions of dark matter in galaxy, groups, and galaxy clusters. N–body simulations represent a very powerful tool to investigate the distribution of the dark matter component. If the dark matter substructures can be associated with galaxies, it is then possible to predict properties such as the spatial and mass distribution of subhalos from the simulations. These can be directly compared to observational results. The large sample of haloes used for the investigation permits to draw statistically robust conclusions. In particular, I investigate how the properties of subhalos vary as a function of the mass of the 'parent' halo in which they are located. I also study the mass accretion and merging histories of these substructures. The investigation presented in this chapter is aimed at understanding the predictions of cold dark matter models for the observed properties of cluster galaxies and how these galaxy properties evolve with redshift.

2.1 Introduction

There is large observational evidence for significant fractions of dark matter in galaxies, groups, and galaxy clusters, ranging from flat rotational curves of spiral galaxies (Courteau & Rix 1997; Jimenez et al. 2003; Salucci et al. 2003) and X–ray emission and mass–to–light ratios of ellipticals (de Paolis et al. 1995; Matsushita et al. 1998) to baryon fraction in clusters of galaxies (White et al. 1993; Evrard 1997; Lin et al.

2003). A convincing evidence for substantial amounts of dark matter, even in the very inner regions of galaxies, comes from recent HI studies of dwarf and low surface brightness galaxies (Warren et al. 2003; Masset & Bureau 2003). If observed galaxies have significant fractions of dark matter, then it is possible to associate the dark matter substructures with real galaxies and use the numerical simulations to predict properties such as spatial and mass distribution that can be directly compared to observational results.

As discussed in the previous chapter, the formation and evolution of structure in the Universe is a topic of fundamental interest. In the last decades, the Cold Dark Matter (CDM) model (see Sec. 1.3.2) has been extensively studied and has had considerable success in reproducing observational results, both on galactic and on cluster scales. In fact, the CDM model with the 'concordance' set of cosmological parameters (ΛCDM) has been so successful that it can now be considered a standard paradigm for the formation of structure in the Universe. According to this model, the dominant force that drives structure formation is gravity, and large systems like galaxy clusters are formed via hierarchical merging of smaller structures.

As explained in Section 1.4, numerical simulations of gravitational clustering of dark matter are an indispensable tool for investigating the non-linear growth of structures in its full geometrical complexity. Until recently, dissipationless simulations suffered from the so-called *overmerging* problem, i.e. substructures disrupt very quickly within dense environments (Katz & White 1993). The overmerging problem was traditionally explained by the lack of dissipation in N–body simulations (Katz et al. 1992; Summers et al. 1995). It was thought that baryons would sink into the centre of dark matter haloes and they would thus be more robust to disruption. However, both analytic work (Moore et al. 1996a) and high resolution simulations (Tormen et al. 1997; Ghigna et al. 1998; Klypin et al. 1999b; Ghigna et al. 2000) have demonstrated that the cores of dark matter haloes that fall into a cluster can actually survive as self-gravitating objects orbiting in the smooth dark matter background of the cluster, provided high enough force and mass resolution are used.

Recent high-resolution simulations (Ghigna et al. 2000; Springel et al. 2001a) have also shown that the abundance of these substructures is in agreement with the observed abundance of galaxies in clusters, suggesting a natural one-to-one identification between luminous cluster galaxies and dark matter substructures.

An interesting claim is that the shape of the substructure *mass function*, i.e. the number density of substructures as a function of mass, is independent of the mass of the parent halo (Moore et al. 1999a). It is not obvious that this should be the case because, in CDM cosmologies, the initial conditions do depend on scale and galaxies form several billion years before clusters. Dynamically, galactic haloes and cluster haloes are fundamentally different: clusters of galaxies are relatively young systems in which galaxies have only had time to make a few orbits; galaxies are significantly older and their satellites have completed many orbits. This implies

that the satellites in galaxy-sized haloes have higher probability to be disrupted, either because of numerical resolution effects or because of physical processes such as dynamical friction and tidal stripping.

Dynamical friction drives the satellites towards energy equipartition with the smooth distribution of the cluster particles. Since satellites are more massive than single particles, they are slowed down, and their orbits shrink and become more circular as the satellites lose energy and angular momentum. Eventually the satellites are deposited in the centre of the cluster potential well. On the other hand, global tides due to the interaction with the main halo, or tides generated by encounters with other satellites, can strip–off some mass from the satellite. Such an effect is more 'extreme' for satellites on very eccentric orbits that pass through the cluster core.

The destruction of the satellites is obviously counteracted by the accretion of new satellites. It is then clear that to correctly predict the abundances and the properties of the substructure population it is necessary to model in a self–consistent way both the orbital dynamics of the satellites and the evolution of the parent halo in a fully cosmological context.

Observationally, the predicted abundance of substructures in clusters is one of the major successes of the CDM model (Springel et al. 2001a), but on galactic scales, it appears that simulations predict more substructures than are visible by almost two orders of magnitude (Kauffmann et al. 1993; Moore et al. 1999b; Klypin et al. 1999b; Tasitsiomi 2002). This is commonly referred to as the 'dwarf galaxy crisis' of CDM. There have been suggestions that the solution to this problem lies in processes such as heating by a photo-ionising background that suppresses star formation in small haloes at early times (Efstathiou 1992; Bullock et al. 2000; Somerville 2002; Benson et al. 2002). Alternatively, it has been suggested that the nature of dark matter may be different than assumed in the canonical ΛCDM model, for example by being *warm* or *self-interacting*, both of which could selectively eliminate small-scale structure. However, self-interactions appear to be relatively ineffective in reducing the number of subhalos, unless the assumed cross-section is unreasonably large (Colín et al. 2002).

A less drastic resolution was suggested by Stoehr et al. (2002) who noted that it might be possible to identify the observed Galactic satellites with the few most massive subhalos and that the rest contain no stars. Direct evidence for the large population of dark satellites predicted by CDM models also comes from the anomalous flux ratios of multiply imaged quasars (Mao & Schneider 1998; Chiba 2002; Dalal & Kochanek 2002).

So far, a detailed numerical analysis of substructures has only been carried out in high resolution re-simulations of a few individual haloes (Moore et al. 1999a; Ghigna et al. 2000; Springel et al. 2001a). In this chapter, we carry out a systematic analysis of substructures as a function of the mass of the parent halo and as a function of environment. We study the mass function of subhalos, their radial distributions and their merging and mass accretion histories.

As explained above, the questions we address in this chapter are related to quantities that are of fundamental interest for galaxy formation, because dark matter haloes and substructures represent the birth places of luminous galaxies. Their accretion and merging histories regulate then the rate at which baryons can cool, determining in this way the rate at which stars form in galaxies as a function of cosmic time.

The layout of the chapter is as follows: in Section 2.2 we describe the simulations that we use in this analysis; in Section 2.3 we give a brief description of the algorithm used to find substructures in haloes; in Section 2.4 we present the subhalo mass function and study its dependence on the mass of the parent halo, in Section 2.5 we analyse the mass distribution of the largest substructures; in Section 2.6 we study the radial distribution of substructures; in Section 2.7 we discuss the merging and mass accretion histories of substructures, both as a function of mass and as a function of environment. A summary and a discussion of the results obtained are presented in Section 2.8.

2.2 N–body simulations

In this work we use collisionless simulations of the formation of structure in a ΛCDM Universe generated using the 'zoom' technique (Tormen et al. 1997; Katz & White 1993, see Sec. 1.4 for a more detailed description of the technique). We study a set of 11 high-resolution re-simulations of galaxy clusters (5 of mass $10^{14}\,h^{-1}\mathrm{M}_\odot$ and 6 of mass $10^{15}\,h^{-1}\mathrm{M}_\odot$), and a high resolution re-simulation of a 'typical' region of the Universe. The simulations were carried out with the parallel tree-code GADGET, designed to run on massively parallel supercomputers with distributed memory. A full description of the code is given in Springel et al. (2001b).

One of our massive clusters was taken from the 'S-series' studied by Springel et al. (2001a), where the parent simulation employed was the GIF-ΛCDM model carried out by the Virgo Consortium (Kauffmann et al. 1999). This parent simulation followed 256^3 particles of mass $1.4 \times 10^{10}\,h^{-1}\mathrm{M}_\odot$ within a comoving box of size $141.3\,h^{-1}\mathrm{Mpc}$ on a side. The other cluster re-simulations and the simulation of the field region were selected from the Very Large Simulation (VLS), carried out by the Virgo Consortium (Jenkins et al. 2001; Yoshida et al. 2001). The simulation was performed using a parallel P^{3}M code (Macfarland et al. 1998) and followed 512^3 particles with a particle mass of $7 \times 10^{10}\,h^{-1}\,\mathrm{M}_\odot$ in a comoving box of size $479\,h^{-1}\mathrm{Mpc}$ on a side. In all cases, the parent simulation and the re-simulations were characterised by the following cosmological parameters: $\Omega_0 = 0.3$, $\Omega_\Lambda = 0.7$, spectral shape $\Gamma = 0.21$, $h = 0.7$ and normalisation $\sigma_8 = 0.9$.

In Table 2.1, we summarise some important numerical parameters of the simulations used. We will refer to our five high-mass clusters of mass resolution $2 \times 10^9\,h^{-1}\mathrm{M}_\odot$ as type 'B1', and to the low-mass clusters as type 'B2'. These simula-

Name	Description	m_p $[h^{-1}\mathrm{M}_\odot]$	z_start	ϵ $[h^{-1}\mathrm{kpc}]$	N
B1	$10^{15}\,h^{-1}\mathrm{M}_\odot$ clusters	2×10^9	60	5.0	5
B2	$10^{14}\,h^{-1}\mathrm{M}_\odot$ clusters	2×10^9	60	5.0	5
S2	$10^{15}\,h^{-1}\mathrm{M}_\odot$ cluster	1.36×10^9	50	3.0	1
M3	field simulation	1.7×10^8	120	1.4	1

Table 2.1: Numerical parameters for the simulations used. All the simulations were carried out assuming a ΛCDM cosmology with cosmological parameters $\Omega_0 = 0.3$, $\Omega_\Lambda = 0.7$, $\Gamma = 0.21$, $\sigma_8 = 0.9$, and $h = 0.7$. In the table, we give the particle mass in the high resolution region m_p, the starting redshift of the simulation z_start, the gravitational softening in the high-resolution region ϵ, and the number of simulations in each group N.

tions were carried out by Barbara Lanzoni as part of her PhD thesis and were previously used in Lanzoni et al. (2003). The 'S2' simulation is taken from the 'S-series' of Springel et al. (2001a). The field region 'M3' was adopted from the 'M-series' studied by Stoehr (2003).

Fig. 2.1 shows density maps for 4 of our massive clusters. The density maps are obtained projecting onto the xy–plane all the particles inside a cubic box of 10 Mpc on a side. The box is centred on the coordinates of the most bound particle of the main halo. Note the variety of cluster structure and the large amount of substructures that is clearly visible in the figure.

2.3 Identification of dark matter substructures

The first basic step in the analysis of cosmological simulations is the identification of virialized groups of particles. The most widely used technique is given by the friends–of–friends (FOF) algorithm. This basically links together all the particles with a separation less than b times the mean inter–particle separation. It has been shown that, with an appropriate choice of the linking length, it is possible to select groups close to the virial overdensity predicted by the spherical collapse model (see Sec. 1.3.4). The FOF algorithm is quite 'easy' to implement and fast and it has been shown by a number of authors that the halo mass function produced is in quite good agreement with the predictions of Press–Schechter theory (Cole & Lacey 1996; van den Bosch 2002). However, the algorithm has the tendency to occasionally link together independent structures across 'bridges' of particles. Most importantly, the FOF algorithm is not able to detect substructures in larger virialized systems. It is therefore not possible to compare the distribution of haloes with the distribution of galaxies, since the latter are usually found within larger systems.

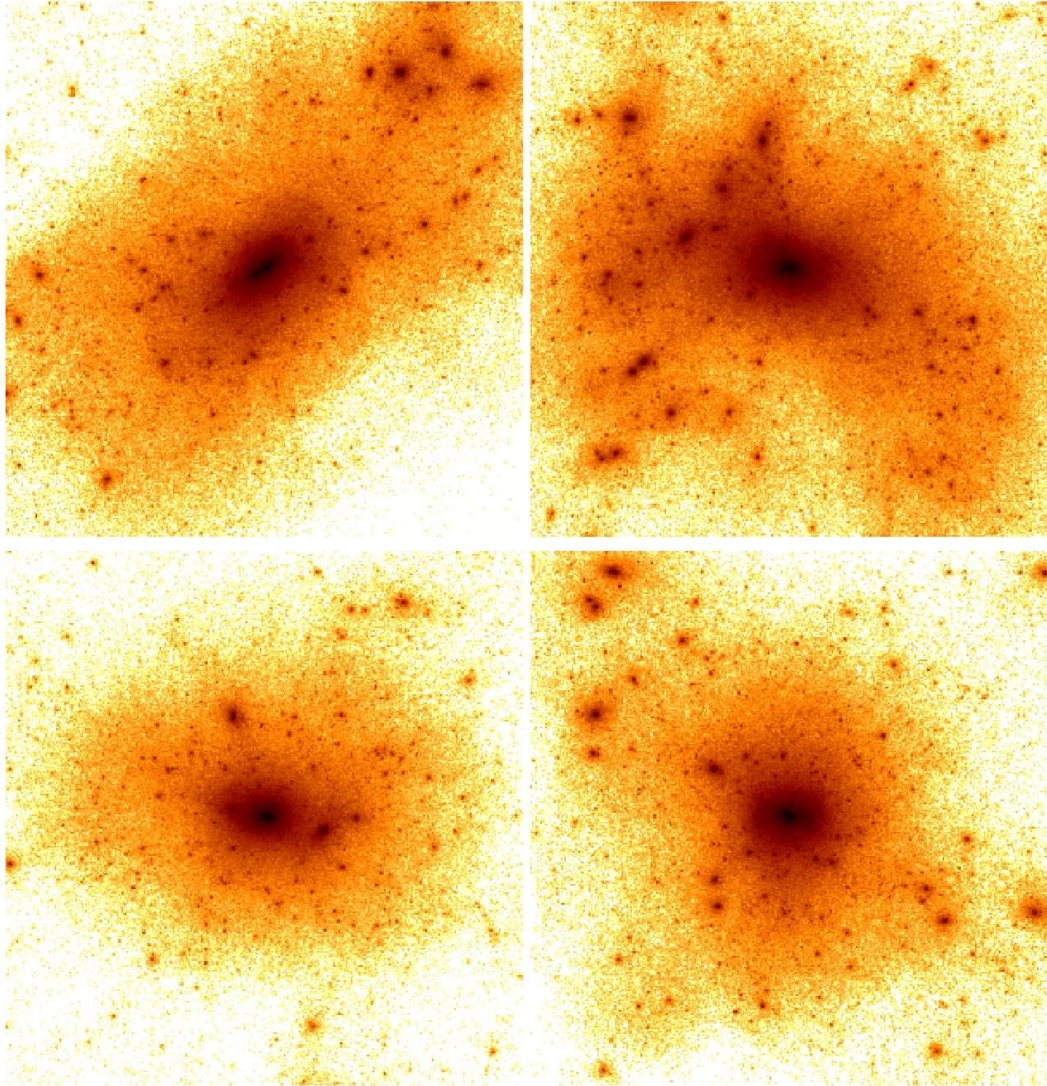The identification of substructures in dark matter haloes is a difficult technical

Figure 2.1: Density maps of 4 of our massive cluster simulations. The maps are built using all the particles inside a box centred on the coordinates of the most bound particle of the main halo and of size 10 Mpc on a side.

problem and many different algorithms have been developed to accomplish this task in the last years. In the hierarchical friends-of-friends algorithm (HFOF) (Gottlöber et al. 1998), the linking length of FOF is reduced in discrete steps, thus selecting groups of higher and higher overdensity. The choice of the different levels of linking lengths

is somewhat arbitrary and the algorithm requires an iterative procedure in order to find different hierarchical levels. The bound density maximum algorithm (BDM) (Klypin et al. 1999a) iteratively determines a bound subset of particles in a sphere around a local density maximum. The BDM algorithm thus estimates the physical properties of substructures more accurately because it separates background particles from particles that are bound to the halo. However, it implicitly assumes that the halo is spherically symmetric. On the other hand, the HFOF algorithm can deal with haloes of arbitrary shapes, non only symmetric systems.

Another approach is given by the SKID algorithm (see http ref: http://www-hpcc.astro.washington.edu/tools) in which the density around each particle is evaluated using an SPH smoothing kernel[1]. The particles are then moved along the density gradients towards a local density maximum. Particles that end–up in the same local maximum are linked together using a FOF algorithm and then checked for self–boundness. Only self–bound groups with more than a user specified minimum number of particles are kept as genuine substructures.

As explained above, each of these algorithms has its own advantages and weaknesses, so that arguably none of them is completely satisfactory yet. In this work, we use the algorithm SUBFIND proposed by Springel et al. (2001a), which combines ideas used in other group finding techniques with a topological approach for finding substructure candidates. SUBFIND can handle haloes of arbitrary shape, does not require an iterative procedure for finding subhalo candidates, and is capable of detecting arbitrary levels of 'subhalos within subhalos'. In the following, we briefly summarise how the method works.

In a first step, a standard FOF algorithm is used to identify virialized parent haloes. We adopt the standard value $b = 0.2$. The next step is to compute an estimate of the local density at the position of each particle in the group. To this end, we employ an adaptive kernel interpolation method similar to the one used in smoothed particle hydrodynamics. In the resulting density field, we define as *substructure candidates* locally overdense regions which are enclosed by isodensity

---

[1]The key advance of SPH is to associate with each particle a *smoothing length h*, representing the finite spatial extent of the particle, which can differ in value for separate particles, as well as vary in time. The smoothing length is used in calculating all hydrodynamic terms, since rather than viewing the density of the particle as a spatial delta-function, the spatial density distribution of particle i is represented by a kernel function, such that:

$$\rho_i = \sum_{j=1}^{N} m_j\, W(\mathbf{r}_{ij}, h_i)$$

where $\mathbf{r}_{ij}$ represents the distance between the particles i and j; m_j is the particle mass and $W(\mathbf{r}, h)$ is the *smoothing kernel*. Different choices are possible for the form of the smoothing kernel. Note, however, that for the method to work, it is necessary that this kernel function has compact support, and that it is at least singly differentiable.

contours that traverse a saddle point. Our method for finding these regions can be visualised as follows: we reconstruct the density field by considering particles in order of decreasing density, thus working our way from high to low density. This corresponds to gradually lowering a global threshold in the density field sampled by the simulation particles. Isolated overdense regions grow slowly in size during this process. When two such separate regions coalesce to form a single region, their density contours join at a saddle point. Each time such an event occurs, we have found two substructure candidates.

After the regions containing substructure candidates have been identified, we apply an unbinding procedure where we iteratively reject all particles with positive total energy in order to eliminate 'background' particles that do not belong to the sub-halo. For the purposes of this study, we consider all substructures that survive this unbinding procedure, and still have at least 10 self-bound particles, to be genuine subhalos.

In summary, the algorithm SUBFIND decomposes a given particle group into a set of disjoint and self-bound substructures, each of which is identified as a locally overdense region in the density field of the background halo.

In Fig. 2.2 we show an example of subhalo decomposition, with SUBFIND, of a FOF halo identified in one of our massive cluster re–simulations at redshift zero. All the particles in the FOF group are shown in the top left panel; the bottom left panel shows all the particles that form the main subhalo, i.e. the self–bound particles of the FOF group. In the top right panel, each of the substructures identified by SUBFIND is shown with a different colour and the bottom right panel shows particles that are not bound to any subhalo.

Note that SUBFIND classifies all the particles inside a FOF group either as belonging to a bound substructure or as being unbound. The self-bound part of the FOF background halo itself (see the bottom left panel of Fig. 2.2) will then also appear in the substructure list. We will exclude it when referring to subhalos or substructures in the following analysis.

Fig. 2.3 shows a case in which the FOF algorithm erroneously links together two independent structures. The algorithm SUBFIND is able to deal with these cases and reliably decomposes the FOF group into its constituent parts.

2.4 The subhalo mass function

The sample of parent haloes used for studying the subhalo mass function consists of 6, 5, 34 and 100 haloes in the mass ranges 8.68×10^{14}–1.79×10^{15} (from simulations B1 and S2), 6.99×10^{13}–1.27×10^{14} (from simulations B2), 7.0×10^{12}–2.0×10^{13} (from simulation M3) and 7.0×10^{11}–$2.0 \times 10^{12}\, h^{-1}\mathrm{M}_\odot$ (from simulation M3).

The resulting subhalo mass functions are shown in Fig. 2.4, where we plot the
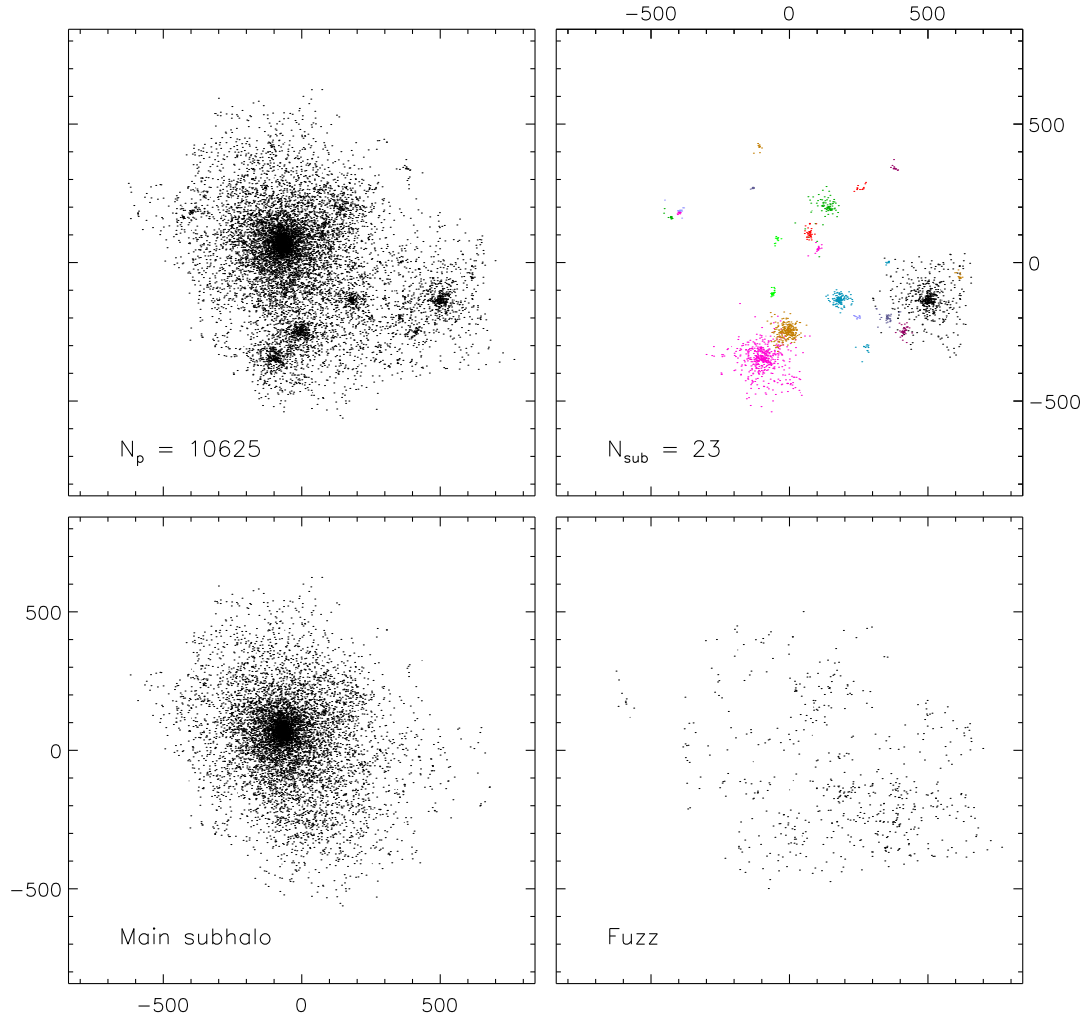
Figure 2.2: Example of a halo decomposition with SUBFIND. The top left panel shows a small FOF-group (10625 particles), identified at $z = 0$ in one of our cluster simulations. SUBFIND identifies 24 subhalos within this group. The largest subhalo represents the background halo and is shown on the bottom left. The other 23 subhalos are plotted on a common panel on the top right. Particles not bound to any of the subhalos represent the "fuzz" component, and are displayed on the lower right. These particles primarily lie close to the outer edge of the group. Spatial coordinates are given in h^{-1} kpc.
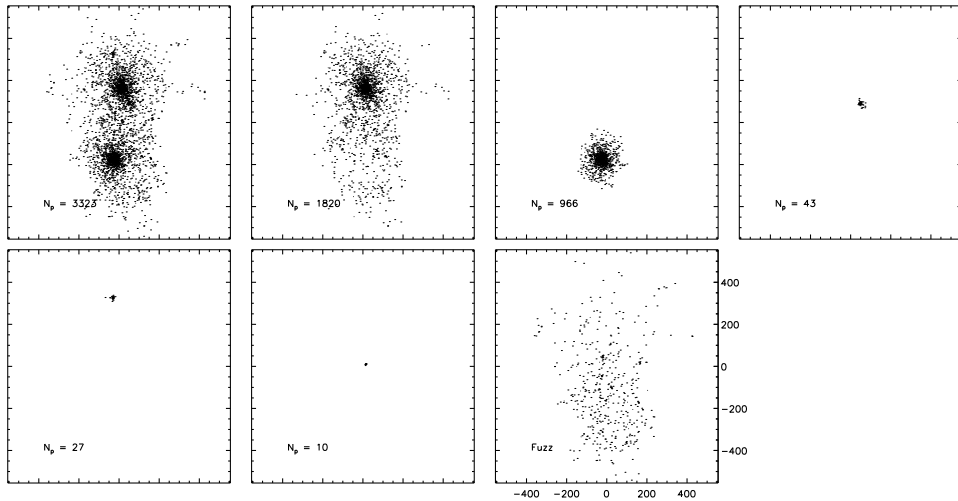
Figure 2.3: A case in which the FOF algorithm erroneously links together two independent structures across a bridge of particles (top left panel). The remaining panels show how SUBFIND decomposes the FOF group into its constituent parts.

differential mass functions for parent haloes of different mass. The histograms are computed by stacking all the haloes in the given range of mass and the error bars represent Poisson errors. The solid line in each of the panels is a power-law fit to the measured differential mass function; the fit is performed using the least absolute deviation method over the range of mass shown by the line. In all the cases the slope of this unrestricted fit is close to -1 (it is equal to -0.98 for the top left panel, -0.97 for the top right panel, -1.11 for the bottom left panel and -1.13 for the bottom right panel). However, we note that the lowest mass bins, which have the smallest statistical errors, are best fit with a slightly shallower slope: if we restrict the fit to the 4 lowest mass bins, the slope is -0.94 for the top left panel and -0.85 for the middle left panel. These are closer to the value -0.8, measured by Helmi et al. (2002) for a single cluster simulation of extremely high-resolution.

Also note that a slope shallower than -1 at the low-mass end implies that the integrated mass in substructures remains bounded and is dominated by the most massive subhalos. It is likely that our subhalo mass functions are steepened somewhat by a cut-off in abundance for very massive substructures.

Fig. 2.5 shows the cumulative mass function for all the haloes used in the sample. To compare the different subhalo mass functions, we have rescaled the subhalo mass by dividing by the virial mass of the parent halo. Each line represents the average cumulative mass function over all the haloes in each mass bin. Note that in this
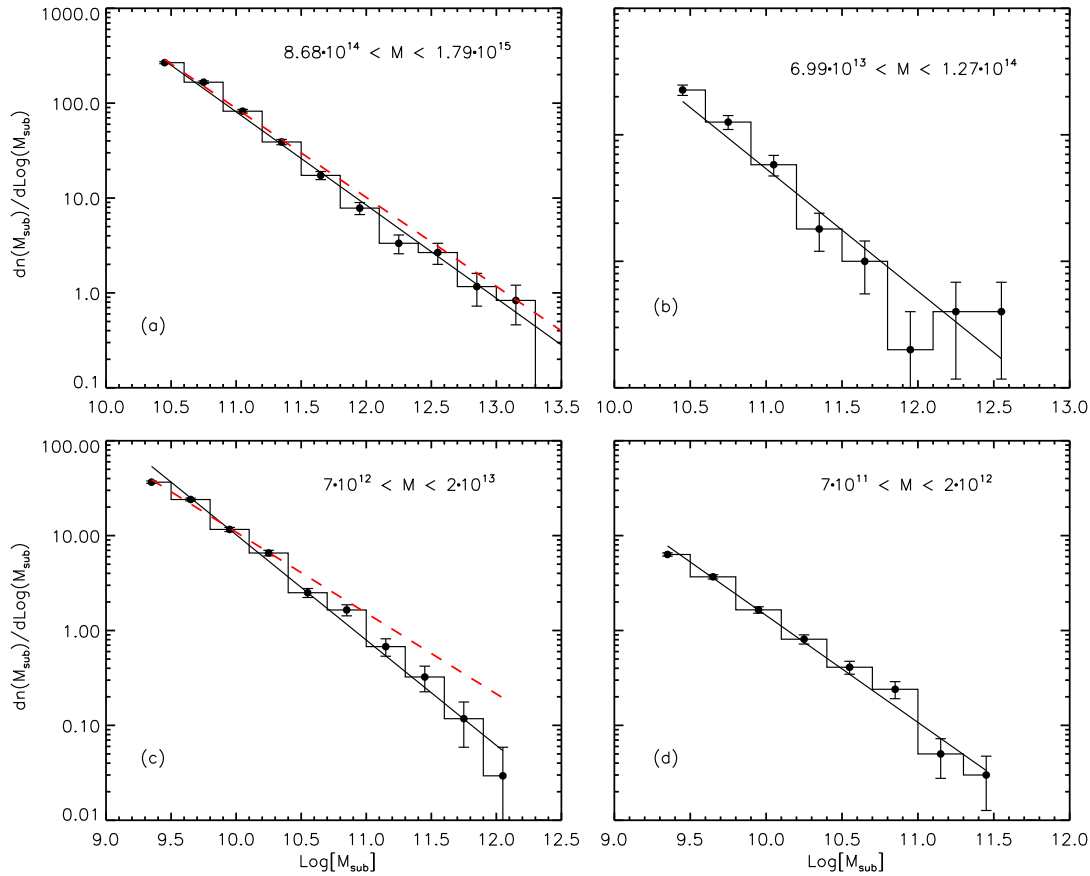
Figure 2.4: Panel (a) – (d): the differential mass function of subhalos residing in parent haloes of different mass. The solid black line represents a power law fit to the mass function. The dashed red line shown in panel (a) and (c) represents a fit restricted to the 4 lowest mass bins. The masses are in units of $h^{-1}M_\odot$. The range of mass of the haloes used in each bin is indicated in each panel.

chapter we define the 'virial mass' as M_{200}, the mass within a sphere of density 200 times the critical value at redshift zero. The lines end at different places because of the differing mass resolution of the simulations (see Table 2.1). Finally, in Fig. 2.6, we show the differential subhalo mass functions in units of rescaled mass. We find that all four cumulative and differential mass functions agree within the statistical errors.

We note that the 'universality' of the subhalo mass function seen here appears to be quite robust with respect to numerical resolution. In Fig. 2.7 we compare the average
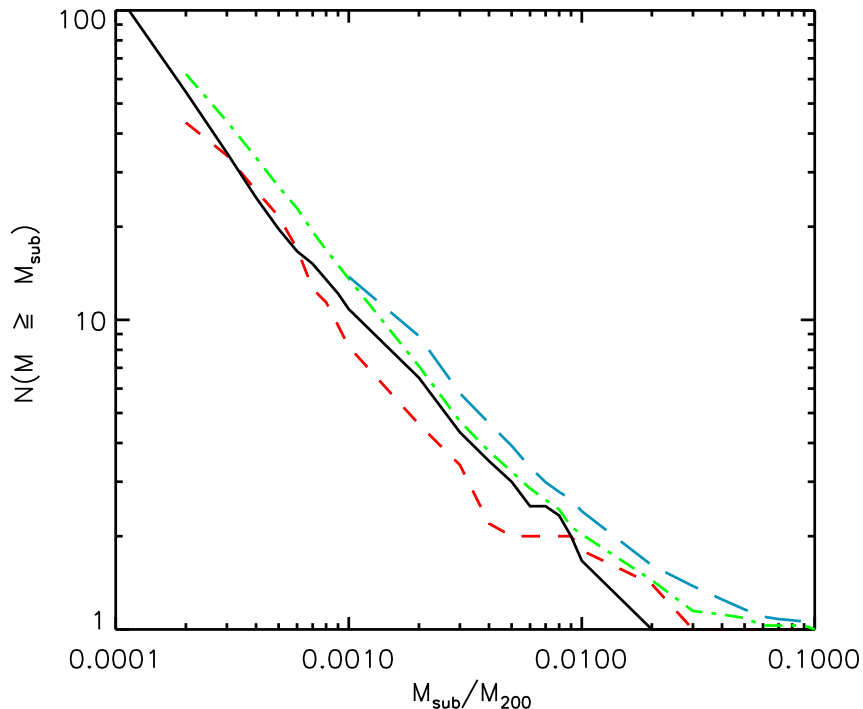
Figure 2.5: The cumulative mass function of subhalos in units of rescaled subhalo mass. The solid black line is for haloes with mass $\simeq 10^{15}\,h^{-1}\mathrm{M}_\odot$, the dashed red line is for haloes with mass $\simeq 10^{14}\,h^{-1}\mathrm{M}_\odot$, the dash-dotted green line is for haloes with mass $\simeq 10^{13}\,h^{-1}\mathrm{M}_\odot$, and the long-dashed blue line is for haloes with mass $\simeq 10^{12}\,h^{-1}\mathrm{M}_\odot$.

cumulative mass functions for haloes with mass $\simeq 10^{14}\,h^{-1}\mathrm{M}_\odot$ from simulations B2 and M3. Here we averaged 5 haloes for simulations B2, and 4 for simulation M3, to reduce the object-to-object scatter that is unavoidable for small numbers of subhalos. Despite an order of magnitude difference in numerical resolution, the agreement between the simulations is good. We are able to resolve the right number of objects in the low-resolution simulation above its resolution limit (shown as a vertical dotted line in the figure). A similar result was obtained by Springel et al. (2001a, see their Fig. 5) using a set of 4 re–simulations of the same cluster with systematically increasing resolution, thereby allowing a direct study of numerical convergence. This showed in particular that the S2 simulation, used here, has well converged to the properties of a much higher resolution simulation above its own resolution limit, as used here. Further support for our results was also found by Stoehr et al. (2003, see
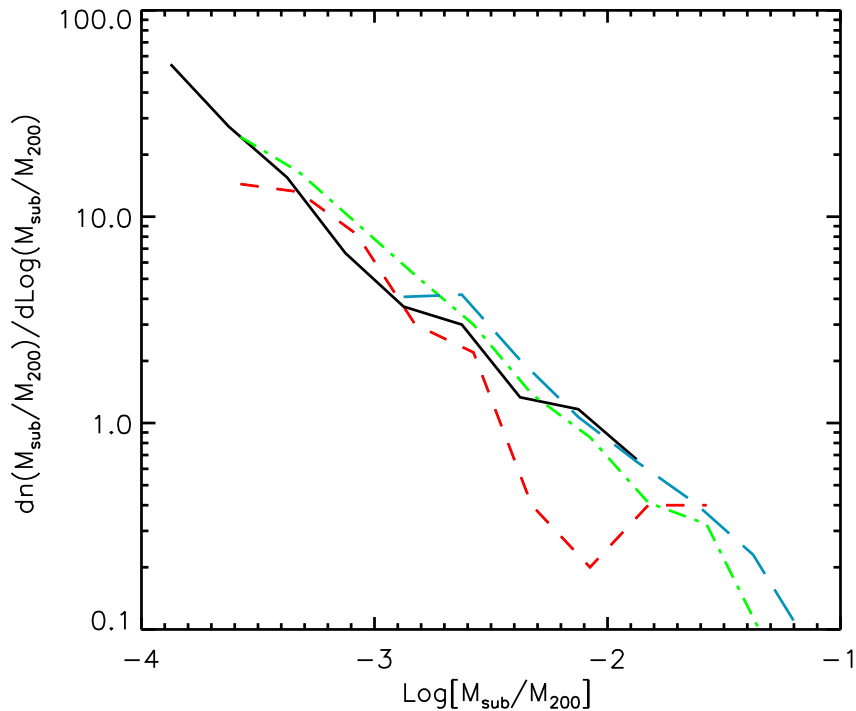
Figure 2.6: The differential mass function in units of rescaled subhalo mass; the different line styles and colours are the same as in Fig. 2.5.

their Fig. 3). They compared the S–series simulations from Springel et al. (2001a) with an extremely well resolved re–simulation of a Milky–Way sized halo. This latter simulation used an updated version of the simulation code and more conservative integration parameters than used here (following Power et al. 2003), suggesting that the subhalo mass function is a relatively robust quantity and that the simulations we discuss here are adequate for our purposes.

As a further check of the robustness of our results we also compare the internal structure of subhalos drawn from our different simulations. Fig. 2.8 shows the correlation between the substructure mass and the third power[2] of the maximum circular velocity, V_{max}, measured directly from the circular velocity curve of each subhalo.

---

[2]From the virial theorem, one finds $V^2 \propto M/R$. For a constant density, $R \propto M^{1/3}$. Therefore $M \propto V^3$. Note that the mass of a subhalo of given V_{max}, depends on its orbital history, which determines the extent of tidal disruption it suffered. However, the orbital distribution does not depend significantly on mass (Ghigna et al. 1998) and therefore we will still have $M \propto V^3$.
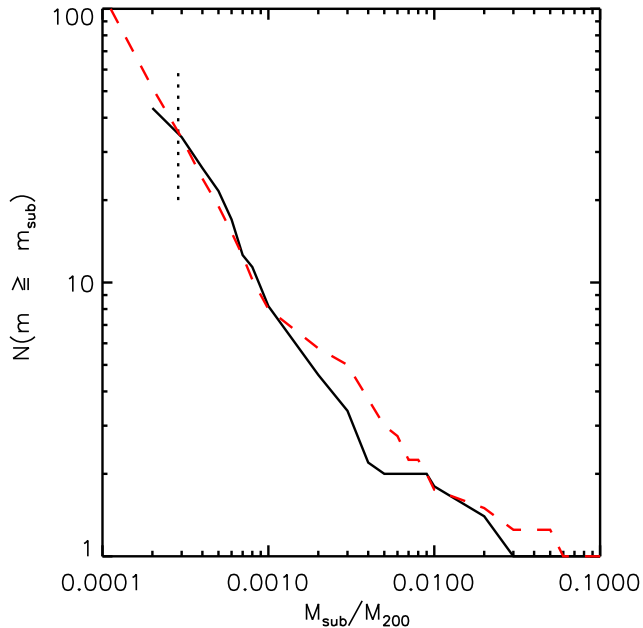
Figure 2.7: The cumulative mass function of subhalos, in units of rescaled subhalo mass, for haloes with mass $\simeq 10^{14}\, h^{-1} \mathrm{M}_\odot$. The solid line corresponds to the average of haloes from simulations B2 and the dashed line to haloes from simulation M3. The vertical dotted line shows the resolution limit corresponding to simulations B2.

Different colours are used for substructures drawn from different simulations. Note that, for the range of masses shown in the plot, substructures drawn from simulation M3 contain at least 60 particles. While the scatter is clearly large for haloes with such a low number of particles, the good general agreement between the runs suggests that the smallest substructures in our lower resolution simulations have an internal structure that is still reliably resolved, at least in a statistical fashion.

Our results confirm the conclusion drawn by Moore et al. (1999a): the mass function of substructures appears to be almost independent of the mass of the parent halo. While our results are consistent with such a 'scale–free' subhalo mass function, the halo–to–halo scatter in our simulation set is quite large, preventing us from putting tight constraints on the accuracy with which the 'scale–free' subhalo mass function is preserved when haloes of different mass are considered. And hence there is still room for weak trends with mass. A clear detection of these would require simulations with larger dynamic range, and larger samples of simulated haloes for each mass bin.

As we discuss in more detail in Sec. 2.7.2, our findings suggest that the destruction of satellites due to the physical processes of dynamical friction and tidal stripping
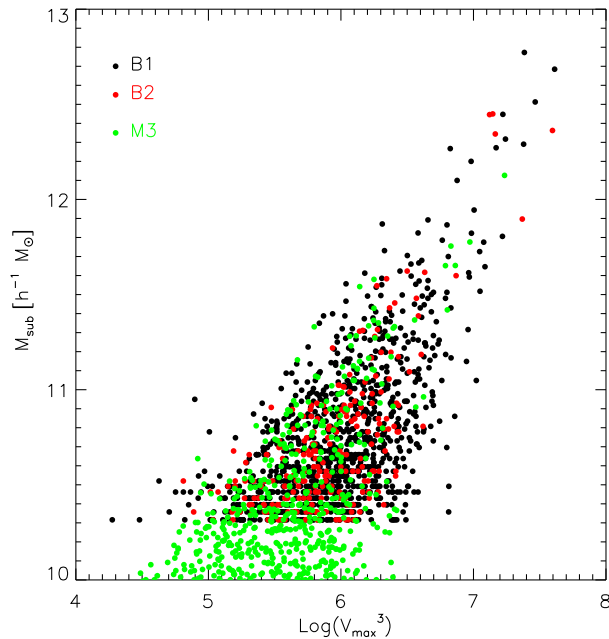
Figure 2.8: Substructure mass as a function of V_{max}^3 for subhalos drawn from our different simulations. Black circles are used for subhalos that reside in haloes with mass $\sim 10^{15} \, h^{-1} \, M_\odot$ (from simulations B1), red circles for subhalos in haloes with mass $\sim 10^{14} \, h^{-1} \, M_\odot$ (simulations B2), and green circles for subhalos in haloes with mass $\sim 10^{13} \, h^{-1} \, M_\odot$ (simulation M3). V_{max} was determined as the maximum of the circular velocity curve of each subhalo.

on one hand, and the accretion of new satellites on the other hand, cancel out in such a way that the subhalo mass function does not depend or at best very weakly depends on the mass of the parent halo. The reason for the invariance of the subhalo mass function may lie in the physical nature of this dynamical balance, which may be insensitive to the slightly broken scale-invariance of dark haloes themselves. This shows up, for example, as a mass–dependence of halo concentrations with more massive haloes having a lower median concentration. Some fully analytic models for the subhalo abundance have been developed (e.g. Sheth 2003), but they are presently not able to account for mass-loss and dynamical friction self-consistently, and so provide little guidance to answer this interesting question. A full understanding of the apparent 'conspiracy' that establishes an almost mass-invariant subhalo mass function will therefore require further simulations.

2.5 The most massive substructures

In this section we investigate whether the properties of the largest substructures depend on the mass of the parent halo. This is interesting since the largest substructures mark the sites where one expects to find the brightest galaxies.

In the following, M_1 refers to the mass of the most massive subhalo and M_2 to the mass of the second most massive subhalo within the virial radius of a given object of virial mass M_{200}. Note that we have excluded from our analysis the subhalo associated with the FOF group itself. In a semi-analytic scheme (see the Chapter 3), it is this 'subhalo' that would host the brightest cluster galaxy (BCG). In Sec. 2.7.2 we will show that, once accreted onto a massive halo, substructures suffer significant stripping, an effect that is more important for substructures accreted at higher redshift. It is then likely that the largest substructures we find within the virial radius at the present time were accreted at relatively low redshift.

In Fig. 2.9, we plot M_1/M_{200} as a function of M_{200} for 434 haloes drawn from all the simulations listed in Table 2.1. This sample includes not only the central clusters in our re-simulations, but also the other haloes found in the high-resolution regions around the re-simulated objects, down to a mass limit of $10^{13}\,h^{-1}\,\mathrm{M_\odot}$. We took care however to exclude *contaminated* haloes that contained low resolution particles. In simulation M3, we selected only haloes with a mass larger than $10^{12}\,h^{-1}\mathrm{M_\odot}$. The small symbols in Fig. 2.9 indicate the value of M_1/M_{200} measured for each individual halo, while the filled red circles represent the median of the distribution. We have taken bins in M_{200} such that there are an equal number (143) of haloes in each bin, except for the last six points, which we treated as a separate bin, corresponding to the central cluster haloes in simulations B1 and S2. The error bars mark the 20th and 80th percentiles of the distribution.

The results in Fig. 2.9 suggest that M_1/M_{200} depends very little on the mass of the parent halo. Interestingly, M_1/M_{200} appears to exhibit less scatter for the most massive haloes, but the number of simulated clusters we have in this high mass regime is rather small, so it is unclear whether this effect is statistically significant.

The results in Fig. 2.9 imply that the median value of M_1 increases in proportion to the mass of the cluster, suggesting that second ranked galaxies will be more luminous in more massive haloes. Note also that the mass of the largest substructure within the virial radius is typically only a few per cent of the virial mass.

In Fig. 2.10, we show the ratio M_2/M_1 as a function of the mass of the parent halo. Once again there is rather little dependence on M_{200} with a possible decrease in the scatter for more massive haloes. Note that the median value of M_2/M_1 is around 0.5. If the stellar masses of the second and third brightest galaxies in a cluster scale simply with the masses of their dark subhalos, they should have K-band luminosities that are equal to within 0.5 mag.
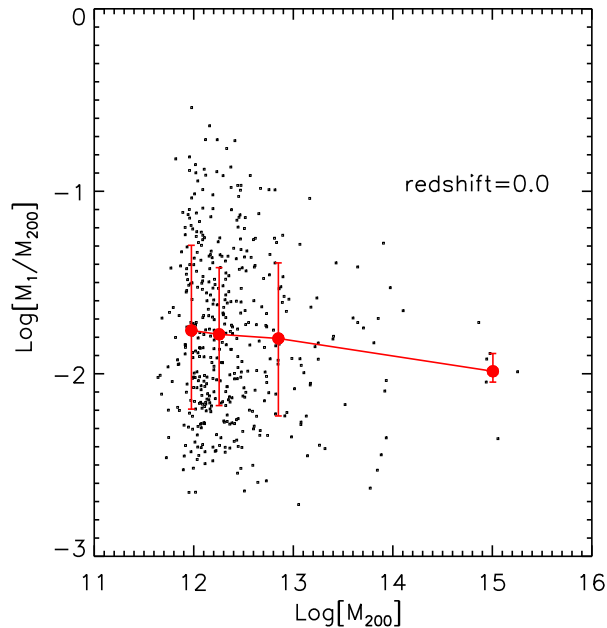
Figure 2.9: Ratio of the mass of the most massive substructure and the parent halo mass as a function of the parent halo mass. The small symbols represent the values measured for each individual halo; the filled red circles are the median in bins of halo mass chosen so that each of them contains the same number of points (143). The last six points, corresponding to the main haloes of simulations B1 and S2, are treated as a separate bin. The error bars mark the 20th and 80th percentiles of the distribution.

2.6 The radial distribution of subhalos

The large sample of subhalos in our simulations allows us to study their radial distribution and to investigate how it depends on the mass of the parent halo. In Fig. 2.11, we plot the number density of substructures as a function of the normalised distance R/R_{200} from the centre of the halo, defined here as the position of the most bound particle in the halo. We show averaged results for haloes with masses $\sim 10^{15}\,h^{-1}\mathrm{M}_{\odot}$, $\sim 10^{14}\,h^{-1}\mathrm{M}_{\odot}$, and $\sim 10^{13}\,h^{-1}\mathrm{M}_{\odot}$, and we limit the analysis to subhalos with masses greater than a fixed fraction (2×10^{-4}) of the virial mass of the parent halo. This fraction is chosen because it lies just above the mass limit where it is possible to identify substructures in all of our simulations. As Fig. 2.5 shows, there are typically ~ 50 subhalos per parent halo with $M_{\mathrm{sub}}/M_{200} > 2 \times 10^{-4}$, so by stacking a large sample of haloes, it is possible to calculate an average density profile that has rather
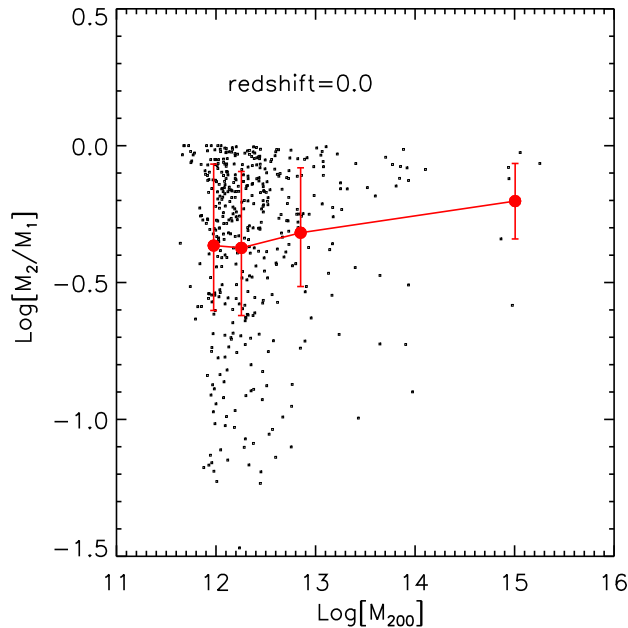
Figure 2.10: Ratio in mass between the two most massive substructures as a function of the parent halo mass. As in Fig. 2.9, small symbols represent the values measured for each individual halo, while the filled red circles give the median in the same bins as in Fig. 2.9. The error bars mark the 20th and 80th percentiles of the distribution.

little noise. Note that the densities plotted in Fig. 2.11 have been normalised to the mean density inside the virial radius. The solid lines with symbols show results for the 3 different parent halo mass ranges defined above. For comparison, we have also plotted the dark matter radial profiles as dashed lines. Note that a small shift in the abscissa has been added to make the plot more readable.

We find that the subhalo profiles are 'anti-biased' relative to the dark matter in the inner regions of the haloes. This agrees with the results of Ghigna et al. (2000). Note that these results have direct consequences on the luminosity profiles in clusters of galaxies. If substructures are the birth place of luminous galaxies, this would imply that the luminosity profile of galaxy clusters will also be anti–biased, i.e. less concentrated with respect to the mass distribution, although this conclusion is substantially complicated by the relation between the substructure mass and the stellar masses of galaxies residing in these substructures (see discussion in Sec. 2.8). Surprisingly, we also find that the radial number density profiles are steeper in low mass haloes than in high mass haloes, a finding that deserves further investigation.
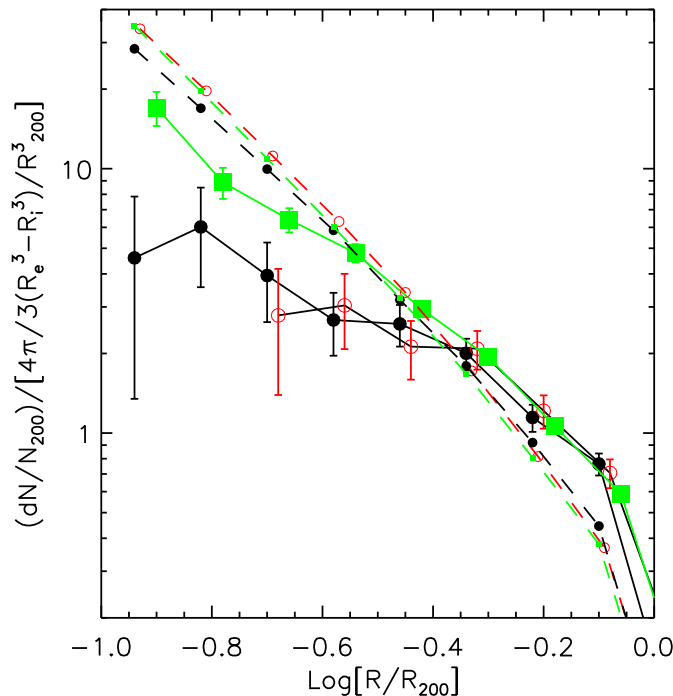
Figure 2.11: Radial distribution of substructures in haloes of different mass. Lengths are given in units of R_{200} and densities are normalised to the mean density inside R_{200}. Symbols connected by solid lines show the number density profile of substructures (filled circles are for $10^{15} \, h^{-1} \mathrm{M_\odot}$ haloes, empty circles for $10^{14} \, h^{-1} \mathrm{M_\odot}$ haloes, and filled squares for $10^{13} \, h^{-1} \mathrm{M_\odot}$ haloes). Symbols connected by dashed lines show the corresponding dark matter profiles.

We now use our highest resolution cluster simulation to investigate whether subhalos of different mass have different radial profiles. In Fig. 2.12, we show the cumulative fraction of substructures as a function of R/R_{200} for subhalos with $M_{\mathrm{sub}} > 0.01 \, M_{200}$ (solid line) and $M_{\mathrm{sub}} \leq 0.01 \, M_{200}$ (dashed line).

As Fig. 2.7 already made clear, there are many more substructures with $M_{\mathrm{sub}} \leq 0.01 \, M_{200}$ than with $M_{\mathrm{sub}} > 0.01 \, M_{200}$ (9749 versus 96). Fig. 2.12 now shows that more massive substructures are preferentially located in the external regions of their parent haloes. This can be understood as a consequence of tidal truncation and stripping effects that quickly decrease the mass of subhalos as they fall into the cluster and reach the dense inner cores of the parent haloes (see Section 2.7.2 for a more quantitative analysis of mass-loss due to stripping).

Also note that this finding can be naturally explained as a consequence of the
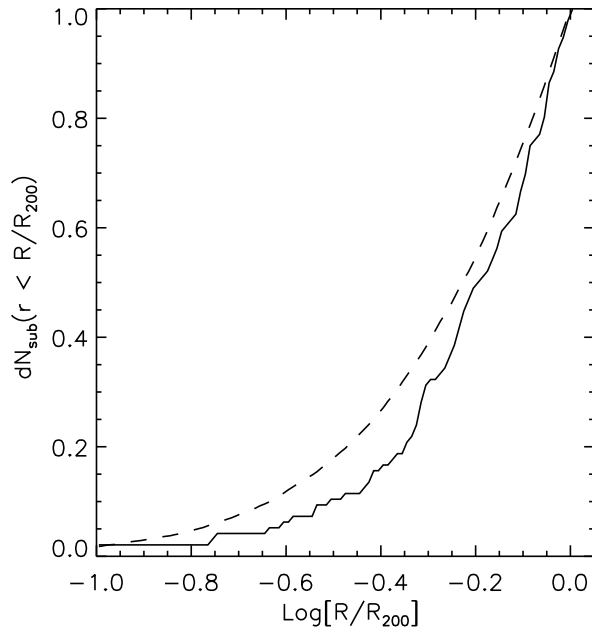
Figure 2.12: Cumulative radial distribution of the number of substructures in two different mass ranges in the simulation M3. The dashed line is for substructures with $M_{\mathrm{sub}} < 0.01\,M_{200}$, and the solid line is for $M_{\mathrm{sub}} > 0.01\,M_{200}$.

orbital decay experienced by substructures. As shown in Tormen et al. (1998), the orbital decay is consistent with expectations based on the combined effects of dynamical friction and mass-loss. As a result, massive substructures are driven to the centre more rapidly than less massive ones: Tormen et al. show that the orbital decay occurs in less than a Hubble time if the initial mass of substructures is larger than 1 per cent of the mass of the main cluster, while the substructures can retain their identity for a significant fraction of the Hubble time if their mass is smaller than 5 per cent of the main cluster mass. Once driven to the centre, massive substructures are destroyed and no longer distinguishable from the central halo; this naturally explains the mass segregation that we see in our simulations.

In Fig. 2.13, we show the cumulative fraction of the total mass of the parent halo that is in substructures as a function of normalised distance from the halo centre. The different lines and symbols have the same meaning as in Fig. 2.11 and represent median relations for all the haloes in each mass bin. The error bars mark the 20th and 80th percentiles of the distribution. The mass fraction in substructures rises from $\simeq 1$ per cent at a radius $\simeq 0.3\,R_{200}$ to ~ 6 per cent at $r \sim R_{200}$. Note that the total mass fraction is dominated by the small number of most massive subhalos, and is
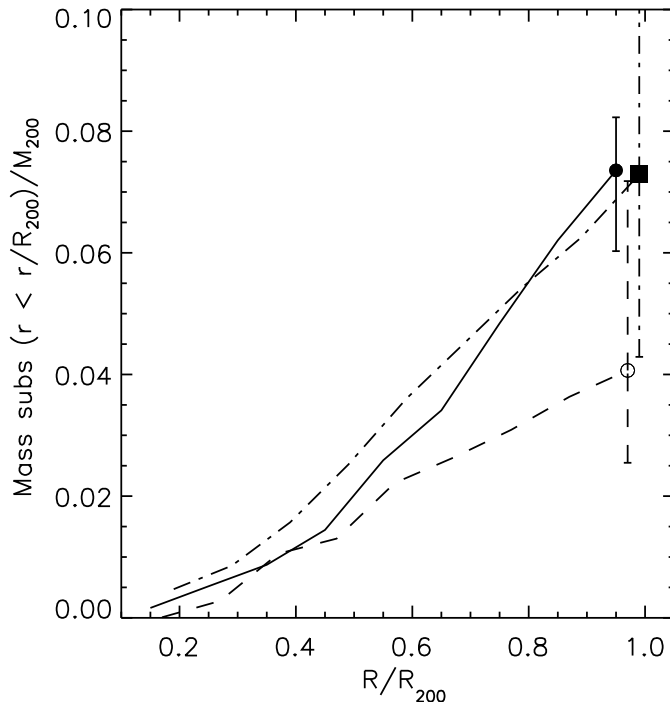
Figure 2.13: Cumulative mass fraction in substructures as a function of the distance from the halo centre. The solid line is for haloes of mass $\simeq 10^{15}\,h^{-1}\mathrm{M}_\odot$, the dashed line for haloes of mass $\simeq 10^{14}\,h^{-1}\mathrm{M}_\odot$, and the dash-dotted line for haloes of mass $\simeq 10^{13}\,h^{-1}\mathrm{M}_\odot$. The error bars on the last point mark the 20th and 80th percentiles of the distribution.

hence a rather noisy quantity that shows large variations from system to system. The mass fraction may also reach values above $\simeq 10$–15 per cent, but then the underlying FOF parent halo is typically quite aspherical, with the most massive subhalo often lying outside the formal radius R_{200} of the parent halo.

2.7 Subhalo histories

So far we have analysed the properties of subhalos only at redshift $z = 0$. In this section, we turn to the time evolution of the masses of subhalos and their merging histories.

In order to carry out this analysis, we have measured *merger trees* for each subhalo from the simulations. These trees allow us to specify all the progenitors (or the descendants) of a substructure at each epoch. To build the merger trees, we use a

slightly modified version of the code described in Springel et al. (2001a). We briefly review the main features of the relevant algorithms in the following section.

2.7.1 Constructing merging trees

Following Springel et al. (2001a), we build the merger trees adopting the following definitions:

- a subhalo S_B at redshift z_B is the *progenitor* of a subhalo S_A at redshift z_A (with $z_A < z_B$) if more than one half of the N_{link} most bound particles belonging to S_B ends up in S_A;

- a subhalo S_B at redshift z_B is the *progenitor* of FOF group G_A at redshift z_A if more than one half of the particles belonging to S_B ends up in G_A and, analogously, we say that a FOF group G_B is a *progenitor* of a subgroup S_A if the former contains more than one half of the particles of S_A.

Note that it may happen that a substructure that was just barely above the particle number threshold at some output, may fall below this limit at the next output either because it is evaporated by interaction with other material or because it temporarily fall below the resolution limit. We label these substructures as *volatile* and drop them from further analysis. Specifically, the systems considered volatile are the following:

- FOF groups without any bound subhalo;

- any subhalo which is neither progenitor of any other subhalo nor progenitor to a non volatile FOF group;

- any subhalo which has no progenitor subhalo, but has a progenitor FOF group (it is likely that this structure is just a chance fluctuation or that it has been overlooked in the analysis corresponding to the previous redshift).

Springel et al. (2001a) adopted $N_{\mathrm{link}} = 10$. However, we obtained considerably better results with a value of N_{link} that varies between 10 for the less massive substructures to 100 for more massive ones. In this way, occasional failures of the code when building the merger trees were more robustly avoided. Particularly if substructures undergo major mergers, the code identified in some cases the wrong progenitor for $N_{\mathrm{link}} = 10$, or lost track of an entire subhalo. We have also updated the code so that volatile links to 'evanescent' substructures are avoided.

With these choices, we manage to trace 85–90 per cent of all the substructures in our simulations back to the point when they were first accreted. This fraction goes up to 87–93 per cent if we only consider substructures with more than 100 particles.

2.7.2 Mass accretion history

We now use our merging trees to study the *mass accretion histories* of the subhalos in our simulations. A similar analysis has been carried out by van den Bosch (2002) who has proposed an analytic expression for the mass accretion function based on the extended Press-Schechter formalism (Press & Schechter 1974; Bond et al. 1991; Bower 1991). This function was found to be in excellent agreement with the results of high-resolution N-body simulations. Our aim is to study the mass accretion function for subhalos and study whether there is any dependence on mass or on environment.

We have selected subhalos at redshift $z = 0$ in two different mass ranges ($\simeq 10^{11} \, h^{-1} \mathrm{M}_\odot$ and $\simeq 10^{12} \, h^{-1} \mathrm{M}_\odot$). In order to test for the effects of environment, we selected on one hand subhalos that reside within the virial radius of the massive clusters that formed in simulations B1 and B2 by the present day, and on the other hand subhalos located within the smaller haloes found in simulation M3. In the following, we will refer to the substructures in the clusters as *cluster subhalos* and to the substructures inside the smaller haloes of M3 as *field subhalos*. Note that, since we have excluded from our analysis the main subhalo associated with the FOF group and since on average the most massive substructure has a mass a few per cent of M_{200} (see Fig. 2.9), we end up with very few substructures selected from M3. In particular we have only 5 substructures with a mass $\sim 10^{12} \, h^{-1} \mathrm{M}_\odot$ and 38 substructures with a mass $\sim 10^{11} \, h^{-1} \mathrm{M}_\odot$. The corresponding numbers for the substructures selected from simulations B1 and B2 are 62 and 338.

For each of these samples, we build the mass accretion histories as follows: we start from a particular subhalo at redshift $z = 0$ and construct its merger tree as described in the previous section. At each redshift we track the history of the selected subhalo by linking it with its most massive progenitor.

In Fig. 2.14 we show a typical example of a mass accretion history for a subhalo with mass $2 \times 10^{11} \, h^{-1} \mathrm{M}_\odot$ at redshift zero. In the lower panel, we show the mass accretion history of the subhalo and in the upper panel, the corresponding mass of the halo in which the subhalo resides at each redshift.

In this example, the subhalo was accreted onto a larger halo at redshift ~ 1 (shown as a dotted line on the plot). For times prior to this event the substructure was a main subhalo, i.e. the subhalo corresponding to a FOF group, and its mass grew monotonically in time. From now on, we will refer to this event as the *accretion time* (t_{accr}) of the subhalo. A few snapshots later, at redshift ~ 0.8, the substructure and its host halo were accreted onto the main progenitor of the cluster (shown as a solid line on the plot).

After the subhalo is accreted, it suffers significant tidal stripping and *decreases* in mass. In this particular example, the final mass of the subhalo is $\simeq 40$ per cent of the value at its accretion time. Note that, in the simulations, the mass is not always a monotonic function of the redshift, as one obtains using the Press-Schechter
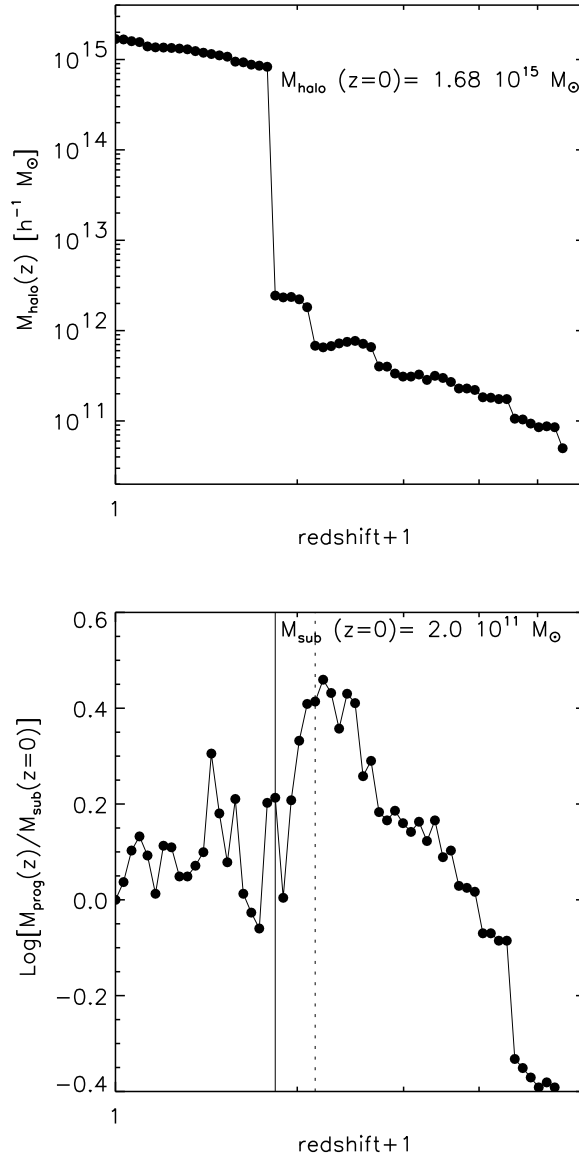
Figure 2.14: Example for a typical mass accretion history for a subhalo of mass $2 \times 10^{11} h^{-1} \mathrm{M}_\odot$ (lower panel), and the corresponding variation of mass for the parent halo in which the subhalo resides (top panel). The vertical solid line corresponds to the last time the subhalo is outside the main progenitor of the cluster; the dotted line corresponds to the time the subhalo becomes a substructure (see the text for details).
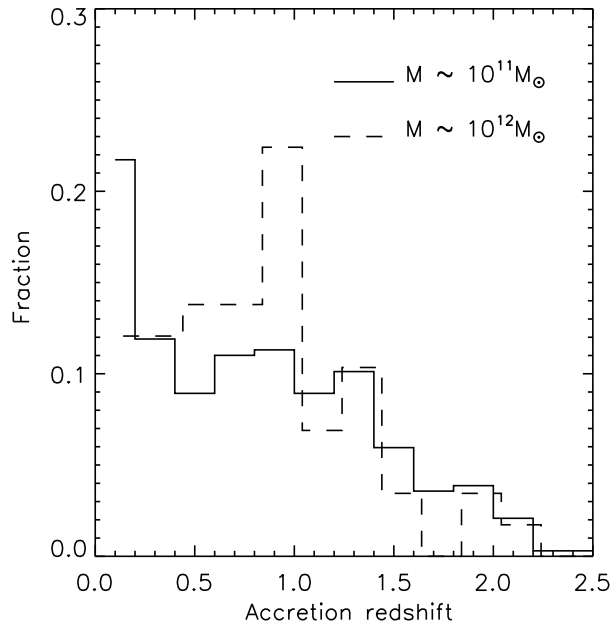
Figure 2.15: Distribution of the accretion redshifts for the cluster subhalo sample. A small shift is added to the abscissa to produce a more readable plot.

formalism (Press & Schechter 1974; van den Bosch 2002). This can be due to two different reasons: (i) subhalos in the simulations suffer from *tidal stripping* and this can produce a decrease instead of an increase in the mass of the main progenitor; (ii) the algorithm used to identify substructures can temporarily link together two different substructures so that $M(z)$ increases and then decreases again.

We find that for ~ 60 per cent of the subhalos in the 10^{11} mass bin and ~ 80 per cent of the subhalos in the 10^{12} bin, t_{accr} corresponds to the accretion of the substructure onto the main progenitor of the cluster itself. For most of the rest of the substructures in the sample, the time elapsed between these two events is fairly short. The results we will show later are essentially unchanged if we adopt as definition of the accretion time, the accretion of the substructure onto the main progenitor of the cluster itself.

Fig. 2.15 shows the distribution of the accretion redshifts for the cluster substructures in our sample. Interestingly, we find that a large fraction of the substructures are accreted at redshift $z < 1$. As noted above, for most of these substructures this accretion event corresponds to the accretion onto the main cluster itself. Our results hint that substructures are constantly erased in the cluster, being replenished by newly infalling haloes.
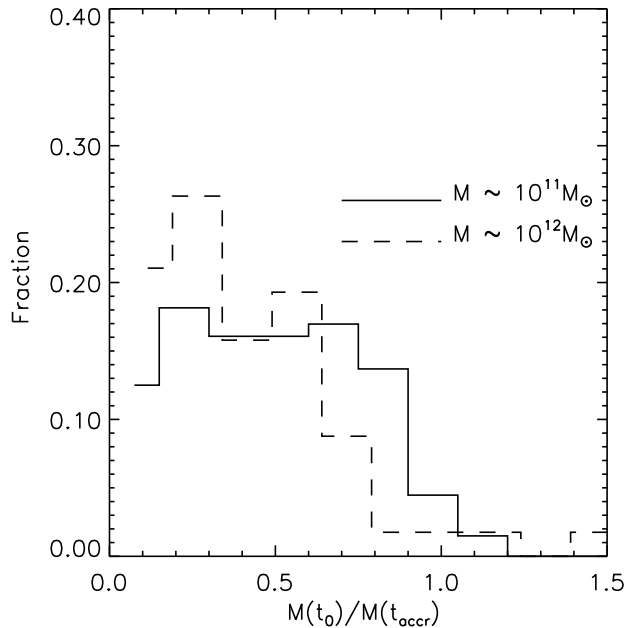
Figure 2.16: Distribution of the quantity $M(t = t_0)/M(t = t_{accr})$ for the cluster subhalo sample. A small shift is added to the abscissa to produce a more readable plot.

In Fig. 2.16, we plot the distribution of $M(t = t_0)/M(t = t_{accr})$, i.e. the ratio of the mass of the subhalo at the present day to the mass it had when it was first accreted. The histograms show that this ratio has a quite broad distribution, varying from a value of ~ 1 to ~ 0.1. We note that most of the subhalos that have lost only small amounts of mass have been accreted very recently.

This is more clearly shown in Fig. 2.17 where we plot the average mass accretion function for the cluster subhalos in the two mass bins considered. Three different accretion redshift intervals are considered and in all cases the subhalo masses are normalised to the mass of the subhalo at t_{accr}. The solid black line shows the mean relation for subhalos with mass $\sim 10^{11} \, h^{-1} M_\odot$, while the red solid line shows the relation for $M_{sub} \sim 10^{12} \, h^{-1} M_\odot$. The mass accretion function increases monotonically for times prior to the accretion event. Once the substructures are accreted, tidal stripping is effective and operates on short time scales. The longer the substructure spends in a more massive halo, the larger is the destructive effect of tidal stripping. Substructures remaining at $z = 0$ that were accreted at redshift larger than 1 (panel c) have been typically stripped of ~ 80 per cent of their mass. There is also a slight indication that stripping is more effective for more massive substructures: panels (a)
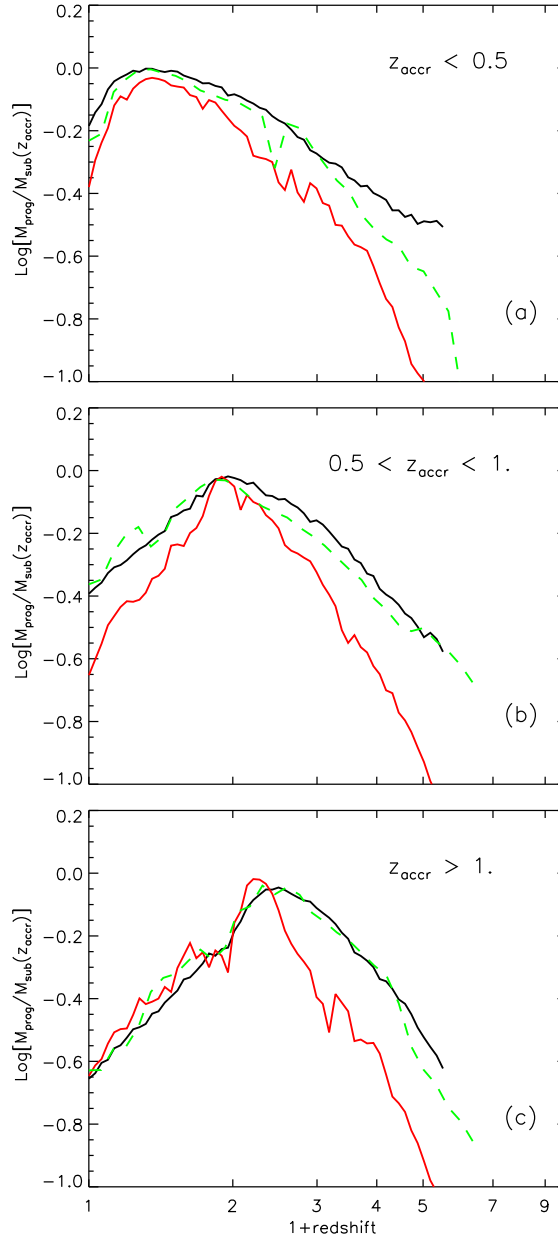
Figure 2.17: Average mass accretion history for $z = 0$ subhalos accreted in three different redshift bins. Solid black lines are used for cluster subhalos with mass $\sim 10^{11} \, h^{-1} \mathrm{M}_\odot$, green dashed lines are used for subhalos in the same mass range but taken from the M3 simulation, and red solid lines are used for cluster subhalos with mass $\sim 10^{12} \, h^{-1} \mathrm{M}_\odot$. The histories are normalised to the mass of the subhalo at the accretion time.

and (b) show that more massive substructures have been stripped significantly more than less massive substructures accreted at the same redshift. This effect does not appear in panel (c) but note that we have very few objects accreted in this redshift bin in our sample of more massive subhalos.

In Fig. 2.17 we also compare the mass accretion histories of field and cluster subhalos. We limit the analysis to substructures with mass $\sim 10^{11}\,h^{-1}\mathrm{M}_\odot$. Their average mass accretion function is shown as a dashed green line. Again the mass accretion function is normalised to the mass of the subhalo at the accretion time. We find that field subhalos and cluster subhalos have remarkably similar histories suggesting that the efficiency of the tidal stripping is largely independent of the mass of the parent halo.

2.7.3 Merging histories

In hierarchical models of galaxy formation, galaxies and their associated dark matter haloes form hierarchically through merger and accretion processes. In this context, the term *merger* is usually used to refer to an interaction between two objects of similar mass, while the term *accretion* is used to describe the infall of small objects onto much more massive haloes.

Observational results and numerical simulations confirm that interactions (such as tidal truncation or collisions) play an important role in the evolution of galaxies. There is, for example, solid evidence (Schweizer & Seitzer 1992; Whitmore et al. 1997; Barnes 1999) that at least some elliptical galaxies are the result of mergers between disc galaxies of similar mass. Mergers may also have a strong effect on the baryonic component of galaxies; they can trigger bar-instabilities in stellar discs and cause an inflow of gas into the galaxies centres, fuelling AGN activity or starbursts.

Following the merger tree of the substructures in our sample, we can analyse in detail the merger history, distinguishing between mergers and accretion events. To build the merger history we proceed as follows: we consider all the substructures within the virial radius at redshift zero and follow their merger trees back in time, checking as substructures are accreted onto the main progenitor. We count as mergers all accretion events involving haloes with mass larger than $2 \times 10^{10}\,h^{-1}\,\mathrm{M}_\odot$ and mass ratio smaller than $5 : 1$. Note that the lower limit on the mass of the merging haloes corresponds to the resolution limit of our cluster simulations (see Table 2.1).

In order to have enough information without running into numerical resolution effects, we limit the present analysis to subhalos with mass $\sim 10^{12}\,h^{-1}\,\mathrm{M}_\odot$. Fig. 2.18 shows the mean number of mergers per subhalo, identified at redshift $z = 0$, occurring after the redshift plotted in the abscissa. As in the previous section, the sample is split into three different accretion redshift intervals.

Merger events are less frequent once a halo is accreted onto a more massive structure. This is because the merging efficiency is higher in environments where the
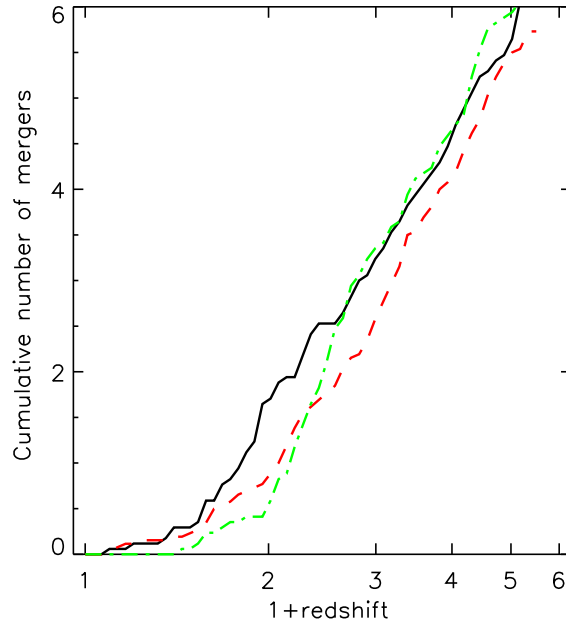
Figure 2.18: The mean number of mergers after redshift z for substructures selected from the simulations B1 and B2 at redshift $z = 0$ and with mass $\sim 10^{12}\, h^{-1} \mathrm{M}_{\odot}$. The solid black line is used for substructures accreted at redshift $z < 0.5$, the dashed red line is used for substructures accreted at redshift $0.5 < z < 1.0$, and the dashed-dotted green line is used for substructures accreted at redshift $z > 1.0$.

relative velocities of subhalos are similar to their internal virial velocities. Once haloes are accreted by a massive halo, merging is suppressed by the large velocity dispersion they aquire. This effect is clearly visible in Fig. 2.18 in the change in slope of the curves near the accretion redshift. Note, however, that when one goes to significantly higher redshift the difference between the three curves vanishes.

In Fig. 2.19 we show the fraction of subhalos that have had at least one merger after the redshift plotted in the abscissa. Note that the merger events we are considering are characterised by similar masses and will most likely influence the morphology of the main galaxy, leading to the formation of a bulge component. The final morphology of the galaxies residing in these substructures will depend on the time between the last major merger and accretion onto the cluster: the longer this time, the larger is the likelihood that the galaxy can grow a new disc.

The results in Fig. 2.19 show that ~ 80 per cent of the $\sim 10^{12}\, h^{-1}\, \mathrm{M}_{\odot}$ subhalos in our $z = 0$ sample have had at least one major merger at redshift below 2; this
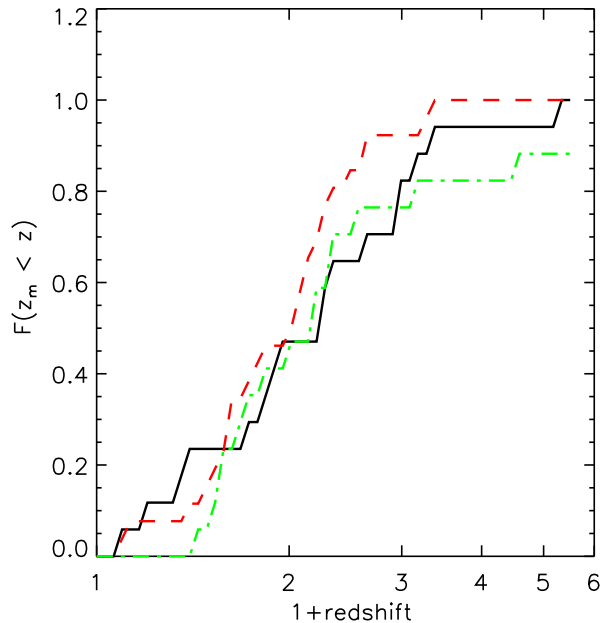
Figure 2.19: Fraction of substructures with at least one merger event at redshift $z_m < z$. Different line styles and colours are for different accretion redshifts as in Fig. 2.18.

fraction decreases to ~ 40 per cent for redshift < 1. Surprisingly, the fraction is almost independent of the accretion time. These results suggest that a large fraction of subhalos in our cluster sample will host early-type galaxies with a significant bulge component.

2.8 Summary and discussion

In this chapter we have used a set of high resolution numerical simulations in a ΛCDM Universe to study dark matter halo substructures. Such dark matter substructures mark the sites where luminous galaxies are expected to be found, so the analysis of their mass functions, radial distributions, merging and mass accretion histories should help us to better understand the properties of the galaxies that form in hierarchical galaxy formation models. Comparison with observational data should then suggest the physics that needs to be included in viable models of galaxy formation and evolution.

In agreement with previous work (Moore et al. 1999a), we find that the shape of

the subhalo mass function is almost independent of the mass of the parent halo, with galactic haloes being essentially scaled versions of cluster haloes. Our results are robust with respect to numerical resolution but the halo–to–halo scatter in our simulation set is quite large, preventing us from putting tight constraints on the accuracy with which the 'scale–free' subhalo mass function is preserved when haloes of different mass are considered. And hence there is still room for weak trends with mass, whose detection requires simulations with larger dynamic range, and larger samples of simulated haloes for each mass bin.

We find that the average mass of the largest substructure within the virial radius (excluding the BCG) scales linearly with the mass of the parent halo. If the stellar masses scale linearly with the dark matter mass of the parent substructure, the second ranked galaxies should have K-band luminosities that increase roughly linearly with the mass of the main halo and are equal to those of the third ranked galaxies to within 0.5 mag.

Note that the assumption that the stellar mass scales linearly with the dark matter mass of the parent substructure cannot generally be true since stars are typically much more concentrated than dark matter. The relation between stellar mass and the mass of parent substructure is then quite complex and should be followed considering the details of star formation and feedback process as is done for example in Springel et al. (2001a). We will address these problems in the next chapter, where we will substantially adapt and extend the semi–analytic technique developed by Springel et al. (2001a) and couple the model to the dark matter simulation of a massive cluster.

We have also used the simulations to study the radial distribution of substructures. In agreement with previous work (Ghigna et al. 2000), we find that the radial profile of substructure number density is 'anti-biased' relative to the dark matter profile in the inner regions of haloes. The most massive substructures reside preferentially in the outer regions of haloes. This is, at least in part, because substructures undergo substantial tidal stripping in the dense inner regions of haloes.

We have studied the evolution with time of this stripping process and find that, once a subhalo is accreted by a larger system, tidal stripping is highly effective; the longer a substructure spends in a more massive halo, the larger is the destructive effect. This suggests that substructures are constantly erased in clusters, being replenished by newly infalling galaxies.

Interestingly, a significant fraction of the substructures found in present-day clusters were first accreted at redshifts $z < 1$, implying that tidal truncation of the dark haloes of cluster galaxies happened relatively recently, and that at $z > 1$ many present-day 'passive' cluster members should still have been central galaxies of their own extended dark haloes. If gas was able to cool in these haloes, the galaxies may have been considerably more active at $z \sim 1$ than at present. Substructures in smaller haloes have histories remarkably similar to those in cluster haloes, suggesting that

the efficiency of tidal stripping is largely independent of the mass of the main halo.

Once a substructure is accreted onto a cluster, its merging probability decreases because of the large velocity dispersion of the system. Observational data are currently being collected on merger rates in different environments (van Dokkum et al. 1999; Patton et al. 1997). In future work, we plan to carry out a more direct comparison with observational data of this kind, and so to test the hierarchical paradigm for galaxy formation in new ways.

*– Puisque ces mystères nous dépassent feignons
d'en être les organisateurs*

Jean Cocteau

3

The physics of galaxy formation and evolution

Abstract

In this chapter I develop a semi–analytic model to follow the formation, the evolution and the chemical enrichment of cluster galaxies in a ΛCDM Universe. I review the general philosophy of the semi–analytic technique and explain in detail the prescriptions adopted to describe the various physical mechanisms that are implemented in my specific model. I model the transport of mass and metals between the stars, the cold gas in galaxies, the hot gas in dark matter haloes, and the intergalactic gas outside virialized haloes. I also model the effects of dust on the radiation emitted by galaxies. The coupling of the semi–analytic model with a high resolution N–body simulation of a galaxy cluster of the kind analysed in the previous chapter, permits me to make a close link with observational results for galaxy clusters. I compare the model results with a variety of observational results, such as the cluster galaxy luminosity function measured from the 2dF survey, and the relations between stellar mass, gas mass and metallicity inferred from new SDSS data. The model also naturally reproduces a morphology–radius relation that is in qualitatively good agreement with the observational results.

3.1 Introduction

Modern N–body simulations are able to follow the formation and the evolution of dark matter haloes from scales typical of clusters of galaxies, down to scales typical of dwarf galaxies. As we have mentioned in Chapter 1 however, dark matter simulations

alone do not provide any information about the baryonic component, that is the direct observable. In order to make a close link between the theoretical predictions and the observational results, it is necessary to model the evolution of the baryonic component.

If, on one hand, the linear and non linear growth of perturbations, the formation of the large scale–structure of the Universe and its evolution represent processes that are now quite well understood (see Sec. 1.3), the actual formation of the luminous part of galaxies within CDM universes is regulated by processes that are still highly uncertain.

In fact, the formation and the evolution of the baryonic component of galaxies involves non–linear processes operating on vastly different scales, for example shocking and cooling of gas, star formation, feedback by supernovae explosions and winds, chemical enrichment, and stellar evolution. Most of these processes are poorly understood even when viewed in isolation; the difficulties grow considerably when one takes into accounts the fact that the physical properties of galaxies are determined by a complex network of actions, back–reactions and self–regulation between the above mentioned physical processes.

The uncertainties inherent the physical processes governing galaxy formation and evolution obviously place strong limits on the accuracy with which galaxies may be simulated using hydrodynamical simulations. In addition, these studies also require an adequate handling of 'subgrid' physics in order to properly take into account the huge range of scales of the different physical processes that are involved. Although recent works have achieved considerable success in reproducing observed galaxy properties (Katz et al. 1999; Steinmetz & Navarro 2002; Marri & White 2003; Springel & Hernquist 2003), the computational time is still highly prohibitive for simulations of galaxies in large volumes. In addition, highly uncertain processes such as star formation and feedback, still have to be modelled using simplified prescriptions. This also means that if one wants to change a particular physical prescription, the whole simulation has to be run again.

Much of our current understanding of galaxy formation has been gained through 'semi–analytic' techniques, where the complicated baryonic physics involved in galaxy formation is approximated using simplified, but physically motivated 'recipes'. The basic idea is very simple: as a halo forms, the gas relaxes to a distribution that exactly parallels that of the dark matter. Gas then cools because of energy dissipation by emitting radiation and condenses onto a galaxy.

The great advantage of such a technique, with respect to direct numerical studies of galaxy formation, is that it is possible to cover a much larger dynamical range. The technique allows one to explore the parameter space quickly and to investigate the influence of the specific assumptions that were chosen.

The semi–analytic models (SAMs) find their seeds in the pioneering work by White & Rees (1978); they have been laid out in a more detailed form in the early 90s

(White & Frenk 1991; Cole 1991) and have been substantially extended and refined in the last years by a number of different groups (Kauffmann et al. 1993; Baugh et al. 1996; Kauffmann et al. 1999; Somerville & Primack 1999; Cole et al. 2000).

The evolution of the underlying dark matter component has been traditionally followed using Monte Carlo realizations of merging histories of individual objects, generated using the extended Press–Schechter theory (Kauffmann et al. 1993; Kauffmann 1995b; Somerville & Primack 1999; Cole et al. 2000). Although it has been shown that this produces results that are in reasonable good agreement with the results from N–body simulations, merger trees based on these analytic approximations do not account for the spatial distribution of galaxies within haloes. In recent years there has been significant progress in coupling SAMs with N–body simulations (Kauffmann et al. 1997, 1999; Mathis et al. 2002; Diaferio et al. 2001; Benson et al. 2000a, 2001; Springel et al. 2001a). In this way it is possible to obtain full spatial and kinematic distributions not only for the galaxy population at redshift zero, but also for their progenitors at any earlier time. This allows the construction of simulated catalogues of galaxies that not only include galaxy properties such as luminosity, colour and bulge-to-disc ratio, but also contain all the spatial and kinematic information of galaxies, as in real redshift surveys.

The only disadvantage with respect to the analytic approach is that merger trees built in this way are limited by the numerical resolution of the N–body simulation. Also, the particle data need to be dumped sufficiently often so that the growth of structure is resolved on a fine enough timescale to construct the merger trees.

In this chapter we describe how we substantially adapted and extended an existing code that combines semi–analytic techniques and N–body simulations, in order to follow the formation and the photometric and chemical evolution of cluster galaxies, as well as the chemical history of the intra–cluster and the intergalactic medium in a self–consistent way. We will describe the details of the semi—analytic technique that we employ and the basic observational results that the code is able the reproduce.

The chapter is structured as follows: in Sec. 3.2 we briefly describe the cluster simulation used in this analysis; in Sec. 3.3 we summarise the semi–analytic technique employed; while in Sec. 3.4 we give a detailed description of the prescriptions adopted to parametrise the physical processes included in the model. In Sec. 3.7 we describe how we set the free parameters in this model and we show the main observational properties that can be fit. In Sec. 3.8 and Sec 3.9 we briefly discuss the cluster mass–to–light ratio and the morphological and colour distribution of model galaxies. Finally we discuss our findings in Sec. 3.10.
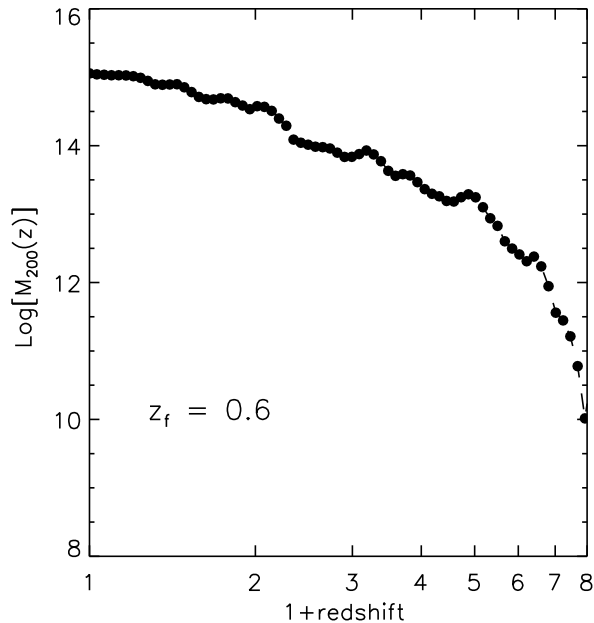
Figure 3.1: The mass accretion history of the cluster simulation used in this chapter. At redshift zero the cluster has $M_{200} = 1.14 \times 10^{15}\, h^{-1}\, \mathrm{M}_\odot$ and $R_{200} = 1.70$ Mpc.

3.2 The simulation

In this chapter we use one of the massive cluster simulations introduced in Sec. 2.2. A density map of the dark matter distribution at redshift zero for this cluster is given in the top left panel of Fig. 2.1. At redshift zero, our cluster is characterised by $M_{200} = 1.14 \times 10^{15}\, h^{-1}\, \mathrm{M}_\odot$ and $R_{200} = 1.70$ Mpc. The most important numerical parameters of the simulation are listed in Table 2.1. For this particular simulation, the number of particles in the high–resolution region is to 1.34×10^6, with about $800,000$ particles in the main halo at redshift zero.

Fig. 3.1 shows the mass accretion history of the cluster halo as a function of redshift. The mass accretion function is built by following, at each redshift, the main progenitor on the cluster halo. If we define the redshift of formation as the redshift when the system has accreted half of its final mass, we find $z_{\mathrm{f}} \sim 0.6$. Let us define as a 'major merger' an event corresponding to a significative increase in mass ($\gtrsim 50$ per cent). The figure then indicates that the mass of the cluster grows quickly at high redshift through a series of major merger events ($z = 6.0, 5.8, 4.7$). Also, the cluster

undergoes a major merger event at relatively low redshift ($z = 1.34$) with a ~ 60 per cent increase in mass.

3.3 Tracking Galaxies in N–body Simulations

The prescriptions adopted for the different physical processes included in our model are described in more detail in the next section. In this section we summarise how the semi–analytic model is grafted onto the high resolution N–body simulation. The techniques we employ in this analysis are similar to those used by Springel et al. (2001a).

In standard semi–analytic models, all galaxies are located within dark matter haloes. Haloes are usually identified in a simulation using a standard friends–of– friends (FOF) algorithm with a linking length of 0.2 in units of the mean particle separation (see Sec. 2.3). The novelty of the analysis technique developed by Springel et al., is that substructure is also tracked within each halo. This means that the dark matter halo within which a galaxy forms, is still followed even after it is accreted by a larger object. The algorithm used to identify subhalos (SUBFIND) is described in detail by Springel et al. (2001a) and in Sec. 2.3. The algorithm decomposes a given halo into a set of disjoint and self–bound subhalos, identified as locally overdense regions in the density field of the background halo. In the previous chapter we presented an extensive analysis of the properties of the subhalo population present in a large sample of haloes with a range of different masses. As in the previous chapter, we consider all substructures detected by the algorithm SUBFIND with at least 10 self-bound particles, to be genuine subhalos.

An important change due to the inclusion of subhalos, is a new nomenclature for the different kinds of galaxies present in the simulation. The FOF group hosts the 'central galaxy'; this galaxy is located at the position of the most bound particle in the halo. This galaxy is fed by gas cooling from the surrounding hot halo medium. All other galaxies attached to subhalos are called 'halo galaxies'. These galaxies were previously central galaxies of another halo, which then merged to form the larger object. Because the core of the parent halo is still intact, the positions and velocities of these halo galaxies can be accurately determined. Note that gas is no longer able to cool onto halo galaxies.

As we have shown in the previous chapter, dark matter subhalos lose mass and are eventually destroyed as a result of tidal stripping effects (see Sec. 2.7.2 for an accurate analysis of the effect of tidal stripping on the substructure population). A galaxy that is no longer identified with a subhalo is called a satellite. The position of the satellite is tracked using the position of the most bound particle of the subhalo before it was disrupted. Note that if two or more subhalos merge, the halo galaxy of the smaller subhalo will become a 'satellite' of the remnant subhalo. A schematic
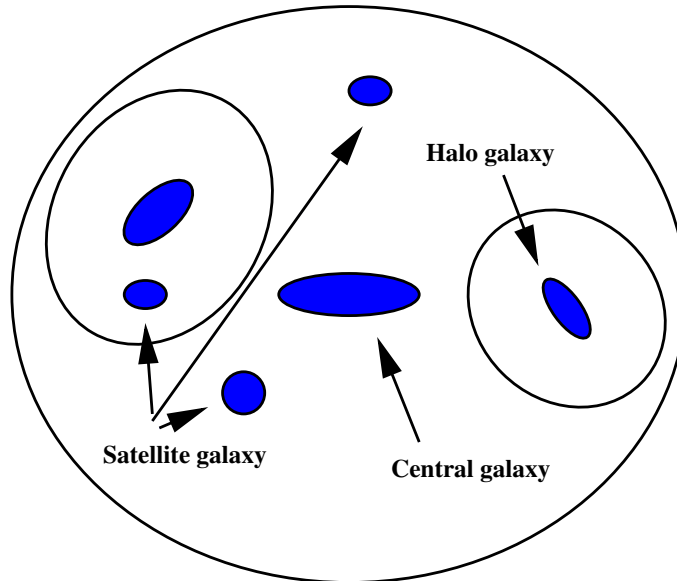
Figure 3.2: A sketch to illustrate the nomenclature used for different types of galaxies in the simulation.

representation of the above nomenclature is given in Fig. 3.2.

Springel et al. (2001a) show that the inclusion of subhalos results in a significant improvement in the cluster luminosity function over previous semi–analytic schemes, and in a morphology–radius relationship that is in remarkably good agreement with the observational data. This improvement is mainly attributed to a more realistic estimate of the merger rate: in the standard scheme too many bright galaxies merge with the central galaxy on short time–scales. This produces first–ranked galaxies that are too bright when compared with observational data. It also depletes the cluster luminosity function around the 'knee' at the characteristic luminosity.

3.4 The physical processes governing galaxy evolution

As we have discussed in Sec. 1.5, the formation of galaxies involves many processes that are strongly non–linear and strongly interconnected. Moreover, the observational and physical understanding of these processes and their dependence on environment is incomplete. For these reasons, we adopt simplified prescriptions in order to describe the physical processes driving galaxy evolution. Our treatment of these processes is similar to the one adopted in Kauffmann et al. (1999) and Springel et al. (2001a). Many prescriptions have been modified in order to

properly take into account the exchange of metals between the different phases. We also include metallicity–dependent cooling rates and luminosities. In the following sections we describe the details of our implementation. The reader is referred to previous papers for more general information on semi–analytic techniques (White & Frenk 1991; Kauffmann et al. 1993; Baugh et al. 1996; Kauffmann et al. 1999; Somerville & Primack 1999; Cole et al. 2000).

3.4.1 Gas cooling

Gas cooling is treated as in Kauffmann et al. (1999) and Springel et al. (2001a). It is assumed that the hot gas within dark matter haloes initially follows the dark matter distribution. In particular, we assume that the hot gas is distributed like an isothermal sphere with density profile $\rho_g(r)$. The local cooling time can then be defined using the following expression:

$$t_{\rm cool}(r) = \frac{3}{2} \frac{kT\rho_g(r)}{\bar{\mu}m_p n_e^2(r)\Lambda(T,Z)}$$

that represents the ratio between the specific thermal energy content of the gas and the cooling rate per unit volume. In this equation $\bar{\mu}m_p$ is the mean particle mass, $n_e(r)$ is the electron density, k is the Boltzmann constant, and $\Lambda(T,Z)$ represents the cooling rate.

Note that the cooling rates are strongly dependent on the virial temperature $T = 35.0(V_{\rm vir}/{\rm km\,s^{-1}})^2$ K of the halo and on the metallicity of the gas. We model these dependences using the collisional ionisation cooling curves of Sutherland & Dopita (1993). At high ($\geq 10^8$ K) temperatures, the cooling is dominated by the bremsstrahlung continuum. At lower temperatures, line cooling from heavy elements dominates (mainly iron in the 10^6–10^7 K regime, with oxygen significant at lower temperatures). The net effect of using metallicity–dependent cooling rates is an overall increase of the brightness of galaxies, because cooling is more efficient. This effect is strongest in low mass haloes.

The cooling radius is defined as the radius for which the local cooling time is equal to age of the Universe at that epoch ($t_{\rm age}$).

At early times and for low–mass haloes, the cooling radius can be larger than the virial radius. In this case the hot gas is never expected to be in hydrostatic equilibrium and the cooling rate is essentially limited by the accretion rate. In this case, we assume that the hot gas condenses out on a halo dynamical time:

$$\frac{dM_{\rm accr}}{dt} = \frac{M_{\rm hot}V_{\rm vir}}{R_{\rm vir}} \tag{3.1}$$

If the cooling radius lies within the virial radius, the gas is assumed to cool quasi–

statically and the cooling rate is modelled by a simple inflow equation:

$$\frac{\mathrm{d}M_{\mathrm{cool}}}{\mathrm{d}t} = 4\pi\rho_{\mathrm{g}}(r_{\mathrm{cool}})r_{\mathrm{cool}}^2 \frac{\mathrm{d}r_{\mathrm{cool}}}{\mathrm{d}t}$$

Note that following Springel et al. (2001a), we define the virial radius R_{vir} of a FOF-halo as the radius of the sphere, centred on its most-bound particle, which has an overdensity 200 with respect to the critical density. We take the enclosed mass $M_{\mathrm{vir}} = 100H^2 R_{\mathrm{vir}}^3/G$ as the virial mass, and we define the virial velocity as $V_{\mathrm{vir}}^2 = GM_{\mathrm{vir}}/R_{\mathrm{vir}}$. The mass of a subhalo, on the other hand, is defined in terms of the total number of particles it contains. The virial velocity of a subhalo is fixed at the velocity that it had just before infall.

Adopting an isothermal sphere for the distribution of the hot gas, i.e.:

$$\rho_{\mathrm{g}}(r) = \frac{M_{\mathrm{hot}}}{4\pi R_{\mathrm{vir}} r^2}$$

one obtains:

$$\frac{\mathrm{d}M_{\mathrm{cool}}}{\mathrm{d}t} = \frac{M_{\mathrm{hot}}}{R_{\mathrm{vir}}} \frac{r_{\mathrm{cool}}}{2t_{\mathrm{age}}} \tag{3.2}$$

The actual cooling rate is adopted as the minimum of equations 3.1 and 3.2.

As noted since the work of White & Frenk (1991), these prescriptions produce central cluster galaxies that are too massive and too luminous to be consistent with observations. This is a manifestation of the 'cooling flow' problem, the fact that the central gas in clusters does not appear to be cooling despite the short estimated cooling time. As in previous models (Kauffmann et al. 1999; Springel et al. 2001a), we fix this problem *ad hoc* by assuming that the gas does not cool in haloes with $V_{\mathrm{vir}} > V_{\mathrm{cut}}$. In our model $V_{\mathrm{cut}} = 350\,\mathrm{km\,s^{-1}}$.

Although our cooling model is extremely simplified, it has been shown that it produces results that are in good agreement with more detailed N–body + hydro-dynamical simulations that adopt the same physics (Yoshida et al. 2002; Helly et al. 2003).

3.4.2 Star formation

The star formation 'recipes' that are implemented in semi–analytic models are always subject to considerable uncertainty. In Kauffmann et al. (1999) and Springel et al. (2001a) it is assumed that star formation occurs with a rate given by:

$$\psi = \alpha M_{\mathrm{cold}}/t_{\mathrm{dyn}} \tag{3.3}$$

where M_{cold} and $t_{\mathrm{dyn}} = R_{\mathrm{vir}}/10V_{\mathrm{vir}}$ are the cold gas mass and the dynamical time of the galaxy respectively, and α represents the efficiency of the conversion of gas

into stars. The radius of the disc is assumed to be a constant fraction of the virial radius of the halo: $R_{\mathrm{disc}} = 2\,\lambda_{\mathrm{H}}\,R_{\mathrm{vir}}$. λ_{H} is the average spin parameter of a dark matter halo and the above expression is simply motivated by conservation of angular momentum: gas collapsing within an isothermal halo will contract by a factor $\sim 2\,\lambda_{\mathrm{H}}$ (Fall & Efstathiou 1980). Simulations show that the average spin parameter of dark matter haloes is ~ 0.05 (Barnes & Efstathiou 1987). The star formation law in Equation 3.3 has received considerable empirical support from a study by Kennicutt (1998). Using a sample of nearby spiral galaxies and starburst systems, Kennicutt finds that such a law can fit the data over several orders of magnitude in star formation rate and gas density. The study also shows that, in normal spirals, about 10 per cent of the available gas is turned into stars per orbital time.

Previous semi–analytic models have assumed that the efficiency parameter α is a constant, independent of galaxy mass and redshift. The observational understanding concerning the star formation efficiency is quite controversial with claims for absence of any statistically significant difference in the star formation efficiency of galaxies of different luminosity (Gavazzi 1993; Boissier et al. 2001) or type (Zasov 1995) on one hand, and indications of dependence of the star formation efficiency on the galaxy size (Young 1999) or on the mass and potential well of the object (Kauffmann et al. 2003; Thomas et al. 2003) on the other. Note that a star formation efficiency that depends on the depth of the galaxy potential well is also expected in detailed models of the effects of supernovae feedback on the interstellar medium (McKee & Ostriker 1977; Efstathiou 2000). More importantly, perhaps, the above prescription leads to gas fractions that are essentially independent of the mass of the galaxy. In practice, we know that gas fractions increase from ~ 0.1 for luminous spirals like our own Milky Way, to more than 0.8 for low–mass irregular galaxies (Boissier et al. 2001).

In this work, we assume that α depends on the circular velocity of the parent galaxy as follows:

$$\alpha = \alpha_0 \cdot \left(\frac{V_{\mathrm{vir}}}{220\,\mathrm{km\,s^{-1}}} \right)^n$$

and we treat α_0 and n as free parameters. Note also that R_{vir} decreases with redshift for a galaxy halo with fixed circular velocity. This means that a galaxy of circular velocity V_{c} will be smaller at higher redshifts and, as a result, the star formation efficiency will be higher.

3.4.3 Feedback

Previous work (Kauffmann & Charlot 1998; Somerville & Primack 1999; Cole et al. 2000) has shown that feedback processes are required to fit the faint end slope of the luminosity function and to fit the observed slope of the colour–magnitude relation of elliptical galaxies. The theoretical and observational understanding of how the feedback process operates is far from complete.

In many models it has been assumed that the feedback energy released in the star formation process is able to reheat some of the cold gas. The amount of reheated mass is computed using energy conservation arguments and is given by:

$$\Delta M_{\text{reheated}} = \frac{4}{3}\epsilon \frac{\eta_{\text{SN}} E_{\text{SN}}}{V_{\text{vir}}^2} \Delta M_{\text{star}} \tag{3.4}$$

where η_{SN} is the number of supernovae expected per solar mass of stars formed ($6.3 \times 10^{-3} M_{\odot}^{-1}$ assuming a universal Salpeter (1955) initial mass function) and E_{SN} is the energy released by each supernova ($\simeq 10^{51}$ erg). The dimensionless parameter ϵ quantifies the efficiency of the process and is treated as a free parameter. Note that changing the IMF would also change the amount of energy available for reheating the gas, because it would change the value of η_{SN}.

One major uncertainty is whether the reheated gas leaves the halo. This will depend on a number of factors, including the velocity to which the gas is accelerated, the amount of intervening gas, the fraction of energy lost by radiative processes, and the depth of the potential well of the halo.

On the observational side, evidence in support of the existence of outflows from galaxies has grown rapidly in the last years (Heckman et al. 1995; Marlowe et al. 1995; Martin 1996). In many cases, the observed gas velocities exceed the escape velocity of the parent galaxies; this material will then escape from the galaxies and will be injected into the intergalactic medium (IGM). Observations of galactic–scale outflows of gas in active star–forming galaxies (Lehnert & Heckman 1996; Dahlem et al. 1998; Heckman et al. 2000; Heckman 2002) suggest that outflows of multiphase material are ubiquitous in galaxies in which the global star–formation rate per unit area exceeds roughly $10^{-1} M_{\odot} \, \text{yr}^{-1} \, \text{kpc}^{-2}$. Different methods to estimate the outflow rate suggest that it is comparable to the star formation rate. The estimated outflow speeds vary in the range 400–800 km s^{-1} and are independent of the galaxy circular velocity. These observational results indicate that the outflows preferentially occur in smaller galaxies. This provides a natural explanation for the observed relation between galaxy luminosity and metallicity.

An accurate implementation of the feedback process is beyond the capabilities of present numerical codes. As a result, published simulation results offer little indication of appropriate recipes for treating galactic winds. In this work we experiment with three different simplified prescriptions for feedback and study whether they lead to different observational signatures:

- in the *retention* model, we use the prescription adopted by Kauffmann & Charlot (1998) and assume that the reheated material, computed according to Eq. 3.4, is shock heated to the virial temperature of the dark halo and is put directly in the hot phase, where it is then once more available for cooling.

- In the *ejection* model, we assume that the material reheated by supernovae explosions in central galaxies always leaves the halo, but can be later re–incorporated. The time–scale to re–incorporate the gas is related to the dynamical time–scale of the halo by the following equation:

$$\Delta M_{\text{back}} = \gamma \cdot M_{\text{ejected}} \cdot \frac{V_{\text{vir}}}{R_{\text{vir}}} \cdot \Delta t \qquad (3.5)$$

where ΔM_{back} is the amount of gas that is re–incorporated in the time–interval Δt; M_{ejected} is the amount of material in the ejected component; R_{vir} and V_{vir} are the virial radius and the virial velocity of the halo at the time the re–incorporation occurs; γ is a free parameter that controls how rapidly the ejected material is re–incorporated. Note that the material ejected in this way is not available for cooling until it is re–incorporated in the hot component.

  For all the other galaxies (halo and satellite galaxies), we assume that the material reheated to the virial temperature of the subhalo is then kinematically stripped and added to the hot component of the main halo.

- In the *wind* model, we adopt prescriptions that are motivated by the observational results. We assume that only central galaxies residing in haloes with a virial velocity less that V_{crit} can eject outside the halo. The outflow rates from these galaxies are assumed to be proportional to their star formation rates, namely:

$$\dot{M}_{\text{w}} = c \cdot \psi \qquad (3.6)$$

Observational studies give values for c in the range 1–5 (Martin 1999), while values in the range 100–300 km s^{-1} are reasonable for V_{crit} (Heckman 2002). We treat V_{crit} and c as free parameters. We also assume that the ejected material is re–incorporated as in the ejection scheme. If the conditions for an outflow are not satisfied, the reheated material (computed according to Eq. 3.4) is treated in the same way as in the retention model. The wind model is thus intermediate between the retention and the ejection schemes. Satellite galaxies are treated as in the ejection scheme.

3.4.4 Galaxy mergers

In hierarchical models of galaxy formation, galaxies and their associated dark matter haloes form through merging and accretion.

In our high resolution simulation, mergers between subhalos are followed explicitly. Once a galaxy is stripped of its dark halo, merging timescales are estimated using a simple dynamical friction formula (Binney & Tremaine 1987):

$$T_{\text{friction}} = \frac{1}{2} \frac{f(\epsilon)}{C} \frac{V_{\text{vir}} R_{\text{vir}}^2}{G M_{\text{sat}} \ln \Lambda}$$

Navarro et al. (1995) show that this analytic estimate is a good fit to the results of numerical simulations. The formula applies to satellites of mass M_{sat} orbiting at a radius R_{vir} in a halo of virial velocity V_{vir}. $f(\epsilon)$ expresses the dependence of the decay on the eccentricity of the orbit and is well approximated by $f(\epsilon) \sim \epsilon^{0.78}$ (Lacey & Cole 1993); C is a constant ~ 0.43 and $\ln\Lambda$ is the Coulomb logarithm. We adopt the average value $< f(\epsilon) > \sim 0.5$, computed by Tormen (1997) and approximate the Coulomb logarithm with $\ln\Lambda = (1 + M_{vir}/M_{sat})$. For the satellite galaxy mass we use the value of M_{vir} corresponding at the last time the galaxy was a central galaxy (either of a halo or of a subhalo).

When a small satellite merges with the central galaxy, its stellar mass and cold mass are simply transferred to the central galaxy and the photometric properties are updated accordingly. In particular, we transfer the stellar mass of the merged galaxy to the bulge of the central galaxy and update the photometric properties of this galaxy. If the mass ratio between the stellar component of the merging galaxies is larger than 0.3 (*major merger*), we assume that the merger completely destroys the disc of the central galaxy producing a spheroidal component. In addition, we assume that the merger consumes all the gas left in the two merging galaxies in a single burst. The stars formed in this burst are added to the bulge. Note that, since the galaxy is fed by a cooling flow, it can grow a new disc later on.

3.4.5 Spectro–photometric evolution

The photometric properties of our model galaxies are calculated using the models of Bruzual & Charlot (1993), which include the effect of metallicity on the predicted luminosities and colours of a galaxy. These models provide the spectral energy distribution of a single–age population of stars as a function of age and metallicity: $f_\lambda(t, Z)$. The stellar population of a galaxy can be viewed as the superposition of single bursts of different age (and also different metallicity). The superposition is regulated by the star formation rate of the system. The spectral energy distribution of the galaxy $(F_\lambda(t))$ can then be computed using a straightforward integration:

$$F_\lambda(t) = \int_0^t f_\lambda(t - t', Z) \cdot \psi(t')dt'$$

where $\psi(t)$ is the galaxy star formation rate.

The stellar population synthesis models are used to generate look–up tables of the luminosity of a single burst of fixed mass, as a function of the age of the stellar population and as a function of its metallicity. When updating the photometric properties of our model galaxies, we interpolate between these tables using a linear interpolation in t and $\log Z$. It is assumed that stars form with the same metallicity as the cold gas. We have adopted a Salpeter (1955) IMF with upper and lower mass cut–offs of 100 and $0.1 \, M_\odot$.

Charlot et al. (1996) have demonstrated that for given IMF and star formation history, the broad–band colours produced by different stellar population codes differ by only a few tenths of a magnitude. The most important sources of uncertainty in our model predictions are therefore given by the IMF (which affects the luminosity quite strongly) and by the associated yield (which influences the colours).

3.5 Dust extinction

Dust plays an important role in the spectra and colours of galaxies. Modelling the effect of dust on the radiation emitted by galaxies is not an easy task, given the variability seen in the galactic population and even within individual galaxies. In fact, properties of dust are dependent on a number of factors like the star formation rate, that regulates the rate of creation, heating and destruction of dust grains, and the distribution of dust and metals within gas clouds. For a single galaxy, all these factors can be taken into account, and it is then possible to model in an adequate way the effect of dust on the galaxy's spectrum. However, the level of detail required goes beyond the capabilities of present code. We therefore adopt a dust model that is based on macroscopic properties of galaxies, i.e. luminosity and inclination. Our model should be appropriate to reproduce the observed average properties of galaxies.

This model has been used in previous work (Kauffmann et al. 1999; Somerville & Primack 1999; Mathis et al. 2002) and is based on the observational results by Wang & Heckman (1996), who studied the correlation between the face–on optical depth of dust in galactic discs and the total luminosity of the galaxy. Wang & Heckman find that this can be expressed as:

$$\tau_\mathrm{B} = \tau_\mathrm{B,*} \left(\frac{L_\mathrm{B}}{L_\mathrm{B,*}} \right)^\beta$$

where L_B is the intrinsic (unextincted) blue luminosity and $L_\mathrm{B,*}$ is the fiducial observed blue luminosity of a Schechter L_* galaxy ($M_*(\mathrm{B}) = -19.6 + 5\log h$). Wang & Heckman find that a relation with $\tau_\mathrm{B,*} = 0.8 \pm 0.3$ and $\beta \sim 0.5$ fit their data very well.

We use $\tau_\mathrm{B,*} = 0.8$, $\beta = 0.5$ and relate the B–band optical depth to the other bands using the extinction curve of Cardelli et al. (1989). We also assign a random inclination to each galaxy and apply the dust correction only to its disc component (i.e. we assume that the bulge is not affected by dust). Assuming a slab model of mixture of dust and emitting sources, the extinction[1] at wavelength λ can be written

---

[1] The extinction A_X of a star in some waveband X is defined to be the difference between the observed X–band magnitude $m(\mathrm{X})$ and the magnitude $m_0(\mathrm{X})$ that would be observed in the absence of dust.

as:

$$A_\lambda = -2.5\log\frac{1 - e^{-\tau_\lambda sec\,\theta}}{\tau_\lambda\,sec\,\theta}$$

where θ is the angle of inclination to the line of sight. All the magnitudes and the colours plotted in this chapter include the effects of dust extinction, unless stated otherwise.

3.5.1 Metal routes

We assume that a yield Y of heavy elements is produced per solar mass of gas converted into stars. All the metals are instantaneously returned to the cold phase (note that this means that we are assuming a mixing efficiency of 100 per cent). We also assume that a fraction (R) of the mass in stars is returned to the cold gas.

Metals are then exchanged between the different gas phases depending on the feedback model (see Sec. 3.4.3). In the retention model, the metals contained in the reheated gas are put in the hot component and can subsequently cool to further enrich the cold phase. In the ejection and wind schemes, the metals can be ejected outside the halo. The ejected metals are re–incorporated into the hot halo gas on a halo dynamical time (see Eq. 3.5). In the wind scheme, metals are only ejected for haloes with $V_{\rm vir} < V_{\rm crit}$. In more massive systems, the metals contained in the reheated gas are mixed with the hot component of the main halo. Some simulations (Mac Low & Ferrara 1999) suggest that low–mass galaxies may lose essentially all their metals, but it is difficult for these galaxies to 'blow–away' their interstellar medium. For simplicity, we do not consider schemes in which metals are selectively ejected from galaxies.

When a satellite galaxy merges, its stars, cold gas and metals are simply added to those of the central galaxy. If a major merger occurs, all the gas is consumed in a starburst and the metals are ejected into the hot phase in the retention scheme and into the ejected phase in the other two schemes (in the wind scheme, ejection occurs only in galaxies that reside in haloes with $V_{\rm vir} > V_{\rm crit}$).

In Fig. 3.3 we sketch the routes whereby mass and metals are exchanged in the model. We now write down the equations that describe the evolution of the mass of the four reservoirs shown in Fig. 3.3. All central galaxies have 4 different components: stars, cold gas, hot gas, and an 'ejected' component. The equations describing these 4 components (in the absence of accretion of external matter) are:

$$\dot{M}_{\rm stars} = (1 - {\rm R}) \cdot \psi$$

$$\dot{M}_{\rm hot} = -\dot{M}_{\rm cool} + \dot{M}_{\rm back} + \sum\nolimits_{\rm sat} \dot{M}_{\rm reheated}$$

$$\dot{M}_{\rm cold} = +\dot{M}_{\rm cool} - (1 - {\rm R}) \cdot \psi - \dot{M}_{\rm out}$$
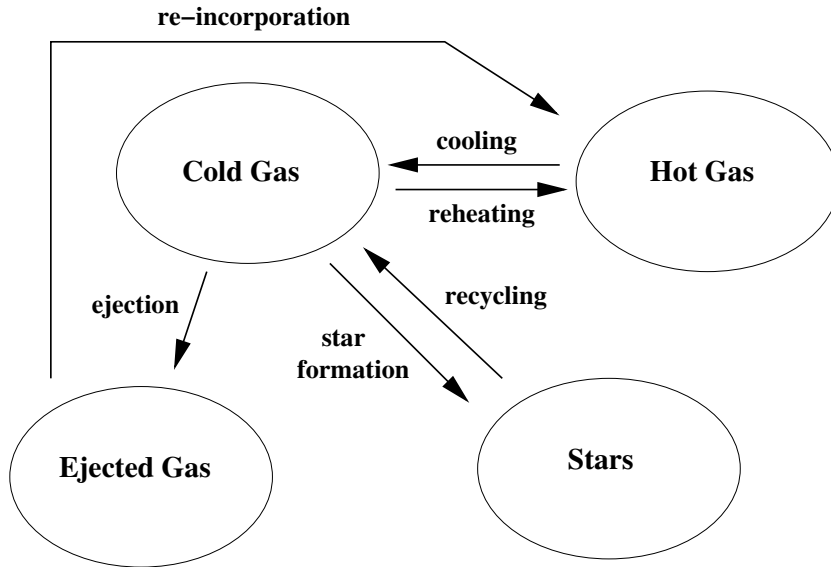
Figure 3.3: A schematic representation of how mass is exchanged between the different phases considered in our models, in the absence of accretion from outside. Each arrow is accompanied by a name indicating the physical process driving the mass exchange. Metals follow the same routes as the mass.

$$\dot{M}_{\mathrm{ejected}} = +\dot{M}_{\mathrm{out}} - \dot{M}_{\mathrm{back}}$$

where $\dot{M}_{\mathrm{out}}$ is the rate at which the cold gas is ejected outside the halo and is given by Eq. 3.4 for the ejection scheme and Eq. 3.6 for the wind scheme; ψ is the star formation rate given by Eq. 3.3; $\dot{M}_{\mathrm{cool}}$ is the cooling rate; $\dot{M}_{\mathrm{back}}$ is the rate at which gas is reincorporated from the ejected material (Eq. 3.5); $\sum_{\mathrm{sat}} \dot{M}_{\mathrm{reheated}}$ is the sum of all material that is reheated by the satellite galaxies in the halo.

Satellite galaxies have no hot gas or ejected component and $\dot{M}_{\mathrm{cool}} = 0$. The equations for the satellite galaxies are:

$$\dot{M}_{\mathrm{stars}} = (1 - \mathrm{R}) \cdot \psi$$

$$\dot{M}_{\mathrm{cold}} = +\dot{M}_{\mathrm{cool}} - (1 - \mathrm{R}) \cdot \psi - \dot{M}_{\mathrm{reheated}}$$

where $\dot{M}_{\mathrm{reheated}}$ is computed using Eq. 3.4.

From the above equations, one can easily obtain the corresponding equations for the evolution of the metal content of each reservoir of material. For central galaxies,

the equations are:

$$\dot{M}^Z_{\text{stars}} = +(1 - \text{R}) \cdot \psi \cdot Z_{\text{cold}}$$

$$\dot{M}^Z_{\text{hot}} = -\dot{M}_{\text{cool}} \cdot Z_{\text{hot}} + \dot{M}_{\text{back}} \cdot Z_{\text{ejected}} + \sum_{\text{sat}}[\dot{M}_{\text{reheated}} \cdot Z_{\text{cold}}]$$

$$\dot{M}^Z_{\text{cold}} = +\dot{M}_{\text{cool}} \cdot Z_{\text{hot}} - (1 - \text{R}) \cdot \psi \cdot Z_{\text{cold}} + \text{Y} \cdot \psi - \dot{M}_{\text{out}} \cdot Z_{\text{cold}}$$

$$\dot{M}^Z_{\text{ejected}} = +\dot{M}_{\text{out}} \cdot Z_{\text{cold}} - \dot{M}_{\text{back}} \cdot Z_{\text{ejected}}$$

where $Z_{\text{cold}} = M^Z_{\text{cold}}/M_{\text{cold}}$, $Z_{\text{ejected}} = M^Z_{\text{ejected}}/M_{\text{ejected}}$ and $Z_{\text{hot}} = M^Z_{\text{hot}}/M_{\text{hot}}$ represent the metallicities in the cold gas phase, in the ejected component and in the hot gas phase respectively.

Note that the above equations assume that material is being ejected outside haloes. In our 'retention' scheme, no material leaves the halo and the applicable equations are obtained by neglecting the equation for $\dot{M}_{\text{ejected}}$ and substituting $\dot{M}_{\text{back}}$ and $\dot{M}_{\text{out}}$ with $\dot{M}_{\text{reheated}}$ (given by Eq. 3.4).

The practical implementation of the prescriptions is described in detail in Springel et al. (2001a). We have stored 100 outputs of the simulation spaced in equal logarithmic intervals in redshifts from $z = 20$ to $z = 0$. For each new snapshot, we estimate the merger timescales of satellite galaxies that have entered a given halo. The 'merger clock' for the other satellites is updated and a galaxy merges with the central object when this time has elapsed. The merger clock is reset if the halo containing the satellites merges with a larger system.

The total amount of hot gas available for cooling in each halo is given by:

$$M_{\text{hot}} = f_{\text{b}} M_{\text{vir}} - \sum_i [M^{(i)}_{\text{star}} + M^{(i)}_{\text{cold}} + M^{(i)}_{\text{ejected}}] \tag{3.7}$$

where the sum extends over all the galaxies in the halo and f_{b} is the baryon fraction of the Universe. In this work we use the value $f_{\text{b}} = 0.15$ as suggested by the CMB experiment WMAP (Spergel et al. 2003). When going from one snapshot to the next, three things may happen:

- a new halo may form. In this case its hot gas mass is initialised to the value $f_{\text{b}} M_{\text{vir}}$;

- the virial mass of the halo may increase because of accretion of 'diffuse' material. In this case the accreted baryons are effectively added to the hot component using Eq. 3.7;

- two haloes can merge. In this case both the ejected component and the hot component of the lower mass halo are added to the hot component of the

remnant halo. The ejected component of the remnant halo remains outside the halo but is reduced by a factor given by Eq. 3.5.

The cooling rate is assumed to be constant between two successive simulation outputs. The differential equations given above are solved using smaller time–steps (50 between each pair of simulation snapshots). At the end of each small time–step, the merger clocks of satellite galaxies are reduced and if this merging time falls below zero, the satellite galaxy is merged with the central galaxy and removed from the list of galaxies.

3.6 Model normalisation and influence of the parameters

As in previous work (Kauffmann & Charlot 1998; Somerville & Primack 1999), the free parameters of the model are tuned in order to reproduce the observed properties of our Galaxy (see Table 3.2). We also check that we get the right normalisation and slope for the Tully–Fisher relation.

Note that the main parameters controlling the physical evolution of our model galaxies are:

- the parameters determining the star formation efficiency: α_0 and n;

- the parameters determining the feedback efficiency: ϵ in the ejection model, and c and V_{crit} in the wind model;

- the amount of metals produced per solar mass of cold gas converted into stars: Y;

- the gas fraction returned by evolved stars: R;

- the parameter γ, that determines how long it takes for the ejected gas to be re–incorporated.

The value of the parameter R can be directly estimated from stellar evolution theory for a given choice of IMF. Population synthesis models show that this re-cycled fraction is roughly independent of metallicity and lies in the range 0.2–0.45 (Cole et al. 2000). Note that this value can be larger for top–heavy IMFs.

Note that there are only a few free parameters in our model. The influence of the different parameters on the observed properties of galaxies can be summarised as follows:

- the yield Y controls the total amount of metals in the stars and gas. Note that the cooling rates in lower mass haloes are strongly dependent on the metallicity. Increasing the yield results in an overall increase of the luminosities of our galaxies and a tilt in the Tully–Fisher relation towards a shallower slope.

Table 3.1: Values adopted for the free parameters in our three models.

	α_0	n	ϵ	Y	R	c	V_{crit}
retention	0.09	2.2	0.45	0.045	0.35	–	–
ejection	0.08	2.2	0.15	0.040	0.35	–	–
wind	0.10	2.5	0.35	0.040	0.35	5	150

- The star formation efficiency α_0 has only a weak influence on the zero–point of the Tully–Fisher relation, but it has an important influence on the gas fraction of galaxies.

- The parameter n, that parametrises the dependence of star formation efficiency on the circular velocity of the galaxy, has a strong effect on the dependence of the gas fraction on the mass or circular velocity of the galaxy. It has negligible effect on all the other observational properties.

- The feedback efficiency has a strong influence both on the zero–point and the slope of the Tully–Fisher relation. An increase in feedback efficiency results in a decrease in the luminosities of galaxies and a tilt in the Tully–Fisher towards a steeper slope.

- The gas fraction returned by evolved stars R has only a marginal influence on the gas metallicity and on the luminosities of the galaxies in our model.

- The parameter γ controls how long it takes for the ejected gas to be re–incorporated back into a dark matter halo. We have experimented with γ values in the range 0.1–1. If $\gamma = 0.1$, the re–incorporation time is of order the Hubble time. If γ is large, the ejection model simply reverts back to the retention scheme. Note that if we decrease γ, gas and metals remain outside dark matter haloes longer and cooling rates are reduced. As a result, the feedback efficiency in our preferred model is smaller. In the next section, we will show results for $\gamma = 0.1$, which should be considered an 'extreme' ejection scheme, where gas and metals remain outside the halo for a time comparable to the age of the Universe. In Sec. 4.5, we will explore in more detail what happens if the re–incorporation timescale is reduced.

A through exploration of parameter space results in the parameters listed in Table 3.1. The requirement that our models agree with a wide range of observational data (see Sec. 3.7) allows only slight changes around the values listed in Table 3.1.

Note that in all three models, we have to assume a value for the yield that is larger than the conventional value. This is consistent with other analyses, which have shown that the observed metallicity of the ICM cannot be explained using a standard IMF

with a standard value of the yield (Gibson & Matteucci 1997; Gibson et al. 1997). A recent review of the problem can be found in Moretti et al. (2003). In this work, we will leave aside this problem. Note also that we will not attempt to distinguish between the heavy elements produced by SNII and SNIa. It is known that the latter are the most important contributors for Fe, while the former mainly contribute α elements. SNII and SNIa events are characterised by different time–scales, so that there is a lag between the ejection of these elements into the interstellar medium. This will be studied in more detail in a future paper (Cora et al., in preparation). We will also not attempt to explore what would happen if the various free parameters listed in Table 3.1 were to depend on redshift. A redshift dependence of the star formation efficiency, for example, may be required to explain the evolution in the number density of luminous quasars (Kauffmann & Haehnelt 2000) and to reproduce the observed properties of Lyman break galaxies at redshift ~ 3 (Somerville et al. 2001).

Note that the only parameter that changes significantly between the three different models is the feedback efficiency and that for the retention and wind schemes, we are obliged to adopt an uncomfortably high value. The value adopted for the parameter c also lies on the upper end of the allowed range. Efficient feedback is required in order to counteract the high cooling rates and prevent overly luminous galaxies from forming at the present day. If the ejected material is kept outside the haloes for substantial periods, then the need for high feedback efficiencies is not as great. Note that a high value of the feedback efficiency is also required in the wind model. This is because most of the galaxies in the simulation box rapidly fall below the conditions required for a 'wind', given the relatively low values adopted for V_{crit}. Efficient feedback is then again required in order to avoid the formation of overly luminous galaxies.

3.7 Comparison with local observations

In this section, we present model results for some of the basic observed properties of galaxies, both in and out of clusters. As explained in Sec. 3.6, the free parameters of our model are mainly tuned in order to reproduce the observed properties of the Milky–Way and the correct normalisation of the Tully–Fisher relation . An extensive exploration of parameter space seems to indicate that the range of acceptable parameters for each model is small.

We select as 'Milky–Way type' galaxies all the objects in the simulation with circular velocities in the range 200–$240 \, \text{km s}^{-1}$ and with bulge–to–disc ratios consistent with Sb/Sc type galaxies (Simien & de Vaucouleurs 1986). More specifically we select all galaxies with $1.5 < \Delta M < 2.6$ ($\Delta M = M_{\text{bulge}} - M_{\text{total}}$). Note that in our model we assume that the circular velocity of a galaxy is ~ 25 per cent larger than the circular velocity of its halo. This is motivated by detailed models (Mo et al. 1998) for

Table 3.2: Properties of *Milky–Way* type galaxies in our models. The masses are in units of $h^{-1}\,\mathrm{M}_\odot$ and the star formation rate (SFR) is in units of $\mathrm{M}_\odot\,yr^{-1}$.

	M_{gas}	M_{star}	SFR	$Z_{\mathrm{stars}}/Z_\odot$
retention	$8.03 \cdot 10^9$	$4.67 \cdot 10^{10}$	3.13	0.80
ejection	$7.53 \cdot 10^9$	$4.94 \cdot 10^{10}$	2.57	0.82
wind	$8.83 \cdot 10^9$	$6.00 \cdot 10^{10}$	3.59	0.87

	$\mathrm{M_B} - 5\log h$	$\mathrm{M_V} - 5\log h$	$\mathrm{M_I} - 5\log h$
retention	-20.49	-21.07	-22.08
ejection	-20.42	-21.03	-22.07
wind	-20.70	-21.27	-22.30

the structure of disc galaxies embedded in cold dark matter haloes with the universal NFW[2] profile (Navarro, Frenk & White 1997). These models show that the rotation velocity measured at twice the scale length of the disc is 20–30 per cent larger than the virial velocity of the halo.

In our three models we find 11, 13 and 11 Milky–Way type galaxies (for the retention, ejection and wind model respectively) that reside in uncontaminated haloes, i.e. haloes that are not contaminated by the presence of low resolution particles. For these galaxies we obtain the stellar masses, gas masses, star formation rates, and metallicities listed in Table 3.2. These values are very close to what is observed for our own Galaxy, which has a stellar mass $\sim 10^{11}\,\mathrm{M}_\odot$ and a total mass of cold gas in the range $6.5 \cdot 10^9$–$5.1 \cdot 10^{10}\,\mathrm{M}_\odot$ (Kauffmann et al. 1999; Somerville & Primack 1999). Rocha-Pinto et al. (2000b,a) give an estimate for the mean SFR in the Milky Way's disc over the last few Gyr of the order of 1–$3\,\mathrm{M}_\odot\,\mathrm{yr}^{-1}$. This is somewhat lower than the values we find for our model galaxies. The Galaxy has a B–band and I–band absolute magnitude of ~ -20.5 and ~ -22.1 respectively, and a V–light weighted mean metallicity of ~ 0.7 solar (Kauffmann & Charlot 1998; Somerville & Primack 1999). All these observed values are in reasonably good agreement with the values

---

[2]Navarro, Frenk & White (1997) found that the dark matter density profile of dark matter haloes have the same shape, independent of the halo mass, the initial density fluctuation spectrum, and the values of the cosmological parameters. The *universal* NFW profile can be written as:

$$\frac{\rho(r)}{\rho_{\mathrm{crit}}} = \frac{\delta_c}{(r/r_s)(1 + r/r_s)^2}. \tag{3.8}$$

where r_s is a characteristic length, δ_c a characteristic density and $\rho_{\mathrm{crit}} = 3H^2/8\pi G$ is the critical density of the Universe, i.e. the density corresponding to a flat Universe. At the scale radius r_s the slope changes from $\propto r^{-1}$ to $\propto r^{-3}$. The finding has been confirmed by later works, although there is still some debate about the exact slope in the very inner part of dark matter haloes.
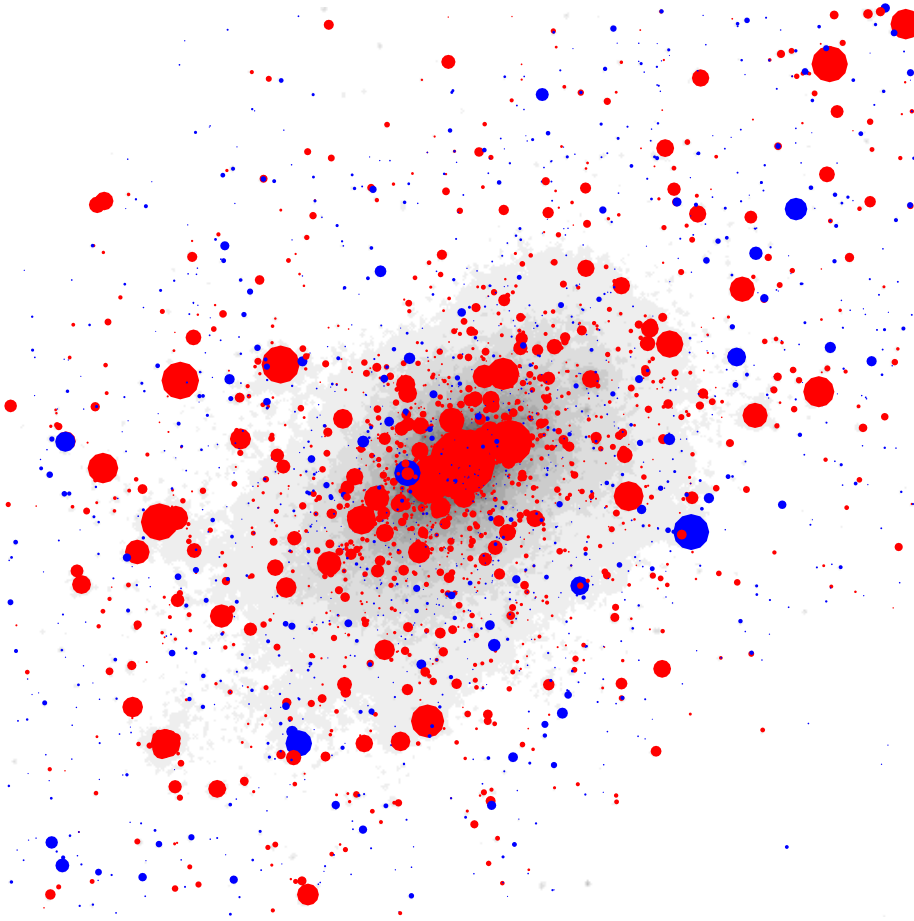
Figure 3.4: Spatial distribution of the galaxies associated with the cluster halo. Symbols area is proportional to the B–band luminosity. Red circles are for objects with B - V > 0.8 and blue circles are for objects with B - V < 0.8. Only objects with $M_B < -16$ are shown. The spatial distribution of galaxies is overlaid to the dark matter density distribution inside a cubic box of size 4 Mpc on a side.

listed in Table 3.2.

Our 'Milky Way normalisation' allows us to obtain a remarkably good agreement with other general properties of the galaxy population. We discuss in some more details these results in the following.

In Fig. 3.4 we show the spatial distribution of galaxies associated with the main halo in a box of 4 Mpc on a side, overlaid to the dark matter density distribution. Symbols area is proportional to the B–band luminosity. Red circles are for objects with B - V > 0.8 and blue circles are for objects with B - V < 0.8. The figure clearly
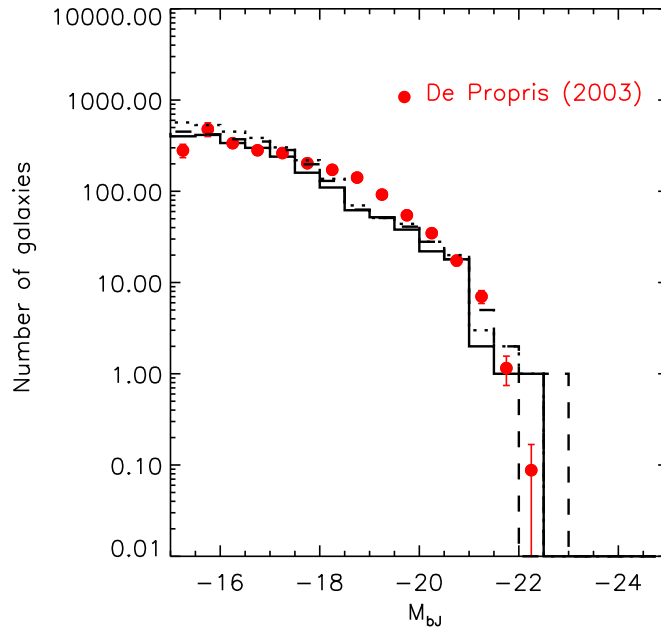
Figure 3.5: Luminosity function in the b_J–band for model galaxies in the retention, ejection, and wind scheme. The red points represent the composite luminosity function by De Propris et al. (2003a). The solid line is for the retention model, the dashed line for the ejection model, and the dotted line for the wind model.

shows that more luminous and red galaxies are more strongly concentrated towards the centre of the cluster, in agreement with observational results.

In Fig. 3.5 we show the cluster luminosity function in the b_J–band for each of our three schemes. We find cluster luminosity functions which are in a reasonably good agreement with the composite luminosity function for cluster galaxies obtained by De Propris et al. (2003a). A fit to a Schechter (1976) function gives a characteristic magnitude of $M^*_{b_J} = -21.47$ and a faint–end power law slope of $\alpha = -1.20$ for the retention model. Note that resolution effects artificially flatten the luminosity function at magnitudes $\gtrsim -15$ (the fit to a Schechter function is performed on the magnitude interval from -16 to -22). For the ejection and wind scheme the results are similar. The cluster galaxies are slightly more luminous and the faint–end slope is somewhat steeper.

Fig. 3.6 shows that our model galaxies correctly reproduce the slope of the observed colour–magnitude relation for cluster ellipticals. The solid line is the fit to data for the Coma cluster ellipticals from Bower et al. (1992). The points are model galaxies with
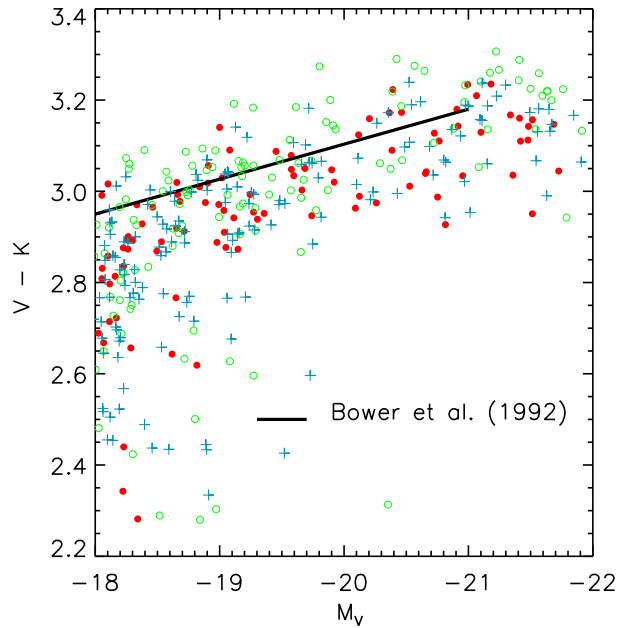
Figure 3.6: Colour–magnitude relation for early type galaxies in the models compared with the observational relation obtained for the Coma cluster ellipticals by Bower et al. (1992). Filled circles are for the retention model, empty circles for the ejection model, and crosses for the wind model.

an early type morphology ($\Delta M < 0.2$) for our three different schemes. Our results confirm the conclusion that the colour–magnitude is mainly driven by metallicity effects (Kodama et al. 1998; Kauffmann & Charlot 1998). Note that the scatter of the model galaxies is larger than the observational value: for all three model we find a scatter of ~ 0.07, while the value measured by Bower et al. (1992) is 0.048.

In Fig. 3.7 we show the Tully–Fisher relation obtained for our model galaxies. We have plotted central galaxies that are in haloes outside the main cluster and that are not contaminated by low resolution particles. We apply a morphological cut that selects Sb/Sc–type galaxies ($1.5 \leq M_{\mathrm{bulge}} - M_{\mathrm{total}} \leq 2.6$) and we select all galaxies brighter than -18 in the I–band. These morphological and magnitude cuts correspond approximately to the ones defining the sample used by Giovanelli et al. (1997). The mean observational relation is shown by a solid line in the figure, and the scatter about the relation is indicated by the dashed lines. The relation of Giovanelli et al. is already corrected for internal extinction. We therefore do not correct our I–band magnitudes for dust extinction in this plot.
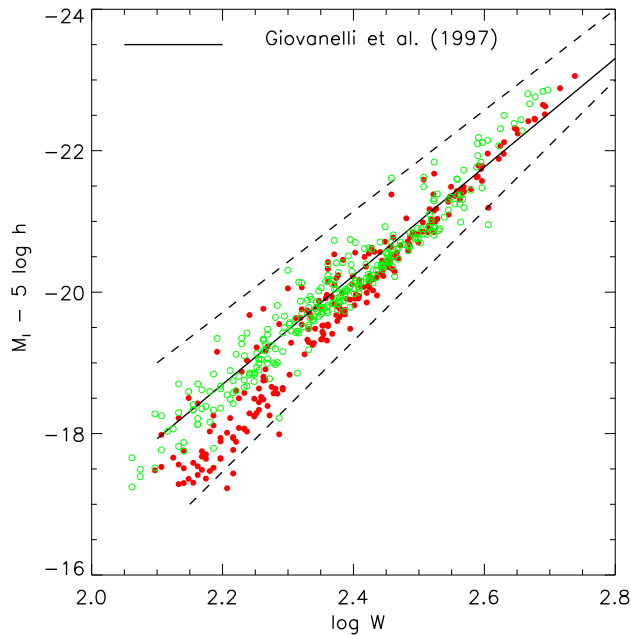
Figure 3.7: Tully–Fisher relation for our model galaxies compared with the observational result by Giovanelli et al. (1997). The scatter in the observational sample is shown with dashed lines while the thick solid line shows the 'best fit' observational relation. Filled circles represent model galaxies in the ejection model while empty circles are used for model galaxies from the wind model.

Note that the Tully–Fisher relations in our simulations have extremely small scatter. There are probably many sources of additional scatter that we do not account for – for example photometric errors and scatter in the relation between halo circular velocity and observed line–widths (here we simply assume that $V_c = 2W$). The slope of our predicted TF relation is also somewhat steeper than the observations for the retention and ejection models (for clarity only model galaxies from the ejection scheme are plotted as filled circles in the figure; galaxies in the retention scheme exhibit a relation that is very similar). We obtain the best fit to the observed Tully–Fisher relation for our wind model (shown as empty circles). This is because, in this scheme, the ejected mass is systematically smaller than in the ejection scheme for low mass galaxies. The slope of the Tully–Fisher relation is strongly dependent on the adopted feedback prescriptions and could in principle be used to test different feedback models if we had better control of the systematic effects in converting from theoretical to observed quantities.
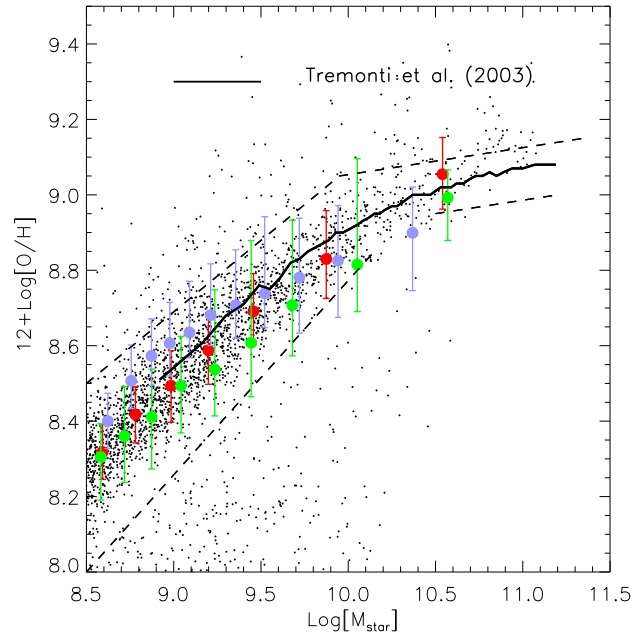
Figure 3.8: Metallicity–mass relation for our model galaxies (shown as points in the plot). The thick solid line represents the median relation between stellar mass and metallicity obtained for a sample of 20,000 galaxies in the SDSS (Tremonti et al., in preparation). The dashed lines indicate the scatter in the observed sample. The solid symbols represent the median obtained from our models in bins containing ~ 400 galaxies each. Red circles are for the retention model, green circles are for the ejection model, and violet circles are for the wind model. The error bars mark the 20th and 80th percentiles of the distribution.

In Fig. 3.8 we compare the relation between metallicity and stellar mass for our simulated galaxies with the stellar mass–metallicity relation derived from new data from the Sloan Digital Sky Survey (Tremonti et al., in preparation). Measuring the metallicities of stars in a galaxy is difficult, because most stellar absorption lines in the spectrum of a galaxy are sensitive to both the age of the stellar population and its metallicity. The metallicity of the gas in a galaxy can be measured using strong emission lines such as [OII], [OIII], [NII], [SII] and Hβ, but up to now, the available samples have been small. Tremonti et al. have measured gas–phase metallicities for $\sim$ 20,000 emission–line galaxies in the SDSS and the median relation from their analysis is plotted as a solid line in Fig. 3.8. Note that the stellar masses for the SDSS galaxies are measured by Tremonti et al. using the same method as in Kauffmann et al.
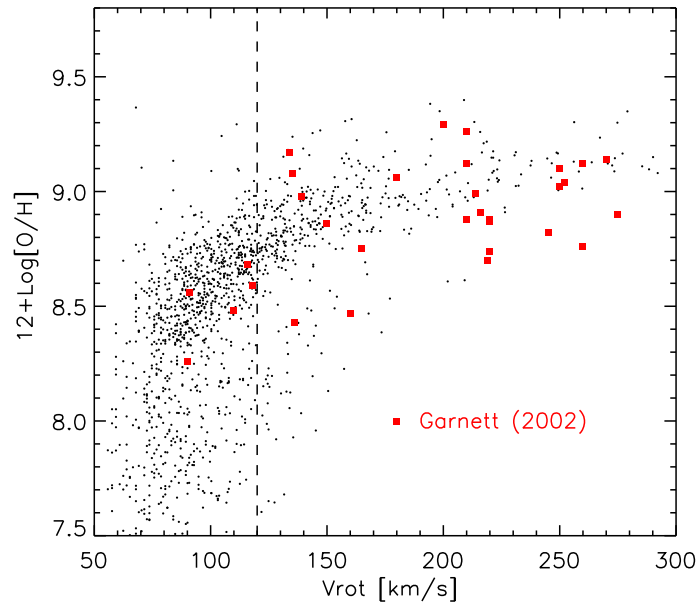
Figure 3.9: Relation between metallicity and rotational velocity for our model galaxies (shown as points). The filled squares represent the observational data from Garnett (2002). The vertical dashed line corresponds to a velocity $120\,\mathrm{km\,s^{-1}}$ (the turn–over velocity claimed by Garnett).

(2003). The dashed lines represent the scatter in the observed relation. The dots in the figure represent simulated galaxies in the retention model. We have only selected galaxies that reside in uncontaminated haloes outside the main cluster and that have gas fractions of at least 10 per cent. All of these galaxies are star–forming and should thus be representative of an emission line–selected sample. We obtain very similar relations for our two other schemes. This can be seen from the solid symbols in the plot, which indicate the median in bins that contain each ~ 400 model galaxies. Given the uncertainties in both the stellar mass and the metallicity measurements, the agreement between our models and the observational results is remarkably good.

In Fig. 3.9 we compare the metallicity versus rotational velocity measurements published by Garnett (2002) to the results obtained for our models. For simplicity, we only show results from the retention model. The other two schemes give very similar answers. Again we have selected only galaxies that reside in uncontaminated haloes outside the main cluster and that have gas fractions of at least 10 per cent. The vertical dashed line in the figure shows a velocity of $120\,\mathrm{km\,s^{-1}}$. According to the analysis of Garnett, this marks a threshold below which there is a stronger
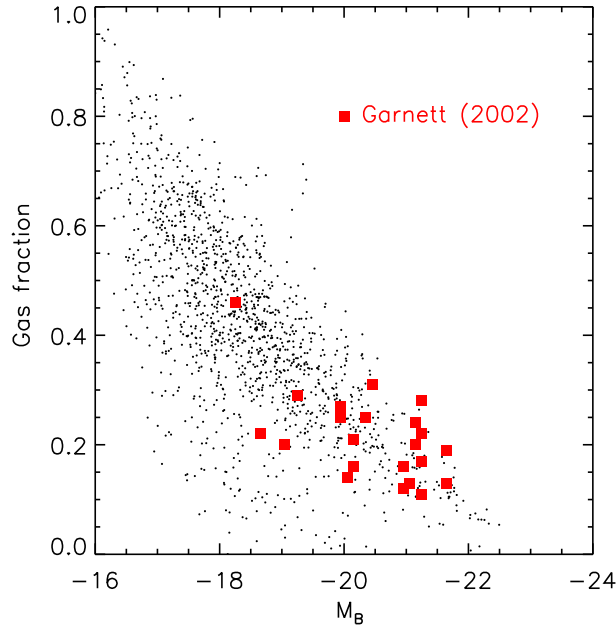
Figure 3.10: Gas fraction as a function of the B–band luminosity for our model galaxies (shown as points). Filled squares are the gas fractions computed by Garnett (2002) for the same sample of data shown in Fig. 3.9. Results are shown for the retention model, but are very similar for the other two schemes.

dependence of metallicity on the potential well depth of the galaxy. (Note, however, that the plot shown by Garnett is in linear units in $V_{\rm rot}$ and that the 'turnover' in the mass–metallicity relation is much more convincing in the data of Tremonti et al.). As can be seen, our models fit the metallicity–rotational velocity data as well. This is not surprising, given that we obtain a reasonably good fit to the observed Tully–Fisher relation.

In Fig. 3.10 we show a comparison between the gas fraction of galaxies in our models and the gas fractions computed by Garnett. The same sample of objects as in Fig. 3.9 is plotted, both for the models and for the observations. Again our model agrees well with the observational data.

3.8 Cluster Mass–to–Light ratio

Table 3.3 lists the total mass–to–light ratios obtained for our cluster in the V and B–bands. The results are given for the 3 different feedback schemes. Note that

Table 3.3: Mass–to–light ratios in the V and in the B–band for our three models. Units are in $h \, \Upsilon_\odot$.

	Υ_B	Υ_V
retention	290	230
ejection	250	200
wind	240	190

the observational determination of a cluster mass–to–light ratios is not an easy task. Both the mass and the luminosity estimates are affected by uncertainties. Estimates based on the virial mass estimator give $\Upsilon_V \sim 175$–252 (Carlberg et al. 1996; Girardi et al. 2000) while B–band mass–to–light ratios are in the range 200–$400 \, h^{-1} \, \Upsilon_\odot$ (Kent & Gunn 1982; Girardi et al. 2002). It has been argued that the virial mass estimator can give spurious results if substructure is present in the cluster or if the volume sampled does not extend out to the virial radius. In general, estimates based on masses derived from X–ray data tend to give lower values.

3.9 Morphological and colour distribution

As already done in previous sections, we determine the morphology of our model galaxies using the B–band bulge–to–disc ratio and taking advantage of the relation found by Simien & de Vaucouleurs (1986) between this quantity and the galaxy morphological type. In the following, we classify as ellipticals all galaxies with $\Delta M < 0.4$, as spirals or irregulars all galaxies with $\Delta M > 1.23$, and as lenticulars (S0) all galaxies with intermediate value of ΔM. We also limit the analysis to galaxies brighter that -18. These galaxies usually reside in substructures whose mass accretion history can be followed back in time for a certain number of snapshots, thus allowing an reliable determination of the morphological type.

In this section we only show the results for our ejection scheme. Similar results are found for the retention and the wind model.

Note that with these morphological cuts, we find a relative fraction of 11, 71 and 18 per cent of ellipticals (E), lenticulars (S0), and spirals and irregulars (Sp+Irr) respectively. These fractions are computed in the field region of our simulation, i.e. all the haloes peripheral to the main cluster and uncontaminated by the presence of low–resolution particles, and are close to the observed relative fractions 13, 67 and 20 per cent measured by Loveday (1996).

In Fig. 3.11 we show the cumulative number of galaxies as a function of the distance from the cluster centre and as a function of the morphological type. Elliptical galaxies are more strongly concentrated towards the cluster centre than spirals. This can be seen more clearly in Fig. 3.12 where we plot the fraction of galaxies of different
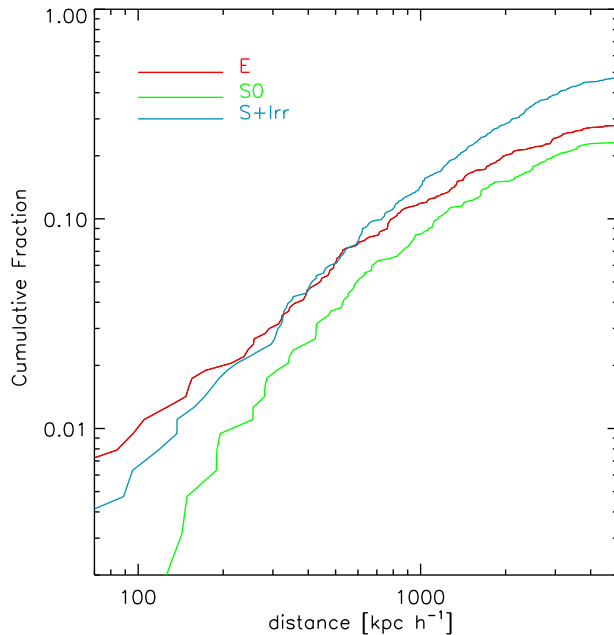
Figure 3.11: Cumulative number of galaxies as a function of their distance from the cluster centre and as a function of the morphological type. The red line is used for ellipticals, the green line for intermediate type galaxies, and the blue line for spirals and irregulars.

morphological types as a function of the distance from the cluster centre. Note that the obtained fractions are in remarkable good agreement with the results shown in Fig. 5 of Dressler (1980), that is here reproduced in Fig. 3.13. Also the *field* morphological fractions we obtain in our simulation are very close to the fractions quoted in Dressler (1980).

We do not attempt here a more accurate comparison with observational data of cluster galaxy population in the nearby Universe. We will undertake this analysis in more details in Chapter 5, where we will compare the results obtained using our model, in terms of cluster structure, with a sample of clusters at high redshift. In that chapter, we will also take into account projection effects, which have been shown to be important when comparing model with observational results (Diaferio et al. 2001).

We note that the morphology of our model galaxies is almost exclusively determined by their merger histories. This means that hierarchical merging is naturally able to reproduce a morphology–radius relation that is in good agreement with the observational results, as already shown by Springel et al. (2001a).
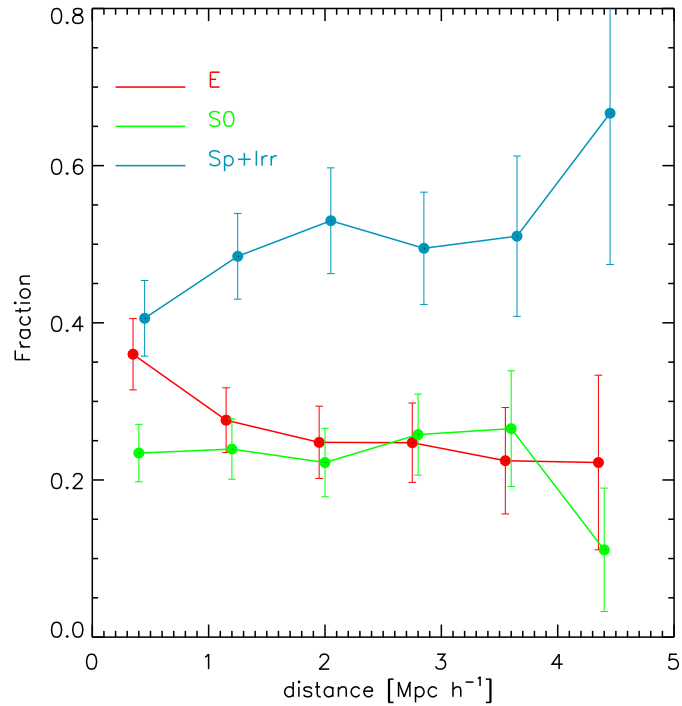
Figure 3.12: Fraction of galaxies with different morphological type as a function of their distance from the cluster centre. Error bars represent Poisson error bars. The red line is used for ellipticals, the green line is used for intermediate type galaxies, and the blue line is used for spirals and irregulars.

Finally, in Fig. 3.14 we show the B-V colour distribution for galaxies in the cluster (dashed histograms) and galaxies that are outside the cluster and that reside in uncontaminated haloes (solid histograms). Blue–dashed histograms are for dust–corrected magnitudes. The correction for dust leaves the colour distribution of cluster galaxies almost unaffected. This is expected because cluster galaxies have star formation rates significantly lower than corresponding field galaxies.

A corresponding plot has been shown by Springel et al. (2001a). We obtain similar results: the distribution of colours is bi–modal and the bimodality mainly reflects differences in star formation histories between elliptical and spiral galaxies.
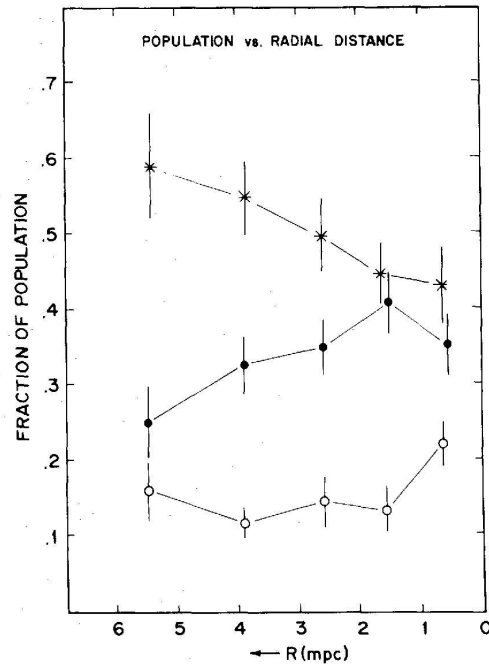
Figure 3.13: Population gradients as observed in 6 clusters from Dressler (1980). Empty circles are used for ellipticals, filled circles are used for S0, and asterisks are used for spirals and irregulars.

3.10 Discussion and Conclusions

In this chapter we have presented a semi–analytic model that follows the formation, evolution and chemical enrichment of galaxies in a hierarchical merger model. Galaxies in our model are not closed boxes. They eject metals and we track the exchange of metals between the stars, the cold galactic gas, the hot halo gas and an ejected component, which we identify as the diffuse intergalactic medium (IGM).

We have explored three different schemes for implementing feedback processes in our models:

- In the retention model, we assume that material reheated by supernovae explosions is ejected into the hot halo gas.

- In the ejection model, we assume that this material is ejected outside the halo. It is later re–incorporated after a time that is of order of the dynamical time of the halo.
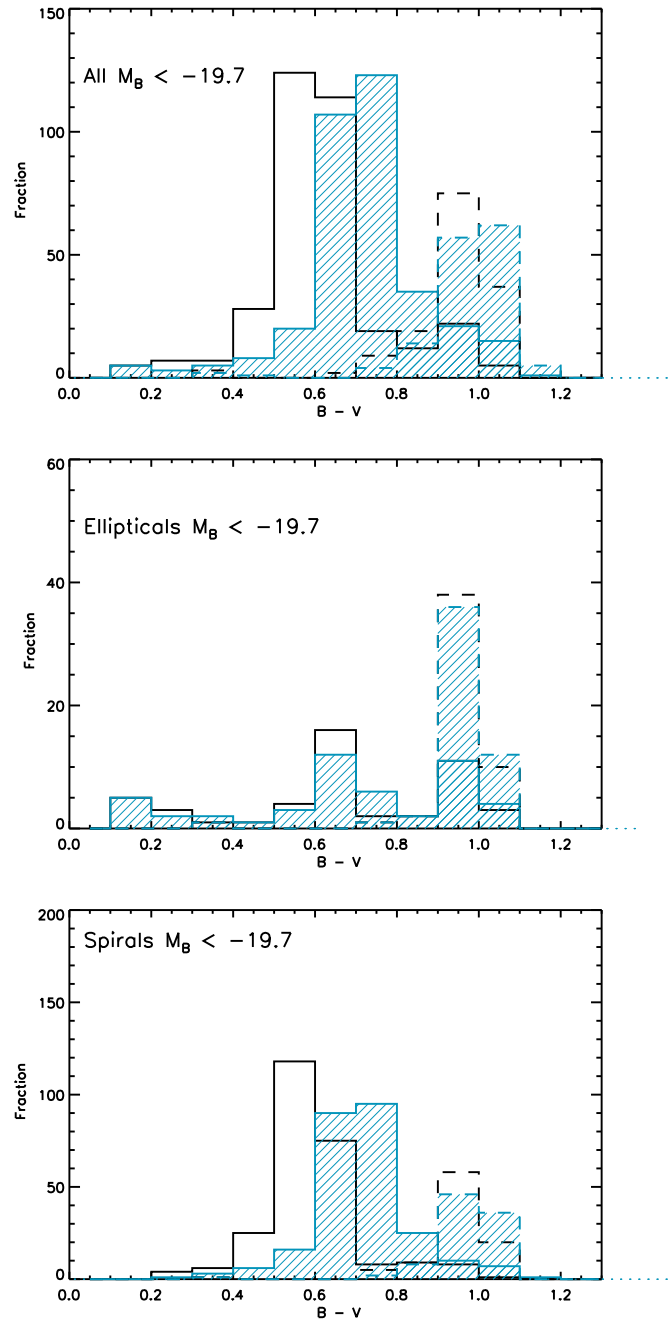
Figure 3.14: Distribution of the colour B-V for all model galaxies brighter that −19.7 (top panel), for ellipticals (central panel), and for spirals (bottom panel). Solid histograms are used for field galaxies and dashed histograms are used for cluster galaxies. Blue–shaded histograms show the corresponding dust–corrected distributions.

- In the wind model, we assume that galaxies eject material until they reside in haloes with $V_{\mathrm{vir}} > V_{\mathrm{crit}}$. Ejected material is also re–incorporated on the dynamical time–scale of the halo. The amount of gas that is ejected is proportional to the mass of stars formed.

In all cases, we can adjust the parameters to obtain reasonably good agreement between our model predictions and observational results at low redshift. The wind scheme is perhaps the most successful, allowing us to obtain remarkably good agreement with both the cluster luminosity function and the slope and zero–point of the Tully–Fisher relation. All our models reproduce a metallicity mass relation that is in striking agreement with the latest observational results from the SDSS. By construction, we also reproduce the observed trend of increasing gas fraction for smaller galaxies. The good agreement between models and the observational results suggests that we are doing a reasonable job of tracking the circulation of metals between the different baryonic components of the cluster.

Our model elliptical galaxies are more strongly concentrated towards the cluster centre than spiral galaxies, in qualitatively very good agreement the observed morphology–radius relation by Dressler (1980).

We have shown that semi–analytic models, coupled with high resolution N–body simulations, represent a powerful instrument for the comparison of theoretical predictions with observational results. In Chapter 5, we will compare in more details the results obtained from our model, in terms of cluster structure, with observational data using a large sample of clusters at high redshift and thus also addressing the question of cluster–to–cluster variation.

*– When conceiving an ideal, we can assume what-
ever we want, but we should avoid the impossibil-
ities*

Aristotelis

4

The chemical enrichment of the intra–cluster and intergalactic medium

Abstract

In this chapter I present an analysis of the chemical enrichment history of the intra–cluster and intergalactic medium. The model developed in the previous chapter represents the ideal tool to carry–out this kind of analysis. The remarkable agreement between the model results and the observational data, in fact, suggests that I am doing a reasonable job of tracking the circulation of metals between the different baryonic components of the cluster. It is then possible to use the model to investigate when the chemical pollution of the intra–cluster gas occurred and which galaxies are mainly responsible for it. I also discuss two observational tests that may provide important constraints on the mechanism by which metals are transported from galaxies into the intra–cluster and intergalactic medium.

4.1 Introduction

In the previous chapter, we developed a semi–analytic model that follows the photometric and chemical evolution of cluster galaxies in a self–consistent way. Since we model the transport of mass and metals between the stars, the cold gas in galaxies, the hot gas in dark matter haloes, and the intergalactic gas outside virialized haloes, our model is also able to follow the chemical enrichment history of the intra–cluster and intergalactic medium.

N–body simulations have shown that the baryon fraction in a rich cluster does

not change appreciably during its evolution (White et al. 1993). Clusters of galaxies can thus be considered as closed systems, retaining all information about their past star formation and metal production histories (Renzini 1997). This suggests that direct observations of elemental abundances in the intra–cluster medium (ICM) can constrain the history of star formation in clusters, the efficiency with which gas was converted into stars, the relative importance of different types of supernovae, and the mechanisms responsible for the ejection and the transport of metals.

The last decade has witnessed the accumulation of a large amount of data on the chemical composition of the intra–cluster gas (Mushotzky et al. 1996; De Grandi & Molendi 2001; Ettori et al. 2002). X–ray satellites have provided a wealth of information about the abundances of many different elements. These studies have shown that the intra–cluster gas cannot be entirely of primordial origin – a significant fraction of this gas must have been processed in the cluster galaxies and then transported from the galaxies into the ICM.

The total amount of iron dispersed in the ICM is of the same order of magnitude as the mass of iron locked in the galaxies (Renzini et al. 1993). Observational data suggest that the mean metallicity of the ICM is about 0.2–0.3 solar, both for nearby (Edge & Stewart 1991) and for distant clusters (Mushotzky & Loewenstein 1997).

Various physical mechanisms can provide viable explanations for the transfer of metals from the galaxies into the ICM, for example ejection of enriched material from mergers of proto–galactic fragments (Gnedin 1998); tidal/ram pressure stripping (Gunn & Gott 1972; Fukumoto & Ikeuchi 1996; Mori & Burkert 2000); galactic outflows (Larson & Dinerstein 1975; Gibson & Matteucci 1997; Wiebe et al. 1999). The actual contribution from each of these mechanisms is still a matter of debate. Observational data suggest that metals are most effectively transferred into the ICM by internal mechanisms rather than external forces. Renzini (1997) has argued that ram pressure cannot play a dominant role, because this process would operate more efficiently in high velocity dispersion clusters (the ram–pressure force is proportional to v^2). A correlation between the richness of the cluster and its metal content is not supported by observational data.

In recent years, supernova–driven outflows have received increasing attention as the most plausible explanation for the presence of metals in the ICM. It was originally suggested by Larson (1974) and Larson & Dinerstein (1975) that the fraction of mass and hence of metals driven from a galaxy increases with decreasing galactic mass, because lower mass galaxies have shallower potential wells. This naturally establishes a metallicity–mass relationship that is in qualitative agreement with the observations. It also predicts the chemical pollution of the ICM as a side–effect of the outflow.

This outflow scenario is not without its problems, however. It has been shown in a number of papers (David et al. 1991; Matteucci & Gibson 1995; Gibson & Matteucci 1997; Moretti et al. 2003) that if a standard IMF and chemical yield is assumed, it is very difficult to account for the total amount of metals observed in rich clusters.

Some authors have suggested that cluster ellipticals may form with a non–standard 'top–heavy' IMF. This would alleviate the metal budget problems and also explain the 'tilt' of the fundamental plane, i.e. the increase in galaxy mass–to–light ratio with increasing luminosity (Zepf & Silk 1996; Chiosi et al. 1998; Padmanabhan et al. 2003). From a theoretical point of view, a skewness of the IMF towards more massive stars at higher redshift might be expected from simple arguments related to the Jeans scale and to the scale of magnetic support against gravitational collapse (Larson 1998). On the other hand, many authors have argued that there is very little real observational evidence that the IMF does vary, at least between different regions of our own Galaxy (Hernandez & Ferrara 2001; Massey 1998; Kroupa & Boily 2002). In this analysis, we will simply sweep the IMF issue under the carpet by treating the chemical yield as one of the parameters in our model.

Many interesting clues about metal enrichment at high redshift have been found by studying Lyman break galaxies (LBGs). Detailed studies at both optical and infrared wavelengths have shown that at redshifts ~ 3 , the metallicity of LBGs is relatively high (in the range 0.1–0.5 $Z_\odot$) (Pettini et al. 2000, 2001). Studies of the spectral energy distribution of these objects have shown, somewhat surprisingly, that 20 per cent of these galaxies have been forming stars for more than 1 Gyr (Shapley et al. 2001). This pushes the onset of star formation in these objects to redshifts in excess of 5. Although there seems to be a general consensus that star formation activity (and hence the chemical pollution of the interstellar medium) must have started at high redshift, the question of *which* galaxies are responsible for this pollution is still controversial. Some theoretical studies show that elliptical galaxies must have played an important role in establishing the observed abundance of the ICM, but these studies often require, as we noted before, an initial mass function (IMF) that is skewed towards more massive stars at high redshift. Most such modelling has also not been carried out in a fully cosmological context (see, however, Kauffmann & Charlot (1998) for an approach closer to that adopted in the present analysis). Other studies (Garnett 2002) suggest that dwarf galaxies have been the main contributors to the chemical pollution of the inter–galactic medium (IGM).

In this chapter we use the semi–analytic model developed in the previous chapter to study the chemical enrichment history of galaxies as well as of the intra–cluster and the intergalactic medium.

The chapter is structured as follows: in Sec. 4.2 we briefly comment on the simulations used in this analysis. In Sec. 4.3 we analyse the stellar population composition of our model galaxies. Sec. 4.4 and Sec. 4.5 present the main results of our investigation into the chemical enrichment history of the ICM and the IGM and investigate two observational tests that may help to distinguish between different feedback schemes. Our conclusions are presented in Sec. 4.6.

Name	Description	$m_{\mathrm{p}}\ [h^{-1}\mathrm{M}_\odot]$	z_{start}	$\epsilon\ [h^{-1}\mathrm{kpc}]$
g1	$10^{15}\,h^{-1}\mathrm{M}_\odot$ cluster	2.0×10^9	60	5.0
M2	field simulation	9.5×10^8	70	3.0

Table 4.1: Numerical parameters for the simulations used in this analysis. Both the simulations were carried out assuming a ΛCDM cosmology with cosmological parameters $\Omega_0 = 0.3$, $\Omega_\Lambda = 0.7$, $\Gamma = 0.21$, $\sigma_8 = 0.9$, and $h = 0.7$. In the table, we give the particle mass in the high resolution region m_{p}, the starting redshift of the simulations z_{start}, and the gravitational softening in the high–resolution region ϵ.

4.2 The simulations

In this chapter we use the same massive cluster simulation used in the previous chapter, and a high resolution re–simulation of a 'typical' region of the Universe. For convenience, the numerical parameters of the simulation used in this analysis are repeated in Tab. 4.1.

Note that M2 is a re–simulation of the same region used for the re–simulation M3 (that we used in Chapter 2), but with a lower resolution. We use M2 in this analysis because of significantly reduced computational time compared to M3.

4.3 The galaxy stellar population

In the previous chapter we have described how we combined semi–analytic techniques with a high–resolution simulation of a galaxy cluster to follow the photometric and chemical evolution of galaxies in a self–consistent way. We have investigated and discussed the influence of each of the free parameters of the model on observational results (see Sec. 3.6). Our analysis has shown that the physical handling of the feedback process and of the self–regulation between feedback and star formation rate, is of critical importance in determining the observational properties of galaxies. Unfortunately, the physical mechanisms that regulate feedback are not well known. Given this uncertainty we have experimented with three different mechanisms that we briefly summarise here (see Sec. 3.4.3):

- in the retention model, we assume that material reheated by supernovae explosions is ejected into the hot halo gas.

- In the ejection model, we assume that this material is ejected outside the halo. It is later re–incorporated after a time that is of order the dynamical time of the halo.

- In the wind model, we assume that galaxies eject material until they reside
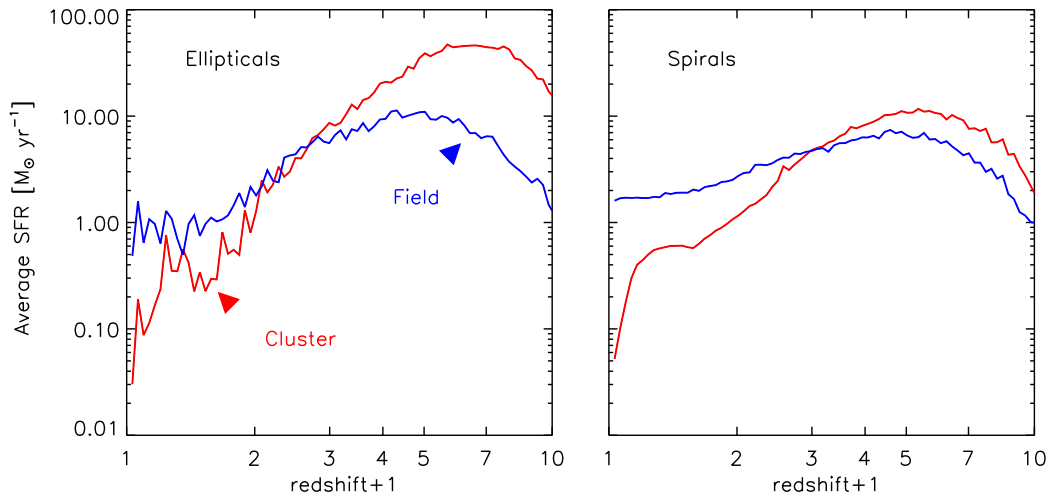
Figure 4.1: Average star formation rate as a function of redshift in the cluster (red lines) and in the field (blue lines). The result for galaxies classified as ellipticals is shown in the left panel, while the right panel shows the result for galaxies classified as spirals (see text for details).

in haloes with $V_{vir} > V_{crit}$. Ejected material is, as in the ejected model, re–incorporated on the dynamical time–scale of the halo. The amount of gas that is ejected is proportional to the mass of stars formed.

In the previous chapter we also showed that with suitable adjustment of the free parameters in the model, all three feedback schemes allow us to obtain a reasonable fit to the observational results at redshift zero. In particular, our models were able to reproduce the cluster galaxy luminosity function measured from the 2dF survey, the colour–magnitude relation of elliptical galaxies, and the relations between stellar mass, gas mass and metallicity inferred from new SDSS data.

Note that the simulation allows us to study how the stellar population of our model galaxies is built up over time. In this section we investigate the stellar populations of different types of galaxies in the cluster and in the field.

As explained in Sec. 3.9, we have classified as ellipticals galaxies with $\Delta M = M_{bulge} - M_{total} < 0.4$, and as spirals or irregulars galaxies with $\Delta M > 1.23$. We also limit the analysis to galaxies brighter that -18. In the following we will show results only for the ejection scheme with $\gamma = 0.1$ (we will show later that this is the model that works best).

Fig. 4.1 shows the average star formation rate (in units of $M_\odot \, yr^{-1}$) for the galaxies classified as ellipticals in the left panel, and as spirals in the right panel. In each

panel, red lines are used for galaxies that are associated with the main halo of the simulation (cluster galaxies) and blue lines are used for galaxies residing in peripheral haloes that are not contaminated by the presence of low resolution particles; we classify these galaxies as 'field' galaxies. The figure shows that the star formation rate of elliptical galaxies is, on average, higher at higher redshift than the star formation rate of spirals. This means that a large fraction of the stars in ellipticals are formed at higher redshifts, i.e. the stellar population of elliptical galaxies is older than the corresponding stellar population of spiral galaxies, in agreement with observational results. For the same kind of galaxy, however, the star formation rate in the cluster is peaked at higher redshift than the star formation rate in the field, i.e. elliptical galaxies in the cluster are older than isolated elliptical galaxies. The same is true for spiral galaxies. Therefore, the hierarchical scenario naturally predicts a strong dependence of galaxy evolution on environment. Note that there are some observational indication of intermediate age in elliptical stellar population that reside in low density environment (Bower et al. 1990; Terlevich et al. 2001), although it is unclear if observational results support the 'strong' differential evolution predicted by hierarchical models.

Note also that the average star formation rate of ellipticals shows a 'bursty' behaviour, while the average star formation rate of spirals is quite smooth over the whole redshift range shown. It is because of these bursts, which occur during major merging events, that these objects are classified as ellipticals (see Sec. 3.4.4). The morphology of our model galaxies is, in fact, almost uniquely determined by mergers: when two galaxies merge the stellar mass and the luminosity of the smaller galaxies are transferred to the bulge of the remnant object; if the stellar mass ratio of the two merging galaxies is larger than 0.3, we assume that the disc is completely destroyed by the merger and the stars formed in the associated starburst are added to the bulge component.

Our model also allows us to follow the mass accretion histories of each galaxy and ask, for example, when 'most' of the stars that are today present in a given galactic system, formed. Defining the formation redshift of a galaxy as the time when 50 per cent of its stars formed, we obtain the results shown in Fig. 4.2.

The red dashed histograms represent the distribution of the formation redshifts for cluster galaxies, while the blue dashed histograms represent the corresponding distribution for field galaxies. The arrows in each panel show the median of the distributions. As discussed above, most of the stars in the elliptical galaxies are formed at redshifts higher than for the spirals. We also repeat the analysis limiting the sample to galaxies brighter that -20. The distributions for these galaxies (right panels) show that brighter ellipticals are older than fainter ellipticals. Note that this result is in contradiction to what previously found by Thomas (1999) and subsequently cited as a 'strong' failure of the hierarchical model. Note, however, that the results from Thomas were not based on a self–consistent approach: he used the star formation
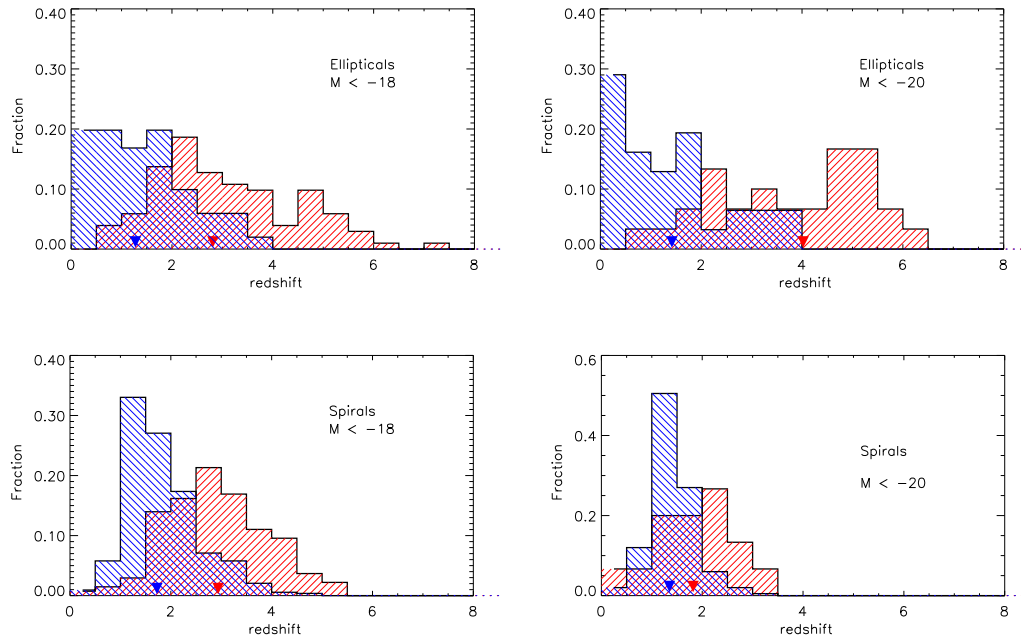
Figure 4.2: Distribution of the redshifts corresponding to the formation time for ellipticals (top panels) and spirals (bottom panels), down to a magnitude limit of −18 (left panels) and −20 (right panels). Red dashed histograms are for cluster galaxies while blue dashed histograms are used for field galaxies. In each panel the arrows show the median of the distributions.

histories predicted by semi–analytic models, but did not treat the chemical evolution in a self–consistent way. In our model, this results naturally arises from the assumption that more massive galaxies have higher star formation efficiency.

Our model also allows us to investigate which is the metallicity of the stars different galaxies are made of. This is illustrated in Fig. 4.3 which shows the fraction of the stars in our elliptical and spiral samples as a function of their metallicity. In each panel we also report the median mass–weighted metallicity of galaxies in the cluster (in red) and in the field (in blue). In all cases the weighted metallicities of galaxies in the cluster are higher than the corresponding values for the field. This is a natural consequence of the fact that cluster galaxies have lower gas fractions and then the material has been processed for longer time allowing the system to reach a higher metallicity. Brighter galaxies have also higher weighted metallicities. This is not a surprise, given the behaviour of the mass–metallicity relation.

Note also that, in this case, the differences between galaxies in different environments is reduced when compared to the 'age' difference. This implies that, if the
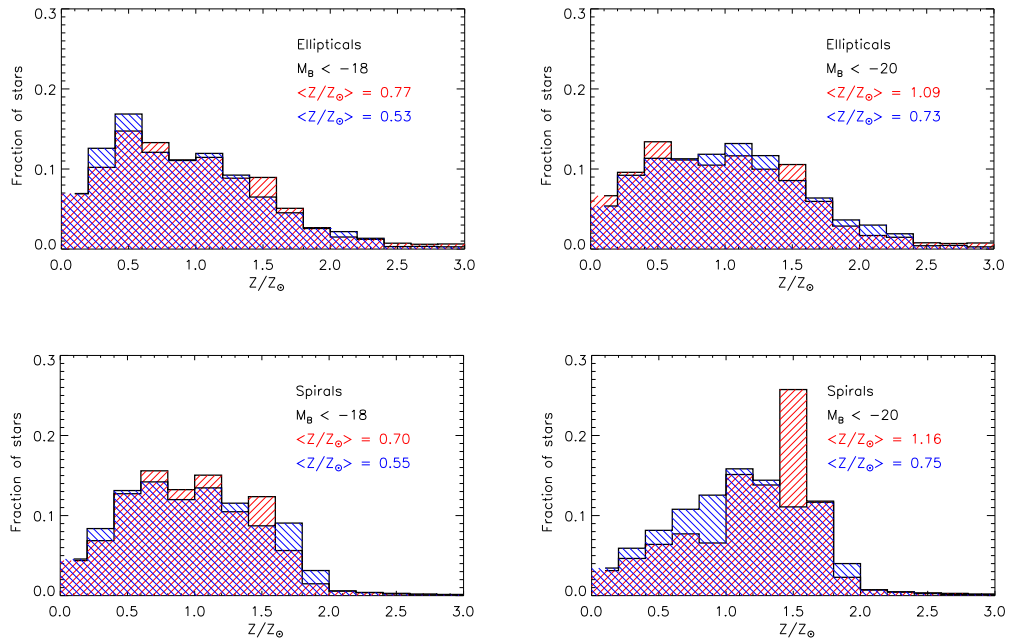
Figure 4.3: Fraction of stars as a function of the metallicity for ellipticals (top panels) and spirals (bottom panels), down to a magnitude limit of -18 (left panels) and -20 (right panels). Red dashed histograms are for cluster galaxies while blue dashed histograms are used for field galaxies. In each panel, median mass-weighted metallicity values are given.

colour–magnitude relation is mainly driven by metallicity effects, the same colour–magnitude holds for cluster and field galaxies, which is in agreement with recent observational results (Bell et al. 2003).

4.4 Chemical enrichment of the ICM

The self–consistency of our model also allows us to follow the chemical enrichment history of the intra–cluster and intergalactic medium.

In our simulated cluster, the metallicity in the hot gas component is $\simeq 0.26$–$0.30\, Z_\odot$, which is in good agreement with X–ray measurements (Renzini et al. 1993).

As discussed by Renzini et al., simple metal abundances in the ICM depend not only on the total amount of metals produced in stars, but also on how much dilution there has been from pristine gas. A quantity that is not dependent on this effect or on the total mass in dark matter in the cluster is the so–called iron mass–to–light

ratio (IMLR), defined as the ratio between the mass of iron in the ICM and the total B-band luminosity of cluster galaxies.

Our simulated cluster has a total mass of $1.14 \cdot 10^{15} \, h^{-1} \, M_{\odot}$ and a total luminosity in the B band of $\sim 10^{13} \, L_{\odot}$. Assuming a solar iron mass fraction from Grevesse et al. (1996), we find IMLR $= 0.015 - 0.020 \, M_{\odot} \, L_{\odot}^{-1}$ for our three models, in agreement with the observational range given by Renzini et al. (1993).

The good agreement between the model predictions and the observational results indicates that our simulation may provide a reasonable description of the circulation of metals between the different baryonic components in the Universe. We can then use our model in order to investigate when the metals in the ICM were ejected and which galaxies were primarily responsible for the chemical pollution.

We recall that we assume that metals are recycled instantaneously and that the chemical pollution of the ICM happens through two routes:

- in the retention scheme the reheated mass (along with its metals) is ejected directly into the hot component. In this model, the enrichment of the ICM occurs at the same time as the star formation.

- In the ejection scheme the reheated material (along with its metals) stays for some time outside the halo and is later re–incorporated into the hot component. This means that there is a delay in the enrichment of the ICM in this scheme.

- The wind scheme sits somewhere in between the retention and ejection models. Metals are ejected out of the halo by galaxies that satisfy the outflow conditions. Otherwise, the metals are ejected directly into the hot gas.

The instantaneous recycling assumption means that the epoch of the production of the bulk of metals in the ICM coincides with the epoch of the production of the bulk of stars. In Fig. 4.4 we show the *average* star formation rate (SFR) of galaxies that end–up in the cluster region and the average star formation rate for galaxies that end–up in the field (the field is defined as consisting of all haloes outside the main cluster that are not contaminated by low resolution particles).

The SFRs in the two regions are normalised to the total amount of stars formed. As already observed in the previous section, the figure shows that star formation in the cluster is peaked at high redshift (~ 5) and drops rapidly after redshift 3. The peak of the SFR in the field occurs at lower redshift (~ 3). The decline in star formation from the peak to the present day is also very much shallower in the field.

Integrating the SFR history of the cluster, we find that ~ 85 per cent of the stars in the cluster formed at redshift larger than 2 and ~ 70 per cent at redshift larger than 3. The corresponding values in the field are 60 per cent and 40 per cent. The results are similar in all the three models.
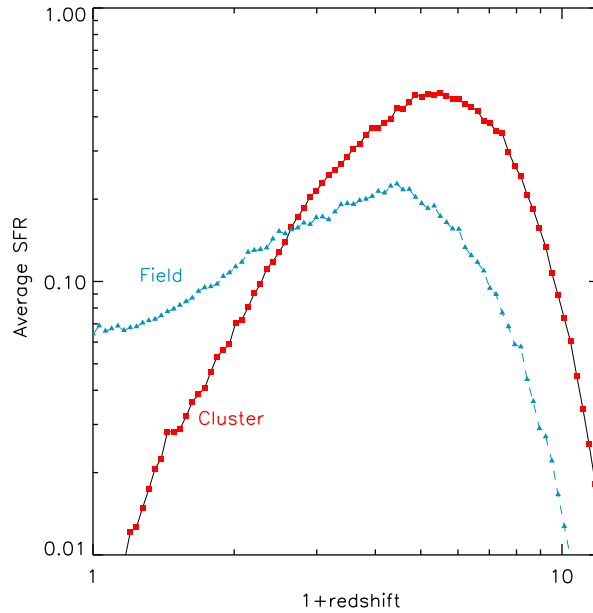
Figure 4.4: Average star formation rate as a function of redshift in the cluster (solid line with red squares) and in the field (dashed line with blue triangles).

Our model then predicts that the chemical enrichment of the intra–cluster medium occurs at high redshift, which is also supported by the observation that the metallicity of the ICM does not vary significantly over the redshift range 0–1 (Tozzi et al. 2003). But which galaxies were mainly responsible for this chemical pollution ? As explained in Sec. 4.1, there is no general consensus on this point. Several theoretical studies have proposed that mass loss from elliptical galaxies is an effective mechanism for explaining the observed amount of metals in the ICM. Some of these studies require an initial mass function (IMF) that is skewed towards more massive stars at high redshift (Matteucci & Vettolani 1988; Gibson & Matteucci 1997; Moretti et al. 2003). Kauffmann & Charlot (1998) used semi–analytic techniques to model the enrichment of the ICM and found that a significant fraction of metals come from galaxies with circular velocities less than $125 \, \mathrm{km \, s^{-1}}$. There have also been a number of more recent attempts to address this question using hydrodynamic simulations (Aguirre et al. 2001; Springel & Hernquist 2003).

In a recent observational study, Garnett (2002) has analysed the dependence of the so–called 'effective yield' on circular velocity for a sample of irregular and spiral galaxies (the data are compared to our model galaxies in Fig. 3.9), concluding, as
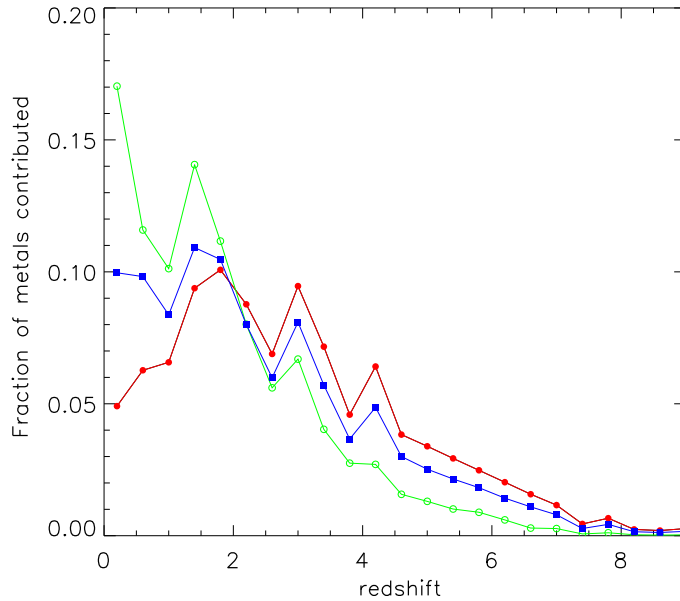
Figure 4.5: Fraction of metals, today present in the ICM, as a function of the redshift they were incorporated into the intra–cluster gas. The red line is used for the retention model, the green line for the ejection model, and blue line for the wind model.

Larson (1974) had earlier, that galaxies with $V_{\rm rot} \leq 100 - 150\,{\rm km\,s^{-1}}$ lose a large fraction of their SN ejecta, while galaxies above this limit retain most of their metals. As we have noted previously, this observational sample is limited both in number and in dynamic range.

Our model predictions are given in Figs. 4.5, 4.7 and 4.8, which show the fraction of the current metals that was incorporated into the ICM as a function of redshift, as a function of the mass and of the circular velocity of the ejecting galaxies respectively.

The expected delay in the chemical enrichment of the ICM is evident if one compares the ejection and wind models with the retention model in Fig. 4.5. Note that a similar delay is also seen in the metallicity of the hot component, although it is very small because the reduction in total accreted ICM almost balances that in accreted metals. Over the redshift range 0–1 the difference between the metallicity of the hot component in the retention and ejection schemes is less than 1 per cent solar, as shown in Fig. 4.6.

As expected, the behaviour of the wind model is intermediate between the ejection and retention schemes. We find that 60–80 per cent of the metals are incorporated
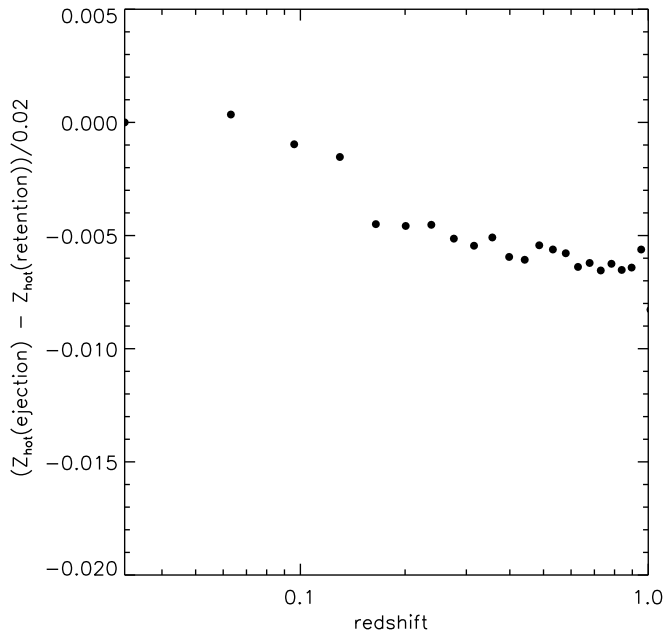
Figure 4.6: Difference between the metallicity of the intra–cluster gas for the retention and the ejection scheme as a function of redshift.

into the ICM at redshifts larger than 1, 35–60 per cent at redshifts larger than 2 and 20–45 per cent at redshifts larger than 3 (we obtain lower values for the ejection scheme, higher values for the retention scheme, and intermediate values for the wind model).

Fig. 4.7 shows that 43–52 per cent of the metals are ejected by galaxies with total baryonic mass less than $1 \times 10^{10} \, h^{-1} \mathrm{M}_\odot$. Baryonic masses at the time of the metal ejection are considered in this analysis. The distribution of the masses of the ejecting galaxies is approximatively independent of the feedback scheme. Although low mass galaxies dominate the luminosity function in terms of number, they do not dominate the contribution in mass. Approximately half of the contribution to the chemical pollution of the ICM comes from galaxies with baryonic masses larger than $1 \times 10^{10} \, h^{-1} \mathrm{M}_\odot$.

In our model, the star formation and feedback processes depend on the virial velocity of the parent substructure. In Fig. 4.8, we show the metal fraction as a function of the virial velocity of the ejecting galaxies. We find that 80–88 per cent of the metals were ejected by galaxies with virial velocities less than $250 \, \mathrm{km \, s^{-1}}$. The 'dip' visible for the wind model in this panel corresponds to the sharp value of V_{crit}
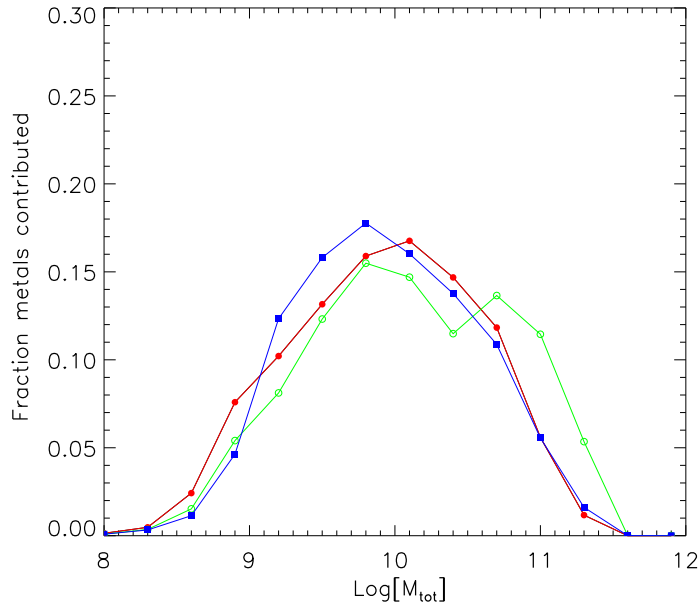
Figure 4.7: Fraction of metals, today present in the ICM, as a function of the total mass of the ejecting galaxy. Different colours are used for the different feedback models as in Fig. 4.5.

we adopt for this feedback scheme. Note that the results we find from this analysis are very similar to the results found by Kauffmann & Charlot (1998), even though the modelling details are different.

4.5 Observational tests for different feedback schemes

Our analysis (see Chapter 3) has shown that properties of galaxies at low redshifts are rather insensitive to the adopted feedback scheme after our free parameters have been adjusted to obtain a suitable overall normalisation.

The observational tests that would clearly distinguish between the different models are those that are sensitive to the amount of gas or metals that have been ejected outside dark matter haloes. In this section we describe two observational tests that may help to put strong constraints on the feedback process.
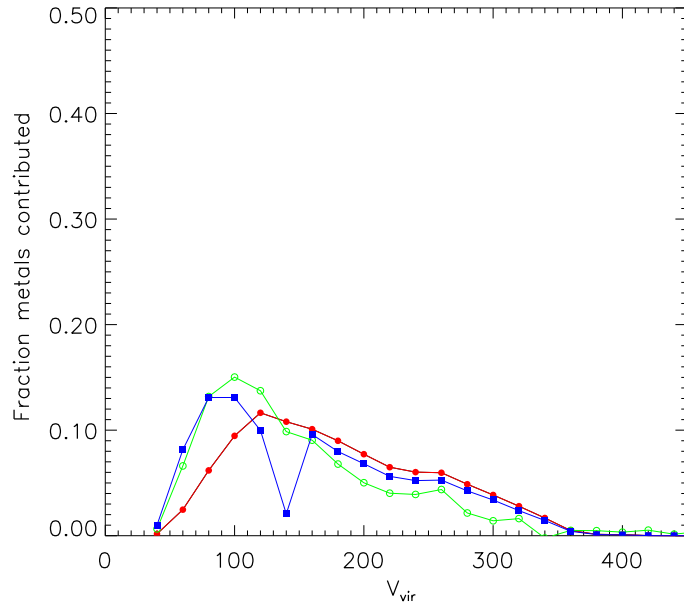
Figure 4.8: Fraction of metals, today present in the ICM, as a function of the virial velocity of the parent substructure. Different colours are used for the different feedback models as in Fig. 4.5.

4.5.1 The hot gas fraction

X–ray observations directly constrain the amount of hot gas in massive virialized haloes. The gas fraction tends to decrease as the X–ray temperature of the system goes down. David et al. (1995) estimated that the gas–to–total mass fraction decreases by a factor ~ 2–3 from rich clusters to groups. In elliptical galaxies, the hot gas fraction is ten times lower than in rich clusters. These results were confirmed by Sanderson et al. (2003) in a recent study of 66 clusters and groups with X–ray data. One caveat is that the hot gas in groups is detected to a much smaller fraction of the virial radius than in rich clusters, so it is not clear whether current estimates accurately reflect global gas fractions (Loewenstein 2000). Another argument for why the gas fraction must decrease in galaxy groups comes from constraints from the soft X–ray background. If galaxy groups had the same gas fractions as clusters, the observed X–ray background at 0.25 keV would exceed the observed upper limit by an order of magnitude (Pen 1999; Wu et al. 2001).

In Fig. 4.9 we plot the gas fraction, i.e. $M_{\text{hot}}/(M_{\text{hot}} + M_{\text{vir}})$, as a function of virial mass for all the haloes in our simulation. The mass of the hot gas is computed using
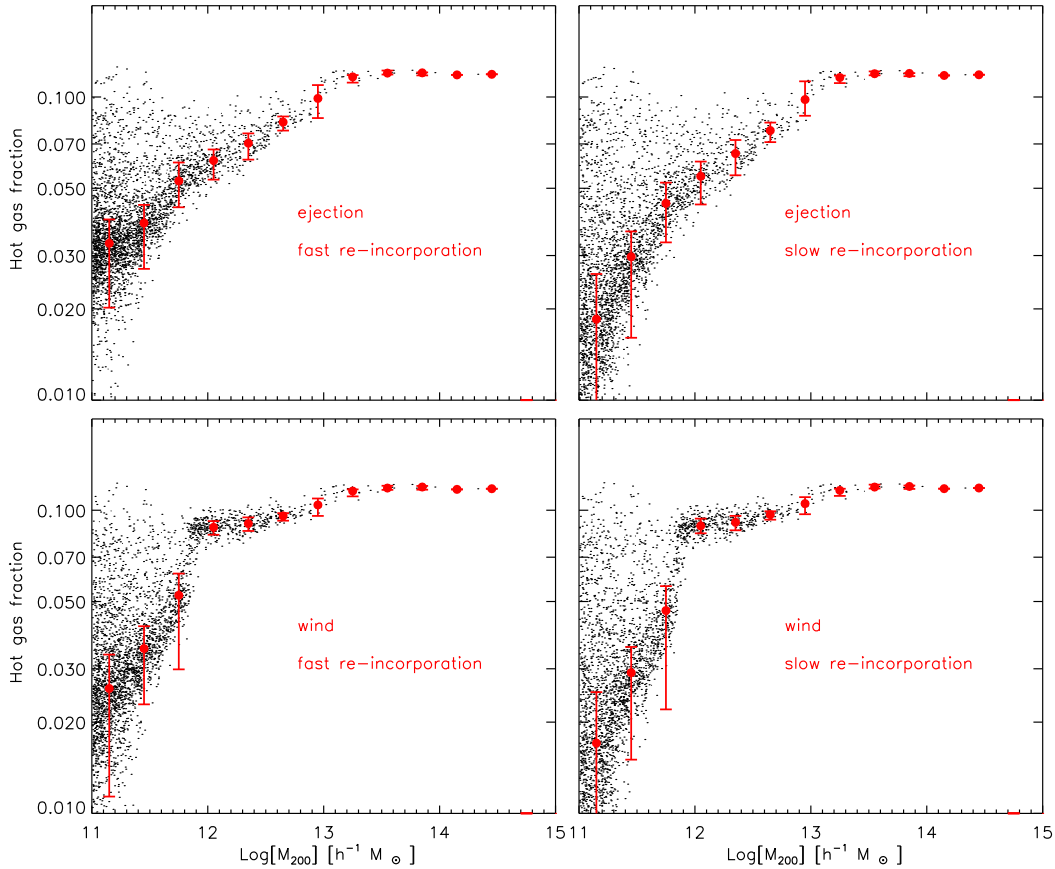
Figure 4.9: Fraction of hot gas as a function of M_{200}. Solid red circles represent the median and the error bars mark the 20th and 80th percentiles of the distribution.

Eq. 3.7. The results are shown for the case of a *short* re–incorporation timescale ($\gamma = 0.3$) in the left column and for a *long* re–incorporation timescale ($\gamma = 0.1$) in the right column. In this figure we plot results for the M2 simulation (see Table 4.1). Note that when we change γ, we also have to adjust the feedback efficiency ϵ so that the model has the same overall normalisation in terms of the total mass in stars formed. We find that the gas fraction remains approximately constant for haloes with masses comparable to those of clusters, but drops sharply below masses of $10^{13} M_{\odot}$. As expected, the drop is more pronounced for the model with a long re-incorporation timescale.

The trends for the wind scheme are similar to those obtained for the ejection scheme, but as can be seen, the 'break' towards lower gas fractions occurs at lower halo masses, because no material is ejected from haloes with circular velocities larger than V_{crit}. In the ejection scheme, material is ejected from haloes up to a circular velocity of $350\,\mathrm{km\,s^{-1}}$. Above this value, cooling flows shut down and no stars form in the central galaxies. Galaxies continue, however, to fall into the cluster. When a satellite galaxy is accreted, we have assumed that its ejected component is re–incorporated into the hot ICM. It is this infall of satellites that causes the gas fractions to saturate in all schemes at halo masses larger than a few times $10^{13}M_{\odot}$.

The ejection model with a long re–incorporation timescale is perhaps closest to satisfying current observational constraints. It reproduces the factor 2–3 drop in gas fraction between rich clusters and groups. By the time one reaches haloes of $10^{12}M_{\odot}$, the gas fractions have decreased to a few percent. This may help explain why there has so far been a failure to detect any diffuse X-ray emission from haloes around late-type spiral galaxies (Benson et al. 2000b; Kuntz et al. 2003).

Note that in the retention model, we have assumed that the material reheated by supernovae explosions never leaves the halo. This translates into a hot gas fraction that is almost constant as a function of M_{200}. This model is therefore not consistent with the observed decrease in baryon fraction from rich clusters to galaxy groups.

4.5.2 The chemical budget

Another possible way of constraining our different feedback schemes is to study what fraction of the metals reside in the diffuse intergalactic medium, well away from galaxies and their associated haloes. We now study how metals are partitioned among stars, cold gas, hot halo gas and the 'ejected component' and we show how this evolves as a function of redshift.

We plot the evolution of the metal content in the different components for our three different feedback schemes. For the ejection scheme we show results for two different re-incorporation timescales. The metal mass in each phase is normalised to the total mass of metals in the simulation at redshift zero. This is simply the yield Y multiplied by the total mass in stars formed by $z = 0$. Note that in the retention scheme, all the reheated gas is put into the halo and there is no ejected component.

Fig. 4.10 shows the evolution of the metallicity for an average 'field' region of the Universe (our simulation M2). In contrast, Fig. 4.11 shows results for our cluster. In this plot we only consider the metals ejected from galaxies that reside within the virial radius of the cluster at the present day. We also normalise to the total mass of metals inside this radius, rather than the total mass of metals in the whole box. Because very little material is ejected from massive clusters in any of our feedback schemes, the ejected component always falls to zero by $z = 0$ in Fig. 4.11.

Let us first consider the field simulation. In the retention scheme (top left panel of

Fig. 4.10), more than 70 per cent of the metals are contained in the hot gas. About 20–30 per cent of the metals are locked into stars, and around 10 per cent of the metals are in cold gas in galaxies. In the ejection scheme (top right and bottom left panels of Fig. 4.10), a large fraction of the metals reside outside dark matter haloes. This is particularly true for the 'slow' re-incorporation scheme, where the amounts of metals in stars, in hot gas and in the ejected component are almost equal at $z = 0$. For the 'fast' re-incorporation model, the metals in the hot gas still dominate the budget at low redshifts.

In the wind scheme (bottom right panel of Fig. 4.10), the amount of metals outside virialized haloes is considerably lower. There are a factor 2 more metals in the hot gas than there are in stars at $z = 0$.

At higher redshifts, the relative fraction of metals contained in cold galactic gas and in the ejected component increases. This is because galaxies are less massive and reside in dark matter haloes with lower circular velocities. As a result, they have higher gas fractions (see Sec. 3.4.2) and are able to eject metals more efficiently. In the ejection scheme, the material that is reheated by supernovae is always ejected from the halo, irrespective of the circular velocity of the system. In this scheme, metals in the ejected component (i.e. in diffuse intergalactic medium) dominate at redshifts greater than 2 in the case of fast re-incorporation, and at all redshifts in the case of slow re-incorporation. In the wind scheme, material is only ejected if the circular velocity of the halo lies below some critical threshold. In this scheme, there are always more metals associated with dark matter haloes than there are in the ejected component.

Turning now to the cluster (Fig. 4.11), we see that the ejected component is negligible in all three schemes. The amount of metals outside dark matter haloes never exceeds the amount of metals locked up in stars up to redshift ~ 3. This is because dark matter haloes collapse earlier and merge together more rapidly in the overdense regions of the Universe that are destined to form a rich cluster. Although metals may be ejected, they are quickly re–incorporated as the next level of the hierarchy collapses. Note that the metals in the cold gas also fall sharply to zero at low redshifts. This is because galaxies that are accreted onto the cluster lose their supply of new gas. Stars continue to form and the cluster galaxies simply run out of cold gas.

Comparison between the metal budget of the cluster and the field regions suggests that cosmic variance effects will turn out to be important when trying to constrain different feedback schemes using estimates of the metallicity of the intergalactic medium deduced from, for example, CIV absorption systems in the spectra of quasars (Schaye et al. 2003). Nevertheless, the strong differences between our different feedback schemes suggest that these kinds of measurements will eventually tell us a great deal about how galaxies ejected their metals over the history of the Universe.

Finally, in Fig. 4.12 we show the evolution of the different phases for the slow ejection scheme, that can be considered as our 'favourite' model. In the top panel,
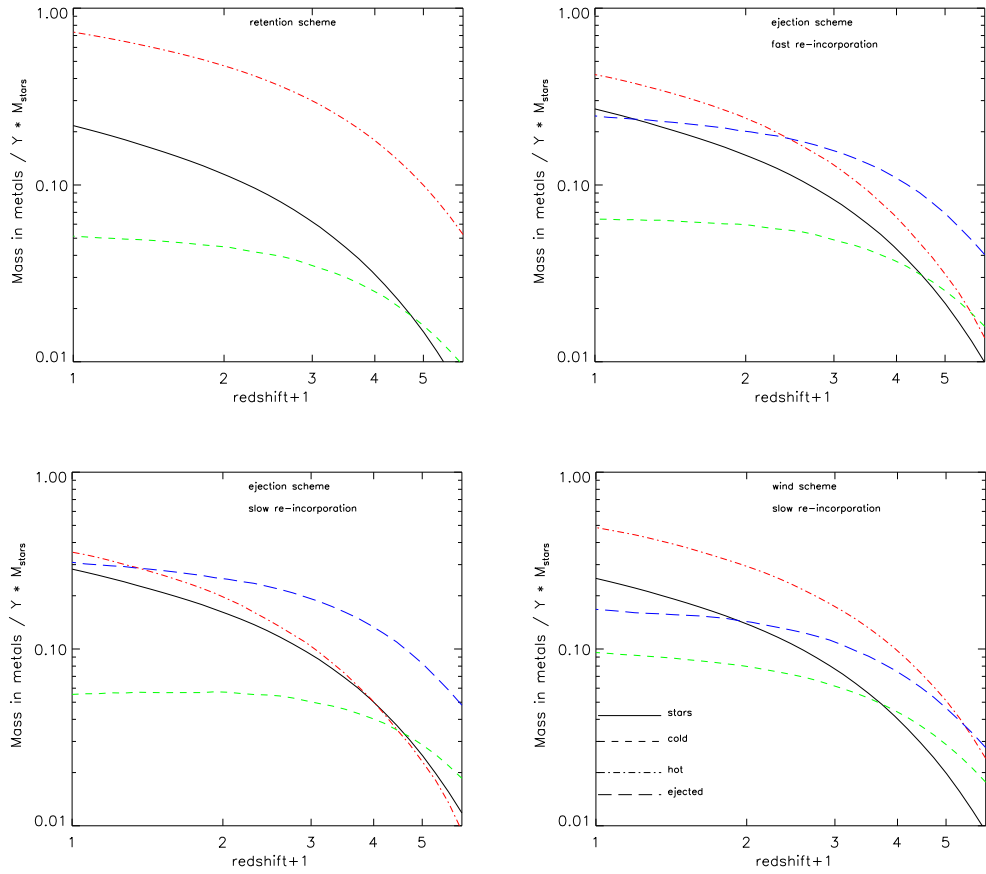
Figure 4.10: Evolution of the metal content of different phases for a typical 'field' region. The solid black line represents the evolution of the metal content in the stars, the dashed green line the cold gas, the dashed–dotted red line the hot gas, and the long–dashed blue line the ejected component (not present in the retention scheme). The metal content in each phase is normalised to the total mass of metals produced from all the galaxies considered.

we plot the evolution in mass of the different phases for all the galaxies within the virial radius in our cluster simulation. In agreement with what is shown in Fig. 4.4, the stellar component grows very slowly after redshift ~ 3, when most of the stars in the cluster have already been formed. The cold gas and the ejected mass decrease as galaxies are accreted onto the cluster and stripped of their supply of new gas. The hot gas mass increases because of the accretion of 'diffuse material'. In the bottom panel, we plot the evolution of the mass density in each reservoir for our field simulation.
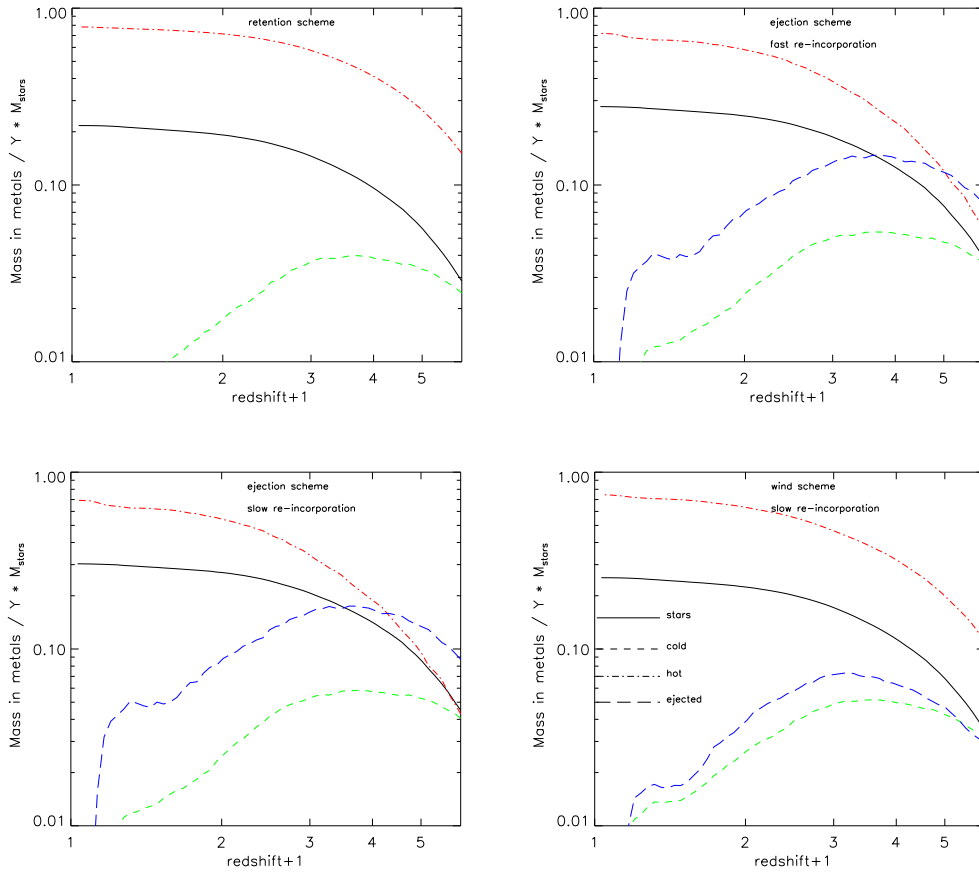
Figure 4.11: As in Fig. 4.10 but for our cluster simulation.

Note that here the evolution in the stellar mass density is more rapid than in the cluster.

4.6 Discussion and Conclusions

In this chapter we have extended the analysis of the semi–analytic model developed as a part of this thesis. We have shown that our model allows us to study in detail the build up of the stellar population of galaxies of different types and residing in different environments. We find that a natural prediction of the hierarchical scenario is a quite strong dependence of the evolution on environment. In agreement with observational data, elliptical galaxies are composed by an old stellar population with

Figure 4.12: Evolution of the different phases for the slow ejection scheme. The top panel shows the results for the galaxies within the virial radius of our cluster simulation, while the bottom panel shows the results for a typical 'field' region.

most of the stars formed at redshifts larger than 2–3. Brighter elliptical galaxies are older and more metal–rich than fainter ellipticals, in agreement with observational results.

The self–consistency of our model also allows us to investigate the chemical enrichment history of the intra–cluster and intergalactic gas and, i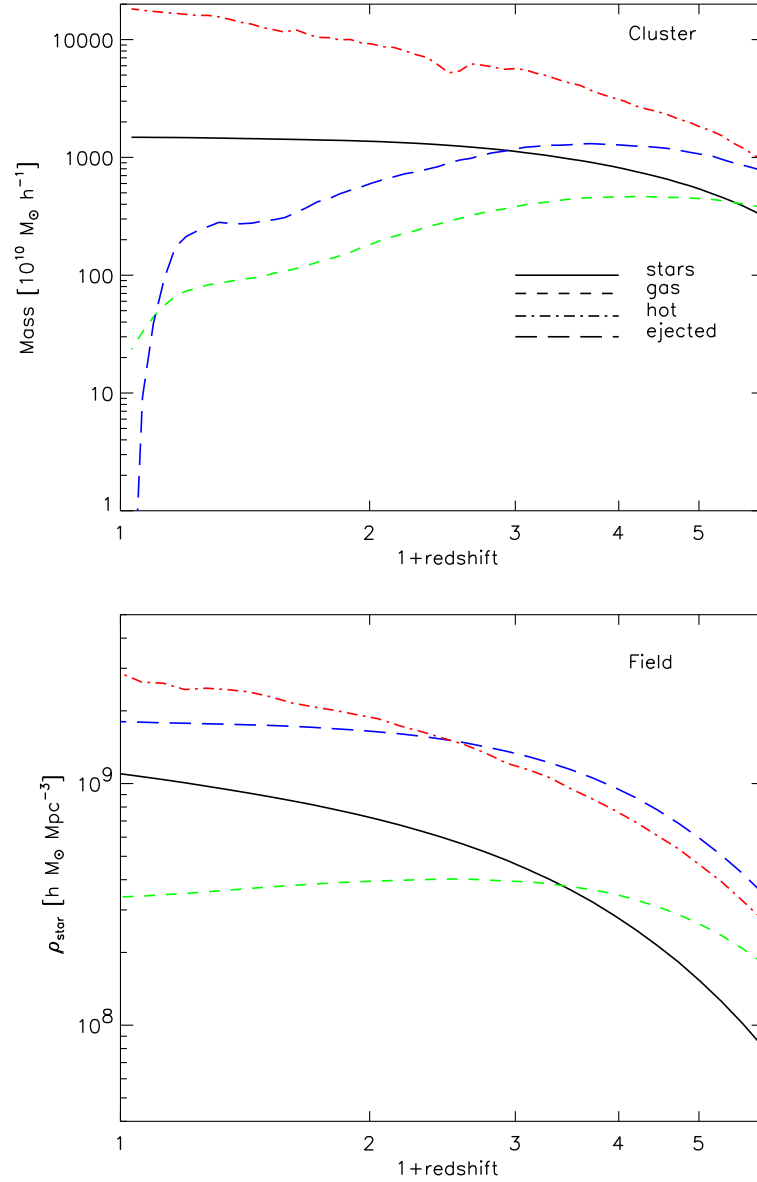n particular, to analyse when the metals in the intra–cluster gas were ejected and which galaxies were mainly responsible for this chemical pollution.

We find that the chemical enrichment of the ICM occurs at high redshift: 60–80 per cent of the metals are ejected into the ICM at redshifts larger than 1, 35–60 per cent at redshifts larger than 2 and 20–45 per cent at redshifts larger than 3. About half of the metals are ejected by galaxies with baryonic masses less than $1 \times 10^{10}\,h^{-1}\mathrm{M_\odot}$. The predicted distribution of the masses of the ejecting galaxies is very similar for all 3 feedback schemes. Although small galaxies dominate the luminosity function in terms of number, they do not represent the dominant contribution to the total stellar mass in the cluster. Approximately the same contribution to the chemical pollution of the ICM is from galaxies with masses larger than $1 \times 10^{10}\,h^{-1}\mathrm{M_\odot}$.

Finally, we show that although most observations at redshift zero do not strongly distinguish between our different feedback schemes, the observed dependence of the baryon fraction on halo virial mass does place strong constraints on exactly how galaxies ejected their metals. Our results suggest that gas and its associated metals must be ejected very efficiently from galaxies and their associated dark matter haloes. Once the material leaves the halo, it must remain in the diffuse intergalactic medium for a time that is comparable to the age of the Universe. In the light of these results, the ejection model should be considered our preferred model.

Future studies of the evolution of the metallicity of the intergalactic medium should also be able to clarify the mechanisms by which such wind material is mixed into the environment of galaxies.

– From our home on the Earth, we look out into the distances and strive to imagine the sort of world into which we were born. Our immediate neighborhood we know rather intimately. But with increasing distance our knowledge fades, and fades rapidly, until at the last dim horizon we search among ghostly errors of observations for landmarks that are scarcely more substantial. The search will continue [. . .] Not until the empirical resources are exhausted, need we pass on to the dreamy realms of speculation.

Edwin Hubble, The Realm of the Nebulae

5

The ESO Distant Cluster Survey
Cluster structure

Abstract

In this chapter I present the ESO Distant Cluster Survey, an ESO Large Programme aimed at the study of cluster structure and cluster galaxy evolution over a significant fraction of cosmic time. I briefly review the motivation and the goals of the survey and present a subset of the final cluster sample for which we have complete photometric and spectroscopic data. I devise a new method that uses both the spatial distribution of the galaxies projected on the plane of the sky and the velocity information, to assess the significance of substructure. I then use a large set of high resolution re–simulations of clusters, coupled with the semi–analytic models developed as a part of this thesis, in order to perform an accurate comparison with the observational results. I demonstrate that this kind of comparison can provide important information on the formation and the evolution of cluster structure and on the physical mechanisms that drive galaxy evolution in dense systems.

5.1 Introduction

As discussed in Chapter 1, clusters of galaxies are important tools for cosmological studies and, at the same time, constitute an ideal laboratory for the study of the physical processes that drive galaxy evolution in different environments. This important role is enhanced by the practical advantage of having many galaxies in a relatively small region of the sky and all approximately at the same redshift, thus allowing

efficient observations to be carried out even with modest field of view and modest amounts of telescope time. With the development of new technologies and instrumentation (like the 8– and 10–meter class telescopes) during the last ten years, it has become feasible to study galaxy properties at intermediate to high redshifts ($\lesssim 1$), thus allowing a direct observation of the evolution both of the galaxy population in clusters and of the cluster structural properties as a function of time.

So far, however, very few clusters have been studied in detail at redshifts $\gtrsim 0.5$, where the evolutionary changes predicted by different theoretical models become dramatic. In addition, most of the studies of clusters at high redshift have been conducted with X–ray selected samples. As we have discussed in Sec. 1.6.2, this selection criterion may bias the sample towards the most massive and regular systems.

The aim of the **E**SO **Di**stant **C**luster **S**urvey (EDisCS) is to carry out a systematic study of cluster structure and cluster galaxies out to redshift ~ 0.8. This study will be carried–out at the level of detail that will allow a quantitative comparison with the large samples of nearby clusters now available. The complete EDisCS dataset will provide a statistically significant sample of clusters at two different redshifts (10 at redshift ~ 0.5 and 10 at redshift ~ 0.8) with homogeneous photometry and spectroscopy.

Our programme pursues a variety of science goals among which are: a study of the morphological evolution of galaxies as a function of their spectral energy distribution; a measurement of the cluster luminosity function at different redshifts and for different galaxy types; an analysis of cluster structure; a measurement of the the chemical abundances, star formation rate, and dust content of cluster galaxies as a function of redshift. This analysis will be complemented by an accurate comparison with a large set of high–resolution simulations of clusters coupled with the semi–analytic model that has been developed as a part of this thesis.

The analysis presented in this chapter is concerned with the characterisation of the cluster structure and quantification of the significance of subclustering in our observed sample and with an accurate comparison with results from numerical simulations. We develop a new methodology that takes into account both the spatial distribution of galaxies projected on the plane of the sky and the radial velocity information.

Numerous recent studies have shown that many, perhaps most clusters are far from dynamical equilibrium. This evidence is based on several observational results including the *clumpy* distributions of galaxies seen in projection on the sky (Geller & Beers 1982; Rhee et al. 1991; Escalera et al. 1994; Kriessler & Beers 1997), the apparent substructures in the distribution of the radial velocities of cluster members (Dressler & Shectman 1988), multiple centres of X–ray emission (Buote & Tsai 1996; Jones & Forman 1999), and recent results coming from gravitational lensing studies (Athreya et al. 2002; Dahle et al. 2002).

As we have already shown (see Chapter 2), N–body simulations demonstrate that substructure is a common phenomenon, at least in a Universe in which large–scale

structure grew in a hierarchical way. Different galaxy formation scenarios have different amounts of power on small and large scales. Therefore, substructure may help to discriminate between different sets of initial conditions (Richstone et al. 1992; Mohr et al. 1995). Note, however, that this analysis is substantially complicated by the uncertainty in the rate at which substructure is erased (see Chapter 2).

In addition to tests of cosmological models, substructure can also provide important information on processes of galaxy evolution. Dressler (1980, see also Sec. 1.6.3) has in fact shown that a correlation between galaxy morphology and local density holds, at some level, both for regular and irregular clusters, implying that local density has more effect on galaxy evolutionary processes than large–scale environment. Likewise, since galaxies located within a substructure have low velocity dispersion, mergers will be more effective in transforming galaxy properties in these environments (see Sec. 2.7.3).

Substructure in rich clusters can take many forms and its detection constitutes a non–trivial technical problem. Many statistical tests have been developed and applied to reasonably large samples of clusters over the last decades. Although all the analyses agree that substructure is indeed an important phenomenon, they often diverge quite significantly on the fraction of clusters that exhibit significant substructure. This controversy may arise from the fact that different methods are sensitive to different forms of substructure (e.g. bimodality, small clumps, filaments). Moreover, the quoted amounts of substructure can also depend on the fact that only partial information (spatial distribution, velocity distribution, X–ray emission) is considered. It is clear that a thorough investigation of the substructure issue should take advantage of all available information: projected galaxy positions, velocity distributions, detailed X–ray maps of the intra–cluster gas, and mass maps from gravitational lensing.

The EDisCS database constitutes an ideal starting point for this kind of analysis because it provides a large sample of clusters covering a wide range of masses and structural properties. In addition, it provides an unprecedentedly large and homogeneous dataset covering a significant fraction of the lookback time.

In this chapter we develop a new method to identify and quantify the amount of substructure in clusters using both spatial and kinematic information. The method is applied to a subsample of the EDisCS database with complete photometry and spectroscopy. We expect that the extension of the method to the complete EDisCS database, and comparisons with high resolution N–body simulations that incorporate semi–analytic techniques, will provide important information on the mechanisms that drive galaxy formation and evolution in different environments.

The chapter is organised as follows: in Sec. 5.2 we briefly review the method that has been used to select cluster candidates; in Sec. 5.3 we give a brief summary of the data that will be available for the complete EDisCS database and in Sec. 5.4 we present the subset of clusters with complete photometric and spectroscopic data that

is used in this work. In Sec. 5.5 we illustrate the method adopted to isolate probable cluster members and in Secs. 5.6 and 5.7 we present our analysis of the dynamics and the structure of the observed clusters. In Sec. 5.8 we present the set of N–body simulations used in this analysis and in Sec. 5.9 we explain how the simulated clusters are treated in order to mimic the analysis carried out on the observed sample. In Sec. 5.10 we compare the results obtained from the simulated clusters to the results from the observations. A discussion and the conclusions are finally presented in Sec. 5.11.

5.2 Selection of cluster candidates

The **E**uropean Southern Observatory **Dis**tant **C**luster **S**urvey (hereinafter EDisCS) is an ESO Large Programme aimed at the study of cluster structure and cluster galaxy evolution over a significant fraction of cosmic time. The Programme represents a detailed follow–up study of 20 clusters, 10 at $z \approx 0.5$ and 10 at $z \approx 0.8$, drawn from the 1073 candidate clusters catalogued in the Las Campanas Distant Cluster Survey (LCDCS, Gonzalez et al. 2001).

As explained in Sec. 1.6.2, several techniques can be used in order to identify galaxy clusters, the two most common being optical searches for projected galaxy overdensities and X–ray searches for extended thermal bremsstrahlung emission. The effectiveness of both methods decreases rapidly at redshifts larger than 0.5. At these high redshifts, optical searches require deep imaging and are therefore limited to very small areas. On the other hand, X–ray searches are strongly limited by detector sensitivity. The LCDCS employs a technique that couples some of the most important advantages of these two methods.

The basic idea is that clusters can be detected as regions of excess surface brightness relative to the background sky, due to the integrated signal from undetected galaxies. To maximise the contrast between the cluster and the background, it is important to perform a good subtraction of the sky and to smooth the image on a scale that is comparable to the core size of the cluster, in order to reduce the Poisson noise. This particular technique has many advantages. In particular, it allows us to survey a large effective area with minimal telescope time and is able to probe to higher redshifts and lower limiting mass than existing X–ray surveys. In addition, it makes no assumption about galaxy colours or the presence of a well defined colour–magnitude sequence. However, other astrophysical phenomena are able to induce surface brightness excesses: low surface brightness galaxies, tidal tails, superpositions of poor groups along the line of sight. It is important to optimise the technique in order to minimise the contamination of the catalogue by these sources. The observed luminosity of the detected surface brightness fluctuation, the concentration of the fluctuation, and the magnitudes of the galaxies around it, are used to eliminate

these sources of contamination.

An original set of 30 cluster candidates, 15 with estimated redshifts ~ 0.5 and 15 with estimated redshifts ~ 0.8, was drawn from the LCDCS. The clusters were selected to be among the highest surface brightness detections at each redshift. This was done in order to recover the most massive clusters at each redshift. Since the spurious detection rate in the LCDCS can be as high as 50 per cent at redshifts ~ 0.8, we used four nights on VLT/FORS2 to obtain two colour images of each field in order to confirm the presence of galaxy overdensities with colours consistent with elliptical galaxies at that redshift. The ten best cluster candidates at each estimated redshift were then chosen for deeper imaging and spectroscopic follow–up.

5.3 Data

Clusters at redshift 0.5 were observed in the B, V, I (VLT) and K (NTT) bands, while the clusters in the higher redshift bin have V, R, I (VLT), J and K (NTT) photometry. At the time this thesis is being written, all the optical and all but one night of NIR imaging is complete. Most of the data were taken under excellent conditions with almost all combined images having $< 1''$ FWHM seeing. The optical and NIR imaging will be described in forthcoming papers (White et al., in preparation; Aragòn-Salamanca et al., in preparation). Multi-object spectroscopy using FORS2 on the VLT for all the clusters is almost completed and will be described in detail in Halliday et al. (in preparation).

I–band selected catalogues have been compiled using the SExtractor software (Bertin & Arnouts 1996) and will be made publicly available in a forthcoming paper (Simard et al., in preparation). The programme will then provide homogeneous multi–colour imaging and spectral information for a large sample of clusters at high redshifts. A weak lensing analysis on all the observed clusters has already been carried–out (Clowe et al., in preparation).

Note that the programme was also been granted 80 orbits of HST time to image ten of our more distant clusters. The acquisition of HST images is almost completed.

On the basis of our current data, we estimate that we will have a total of 850/480 and 600/330 redshifts/cluster members for the clusters at redshift ~ 0.8 and ~ 0.5 respectively.

5.4 A subset of the complete sample

In this chapter we will use a subset of the complete EDisCS dataset for which we already have complete photometry and spectroscopy. In Table 5.1 we list the ID of the objects identified as Brightest Cluster Galaxies (BCGs) and their spectroscopic redshifts. Note that the ID of each object contains its coordinates (RA and DEC).
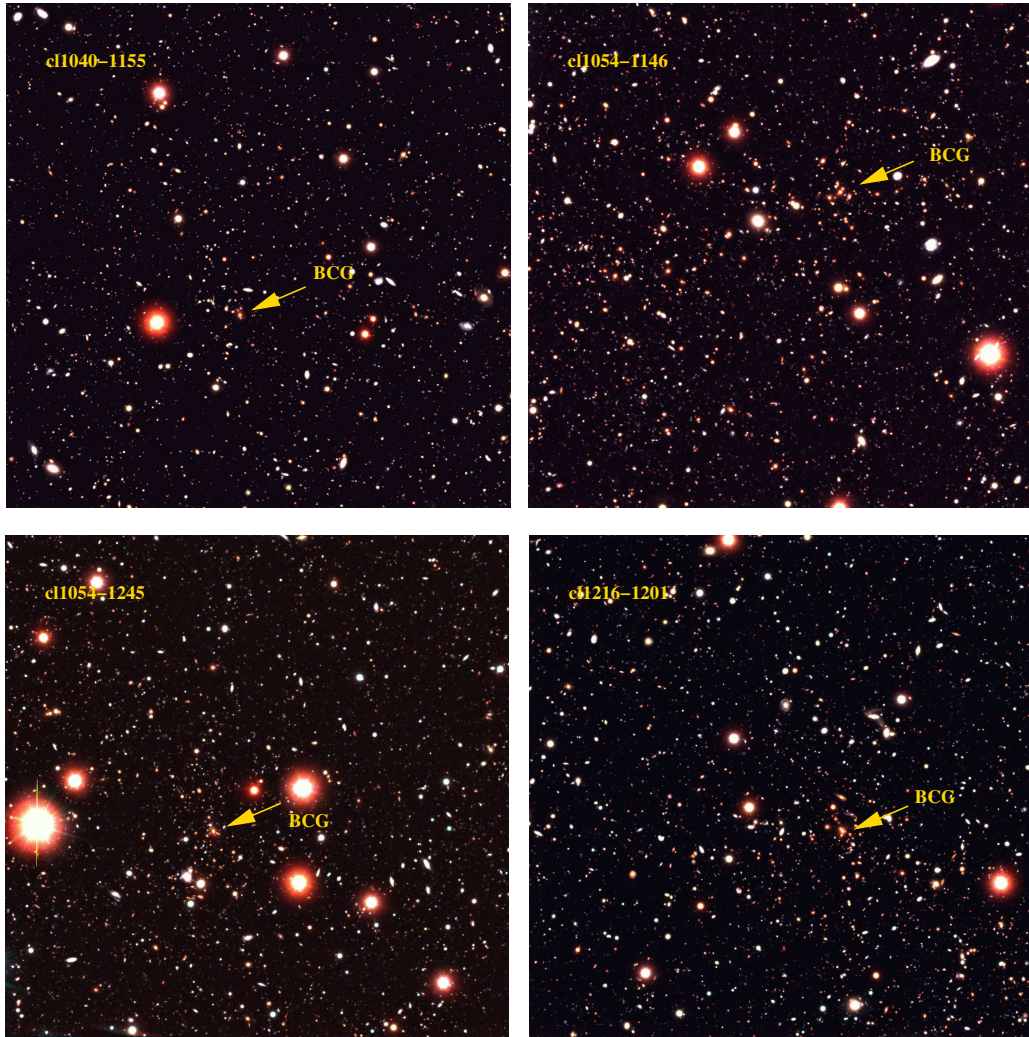
Figure 5.1: 3–colour (I, R and V) images for the four fully reduced clusters in the high redshift bin. The yellow arrow in each panel indicates the position of the BCG.

In Figs. 5.1 and Fig. 5.2 we present 3–colour images for our clusters (I, R and V for the high redshift clusters and I, V and B for the low redshift cluster). The BCGs are marked using a yellow arrow in each panel. Because of the geometry of the CCDs and the fact that they are read from the four corners, the cluster centre has been placed about 1 arcmin along the diagonal away from the centre, thus avoiding the edges of the quadrants and the gap between the chips.

In Figs. 5.3 and 5.4 we show spectroscopic redshift histograms of all the objects
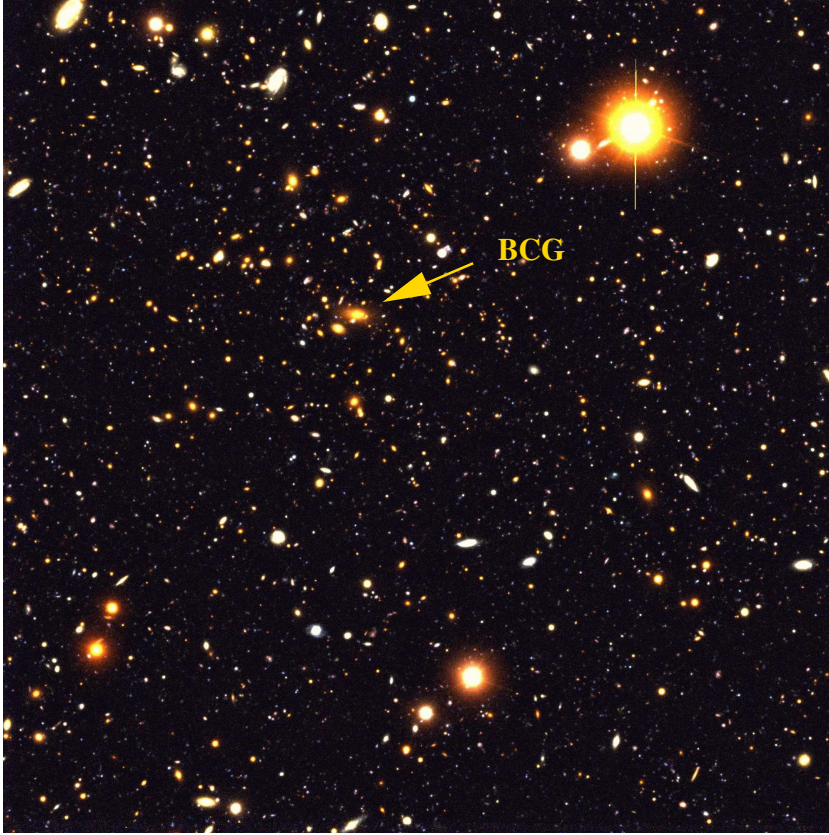
Figure 5.2: As in Fig. 5.1 but for the cluster cl1232–1250 and using the bands I, V and B.

Cluster name	ID	$z_{\rm spec}$
cl1232–1250	EDCSJ1232302–1250364	0.5419
cl1040–1155	EDCSJ1040404–1156042	0.7020
cl1054–1146	EDCSJ1054244–1146195	0.6965
cl1054–1245	EDCSJ1054436–1245519	0.7503
cl1216–1201	EDCSJ1216453–1201176	0.7955

Table 5.1: Objects identified as BCG: ID (containing the objects coordinates) and spectroscopic redshifts.

targeted in the field of the five clusters. A clear peak is visible in all the histograms. Note that spectroscopic analysis was completed first for the clusters in the sample
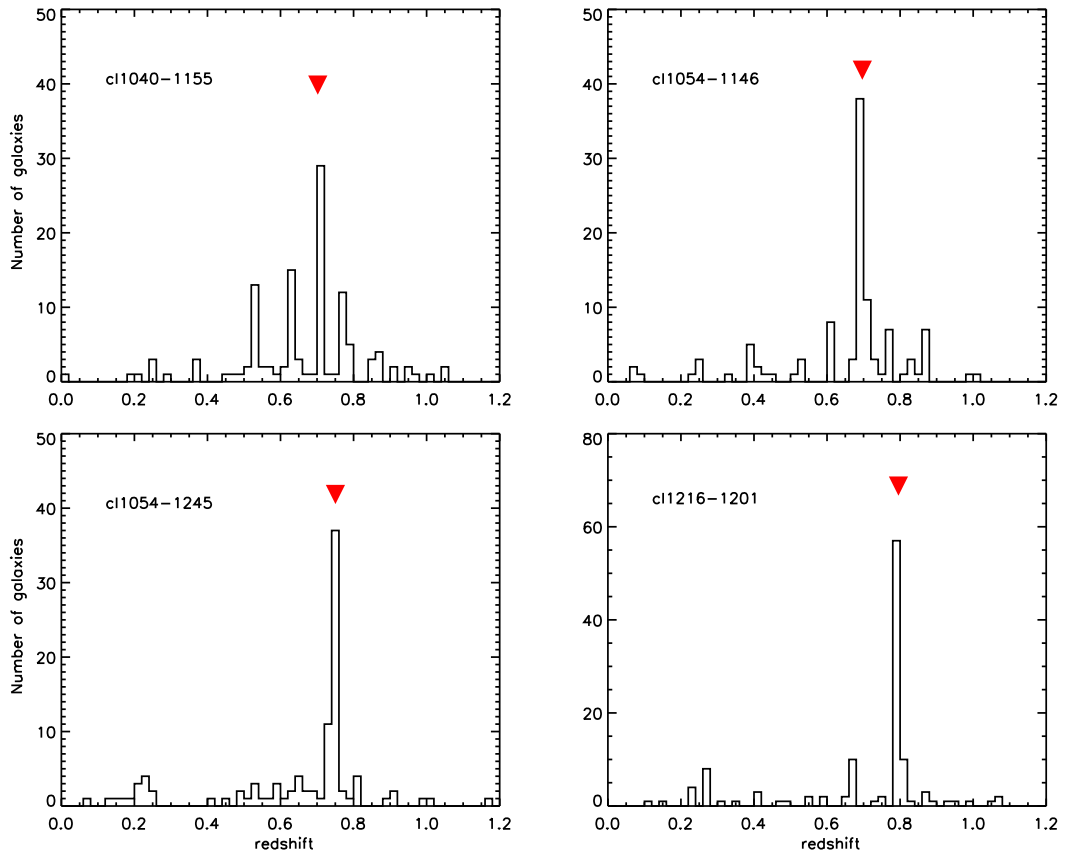
Figure 5.3: Spectroscopic redshift histograms for all the objects targeted in the field of the four clusters in the high redshift bin. Red arrows mark the redshifts of the BCGs.

that were classified as our *best* candidates. It is therefore not surprising that these clusters show such a marked overdensity in redshift space. We will show in the subsequent sections that these systems cover a wide range of masses and exhibit a variety of structural properties, both by analysing the projected spatial distribution of the galaxies and by performing a dynamical analysis using the radial velocity information.

5.5 Cluster membership

Obviously the only way to unambiguously determine cluster membership is to use spectroscopic redshifts, whose reliability is in general quite high, with quoted errors
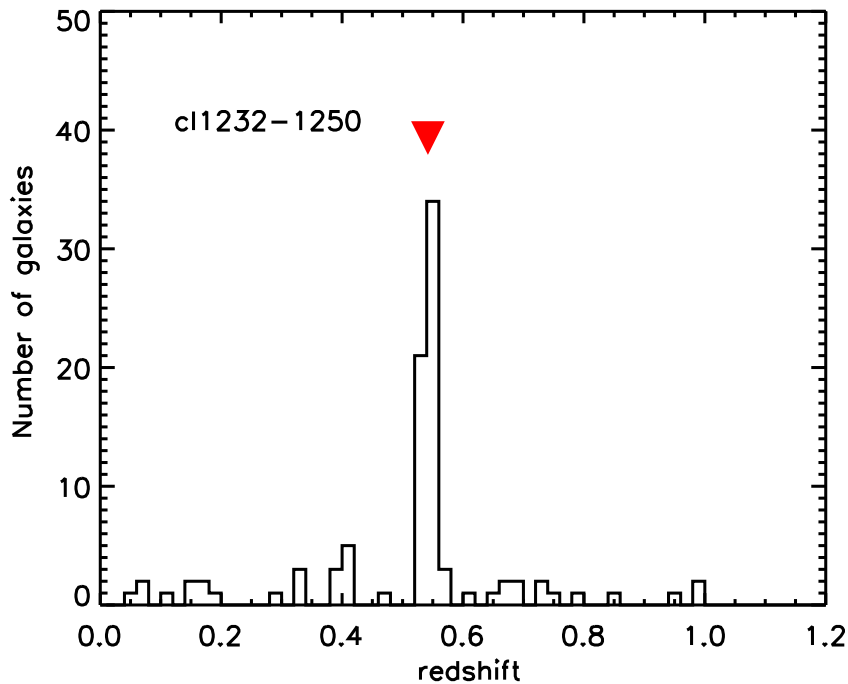
Figure 5.4: Spectroscopic redshift histogram for all the objects targeted in the field of the cluster cl1232–1250.

of the order of 0.001[1]. This technique is, however, unavailable for a large number of faint objects in each field. With current instruments, it would be unacceptably time–consuming to obtain spectra for many cluster members at our relatively high redshifts ($z > 0.5$).

A standard method to correct for field contamination, in absence of spectroscopy, is to use statistical subtraction (Aragon-Salamanca et al. 1993; Smail et al. 1997; Dressler 1980; Stanford et al. 1998): a 'cluster–free' field, preferably close to the cluster under consideration, is used to determine the number of contaminating galaxies as a function of magnitude and colour. It is known that this method becomes increasingly uncertain at high redshift, as the contrast of the cluster against the background decreases. Driver et al. (1998, see also Diaferio et al. (2001)), for example, use simulations to show that errors can be large at redshifts > 0.3. In addition, this method does not give any kind of information on the likelihood of being a cluster member on a galaxy–by–galaxy basis.

On the other hand, techniques for determining photometric redshifts[2] have become

---

[1]In our sample the estimated uncertainty in the spectroscopic redshifts is ~ 0.0003.

[2]In essence, the photometric redshift technique employs the magnitudes observed in different bands

much more precise in recent years, suggesting that this method can be used to address many scientific questions (Lynden-Bell 1967; Kodama et al. 1999; Dahlén et al. 2002). An important by–product of these techniques is an estimate of the spectral type for each observed galaxy, although it is important to remember that this is a crude spectroscopic classification, rather than a morphological one, since it is derived using the broad spectroscopic characteristics of the observed objects.

Photometric redshifts therefore provide an inexpensive tool to estimate the probability of cluster membership, and they have been used in a number of recent studies of galaxy clusters. In this section we briefly summarise the technique we use to estimate photometric redshifts for our sample and how we employ this technique to isolate cluster members.

5.5.1 Photometric redshift estimates

Photometric redshifts were computed using two independent codes (Rudnick et al. 2001; Bolzonella et al. 2000). The code by Bolzonella et al. is publicly available and is named *Hyperz*. The use of two codes allows us to control the systematics in the identification of likely non–members.

In both codes, an estimate of the redshift of each object is computed by means of a standard SED fitting procedure. The main difference between them lies in the set of template spectra used to fit the observed SEDs: Rudnick et al. use "Hubble type" templates E, Sbc, Scd and Im from Coleman et al. (1980), and two starburst templates with low reddening, SB1 and SB2, from Kinney et al. (1996). It has been shown (Sawicki et al. 1997; Benson et al. 2002) that the addition of the starburst templates significantly improves the photometric redshift estimation. They are needed because even in the nearby universe there are a number of galaxies that are bluer than the bluest template from Coleman et al.

Hyperz makes use of a wide set of template spectra obtained using the empirical spectral templates from Coleman et al. and Kinney et al., and a wide set of synthetic spectra obtained using the population synthesis code by Bruzual & Charlot (1993).

The two codes also perform the fit in a slightly different way: in both cases a standard χ^2 minimisation procedure is employed, but while *Hyperz* compares the observed SEDs directly to the library of template spectra, in the code by Rudnick et al. the observed SEDs are fit by a linear combination of redshifted templates. In addition, in the latter code a realistic estimate of the errors on the photometric redshifts is obtained by performing a series of Monte Carlo simulations where, for each object, a certain number of synthetic photometric measurements are created by perturbing the observed values according to the observational estimate of the

---

to reconstruct the spectral energy distribution of the object. This is then compared to the spectral energy distributions of different template galaxies at different redshifts. The best fit provides an estimate of the redshift and of the spectral type of the galaxy.

photometric errors. The two codes differ in a number of other details, so we refer the reader to the original papers for more information. An analysis of the performance of these codes on the EDisCS dataset will be presented in Pelló et al. (in preparation).

For the purposes of the analysis presented in this chapter, the codes were run allowing a maximum photometric redshift of 2^3 and adopting a 5 per cent minimum flux error for the photometry. Comparison with the current spectroscopic sample shows that the photometric redshifts of the galaxies in our sample are quite accurate with $< |z_{\mathrm{spec}} - z_{\mathrm{phot}}| >= 0.06$–$0.08$. There is no systematic offset between z_{phot} and z_{spec} and the percentage of catastrophic failures, i.e. objects with $|z_{\mathrm{spec}} - z_{\mathrm{phot}}| > 0.3$, is of the order of 10 per cent. There are obviously some small differences between the two codes, on a object–by–object basis, but the results are in general agreement with each other, which is remarkable taking into account the many differences between the codes.

5.5.2 Isolating cluster members

As pointed out by Brunner & Lubin (2000), the method usually used to determine cluster membership from photometric redshifts is too simplistic, based only on a cut around the spectroscopic redshift of the cluster. Basically, every galaxy with photometric redshift falling in a shell centred on the cluster redshift is retained as a probable cluster member. Since the uncertainties in the photometric redshifts are large (and they usually increase at higher redshifts), quite a large shell is used to select cluster members. While this method allows the bulk of the cluster population to be identified, it is obviously not a good method for removing field contamination, and may affect in a systematic way the study of cluster galaxy populations.

The photometric redshift technique based on the template fitting method, not only produces a *best fit* between a template spectral energy distribution (SED) and the photometric points, but also the full *probability distribution* of the estimated redshift. We use this as a quantitative probabilistic tool to determine the likelihood of cluster membership.

Let us define the integrated probability distribution around the cluster redshift $\mathrm{P}_{\mathrm{clust}}$ as:

$$\mathrm{P}_{\mathrm{clust}} = \int_{z_{\mathrm{clust}}-\Delta z/2}^{z_{\mathrm{clust}}+\Delta z/2} \mathrm{P}(z)dz \qquad (5.1)$$

In Eq. 5.1, Δz represents an interval defined around the cluster spectroscopic redshift (z_{clust}) which reflects the dispersion in the photometric redshift (z_{phot}) with respect to the spectroscopic redshift (z_{spec}).

---

[3]In magnitude limited samples of depth comparable to that reached by EDisCS observations, only ~ 1 per cent of the objects are found at higher redshifts.

This probabilistic interpretation of the photometric redshift is based on an approach similar to that used by Brunner & Lubin (2000). These authors, however, use an empirical photometric redshift technique. This is based on an empirical fit between the spectroscopic redshift and the photometric data points, and it requires an adequate training set. Although this empirical redshift technique is relatively insensitive to uncertainties concerning the SED and its redshift evolution, obtaining an error estimate for each galaxy is quite difficult. In addition, the method does not provide directly a redshift probability distribution. Brunner & Lubin adopt a Gaussian redshift probability distribution with mean given by the estimated photometric redshift and standard deviation defined by the estimated error in the photometric redshifts. Our investigation shows that the redshift probability distributions are in general strongly *non–Gaussian*. This means that the full probability distribution should be used to provide a better estimate of the real uncertainty on the photometric redshifts.

By using our spectroscopic sample as a calibrator (including also spectroscopic redshifts for clusters not presented in this chapter), we can determine an optimal *threshold* (P_{thresh}) for cluster membership which maximises the number of retained members and minimises the contamination. Moreover, in order to control the systematic errors in the determination of the photometric redshift, we use probability distributions from both codes together with a conservative criterion which keeps an object as a probable cluster member only when its integrated probability around the spectroscopic redshift of the cluster is larger than a given threshold for both codes.

A demonstration of how the retained fraction of members and the rejected fraction of non–members vary as a function of this threshold is shown in Fig. 5.5. This figure also shows how the efficiency of the rejection varies as a function of galaxy colour. For this purpose the sample is arbitrarily split into two halves on the basis of the object rest–frame $B - V$ colour (this is given by the photometric redshift code of Rudnick et al.).

Note that for $P_{thresh} < 0.35$, red non–members are slightly more efficiently rejected and red members slightly more efficiently accepted than their blue counterparts. This is a consequence of the poorer constraints on z_{phot} for blue galaxies due to their 'featureless' SEDs[4], and will result in a lower contrast for the blue population than for the red population.

For the purposes of the present analysis, we will adopt a P_{thresh} of 0.25 for both codes. Fig. 5.5 shows that, with this threshold, ~ 90 per cent of the spectroscopic cluster members can be retained while rejecting ~ 45 per cent of the confirmed non–members. With this choice, the efficiency of the rejection for the bluest and reddest halves of the sample, in $(B - V)_{rest}$, is similar to within ≤ 10 per cent.

In order to give a visual impression of the performance of our membership criterion,

---

[4]The spectral energy distribution of star forming galaxies is essentially a power–law.
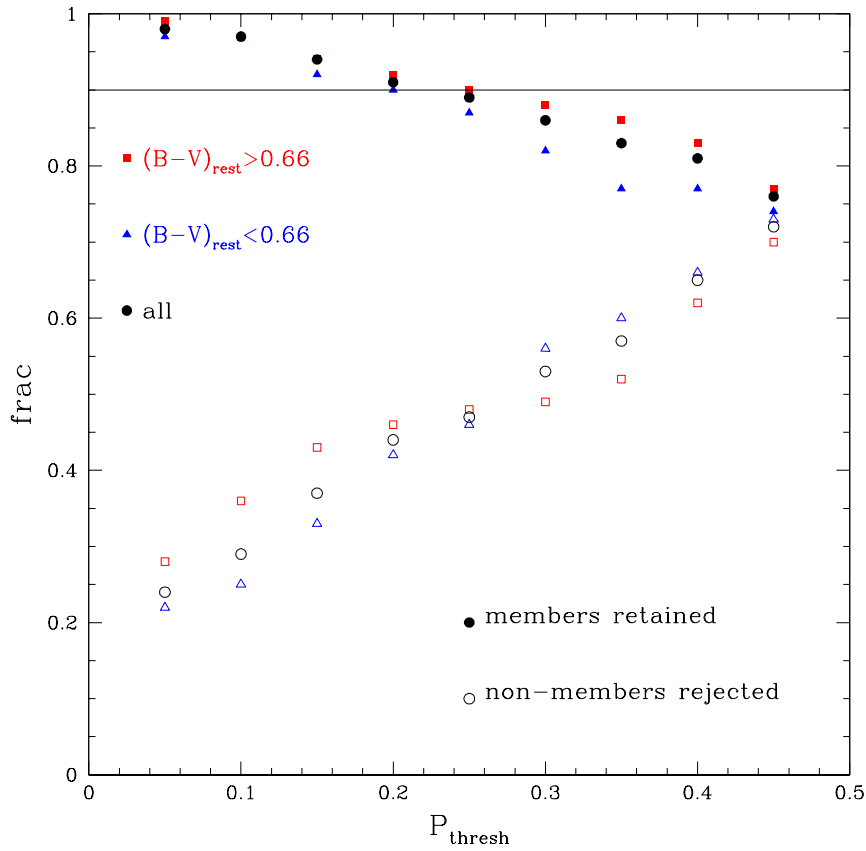
Figure 5.5: The fraction of members retained (filled symbols) and the fraction of non–members rejected (empty symbols) as a function of P_{thresh} and as a function of $(B - V)_{rest}$. The solid horizontal line at 0.9. is to guide the eye.

we show in Figs. 5.6 and 5.7 the spatial distribution of all the objects that are retained as probable cluster members in the field of each of the clusters used in this analysis. Red crosses mark the position of the BCGs, while red circles mark the position of all the objects in the spectroscopic sample whose redshift differs from the redshift of the BCG by less than ±0.015. All the objects brighter than 25 in the observed I–band are shown. This magnitude corresponds to a preliminary estimate of our completeness limit, based on a fit of the observed distribution of detected objects as a function of magnitude. As a first approximation, one can assume that a given photometric catalogue is complete down to the magnitude where this distribution starts to deviate
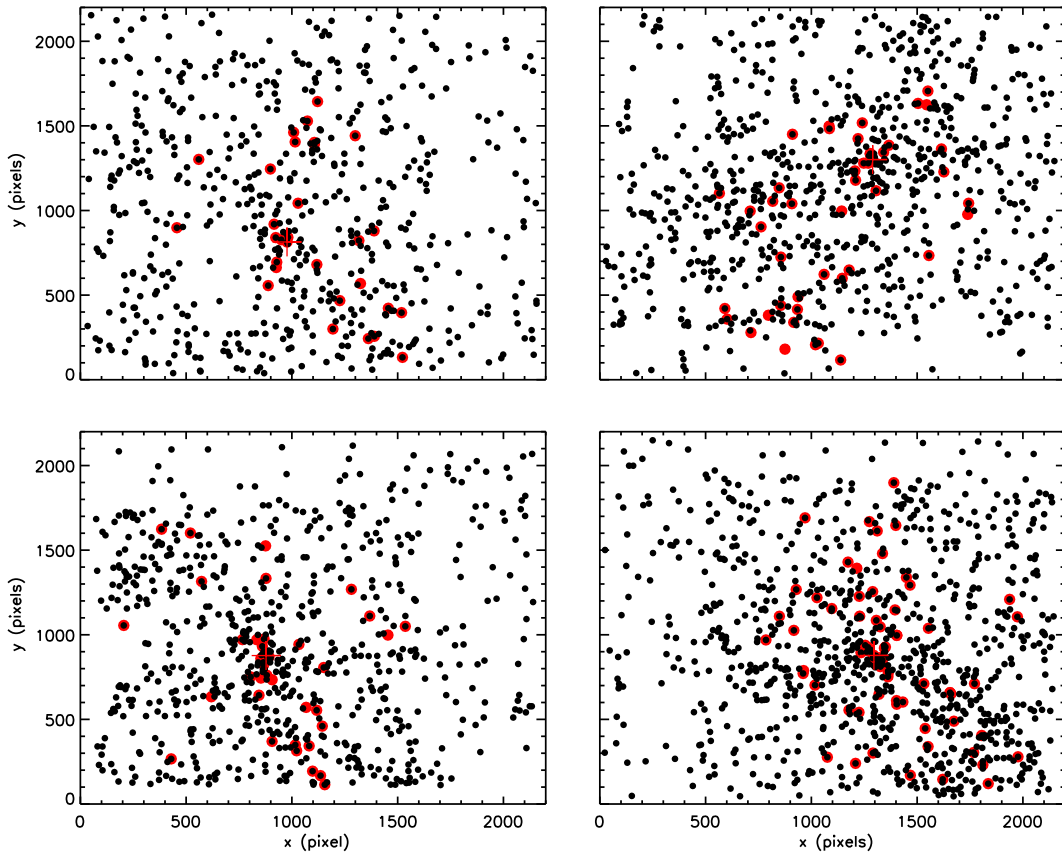
Figure 5.6: Spatial distribution of all the objects that are kept as probable cluster members on the basis of their photometric redshifts for the four clusters in the high redshift bin. Clusters are shown in the same order as in Fig. 5.3. Red crosses mark the position of the BCGs while red circles mark the position of all the objects in the spectroscopic sample whose redshifts differ from the redshift of the BCG by less than ±0.015.

from a power–law. At this point, the detection becomes too noisy and the catalogue is *incomplete*. A more accurate determination of the completeness as a function of different galaxy properties, will be presented in a forthcoming paper (Simard et al., in preparation). This is usually achieved by adding a series of simulated objects to the real images and checking how many of these objects can be retrieved using the same parameter set as for the real galaxies.

Figs. 5.6 and 5.7 clearly show that although we reject a few spectroscopically confirmed members, the majority of these are retained. In all cases, the retained
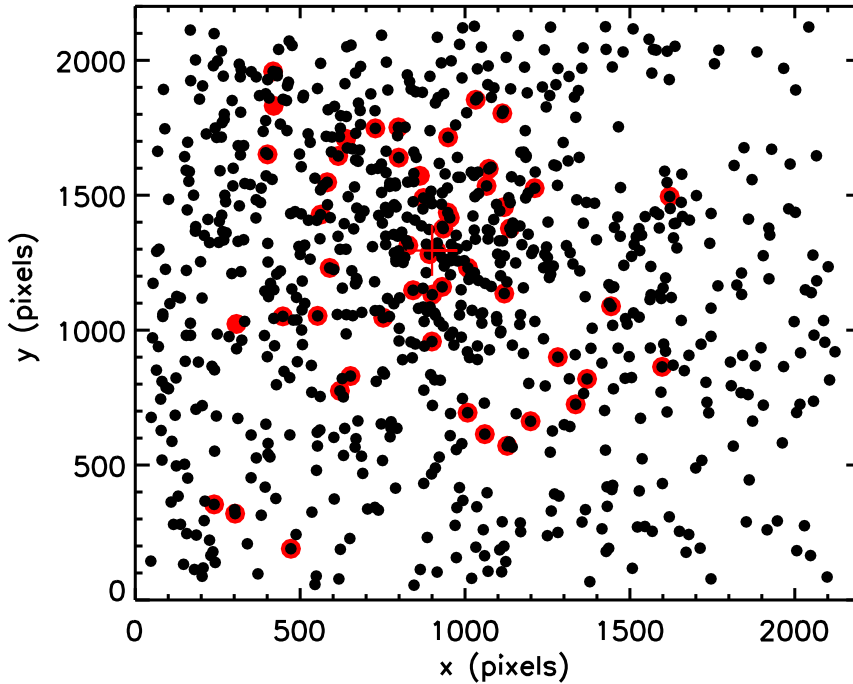
Figure 5.7: As in Fig. 5.7 but for the cluster cl1232–1250.

objects show a marked concentration around the BCGs, although a wide range of structure is visible.

5.6 Dynamical analysis

At first glance, all the clusters used in this analysis appear as well isolated peaks in redshift space. In this section we will use the radial velocity information to compute the cluster velocity dispersions and to study the presence of three–dimensional substructure. The number of spectroscopically confirmed members for each cluster is sufficient to perform such a dynamical analysis. Note that, on the basis of our current sample, we estimate that we will be able to extend the present analysis to all the clusters in the EDisCS database, once their spectroscopy is complete.

5.6.1 Cluster velocity dispersion

We have estimated the line–of–sight velocity dispersions using the bi–weight estimator (Beers et al. 1990). This algorithm is usually employed in astronomy (see also Sec. 6.4) and represents a *robust* method for the determination of the location (the

mean) and the scale (dispersion). It gives higher weight to points that are closer to the centre of the distribution and is therefore insensitive to the presence of outliers. For a Gaussian distribution, the bi–weight location estimator reduces to the conventional mean and the bi–weight scale estimator reduces to the conventional standard deviation.

For each cluster, we simply take all the galaxies within the redshift interval ± 0.015 from the BCG and compute the line–of–sight velocity with respect to the cluster centre of mass as:

$$v_{||} = \frac{V_{||} - \bar{V}_{||}}{1 + \bar{V}_{||}/c}$$

where $V_{||}$ is the recessional velocity of the galaxy (redshift times the speed of light), $\bar{V}_{||}$ is the median recessional velocity of the cluster members and c is the speed of light.

These values are then used to determine a robust estimate of the line–of–sight velocity dispersion. Errors on the measured values are determined using the bootstrap method (Press et al. 1992). 1000 Monte Carlo realizations are carried–out for each cluster.

Figs. 5.8 and 5.9 show the velocity histograms for all five clusters used in this analysis, in bins of $500\,\mathrm{km\,s^{-1}}$. In each panel, the red arrow marks the median recessional velocity of the cluster members, while the blue arrow marks the recessional velocity of the BCG. The red Gaussians correspond to the measured velocity dispersions. In each panel we also give the number of spectroscopically confirmed members and the estimated velocity dispersions, together with the 68 per cent confidence levels, estimated using the bootstrap method.

Note that this subset of clusters covers a wide range in σ, from systems with relatively low velocity dispersion (like cl1040–1155) to systems with a very high velocity dispersion (like cl1216–1201 and cl1232–1250). Note, however, that all the velocity histograms show clear signs of deviation from a pure Gaussian. This is a clear evidence of a complex dynamical structure. We will investigate in more detail the presence of dynamical substructures in the following section.

5.6.2 3D–substructures

In order to check for the presence of substructure in the three-dimensional space, we combine velocity and positional information by computing the statistics devised by Dressler & Shectman (1988). The test works in the following way: for each galaxy with a measured radial velocity, the ten nearest neighbours are found, and the local velocity mean and velocity dispersion are computed from this sample of 11 galaxies. These quantities are compared to the global dynamical parameters computed for the
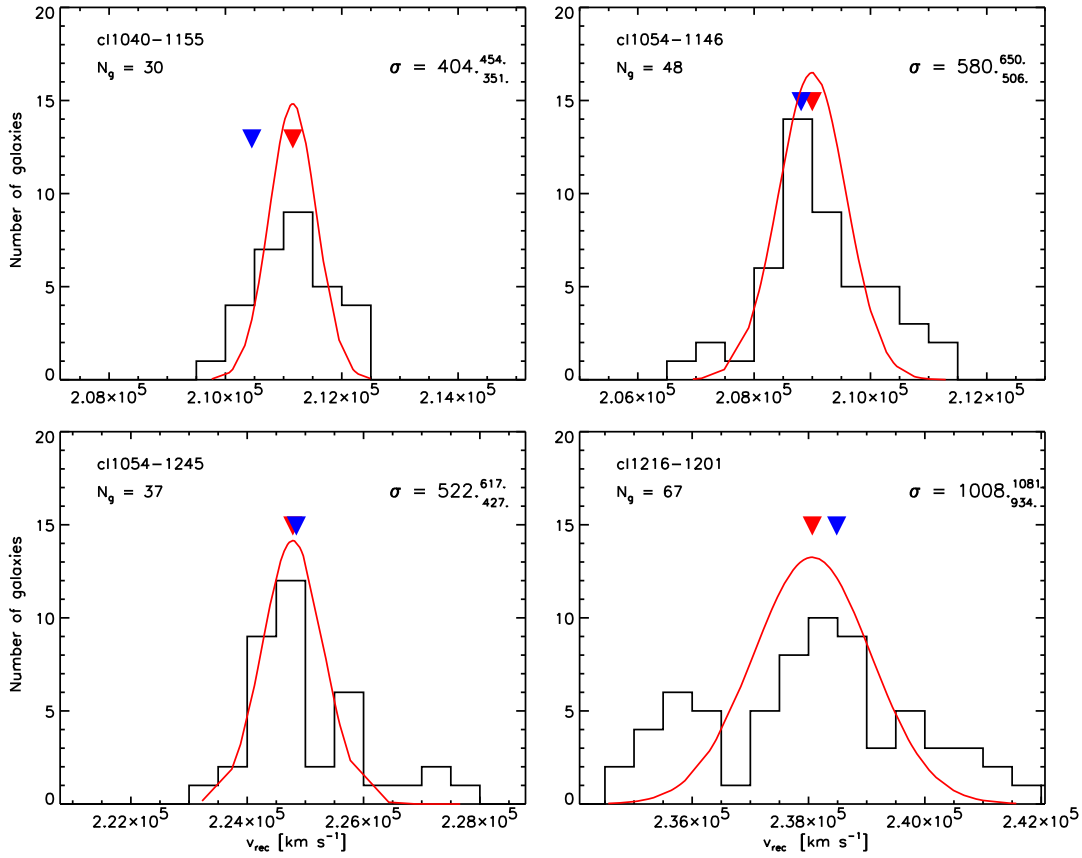
Figure 5.8: Recessional velocity histograms for the four clusters in the high redshift bin. The red arrows mark the median recessional velocity of all the galaxies in the spectroscopic sample whose redshifts differ from the redshift of the BCG by ±0.15, while the blue arrows mark the recessional velocity of the BCGs. The red Gaussians correspond to the measured velocity dispersion.

clusters (see previous section) by defining the deviation δ as:

$$\delta^2 = (11/\sigma^2) \left[(\bar{v}_{\text{local}} - \bar{v})^2 + (\sigma_{\text{local}} - \sigma)^2 \right]$$

where σ and $\bar{v}$ are the global dynamical parameters and σ_{local} and $\bar{v}_{\text{local}}$ are the local mean recessional velocity and velocity dispersion, determined using the 10 closest galaxies with measured radial velocities.

Dressler & Shectman also define the cumulative deviation Δ as the sum of the δ for all the cluster members N_{g}. Note that the Δ statistic is similar to a χ^2: if the cluster

Figure 5.9: As in Fig. 5.8 but for the cluster cl1232–1250.

velocity distribution is close to Gaussian and the local variations are only random fluctuations, then Δ will be of the order of N_g.

The technique devised by Dressler & Shectman does not allow a direct identification of galaxies belonging to a detected substructure. However, it can roughly 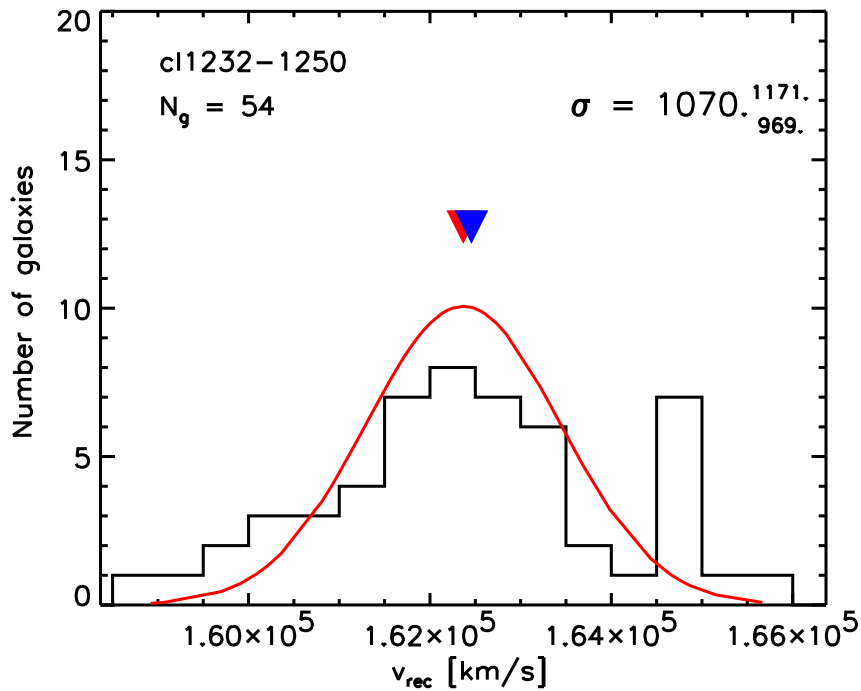identify the positions of substructures. This can be achieved by plotting the spatial distribution of the galaxies using symbols whose size is proportional to the parameter δ, that quantifies the local deviation from the global dynamical properties of the cluster. This is done in Fig. 5.10 for the four clusters in the high redshift bin and in Fig. 5.11 for the cluster in the low redshift bin. In each panel, the size of the symbols is proportional to e^δ and the red cross marks the position of the BCG. A visual inspection of these figures suggests that a complex structure is present in all the clusters studied in the present analysis.

The Δ statistic can be used to give a quantitative estimate of the significance of substructure. Note that the actual value of this number does not have great statistical significance, since individual points are not statistically independent. In order to calibrate the Δ statistic, we perform 1000 Monte Carlo models for each cluster by randomly shuffling the velocities of the galaxies used for the analysis. This is done in order to remove any significant substructure in the 3–D space. The significance
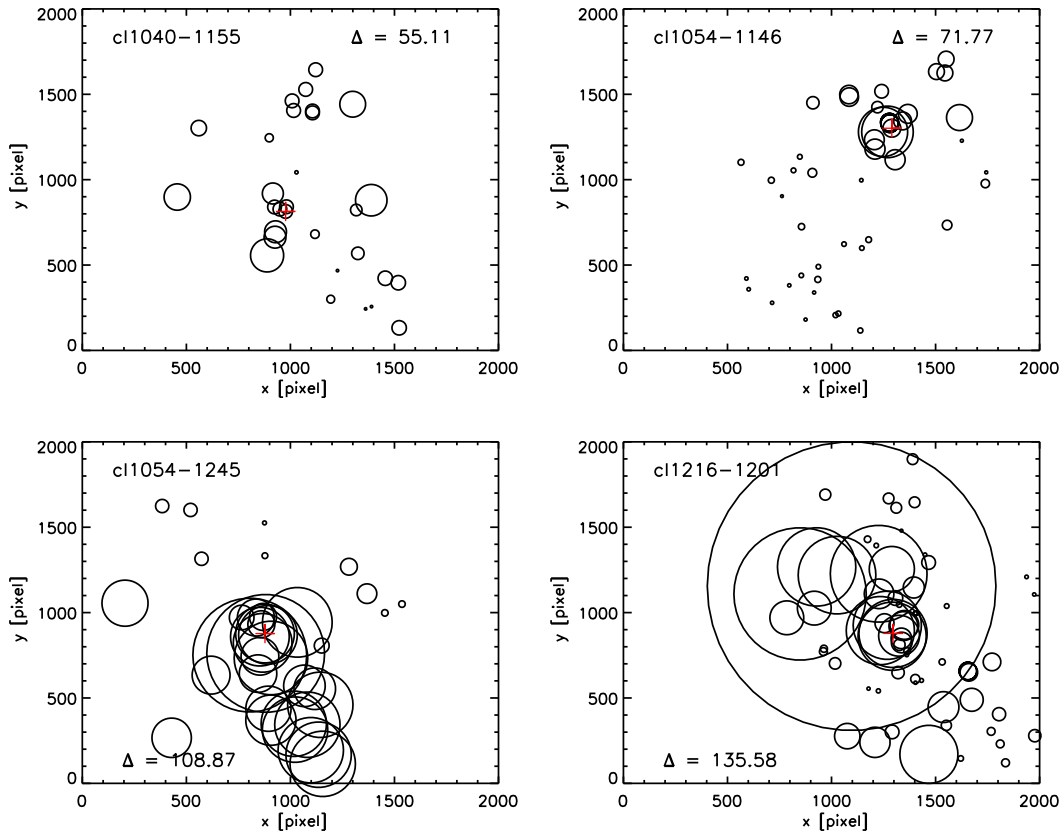
Figure 5.10: Spatial distribution of all the galaxies in the spectroscopic sample whose redshifts differ from the spectroscopic redshift of the BCG by ± 0.015, for the four clusters in the high redshift bin. The size of the symbols is proportional to e^{δ}, where δ is the parameter that quantifies the local deviation from the cluster dynamical properties (see text for details). The red cross in each panel marks the position of the BCG.

of the occurrence of dynamical substructure can be then quantified using the ratio P between the number of simulations in which a value of Δ that is larger than the observed value occurs, and the total number of simulations.

In Table 5.2 we list, for each of the clusters used in this analysis, the number of spectroscopic members, the measured Δ statistic, and the significance P.

For three out of the five clusters, a Δ statistic higher than that measured occurs in fewer than 10 per cent of the Monte Carlo realizations carried–out. In one case (cl1054–1245), it occurs in fewer than 20 per cent of the realizations and for the last
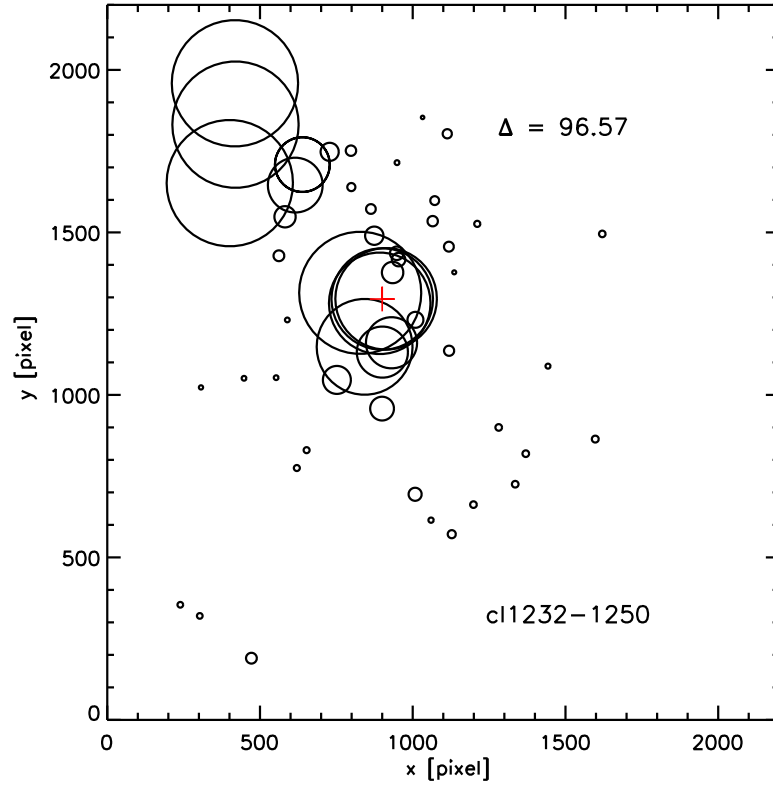
Figure 5.11: As in Fig. 5.10 but for the cluster cl1232–1250.

Cluster name	N_g	Δ	P
cl1232–1250	54	96.57	0.04
cl1040–1155	30	55.11	0.08
cl1054–1146	48	71.77	0.60
cl1054–1245	37	108.87	0.15
cl1216–1201	67	135.58	0.03

Table 5.2: Number of spectroscopic members (N_g), value of the Δ statistic, and its significance for each of the cluster used in the present analysis (see text for details).

case (cl1054–1146), a value of Δ higher than that measured occurs in 60 per cent of the realizations. On the basis of spectroscopic and positional data then, all but one of the clusters used in this analysis exhibit a significant amount of substructure.

5.7 Cluster structure

The wealth of information we have at our disposition for each cluster in our sample, allows us to investigate *if* and *how* the evidence of dynamical substructure found above is correlated with clumps in the spatial distribution of cluster galaxies. In the following sections, we will present the radial profiles of our observed clusters and we will investigate the spatial distribution of cluster galaxies using adaptive kernel techniques. By cross–correlating the spatial information with the radial velocity data, we will *quantify* the relevance of the substructuring phenomenon in the observed sample.

5.7.1 The radial profiles

Figs. 5.12 and 5.13 show the radial density profiles of the five clusters used in this analysis. All the galaxies retained as probable cluster members and above our limit magnitude (I= 25) are used. The geometry of the CCD is properly taken into account when computing the radial profiles at large distances from the BCG.

In each panel, the red dashed line represents a fit with a projected NFW (Navarro, Frenk & White 1997) profile. The analytical expression for this projected distribution has been computed by Bartelmann (1996). The surface mass density can be expressed as a function of a dimensionless radius $x \equiv R/r_{\mathrm{s}}$:

$$\Sigma(x) = A \ f(x)$$

where

$$
\begin{aligned}
f(x < 1) &= \frac{1}{x^2 - 1}\left(1 - \frac{\ln\frac{1+\sqrt{1-x^2}}{x}}{\sqrt{1-x^2}}\right) \\
f(x = 1) &= \frac{1}{3} \\
f(x > 1) &= \frac{1}{x^2 - 1}\left(1 - \frac{\mathrm{atan}\sqrt{x^2-1}}{\sqrt{x^2-1}}\right)
\end{aligned}
$$

and

$$A = 2 \ r_s \ \bar{\delta} \ \bar{\rho}_c \ .$$

In each panel of Figs. 5.12 and 5.13, we also give the scale radius provided by the fit. The conversion from angular to physical distances has been performed adopting a ΛCDM cosmology ($\Omega_{\mathrm{m}} = 0.3$ and $\Omega_\Lambda = 0.7$) with $H_0 = 70 \, \mathrm{km \, s^{-1} \, Mpc^{-1}}$. Note that in this case we assume a constant background that is evaluated using the number counts in the most external annulii. Given the relatively small field of view of our images ($6.8 \times 6.8 \ \mathrm{arcmin}^2$), the fit does not converge if this parameter is left free to
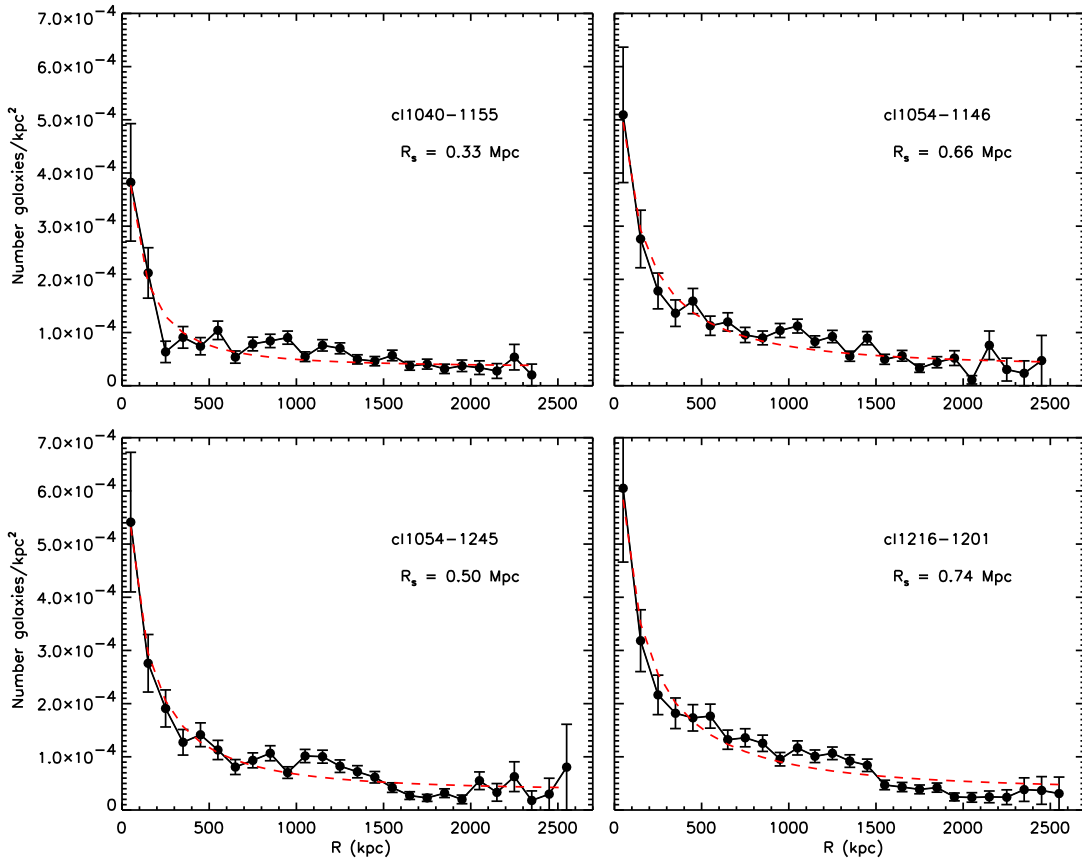
Figure 5.12: Radial profiles for the four clusters at high redshift. Error bars represent Poisson errors and the red dashed line in each panel represents a fit with a projected NFW. In each panel we also give the scale radius corresponding to fitted profile.

vary. We therefore allow only for very small variations around the value determined by hand. Note also that our relatively small field of view and the limited number of clusters with complete spectroscopy and photometry do not allow us to carry–out a systematic analysis of the radial number density profile. We reserve this analysis for future work (in the future we will also have WFI images of the EDisCS clusters in three bands; the much larger WFI field of view will be more appropriate for this kind of analysis). It is interesting to note, however, that although the overall behaviour of the radial profile is relatively well reproduced by the NFW fit, significant deviations are visible. These deviations are due to secondary clumps present in the spatial distribution of the clusters, that we will analyse in more detail in the following
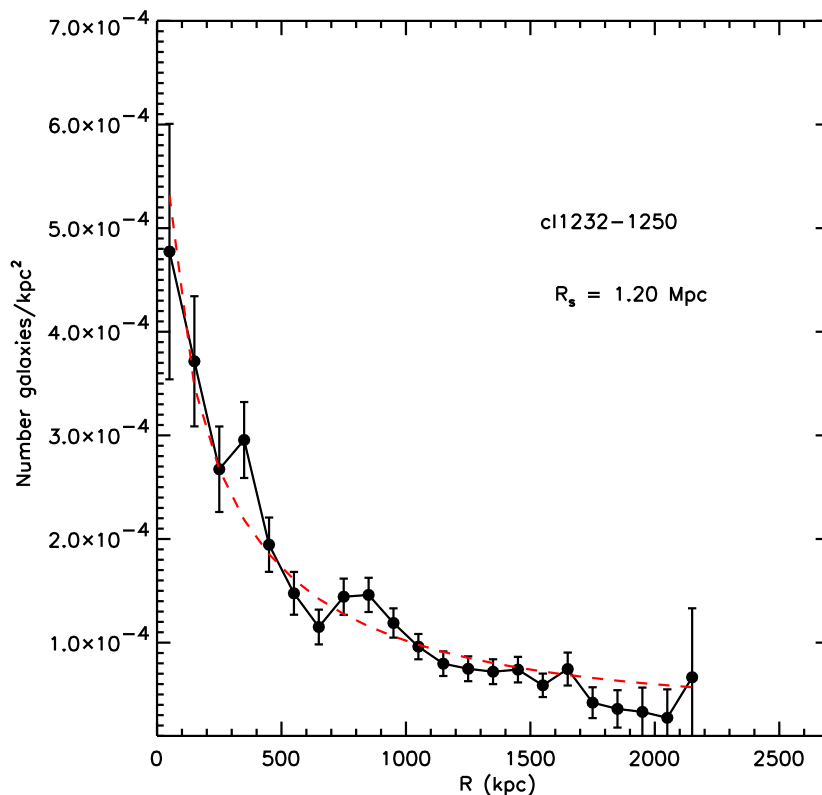
Figure 5.13: As in Fig. 5.12 but for the cluster cl1232–1250.

sections.

5.7.2 Adaptive kernel maps

It was realized a long time ago (Geller & Beers 1982) that substructure in the galaxy number density distribution on the sky can be more easily identified and evaluated by using contour plots. Geller & Beers constructed very simple maps using an overlapping box smoothing technique. At that time, no better methodology was available, and the authors were aware of the limits due to the use of a fixed window width. The main conclusion of this work was the finding of a significant amount of substructure in about 40 per cent of the cluster sample. Although these results were heavily criticised by many later studies, it is interesting to note that the fraction of clusters in which the detected substructure is claimed to be 'significant' has remained approximately the same. However, different studies have yielded different results for

the same clusters. As we have mentioned in Sec. 5.1, this can originate from the fact that different statistical tests are sensitive to different kinds of substructures (bimodality, groups aligned along the line of sight).

In the last years, improved methods for obtaining maps of projected galaxy positions have been developed. In this analysis we will use the *adaptive kernel* technique. In a nutshell, the kernel density estimator is a generalisation of the histogram. To build a histogram, one simply places a box over each data point and then sums the boxes. The adaptive kernel method uses of a 'bump' whose shape is determined by the kernel function, and whose width is specified by the smoothing parameter. The exact value of the smoothing parameter is determined from the distribution of the neighbouring points.

It is a well–known result that using a fixed smoothing length produces a density estimate that is over–smoothed in high density regions and under–smoothed in low–density regions, because of Poisson noise. It is obvious that an over-smoothing in the high–density region can potentially hide statistically significant substructures. In the adaptive kernel method, this problem is avoided by adjusting the 'local band–width factors' (i.e. the smoothing length) across the field to match the local density of events[5].

Different implementations of adaptive kernel methods using different kernel functions are possible. The technique we use in this analysis has been developed by Pisani (1993, 1996, see also references therein) and employs a Gaussian kernel.

It is possible to obtain more efficient algorithms by choosing other kernel functions (see discussion in Pisani (1996)). However, it has been shown that the choice of the kernel is not critical, as different choices differ only slightly in the form of the contours produced. The algorithm developed by Pisani has the advantage of being *non–parametric*, which means that the amount of smoothing is dependent solely upon the data points, rather than any prior estimate of what the cluster should look like. In order to avoid excessive under–smoothing that can arise because of Poisson noise, the iterative procedure that determines the optimal kernel size corresponding to each point, is stopped the first time the kernel size falls below a value corresponding to about 100 kpc.

As an example of the performance of this technique, we show in Fig. 5.14 the density map obtained for the cluster cl1216–1201.

It is important to realize that, although adaptive–kernel maps represent a powerful visual aid in the detection of substructures in data, the presence of multiple density peaks does not provide any 'quantitative' indication about their statistical significance. In order to isolate 'real' substructures, we now cross-correlate the substructure found in the adaptive kernel maps with the radial velocity information.

As a first step, we assign all the spectroscopically confirmed cluster members (recall

---

[5]It is essentially the same method that is used in in smoothed particle hydrodynamics.

Figure 5.14: Adaptive kernel map (see text for details) for cl1216–1201. The map is built considering all the objects retained as probable cluster members on the basis of their photometric redshifts and brighter than 25 in the I–band.

that we define these to be all the galaxies within the redshift interval ±0.015 from the BCG) to the closest peak in the density distribution. In practice, we move each galaxy along the density gradients towards a local density maximum.

Note that because of the noise in the density maps, it may happen that the above procedure finds multiple small peaks closely–spaced. We visually investigate each map and sometimes merge clumps that we *judge* not to be statistically significantly different. Note, however, that this occurs in a very small number of cases.

For each peak identified using the above procedure, we compute the local mean recessional velocity and velocity dispersion. In order to assess the statistical significance of each subclump, we use a bootstrap procedure: we randomly draw, from the actual radial velocity distribution, a number of galaxies equal to the number of galaxies that are assigned to the subclump under investigation. We repeat the procedure 5000 times for each subclump, and define a subclump to be 'statistically significant' if the measured velocity dispersion is at least 1σ less than the most probable value measured using the bootstrap procedure. Only subclumps associated with at least

Cluster name	z_{cl}	N_{clump}	N_{g}	$\bar{z}$	$\sigma\ [\mathrm{km\,s^{-1}}]$
cl1232–1250*	0.5419	1	10	0.5478	510
cl1040–1155	0.7044	1	7	0.7046	152
cl1054–1146	0.6972	1	10	0.6962	261
cl1054–1245	0.7498	0			
cl1216–1201	0.7941	1	6	0.8000	437
		2	18	0.7873	500

Table 5.3: Number of subclumps detected for each of the clusters used in this analysis (z_{cl} is the spectroscopic redshift of the cluster). For each of the subclumps we give the number of galaxies with measured velocity dispersion associated to the subclump, its median redshift and its velocity dispersion. (*) This subclump is not detected by our algorithm, as the associated galaxies are not spatially clustered with respect to the overall distribution of cluster galaxies.

four galaxies with measured velocity dispersion are considered. For each subclump, we also apply a clipping procedure, iteratively rejecting the galaxy with the largest deviation from the median local recessional velocity. In this case, we also update the bootstrap procedure by comparing the mean recessional velocity and velocity dispersion measured for the subclump under consideration with the values obtained for an equal number of galaxies drawn at random from the actual velocity distribution, after clipping an equal number of objects that deviate most from the median recessional velocity.

Figs. from 5.15 to 5.19 show the results obtained for the five clusters used in this analysis. In each figure, we show the density map obtained using the kernel method estimator; red crosses mark the positions of the local density peaks, while empty circles mark the positions of the galaxies with measured radial velocities. The size of the symbols is proportional to e^{δ}, where δ is the parameter that quantifies the local deviation from the cluster dynamical properties (see Sec. 5.6.2). Solid black lines indicate to which peak each galaxy with measured radial velocity is associated, and filled coloured circles mark the position of galaxies that belong to a statistically significant subclump, as defined above.

The figures show that only for the clusters cl1054–1245 and cl1232–1250 we do find no evidence for any statistically significant subclump. In the other three cases, we find at least one subclump that appears to be statistically significant. The results are summarised in Table 5.3 where we give, for each cluster, its spectroscopic redshift (z_{cl}), the number of subclumps that are found to be statistically significant (N_{clump}), the number of objects in each of these subclumps (N_{g}), their mean redshift ($\bar{z}$), and their estimated velocity dispersion (σ). As an example of the performance of our procedure, we also show in Fig. 5.20 the comparison between the mean redshift and
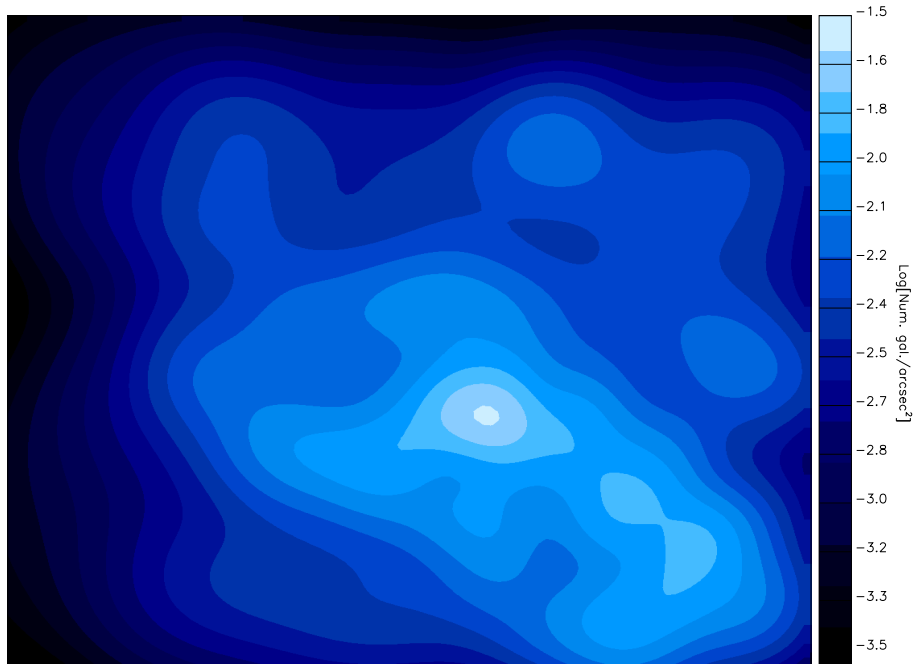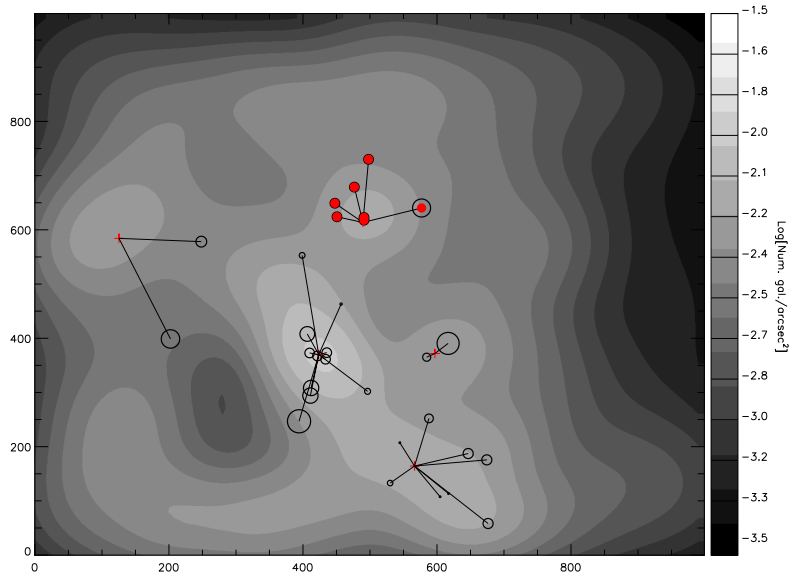
Figure 5.15: Adaptive kernel map (see text for details) for cl1040–1155. The map is built considering all the objects retained as probable cluster members on the basis of their photometric redshifts and brighter than 25 in the I–band. Red crosses mark the position of the maxima in the density field, and empty circles the position of all the galaxies with measured radial velocity. The size of the symbols is proportional to e^{δ}. Solid black lines indicate to which peak each galaxy with measured radial velocity is associated, and filled coloured circles mark the position of galaxies that belong to a statistically significant subclump.

velocity dispersion for the statistically significant subclump identified in the cluster cl1040–1155, and the distribution of values found by randomly drawing the same number of objects in this subclump from the actual radial velocity distribution of cluster members. In this particular case, the mean redshift of the subclump does not differ significantly from the redshift of the cluster (i.e. there is no significant offset in velocity), but the velocity dispersion is more than 1σ smaller than the typical value found for an equal number of objects randomly drawn from the actual velocity distribution of cluster members. Therefore, there is a high probability that the object under investigation represents a 'real' substructure.

Note that the radial velocity histogram of the cluster cl1232–1250 exhibits an obvious subclump with average recessional velocity of $1.65 \times 10^5 \, \mathrm{km \, s^{-1}}$. The P statistics of the Dressler & Schectman test also indicate a complex dynamical structure. However, our algorithm is unable to detect the presence of any significant subclump. This

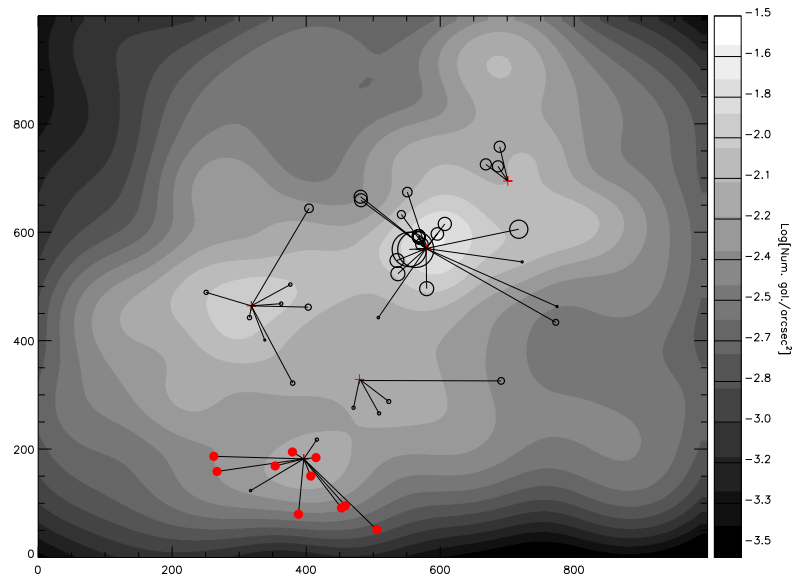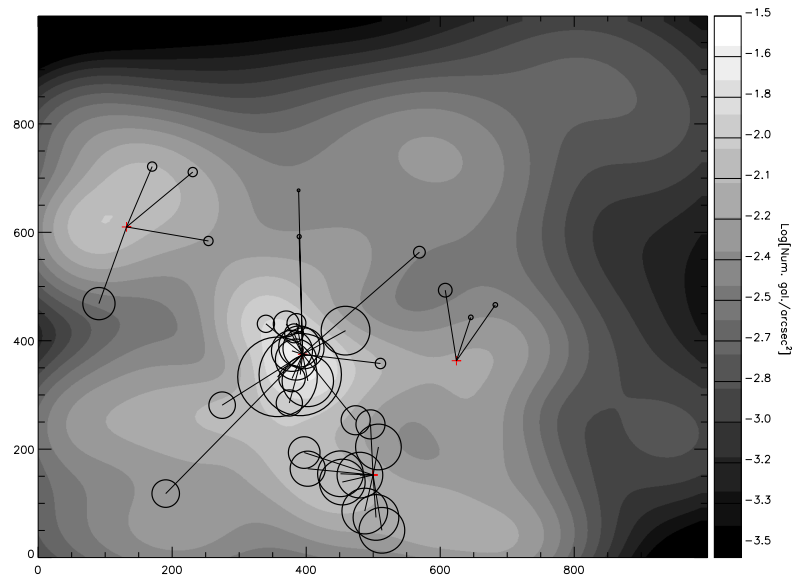**Figure 5.16:** As in Fig. 5.15 but for the cluster cl1054–1146.

Figure 5.17: As in Fig. 5.15 but for the cluster cl1054–1245.
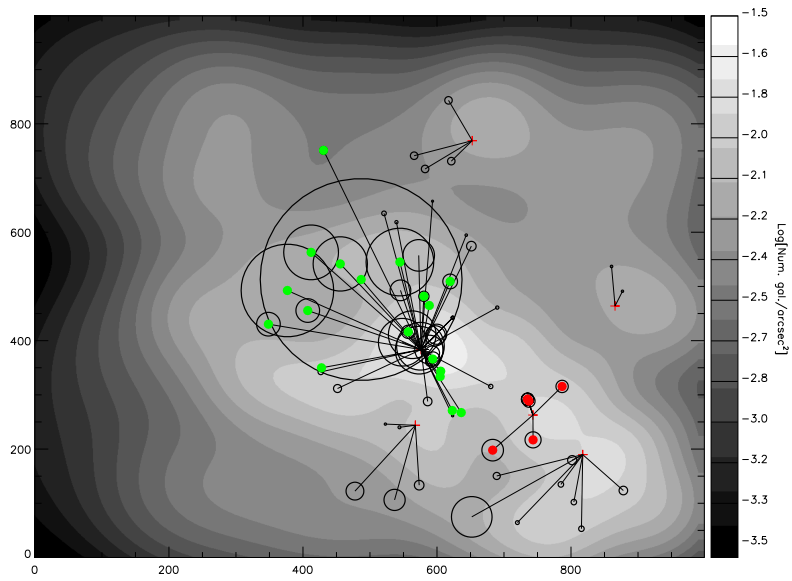
Figure 5.18: As in Fig. 5.15 but for the cluster cl1216–1202.
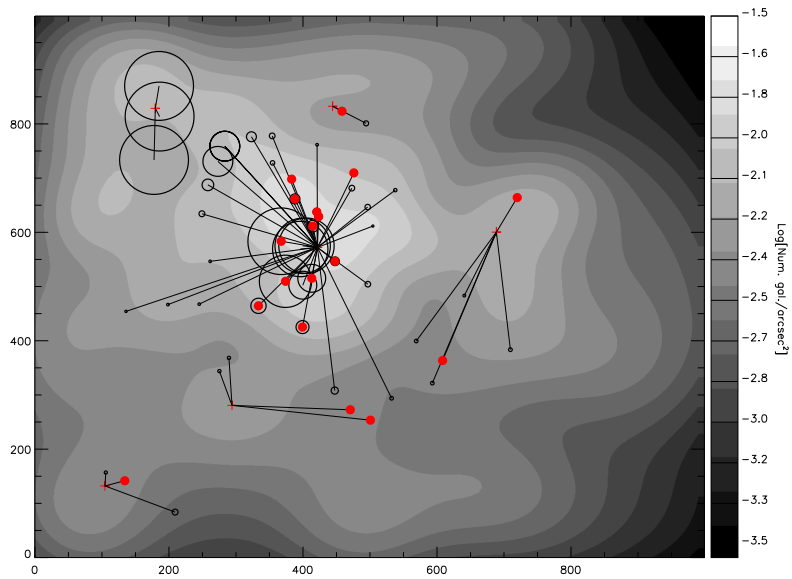
Figure 5.19: As in Fig. 5.15 but for the cluster cl1232–1250.
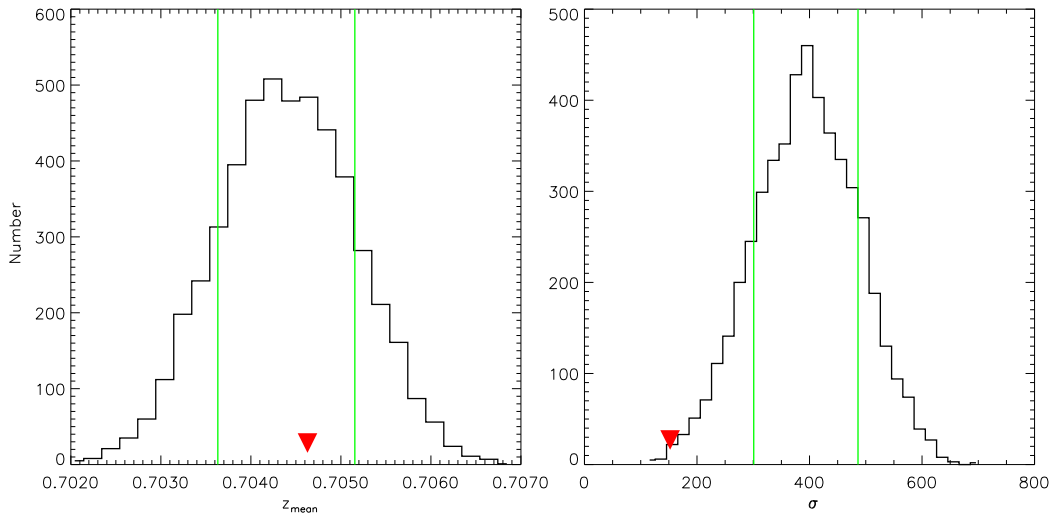
Figure 5.20: An illustration of our bootstrap procedure to asses the significance of a subclump identified in the adaptive kernel map. We plot the distributions of the median redshift (left panel) and of the velocity dispersion (right panel) measured for each of the Monte Carlo realizations (see text for details).

is because the galaxies populating the high velocity peak in the velocity histogram are not spatially clustered, as indicated by the red filled circles in Fig. 5.19 that mark the positions of these galaxies. Using our bootstrap procedure on these galaxies, we detect a significant subclump of 10 objects with a mean redshift of 0.5478 and a velocity dispersion of $510\,\mathrm{km\,s^{-1}}$. This case shows that our algorithm is unable to detect the presence of groups projected along the line–of–sight, if the galaxies in these groups are not spatially segregated on the sky with respect to the overall distribution of cluster galaxies.

In addition, it should be noted that the number and the spatial distribution of galaxies for which we have spectroscopic information, is somewhat limited by the spectroscopic magnitude limit (this roughly corresponds to I= 22 for the high redshift clusters and I= 23 for the low redshift clusters) and by geometrical constraints due to the mask design (see also Sec. 5.9). It could be the case that by increasing the number of objects with spectroscopic information, other significant groups would be detected. The number of subclumps detected for each cluster has then to be taken as a lower limit to the true amount of substructure.

Redshift	Cluster name	M_{200} $[\mathrm{M}_\odot\,h^{-1}]$	R_{200} $[\mathrm{Mpc}\,h^{-1}]$
0.00			
	g1	1.14×10^{15}	1.70
	g8	1.79×10^{15}	1.98
	g51	8.68×10^{14}	1.55
	g72	9.48×10^{14}	1.60
	g696	8.78×10^{14}	1.56
0.73			
	g1	4.93×10^{14}	1.28
	g8	7.43×10^{14}	1.47
	g51	4.19×10^{14}	1.21
	g72	1.39×10^{14}	0.84
	g696	2.36×10^{14}	1.00

Table 5.4: Virial masses and virial radii for our simulated clusters at redshift zero and at redshift 0.73, corresponding to the snapshot we use for the comparison with our observed sample.

5.8 The cluster simulations set

In this chapter we use five high resolution re–simulations of clusters generated using the 'zoom' technique (Tormen et al. 1997, see also Sec. 1.4). In Table 5.4 we list the virial masses and the virial radii of these clusters as measured at redshift zero and at redshift ~ 0.73, which is the snapshot we use for the following analysis.

Note that our simulated clusters are re–simulations of massive clusters identified *at redshift zero*. The selection of the haloes[6] was carried out on the basis of their masses and by also trying to avoid very massive neighbouring haloes. This is something to keep in mind when comparing the observed clusters to our set of simulations. Table 5.4 shows that the most massive haloes in the simulation boxes at $z = 0.73$ contain between 14 per cent and 48 per cent of the mass of the clusters at $z = 0$. This is not surprising given the fact that massive haloes are 'rare' objects that lie on the tail of the mass distribution, and whose assembly occurs at relatively low redshifts. Our set of simulations is thus not *ideal* for comparison with the EDisCS dataset, which is composed of clusters selected as virialized systems at redshift 0.5 to 0.8, the epoch when they are observed. Nevertheless, the range of masses of the simulated clusters at $z = 0.73$ is plausibly similar to that of our EDisCS clusters, so that the "problem" with our simulations lies in the fact that they are constrained to produce massive clusters at redshift zero.

---

[6]We recall that the parent simulation is the Very Large Simulation (VLS) carried out by the Virgo Consortium (Jenkins et al. 2001; Yoshida et al. 2001)

With these caveats in mind, we have coupled these dark matter cluster simulations with the semi–analytic model described in Chapter 3. For the purposes of this analysis, we have used only the *slow ejection* scheme, which we showed to be our preferred model in Chapter 4. This is the only model that allows us to reproduce the observed decline in baryon fraction from rich clusters to galaxy groups.

5.9 Simulating the observation of a simulated cluster

The detail of our simulations allows us to apply the same methodology that we used for the observed clusters to the simulated haloes.

The first step is to produce a catalogue of cluster galaxy candidates equivalent to those available for the observed sample. For each simulated cluster, we have built a *mock* galaxy catalogue for the snapshot corresponding to the redshift 0.7298, which approximately corresponds to the high redshift bin of our observed sample. For each cluster, we have then selected all the galaxies falling in a region equivalent to the physical sizes[7] of the observed fields, and we have only included galaxies brighter than -18.5 in the V–band. This corresponds to the magnitude cut applied to the observed sample. We have then converted the positions of the simulated galaxies into pixel positions on a grid of 2550×2250, which is the number of pixels in the images used for the catalogue extraction. In an attempt to mimic as closely as possible our observed sample, we have also displaced the position of the BCG by 1 arcmin along the diagonal. We also only select galaxies with recessional velocity of $\pm 4500\,\mathrm{km\,s^{-1}}$ with respect to the BCG.

For each simulation, we have considered the three projections on the planes xy, xz and zy, thereby producing a total of 15 simulated observations. In order to take into account the finite resolution of our images, we have checked if there are objects whose projected separation is smaller than 1 arcsec. If this occurs, we reject the less luminous objects. Note, however, that such cases occur for fewer than 5 per cent of the galaxies.

Fig. 5.21 shows the spatial distribution of galaxies selected in one projection of one of the simulated clusters. The symbol size scales with the stellar mass of the galaxies, as computed from our semi–analytic model (see Chapter 3).

For each projection, we have selected 'spectroscopically confirmed' members by using a procedure that mimics as closely as possible the one used to build the masks for the spectroscopic observations. For the spectroscopic observations of the EDisCS clusters, we have used 4 masks per field. Slits are typically 10 arcsec tall with a typical separation of 1 arcsec. In the y–direction about 6.5 arcmin is available

---

[7] The catalogue extraction is performed on images of 2250×2250 pixels with a pixel scale of 0.2 arcsec/pixel. Adopting a ΛCDM cosmology, the observed fields correspond to ~ 3.37 Mpc^2 at redshift 0.8, and to ~ 2.7 Mpc^2 at redshift 0.5.
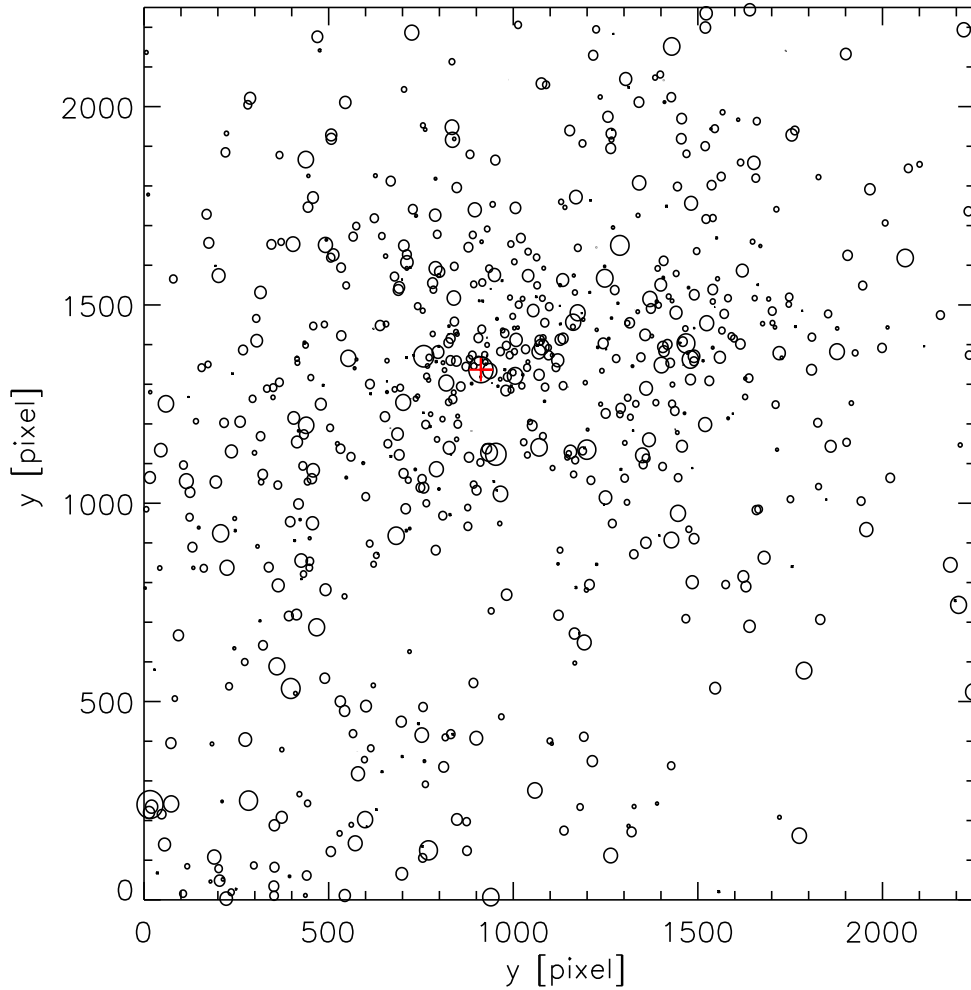
Figure 5.21: Projected distribution of galaxies selected from one of the simulated clusters. The red cross marks the position of the BCG. Empty circles mark the positions of the simulated galaxies. The radius of the symbols scales proportionally to the logarithm of the stellar mass.

for slits, while in the x–direction the slits typically cover about 5 arcmin, for the required rest–frame wavelength range at the redshifts of the cluster (the x–position of the slit determines the wavelength range of the spectrum). Similarly to what has been done for the observed clusters, we build, for each projection, 4 'artificial
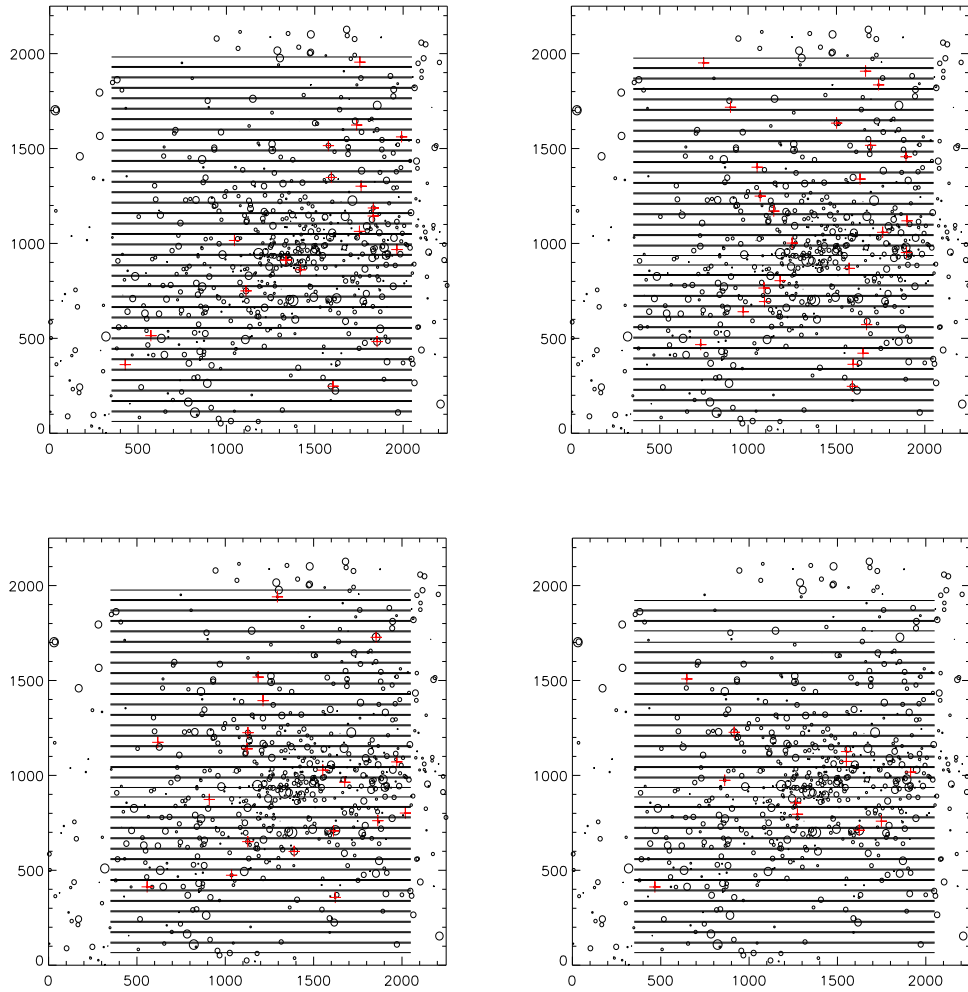
Figure 5.22: Simulated masks for one projection of one of our simulated clusters. Red crosses mark the position of the galaxies selected as spectroscopic targets.

masks'. Starting from the BCG (that is given the highest priority in the construction of the masks), we move up and down and select, in each slit, the most luminous object. We also require that the objects selected as spectroscopic targets are more luminous than −20 in the V–band, which corresponds to the magnitude limit of the observed spectroscopic sample. In order to make the selection even more realistic, we also impose the criterion that an object cannot be closer than 3 arcsec to the edges of its slit. Fig. 5.22 shows the 'simulated masks' for the same projection shown in

Fig. 5.21. The positions of the objects selected as spectroscopic targets are marked as red crosses.

Note that in reality, not all the slits will be placed on cluster members. Some slits are placed on stars for calibration purposes, and some slits will be taller if the size of the selected object is larger than the typical size of the slit. In order to take into account these effects, we randomly select a subset of 30 to 67 spectroscopic targets (this corresponds to the total number of spectroscopically confirmed members for the 4 clusters in the high redshift bin).

5.10 Models & Observations

With the choices described in the previous section, we have created *mock* catalogues that can be directly compared with the results obtained from our observed sample. We recall that great care is required in the interpretation of the results coming from this comparison, since the observational and the simulated sample were actually built using different criteria. Also, the number of clusters in the observed sample is still too small to draw any definitive conclusion.

Figs. 5.23 and 5.24 show the radial profiles for each of the three projections considered for the simulated clusters. As for the observed clusters, the overall profile is generally relatively well reproduced by a projected NFW profile (see Sec. 5.7.1), although in many cases the fit does not converge (e.g. g8zy, g51xz, g72xz, g72zy, g696xz, and g696zy). Note that for the cases in which a relatively good convergence of the fit is obtained, the values of the scale radii are similar to those obtained for the observed clusters. For the simulations g72 and g696, the 'failure' of the fit is probably due to the fact that these systems are still in an early state of assembly at this redshift (see following discussion concerning the adaptive kernel maps).

We also apply to the simulated clusters the analysis relative to the adaptive kernel maps. We show some examples of these maps in Fig. 5.25.

For each of the projections obtained for the simulated sample, we have repeated the procedure applied to the observational sample in order to quantify the amount of substructure and assess its significance. The results can be summarised as follows: for 4 out of the 15 projections, we find no evidence for significant substructures; for 8 projections our algorithm detects the presence of one significant substructure and for the remaining projections (3) we find 2 or 3 significant substructures. Considering these values, it seems that on average the simulated clusters are characterised by an amount of substructure that is comparable to that found for the observed sample.

We have already noted that our observed sample is still too small to draw any definitive conclusion. It is also important to keep in mind that our simulated clusters were constrained to produce massive virialized systems at redshift zero. Simulations show that such massive systems assemble at relatively low redshift from the mergers
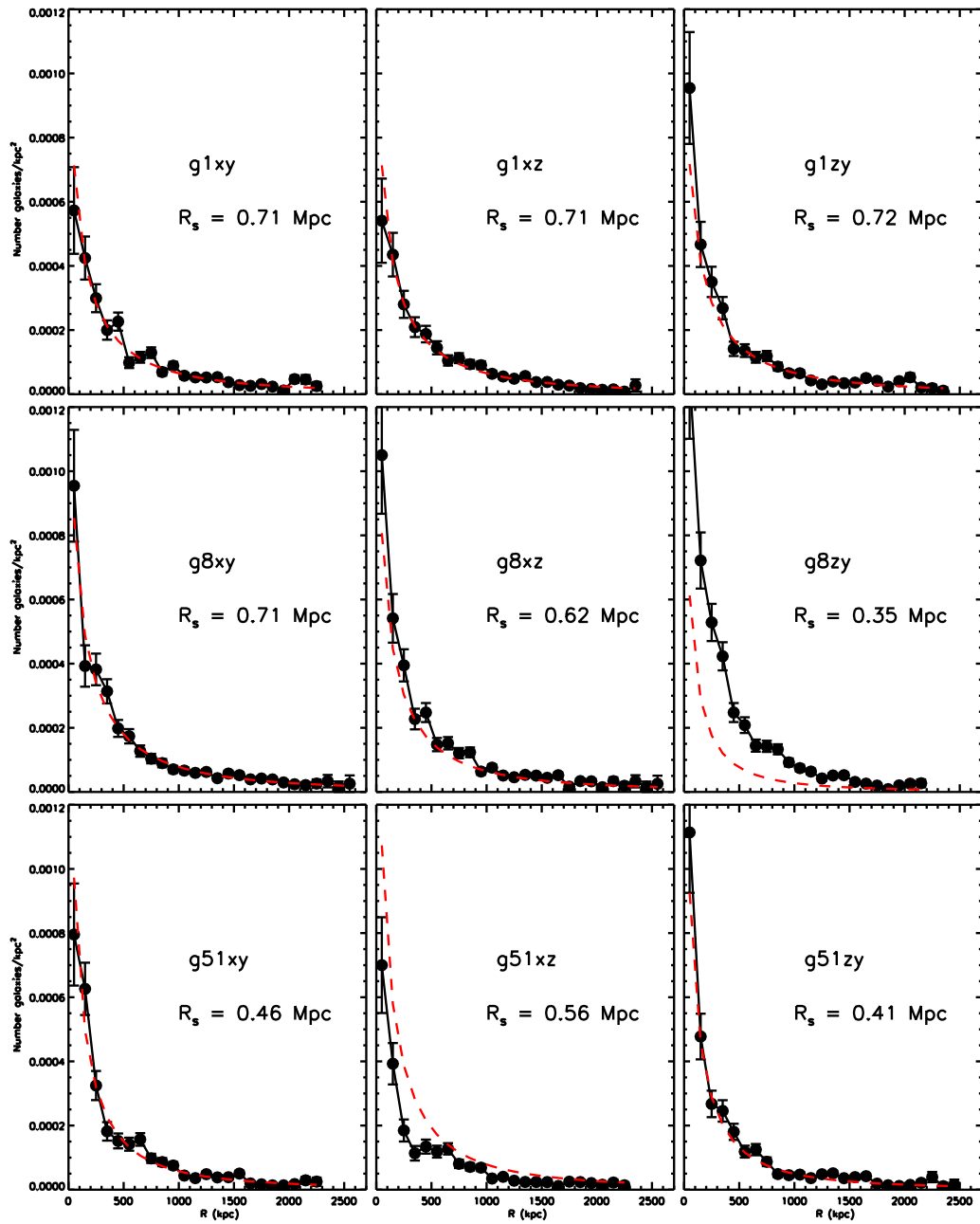
Figure 5.23: Radial profiles for the simulated clusters. Error bars represent Poisson errors and the red dashed line in each panel represent a fit with a projected NFW. In each panel we also give the scale radius corresponding to fitted profile.
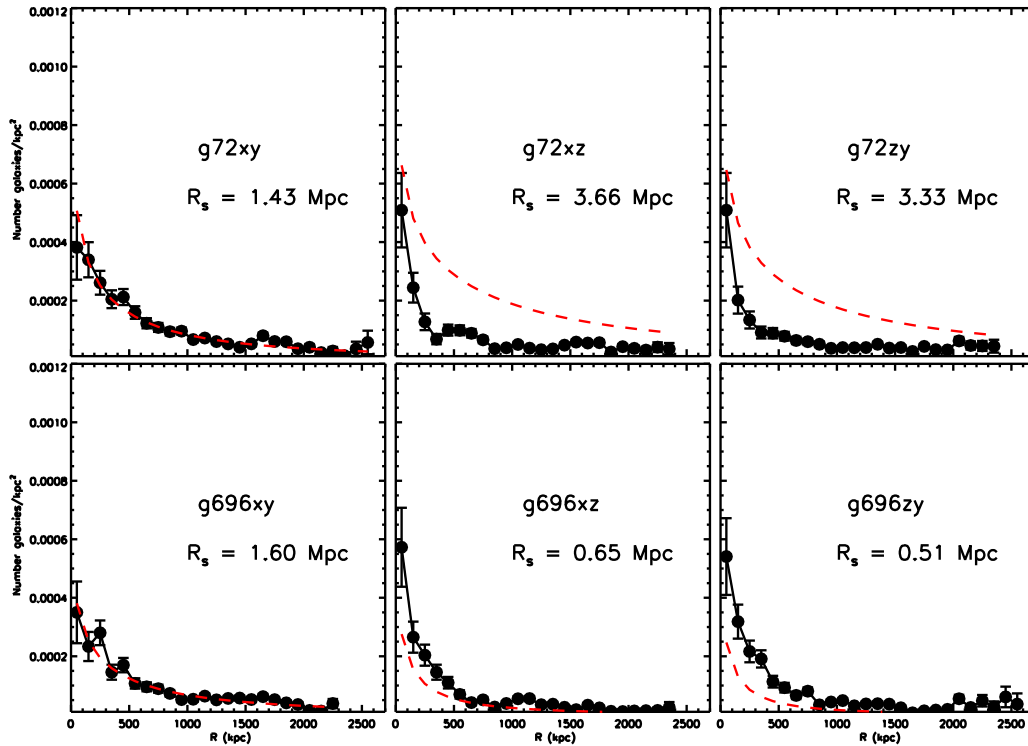
Figure 5.24: As in Fig. 5.23.

of big lumps whose separation can be of the order of 1 Mpc at redshift 1 (see the top right panel of Fig. 5.25). In that case, one would naively expect to find *more* substructure in the simulated clusters than in the observed ones. As a remark, we note that the projections for which we find 2 or 3 statistically significant subclumps, come from the simulation g72 and g696. The numbers in Table 5.4 indicate that the virial masses of the more massive haloes identified at this redshift for these simulations, only represent a very small fraction of the virial masses in the final massive haloes at redshift zero. This means that, at this epoch, these clusters are still in an early stage of assembly. A comparison with the observed sample might, in this case, not be appropriate.

It will be extremely interesting to see if the substructure fractions we find in the observed sample stay the same for the full EDisCS dataset. We expect, in fact, that the remaining clusters in the observed sample will be characterised by smaller masses. This suggestion comes from preliminary weak lensing analysis (Clowe et al., in preparation).
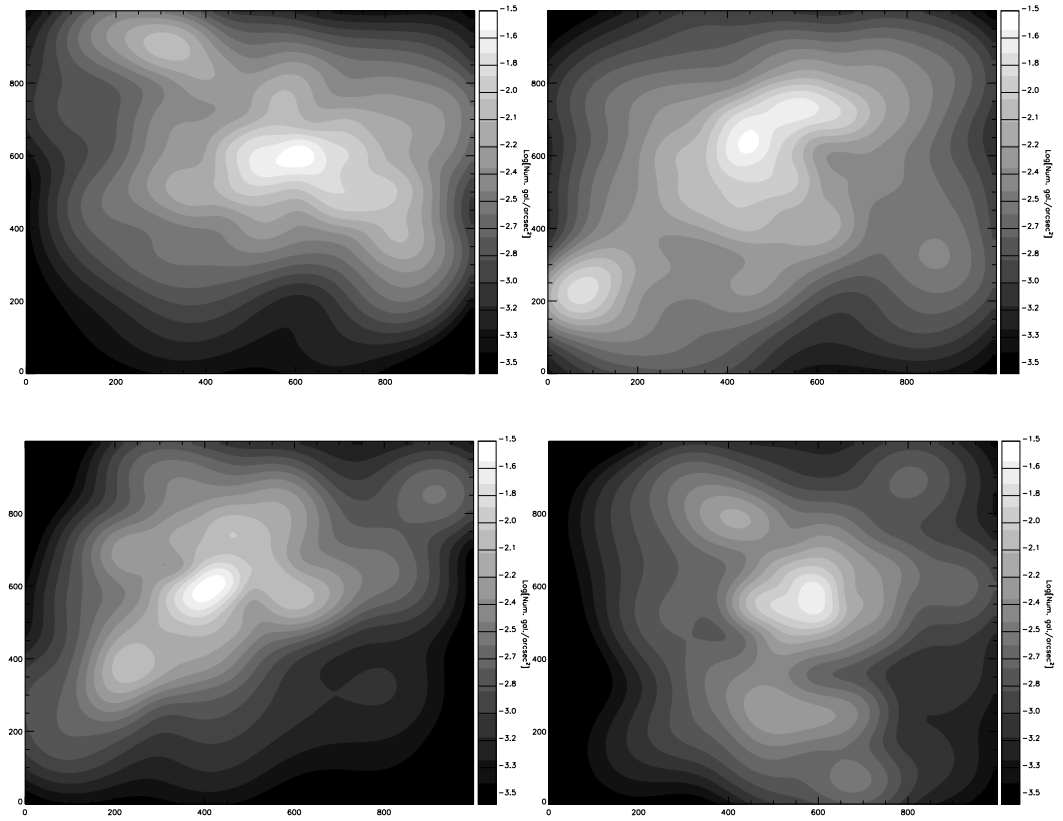
Figure 5.25: Four examples of adaptive kernel maps obtained for the simulated clusters.

Note also that the simulations allow comparisons to be made as functions of colour, magnitude, morphology, star formation rate, and other observable properties. Such an analysis will then provide important constraints on how the efficiency and relative importance of processes like quiescent and interaction–driven star formation, ram pressure stripping, harassment, strangulation, and merging affect the observable structure and stellar populations of cluster galaxies.

5.11 Discussion and Conclusions

In this chapter we have analysed in detail the internal dynamics and the structure of five clusters drawn from the ESO Distant Cluster Survey, an ESO Large Programme aimed at the study of the evolution of cluster structure and cluster galaxy population

at a significant fraction of the Hubble time.

All the clusters of our observed sample exhibit a complex dynamical structure with indications of a significant amount of substructure. We have developed a new method to assess the statistical significance of substructure that couples the information on the spatial distribution of cluster galaxies projected on the plane of the sky, with the information on the velocity distribution. The analysis of the observed sample is complemented by an accurate comparison with a large set of high–resolution numerical simulations.

The detailed information in the simulations allows us to treat the simulated clusters in exactly the same way as the observed sample. We have shown that it is possible to build *mock catalogues* using selection criteria that resemble as closely as possible the criteria that have been used to build the observed sample.

The analysis shows that the amount of substructure found in the simulated clusters is comparable to that found in the observed clusters, although it is unclear how the simulations are influenced by the fact that they are required to produce massive virialized clusters at redshift zero.

A definitive conclusion is hampered by the small number of clusters in the observed sample analysed here and also by the fact that different selection criteria have been used for the observed and the simulated sample. The simulated clusters correspond to large virialized systems at redshift zero and simulations show that these systems assemble at relatively low redshifts from the mergers of big lumps at large distances. Instead, the observed clusters have been selected as virialized systems at redshifts $\sim$ 0.5 and $\sim$ 0.8, the epochs when they are observed. The simulated sample, therefore, is not *ideal* for this analysis, although the extension to the whole EDisCS dataset could actually improve the match. Ideally, we should use a large cosmological simulation in order to select a number of massive haloes at epochs corresponding to the redshifts of the observed clusters.

The complete EDisCS dataset will provide a large number of clusters at two different redshifts, at a level of detail that will also permit an accurate comparison with the large sample of clusters available at low redshift. Then, it will be possible to investigate the significance of substructure as a function of different galaxy observables, the colour, the luminosity, and the star formation rate. This kind of comparison may place important constraints on the evolution of cluster structure as a function of redshift, as well as on the relative importance of different physical mechanisms that drive galaxy evolution in clusters.

– Where there is much desire to learn, there of necessity will be much arguing, much writing, many opinions; for opinion in good men is but knowledge in the making.

John Milton, Areopagitica

6

The build–up of the CM sequence at redshift ~ 0.8

Abstract

In this chapter I analyse the colour–magnitude relation of a subset of the EDisCS clusters at high redshift. The invariance of the colour–magnitude relation up to high redshift, has traditionally been interpreted as one of the most convincing evidence for elliptical galaxies representing an old, passively evolving population formed at high redshift ($\gtrsim$ 2–3). This is in apparent contradiction with hierarchical models of galaxy formation where elliptical galaxies are the result of merging processes, and a significant number of early–type galaxies assemble at relatively low redshifts. In this chapter I analyse the colour–magnitude relation in three clusters at a significant fraction of the Hubble time. By comparing the results obtained for high redshift clusters with observational data in the nearby Coma cluster, I find evidence for a significant deficit of low–luminosity objects on the red–sequence. The results rule out a single formation scenario in which all red galaxies in clusters have evolved passively after a monolithic collapse at $z \gtrsim 2$–3, and indicate that passive galaxies observed in clusters today follow different evolutionary paths, depending on their luminosity. The results are qualitatively consistent with the predictions of hierarchical models of galaxy formation.

6.1 Introduction

Throughout this thesis we have emphasised that clusters of galaxies constitute an interesting laboratory for the study of galaxy evolution, offering the unique opportu-

nity to trace the average properties of galaxies in similar environments as a function of cosmic time. The technical capabilities achieved in the last years are providing a rapidly growing amount of data on high redshift clusters (Stanford et al. 1998; van Dokkum et al. 2000, see also Chapter 5) that, together with the latest theoretical developments (Cole et al. 2000; Springel et al. 2001a, see also Chapters 3 and 4), will likely provide important constraints on the physical mechanisms driving the formation and the evolution of the cluster galaxy population.

It has been known for a very long time (Visvanathan & Sandage 1977) that bright elliptical galaxies form a tight sequence in the colour–magnitude diagram which, in nearby clusters, extends over a range of at least 5–6 mag below the luminosity of the BCG (De Propris et al. 2003a).

At the present epoch, the colour–magnitude relation (hereinafter CMR) can be interpreted as either an age effect (bluer galaxies being younger) or a metallicity effect (bluer galaxies being more metal poor). However, the mere existence of a tight relation at high redshift tends to favour the metallicity interpretation and makes the age explanation untenable. In the latter case, in fact, one expects a drastic change in the CMR at high redshift because small galaxies become progressively brighter and bluer as they approach their formation epoch (Kodama et al. 1998). This expectation is in conflict with observational results, which show that the slope of the CMR does not change appreciably over the redshift interval 0–1 (Gladders et al. 1998).

The most common interpretation of these findings is that cluster elliptical galaxies constitute a passive evolving population formed at high redshift ($z \gtrsim 2$–3) in a monolithic collapse (but see the discussion by Bower et al. (1998)). In this context, the CMR arises naturally when the effects of supernovae winds are included (Arimoto & Yoshii 1987, see also Chapter 3): when the thermal energy of the gas exceeds the gravitational binding energy, supernovae explosions heat the interstellar medium triggering galactic winds. This produces a selective loss of mass by smaller galaxies because of their shallower potential wells, thus naturally establishing the observed CMR.

An alternative explanation has been proposed by Kauffmann & Charlot (1998). In their model, elliptical galaxies form through mergers of disc systems and a CMR arises as a result of the fact that more massive ellipticals are formed by mergers of more massive, and then more metal rich, disc systems. In the analysis by Kauffmann & Charlot, the evolution of the underlying dark matter component is followed using the generalised Press & Schechter formalism (Press & Schechter 1974; Bond et al. 1991). In Chapter 3 of this thesis we have shown that our model, in which the evolution of the underlying dark matter component is followed using full N–body simulations, also reproduces a tight CMR that is in agreement with observational results for nearby clusters. Our model also differs from that of Kauffmann & Charlot in a number of other details.

For a long time it has been claimed that it is not clear if the hierarchical scenario

can produce an 'universal' CMR, since the merging history will vary from cluster to cluster. We have analysed the results from five high resolution re-simulations of clusters (the same used in Chapter 5). In all cases, our model reproduces a colour–magnitude relation that is in agreement with the observational data in nearby clusters, although with a somewhat larger scatter.

In Chapter 4, however, we showed that a natural prediction of the hierarchical scenario is that the evolution of early–type galaxies depends quite strongly on environment. Although there are some indications of intermediate age in elliptical stellar populations in lower density environments, that would suggest that this is actually the case (Bower et al. 1990; Terlevich et al. 2001), it is unclear if observational results support the 'strong' differential evolution predicted by hierarchical models.

Indeed, Stanford et al. (1998) find that there is a striking homogeneity in the observed properties of cluster ellipticals for clusters spanning a broad range in optical richness and X–ray luminosity. This is also confirmed in a recent analysis by Andreon (2003) who uses a sample of 158 galaxy clusters and groups detected in the Early Data Release of the Sloan Digital Sky Survey and shows that the observed red sequence colour does not vary by more than 0.02 mag.

It is important to contrast this homogeneity of early–type galaxies with the observed evidence that star formation activity becomes more important in high redshift clusters (Butcher & Oemler 1978, 1984; Dressler et al. 1999; Poggianti et al. 1999).

This apparent paradox can be understood when considering some of the selection effects that can produce a biased view of the evolution of this class of objects: (i) the population of early–type galaxies in high redshift clusters does not necessarily include *all* the progenitors of the early–type galaxies residing in clusters at redshift 0 – an effect that has been named 'progenitor bias' by van Dokkum & Franx (1996, see also Sec. 1.6.3); (ii) clusters of galaxies are 'rare objects' (see Sec. 1.1). This is increasingly true for higher redshift clusters, that have a different evolutionary history compared with their lower redshift counterparts (Kauffmann 1995a).

Therefore, the observed passive evolution of early–type galaxies in clusters could simply be the result of the fact that we are increasingly biased toward old galaxies at higher redshift. These considerations suggest that the CMR today may be composed of a variegated population of galaxies with different star formation histories. It is clear that these effects can only be understood by studying the evolution of the cluster population as a *whole*, and by trying to understand how galaxies are accreted from the field, how the dense environment of the cluster affects their star formation rates, and how these galaxies fade and move onto the observed red sequence. There have only been few attempts in this direction in the last years (Smail et al. 1998; Kodama & Bower 2001; Diaferio et al. 2001).

There have been some recent interesting claims that in clusters at redshift $z \sim 1$, there is a *truncation* of the red sequence (Kajisawa et al. 2000; Nakata et al. 2001). This result certainly deserves a more detailed investigation since it places strong

constraints on the relative importance of star formation and metallicity in establishing the observed red sequence.

In this chapter we present a detailed analysis of 3 clusters in the redshift interval 0.7–0.8 from the EDisCS sample (see Sec. 5.2). As we have already discussed in the previous chapter, EDisCS provides a large and homogeneous (in terms of data analysis and quality) sample of clusters at high redshift with a wide range of structural properties. It is the ideal data sample for studying the evolution of cluster structure and the galaxy cluster population as a function of cosmic time and to investigate the influence of environment on galaxy evolution. In the present analysis, we will use only a subset of the complete EDisCS sample.

The layout of the chapter is as follows. In Sec. 6.2 we briefly review the observational sample used in this analysis. In Sec.6.3 we describe the technique used to correct for background and foreground contamination and in Sec. 6.4 we present the CMR for the clusters used in this analysis. In Sec. 6.5 we compare the results obtained for our cluster sample to the results obtained for the Coma cluster. A discussion of our findings and the conclusions are presented in Sec. 6.6.

Throughout this chapter we will use the following cosmological parameters: $H_0 = 70 \, \mathrm{km \, s^{-1} \, Mpc^{-1}}$, $\Omega_{\mathrm{m}} = 0.3$ and $\Omega_{\Lambda} = 0.7$. Note that with this cosmology $z \sim 0.8$ corresponds to more than 50 per cent of the look-back time.

6.2 The data

As we have explained in the previous chapter, the complete EDisCS dataset will provide homogeneous photometry and spectroscopy for 10 clusters at redshift ~ 0.5 and 10 clusters at redshift ~ 0.8. Cluster candidate selection and preliminary confirmation tests are discussed in Gonzalez et al. (2002) and in the previous chapter. The data acquisition phase is almost completed (see Sec. 5.3) and most of the data were taken under excellent conditions with almost all combined images having $< 1''$ FWHM seeing.

In this chapter we concentrate our analysis on the three clusters at high redshift for which we have complete imaging and spectroscopy and a reasonably large number of objects that are spectroscopically classified as 'absorption line' systems[1], in order to reliably determine the parameters of the colour–magnitude fit (see Sec. 6.4). The number of spectroscopically confirmed members, for these clusters, ranges from ~ 50 (for cl1054–1245) to ~ 70 (for cl1216–1201). The clusters are at redshift z=0.70 (cl1054–1146), z=0.75 (cl1054–1245) and z=0.80 (cl1216–1201). In the following, we use magnitudes and colours computed using our 1 arcsec radius aperture. At the

---

[1] Most elliptical galaxies contain old, cool stars. There is little or no free dust and gas in ellipticals, and certainly no massive star formation. The spectra of elliptical galaxies are dominated by absorption lines, especially lines of ionized calcium (CaII H & K) and hydrogen.

redshifts of the clusters, this aperture corresponds to a physical radius of 7.13–7.50 kpc. This choice is adopted in order to simplify the comparison with galaxies in the Coma cluster (see Sec. 6.4).

6.3 Cluster membership

As we have explained in Sec. 5.5, photometric redshifts have been computed using two independent codes (Rudnick et al. 2001; Bolzonella et al. 2000) in order to keep under control systematics in the identification of likely non–members. We recall that results based on the current spectroscopic sample show that our photometric redshifts are quite accurate, with $< |z_{\mathrm{spec}} - z_{\mathrm{phot}}| > = 0.06$–$0.08$ for both the clusters at $z \sim 0.5$ and $z \sim 0.8$. In order to correct for foreground and background contamination, we have adopted here a two–steps procedure.

As a first step, we have used the full probability redshift distributions from both codes to isolate objects with a high probability to be at the cluster redshift. The method is explained in detail in Sec. 5.5.2. Results based on the current spectroscopic sample show that the remaining foreground/background contamination can be as high as 40–50 per cent. In order to take this contamination into account, we have performed a statistical subtraction on the remaining objects using the distribution on the CMR of all the objects residing at a physical distance from the BCG larger than 1 Mpc. For this purpose, we use a procedure similar to the one employed by Pimbblet et al. (2002). We refer to the original paper for more details about the procedure that we only briefly summarise in the following.

For each cluster used in our analysis, the field population is determined from regions at a radius larger than 1 Mpc (at the corresponding redshift of the cluster). Both the cluster region and the field region are binned onto a gridded colour–magnitude diagram (we use a 0.3 bin in colour and a 0.5 bin in magnitude). The field region is then scaled to the same area of the cluster region we wish to correct, and each galaxy is assigned a probability to be a cluster member simply counting how many galaxies lie in the colour–magnitude bin in the two different regions. If A_{c} and A_{f} represent the area of the cluster and the field region respectively and N_{c} and N_{f} represent the number of objects at a given grid position in the cluster and field region, we can define the probability of a galaxy, in a given colour magnitude grid position, of being a field galaxy as:

$$P = \frac{N_{\mathrm{f}}}{N_{\mathrm{c}}} \frac{A_{\mathrm{c}}}{A_{\mathrm{f}}}$$

Note that the 'field' and the 'cluster' area are computed properly taking into account the geometry of the CCD. Using a series Monte Carlo simulations, the field population is simply subtracted off on the basis of these probabilities: for each galaxy a random number between 0 and 1 is generated and if the value of P is larger than this number,
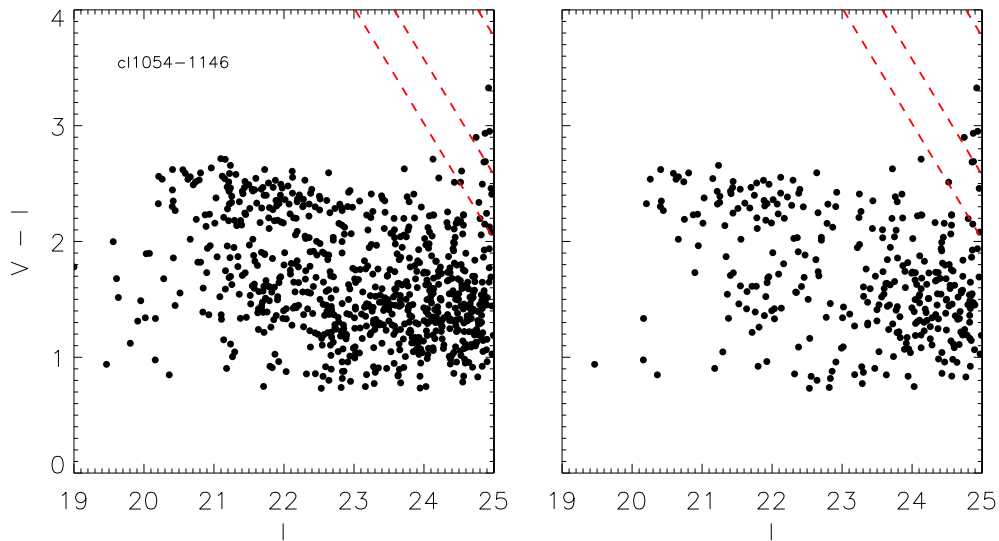
Figure 6.1: Example of the performance of the statistical rejection procedure. In the left panel, filled circles represent all the objects retained as probable cluster members on the basis of their photometric redshifts. In the right panel, only objects that are kept on the basis of their photometric redshifts *and* that survive the statistical rejection (in one Monte Carlo realization) are shown.

the galaxy is rejected.

When the above procedure produces a value of P that is larger than 1, the grid size is increased for that particular position. As explained in Appendix A of Pimbblet et al. (2002), this approach has the advantage of preserving the original probability distribution better than methods where the excess probability is distributed evenly between the neighbours of the critical grid position (Smail et al. 1998; Kodama & Bower 2001). For each cluster we run 100 Monte Carlo realizations of the above described procedure.

As an example of the performance of this procedure, we show in Fig. 6.1 the CMR for the cluster cl1054–1146 for all the objects retained as probable cluster members on the basis of their photometric redshifts (left panel), and for the objects kept in one realization of the statistical subtraction applied to this galaxy sample (right panel). The red dashed lines represent the 3 and 5–σ detection threshold in the V–band.

Note that regions outside 1 Mpc are most likely still 'dominated' by the cluster. Therefore, using this method we are probably over-estimating or under–estimating (depending on the colour) the field subtraction. However, we will show later that several tests demonstrate that our results are robust and are not affected by the criteria adopted for cluster membership.

The statistical rejection removes on average 43–55 per cent of the objects that are kept as probable cluster members on the basis of their photometric redshifts, down to the magnitude limit I= 25. Note that this fraction is in good agreement with the residual contamination fraction that can be estimated from Fig. 5.5, suggesting that the performance of the technique is reasonably good.

6.4 The colour–magnitude relation

Fig. 6.2 shows the V-I *vs* I diagram for the 3 clusters used in this analysis. At the clusters redshifts, V−I approximatively samples the rest–frame U−V colour. It is therefore very sensitive to any recent or ongoing episode of star formation. A red sequence is clearly visible in the CM diagram of each cluster, together with a significant population of blue galaxies that are known to populate clusters at high redshift. The solid thick line is a bi-weight linear fit (Beers et al. 1990) to the spectroscopically confirmed members with absorption–line spectra. As explained in Sec. 5.6.1, this algorithm gives higher weight to points that are closer to the centre of the distribution and is then insensitive to the presence of outliers. The dashed lines correspond to $\pm 3\sigma$ from the best fit line, where σ is the dispersion of the objects used for the fit and is, in all 3 clusters ~ 0.1. Thin solid lines correspond to the 3 and 5σ detection limits in the V–band. Empty symbols represent galaxies retained as cluster members after using the photometric redshift and one Monte Carlo realization of the statistical subtraction. Filled circles are spectroscopically confirmed members with absorption–line spectra, while crosses represents spectroscopically confirmed members with emission–lines.

For comparison, Fig. 6.3 shows the colour–magnitude relation for the Coma cluster using all the objects in the photometric catalogue by Terlevich et al. (2001), who give observed U and V photometry in different apertures. We use the magnitudes in 25.2 arcsec diameter aperture that, at the redshift of Coma (0.023), corresponds to a physical size of 11.71 kpc. We do not apply any further aperture correction to account for the fact that our apertures are slightly larger that the one used for Coma. Observed magnitudes are converted to absolute magnitudes using the distance modulus of Coma (35.16) and observed colours are converted to rest–frame colours using the tabulated K–correction[2] given by Poggianti (1997). According to these tables, the K–correction to apply amounts to 0.033 for E type galaxies, 0.033 for Sa and 0.038 for Sc. We apply a single correction of 0.035 to all the objects in the photometric catalogue.

---

[2]The K correction "corrects" for the fact that sources observed at different redshifts are, in general, compared with other objects or each other at different rest-frame wavelengths. It simply arises from the relation between the emitted or rest–frame absolute magnitude of a source in one broad photometric bandpass to the observed–frame apparent magnitude of the same source in another broad bandpass.
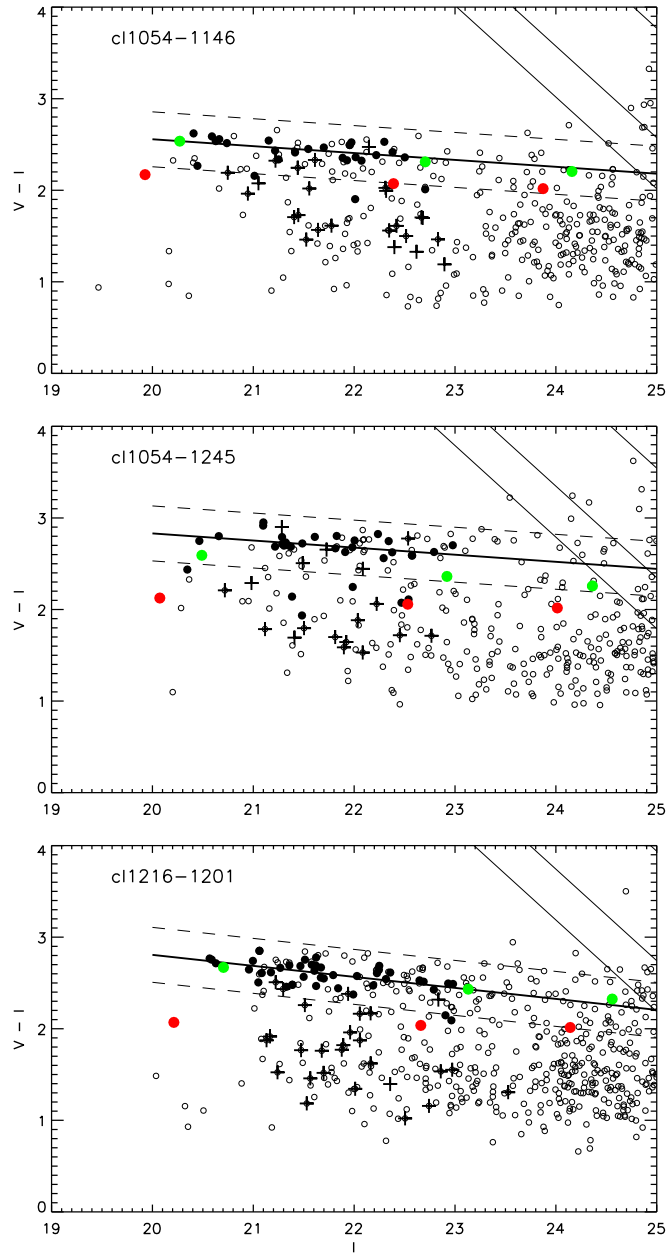
Figure 6.2: Colour–magnitude diagrams for the 3 EDisCS clusters under analysis. The solid thick line marks the best fit relation, the dashed lines correspond to $\pm 3\sigma$ from the best fit line (σ is the dispersion of the objects used for the fit). Thin solid lines correspond to the 3 and 5σ detection limits in the V–band. Filled circles are spectroscopically confirmed members with absorption–line spectra, while crosses represents spectroscopically confirmed members with emission–lines. Coloured symbols represent two families of models (see text for details).
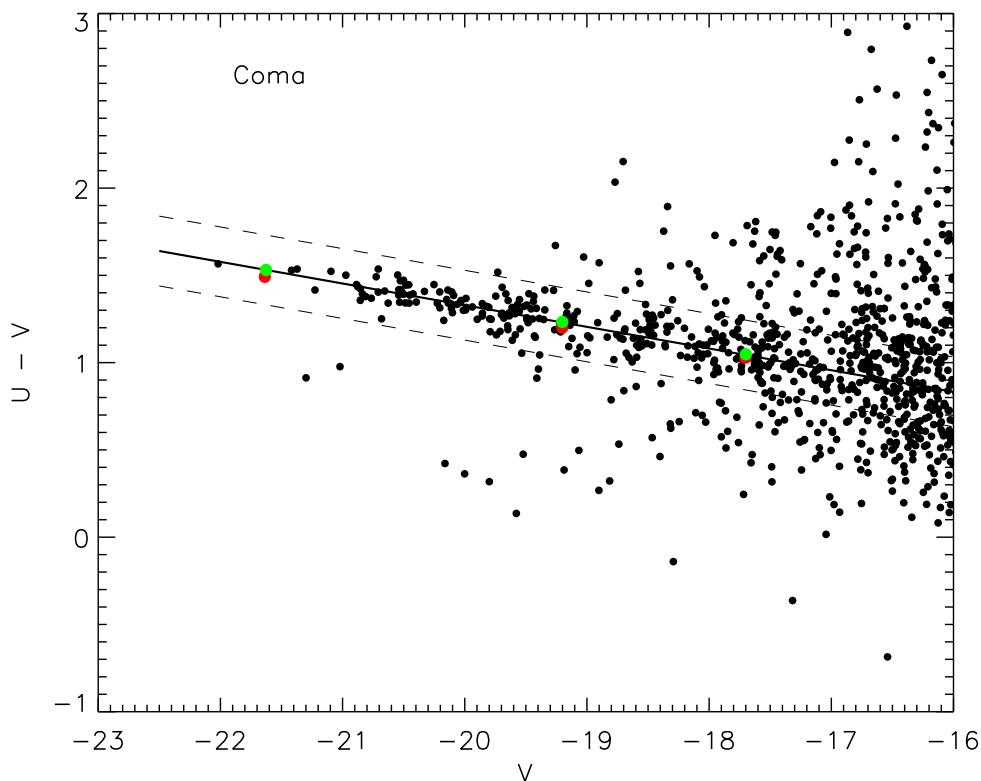
Figure 6.3: Colour–magnitude relation of Coma for all the galaxies in the catalogue by Terlevich et al. (2001). Observed magnitudes have been converted to absolute magnitudes using the distance modulus of Coma (35.16) and observed colours were converted to rest–frame colours using tabulated K–corrections (Poggianti 1997). Solid and dashed lines have the same meaning as in Fig. 6.2. Coloured symbols represent two families of models (see text for details).

The coloured points in Fig. 6.2 show the location of galaxy models with two different star formation histories: a single burst occurred at $z = 3$ (green points) and a 1 Gyr exponentially declining SFR beginning at $z = 3$ (red points), calculated with the population synthesis code by Bruzual & Charlot (2003). For each one of these two star formation histories, three different metallicities are shown: 0.02 (solar), 0.008 and 0.004, going from the brighter to the fainter objects. The relation between metallicity and luminosity in these models has been calibrated by requiring that they reproduce the observed colour–magnitude relation in Coma (see Fig. 6.3). (Note, in fact, that population synthesis models need to be normalised to a certain

Cluster	Slope	error	Zero–point	error	Dispersion	error
cl1054–1146	−0.07	0.05	4.01	1.00	0.11	0.03
cl1054–1245	−0.07	0.05	4.18	1.10	0.11	0.04
cl1216–1201	−0.11	0.03	5.04	0.68	0.11	0.02

Table 6.1: Coefficients and corresponding errors for the best fit relation obtained for each of the clusters used in this analysis.

mass since they usually give magnitudes for a stellar population of a total mass equal to $1\,M_\odot$). This calibration has been found *a posteriori* to be in good agreement with the metallicity–luminosity relation derived from spectral indices of Coma galaxies (Poggianti et al. 2001). When these models are evolved back in time, the single burst models provide a remarkably good fit to the red sequence observed in the high redshift clusters, thus confirming that the location of the CM sequence observed in distant clusters requires high redshifts of formation, and that the slope is consistent with a correlation between galaxy metal content and luminosity.

The coefficients of the fit and the corresponding errors are determined using a bootstrap method over 100 Monte Carlo realizations. Both the slope and the zero–point are allowed to vary. In Table 6.1 we report the values of the coefficients and the corresponding errors obtained for each of the clusters used in this analysis. Although the number of objects used to fit the CMR is in general not high, and therefore the uncertainties on the coefficients are quite large, the agreement between the values obtained for the different clusters is remarkable. We have shown in Sec. 5.7 that the clusters used in this analysis exhibit a wide range of structures and cover a wide range of masses. Our analysis shows that the average colour of early–type galaxies is nearly the same in these clusters. In addition, the scatter about the CMRs also remains approximatively constant, although the uncertainties are too large to make more quantitative comparisons. This result, already pointed out by Stanford et al. (1998), suggests that the evolution of the bulk of the early–type population does not depend on cluster richness or on the degree of the concentration of the cluster itself. This is already an important result, given the fact that so far there is only one cluster at this redshift studied at this level of detail (van Dokkum et al. 2000). One cluster is obviously not enough to disentangle different formation scenarios for the formation and evolution of elliptical galaxies in clusters.

Note also that the dispersion we find around the red–sequence is larger than the canonical values found for closer clusters, although a quantitative comparison is hampered by the fact that we are not using objects that are *morphologically* classified as elliptical galaxies, as is usually done in the literature. In future, we will have HST images of EDisCS clusters, that will allow us to undertake an analysis of the CMR as a function of the morphological type. Preliminary results, obtained using bulge/disc

decomposition automatic algorithm (Simard et al., in preparation), indicate that the red–sequence shows a surprisingly large number of disc–dominated systems (see also Rudnick et al. (2003)). Analysis of the HST data will help us to understand the nature of these objects.

As a last remark, we note that the colour of early–type objects in the cluster cl1054–1245 seems to be systematically redder than the elliptical colour of all the other clusters. This is puzzling given the fact that the redshift of this cluster lies between the redshifts of the clusters cl1054–1146 and cl1216–1201 and therefore we would expect that also the colour of the red sequence falls between those of these two clusters. It is likely that there is a zero–point problem for this cluster.

Note that there have been claims (Scodeggio 2001) that much of the slope of the CMR is due to the use of fixed metric apertures for the measurement of colours. This means that different portions of a galaxy are used to compute the colour, depending on the intrinsic size (and hence on the luminosity) of the galaxy and, because of the presence of colour gradients in elliptical galaxies (Peletier et al. 1990a,b; Saglia et al. 2000), this introduces a spurious effect in the slope of the CMR. Scodeggio (2001) shows that, when using colours measured within each galaxy effective radius[3], the CMR slope gets significantly flatter. Although this is certainly true, it does not affect our conclusions that, as we will show, are not based on the 'absolute' value of the CMR slope but on their relative comparison. The analysis by Scodeggio (2001) also points out another important result, i.e. the fact that using an average gradient value to correct colour measurements is not appropriate since the scatter in the observed gradient values is comparable in magnitude with its mean value itself.

6.5 The truncation of the red sequence

If on one hand it is interesting to note that the colour of early type galaxies at high redshifts are in agreement with the predictions of simple passive evolution models, the most important result of our analysis is that the red sequence in the three clusters under analysis appears to be *truncated* at magnitudes corresponding approximatively to I= 23. A deficiency of low luminosity objects on the CMR is evident in all panels of Fig. 6.2. The paucity of red low–luminosity galaxies at high–z occurs at magnitudes well above our completeness limit and in all the clusters we have studied.

It is possible to quantify this effect deriving the 'luminosity function' (LF) of galaxies residing on and around the red sequence, i.e. the number of objects on and around the red sequence per magnitude bin. The numbers of *bona fide* cluster members within $\sim 3\sigma$ (the interval is shown in Fig. 6.2) from the best fit relation to the red sequence are presented as a function of galaxy magnitude in Fig. 6.4. In each panel the histograms represent the average obtained considering 100 Monte Carlo
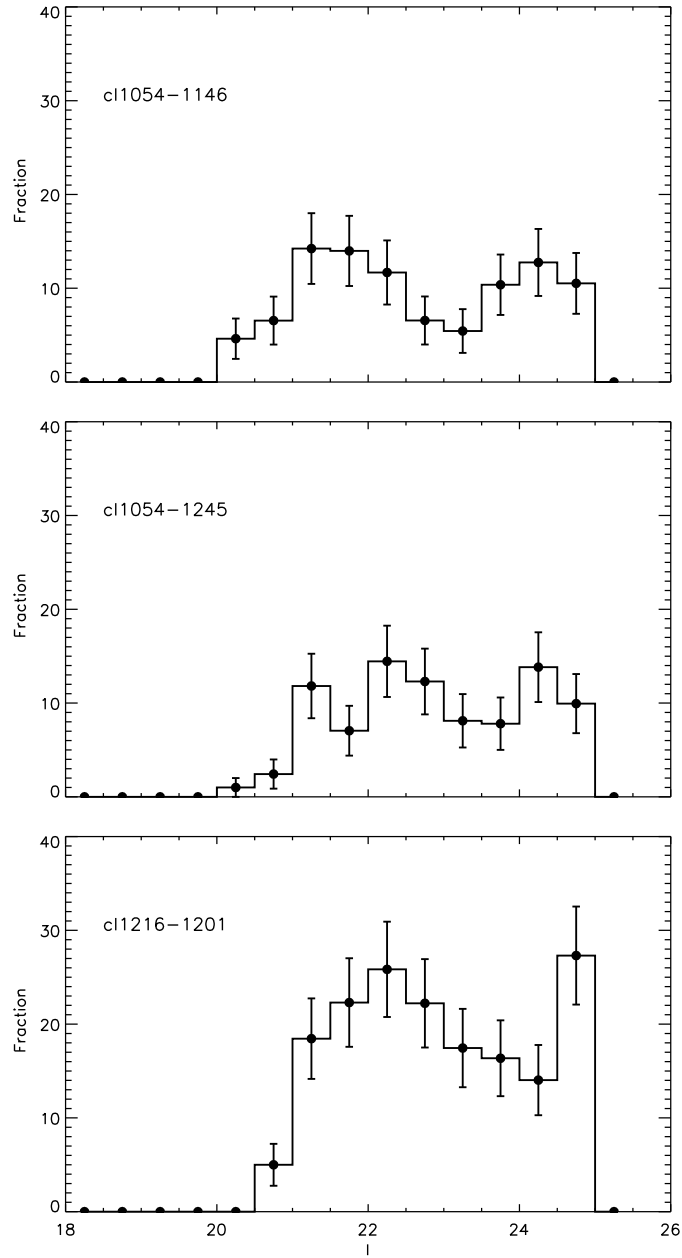
---

[3]The radius that contains half of the light.

Figure 6.4: LF of the objects on the red-sequence (see text for details) for the three clusters under investigation. Error bars represent Poisson error bars.

realizations of the statistical rejection. Error bars represent Poisson error bars. In all cases, the histograms show a 'deficiency' of red–sequence objects at a magnitude ~ 23. Note also that at even fainter magnitudes, the number of red–sequence objects seems to increase again. It is not clear if this effect is real, as the noise increases going to fainter magnitude and an accurate analysis of the magnitude completeness is necessary in order to assess the reality of this effect. The results presented are robust to the technique adopted for removing non–cluster members. In fact, the red galaxy deficit is detected also when rejecting non–members using a purely statistical subtraction or a more stringent criterion for membership based solely on photometric redshifts. Indeed, a deficit is evident also in the *full* photometric catalogue, when no field correction is attempted. This effect is present in each of the three EDisCS clusters, that have similar red galaxy luminosity functions despite of their variety in cluster velocity dispersion, richness, concentration, and presence of substructure (see Chapter 5).

How do these results compare to the number of passive systems in the Coma cluster?

Note that the full catalogue by Terlevich et al. is not corrected for contamination by non–members, so we cannot directly compare the number of objects on the CMR in Coma with the histograms shown in Fig. 6.4. The membership information is however available from spectroscopy for a large number of galaxies and it has been possible to correct the number of red galaxies in each magnitude bin for background and foreground contamination using a redshift catalogue kindly provided by Matthew Colless and the same procedure as in Mobasher et al. (2003), that we briefly summarise in the following.

We assume that the spectroscopic sample is representative, in the sense that the fraction of galaxies that are cluster members (which depends both on magnitude and on position) is the same in the spectroscopic as in the photometric sample. Let us indicate with $N_{\mathrm{c}}(m)$ and $N_{\mathrm{t}}(m)$ the number of cluster members (based on their redshifts) and the total number of galaxies in the spectroscopic sample in given ranges of magnitude. Then, the probability for a galaxy that is randomly selected from the spectroscopic sample to be a member of the Coma cluster can be written as:

$$P(m) = \frac{N_{\mathrm{c}}(m)}{N_{\mathrm{t}}(m)}$$

Counting the numbers of red–sequence objects in the same way done for the EDisCS clusters, and correcting for membership as explained above, we obtain the histogram shown in Fig. 6.5. This shows that the number of passive red galaxies in low redshift clusters tends to increase going to fainter magnitudes. This is in agreement with the luminosity function of early (passive) spectral types in clusters in the 2dF Galaxy Redshift Survey (De Propris et al. 2003a).
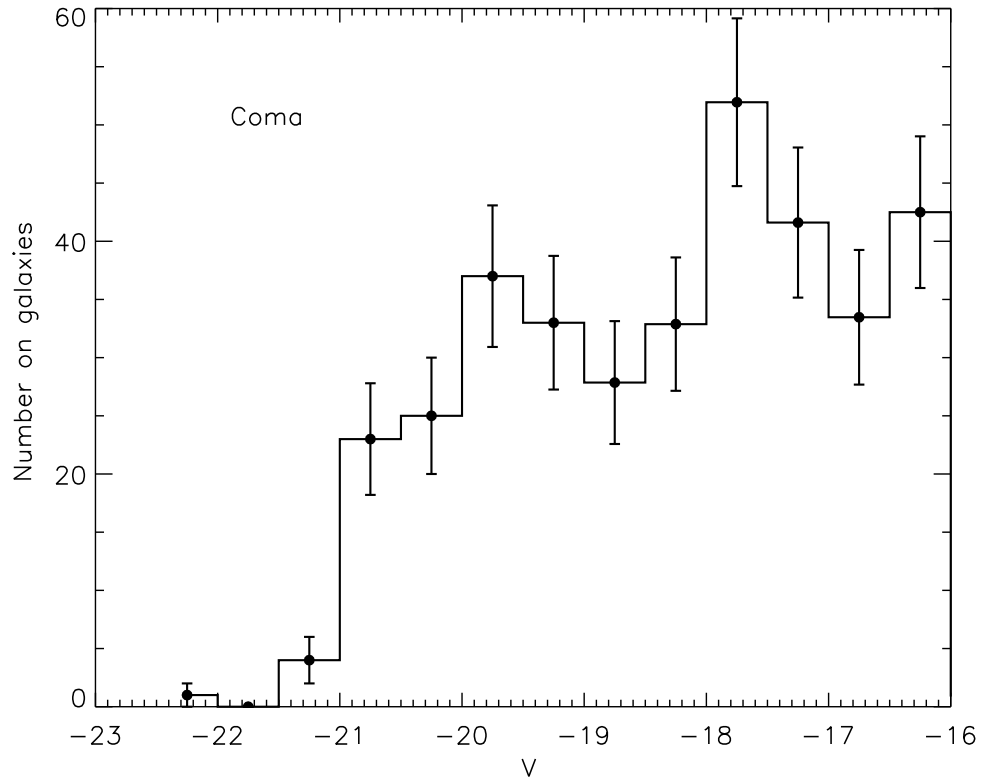
Figure 6.5: As in Fig. 6.4 but for the Coma cluster. Membership has been assigned using a procedure similar to the one adopted by Mobasher et al. (2003) (see text for details) and a redshift catalogue kindly provided by Matthew Colless.

In order to quantify the deficit of low–luminosity red–sequence galaxies in the high redshift clusters, we combine the histograms obtained for the EDisCS clusters after correcting colours and magnitudes to a common redshift = 0.75. The corrections are applied to the clusters cl1054–1146 and cl1216–1201 and are obtained using the single burst model with redshift of formation equal 3 that, as shown in Fig. 6.2, reproduces remarkably well the observed colour–magnitude sequence in these two clusters. Note that the model does not reproduce correctly the red–sequence colour of the cluster cl1054–1245. As we have mentioned before, it is likely that there is a zero–point offset in the colour of this cluster. As we are currently investigating the problem, for the moment we concentrate our attention on the clusters cl1054–1146 and cl1216–1201.

The results are shown in Fig. 6.6. Panel (a) shows the result obtained combining
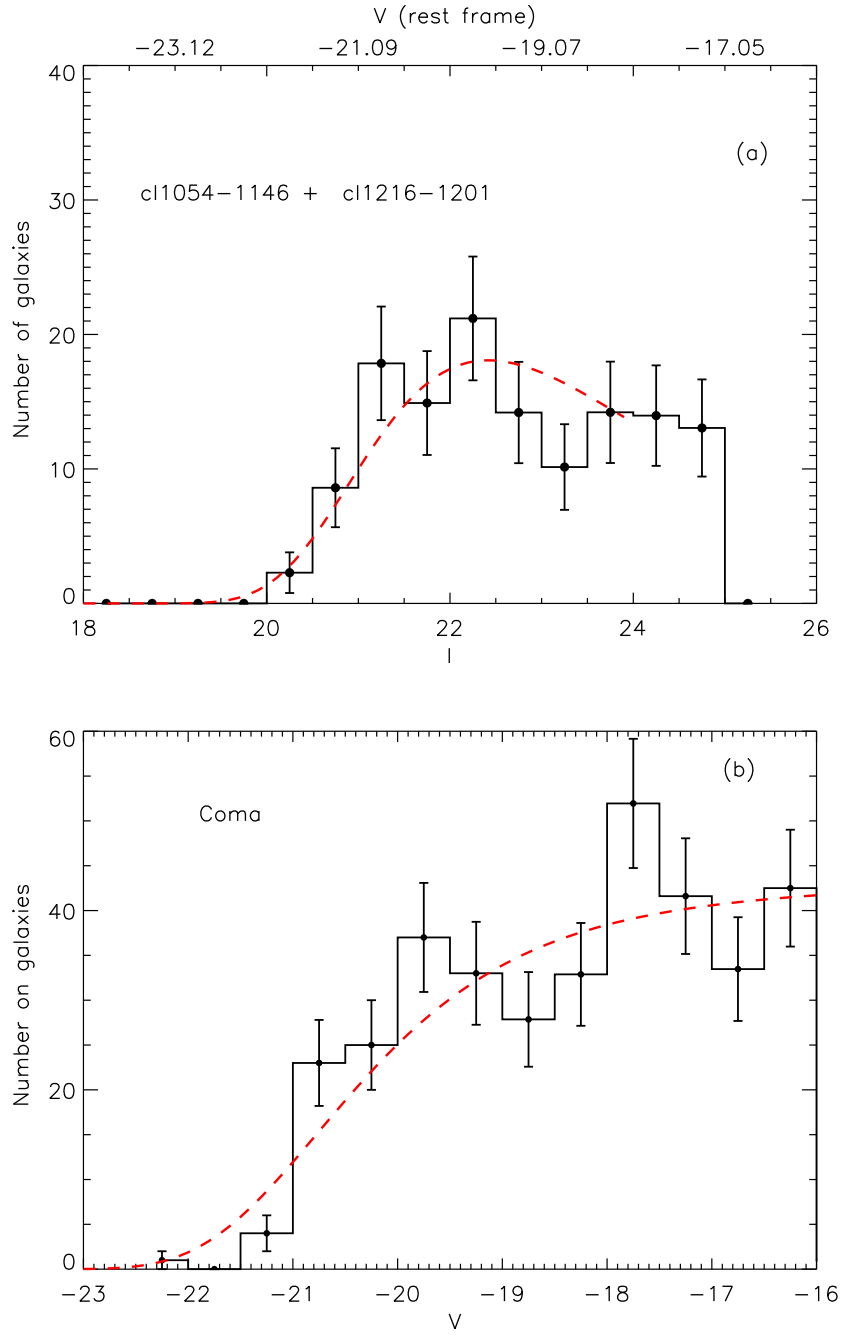
Figure 6.6: Number of red–sequence galaxies for a 'composite' cluster obtained using the data from cl1054–1146 and cl1216–1201 (see text for details) and the Coma cluster. The red dashed lines represent Schechter fits to the histograms. Error bars are Poisson error bars.

the two EDisCS clusters together, while panel (b) shows again, for comparison, the result obtained for the Coma cluster. In both panels, the red dashed line represents a Schechter fit to the histograms. This fit yields a faint–end slope of -0.82 for the composite EDisCS cluster and -1 for Coma. Note that the error bars are quite large and therefore the results of the fit are just indicative.

The scale on the top of panel (a) shows the rest–frame V–magnitude corresponding to the observed I–band magnitudes. The conversion is obtained again using the single burst model at redshift 0.75, and properly correcting for the passive luminosity evolution predicted by this model.

If we arbitrarily classify as 'luminous' galaxies those brighter than -19.5 in the rest–frame V–band (this corresponds to an observed I–band magnitude of 22.57 at redshift 0.75), and as 'faint' galaxies those fainter than this magnitude and brighter than -17 (this corresponds to the limit magnitude for our high redshift clusters), we obtain a luminous–to–faint ratio for the Coma cluster:

$$\text{Ratio} = \frac{N_{\text{lum}}}{N_{\text{faint}}} = 0.48 \pm 0.06$$

where the error has been estimated assuming Poisson statistics, i.e.

$$\frac{\Delta \text{Ratio}}{\text{Ratio}} = \left[\frac{1}{N_{\text{lum}}} + \frac{1}{N_{\text{faint}}} \right]^{1/2}$$

The corresponding value of the luminous–to–faint ratio for the composite EDisCS cluster is equal to 0.99 ± 0.17. This ratio is then different between the composite high redshift cluster and the Coma cluster at 3σ level.

6.6 Discussion and Conclusions

In this chapter we have analysed the colour–magnitude relation for three high redshift clusters spanning the redshift range 0.7–0.8. Our analysis shows that the high redshift clusters exhibit a clear *deficit* of low–luminosity red–sequence galaxies. The results are robust both to the technique adopted for removing non–cluster members and to photometric errors. Photometric errors in the EDisCS catalogue are comparable to the errors on Terlevich data, therefore the differences observed in the distributions of Fig. 6.6 cannot be a spurious result arising from photometric errors. Only if the errors were larger for fainter galaxies and at high z, these might have been scattered out of the red sequence. As a further confirmation for this argument, we performed a series of Monte Carlo realizations (100) where each point in the Coma histogram was scattered around the CMR taking into account the typical error on the colour and the magnitude. The faint end slope was found not to vary significantly. The results of this test are shown in Fig. 6.7 where the red histogram represents the average of 100
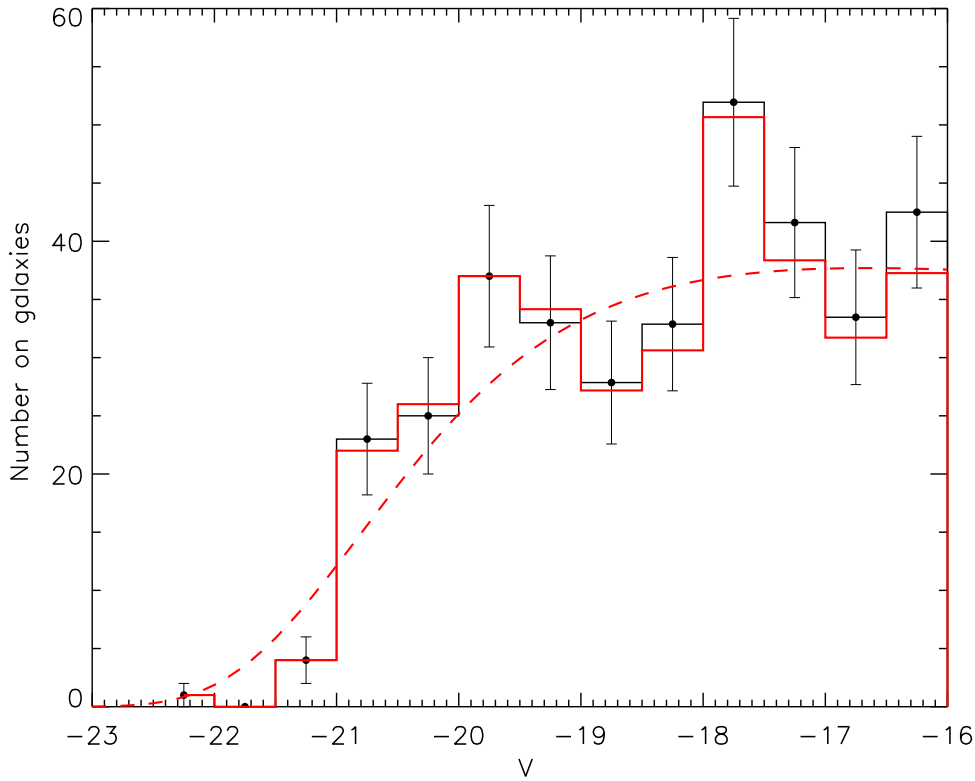
Figure 6.7: Number of red–sequence galaxies for the Coma clusters without considering the photometric errors (black histogram) and average of 100 Monte Carlo realizations obtained scattering each point in the photometric catalogue taking into account the error on both the magnitude and the colour (red histogram).

Monte Carlo realizations obtained scattering randomly the data in the photometric catalogue from Terlevich et al., taking into account both the magnitude and the colour photometric error. The faint–end slope of the fitted luminosity function varies from -1.00 to -0.99.

A decline in the number of red sequence members at magnitudes fainter than $0.1L_*$ was observed in clusters at $z = 0.25$ by Smail et al. (1998). The populations of blue galaxies observed in distant clusters are the logical progenitors for a significant fraction of the faint red galaxies at $z = 0$ (Smail et al. 1998; Kodama & Bower 2001; De Propris et al. 2003b). Evidence for a 'truncation' of the colour–magnitude sequence has been noted in a cluster at $z = 1.2$ by Kajisawa et al. (2000) and

Nakata et al. (2001), who suggested that faint early–type galaxies might not have been in place until $z \sim 1.2$. The colour–magnitude diagrams of EDisCS clusters at $z \sim 0.8$ show that a deficit of relatively faint red galaxies appears to be a universal phenomenon in clusters at high redshift. Our investigation unambiguously shows that a large fraction of passive galaxies must have moved onto the CMR at redshifts lower than 0.8, most likely as a result of the halting of the star formation activity in previously star forming galaxies. Note that our finding is not in contradiction with the observation of a tight CMR at low redshift, that extends over a large range of magnitudes. In fact, if the evolution of the blue systems is passive after they enter the hostile cluster environment, the younger (and bluer) galaxies will evolve faster that the more luminous (and redder) ones, producing a tight CMR with a small scatter at low redshift (Smail et al. 1998; Kodama & Bower 2001).

Note that the deficiency of red–sequence galaxies and its dependence on the galaxy luminosity can provide strong constraints on the possible evolutionary paths followed by the galaxy populations in clusters. The observed evolution in the shape of the luminosity function of red galaxies indicates that the evolution from blue to red since $z = 0.8$ has involved a higher number of faint than bright galaxies. In fact, if the cluster environment suppresses the star formation of infalling galaxies, these will both redden and fade. The 'morphology' of the CMRs in clusters at high redshift and, in particular, the number of bright blue galaxies, suggest that this mechanism preferentially populates the faint–end of the red sequence, although there are some bright galaxies that may end up among the most luminous ellipticals. The above argument, however, ignores the occurrence of mergers, that are shown to be an effective mechanism to form systems whose morphology well resemble that of early type galaxies.

Our results rule out a single formation scenario in which all red galaxies in clusters have evolved passively after a monolithic collapse at $z \gtrsim 2$–3, indicating that passive galaxies observed in clusters today follow different evolutionary paths, depending on their luminosity. Note that our results are in qualitatively good agreement with the predictions of hierarchical models. In these models, it is assumed that when a galaxy is accreted onto a more massive structure, the gas supply can no longer be replenished by cooling that is suppressed. After the accretion event then, the galaxy evolves passively. Note also that mergers are suppressed because of the large velocity dispersion of the system (see Chapter 2) and that the merger histories in hierarchical models are not 'random', with a tendency for large galaxies to form from mergers of massive galaxies (Kauffmann & Charlot 1998). It has been shown that these merger histories can preserve a tight colour–magnitude relation up to redshift ~ 1 (Bower et al. 1998).

Our analysis highlights the importance of studying the evolution of the cluster population as a whole, trying to understand how galaxies are accreted from the field, how the dense environment of the cluster affects their star formation rate, and

how these galaxies fade and evolve onto the red sequence. An analysis of this kind may help to unveil the evolutionary paths of galaxies that lie on the red–sequence today and place strong constraints on the relative importance of star formation and metallicity in establishing the the observed red–sequence. In future, we plan to investigate these questions in more detail.

*– Yo aquí me despido, vuelvo a mi casa, en mis
sueños, vuelvo a la Patagonia en donde el viento
golpea los establos y salpica hielo el Océano. [. . .]
Yo no vengo a resolver nada. Yo vine aquí para
cantar y para que cantes conmigo.*

Pablo Neruda, Canto General

7

Concluding remarks

Abstract
In each of the previous chapters, I have provided a summary and a discussion of
the corresponding findings. In this chapter, I will briefly reiterate some of the
main results of the analysis presented in this thesis, and try to put them into
perspective of future works and developments.

7.1 Results

In this thesis I have studied a number of aspects related to the formation and the
evolution of galaxies in clusters, both from a theoretical and an observational point of
view. I have made large use of high–resolution numerical simulations of the structure
formation in a cold dark matter (CDM) Universe. This theoretical model currently
provides the most successful description of structure formation both on galactic and
on cluster scales. In particular, the CDM model with the 'concordance' set of cos-
mological parameters (ΛCDM) has been so successful that it can now be considered
the 'standard paradigm' for the formation of structure in the Universe. According to
this model, the dominant force that drives structure formation is gravity, and large
systems like galaxy clusters are formed via hierarchical merging of smaller structures.

In Chapter 2 of this thesis, I have used a large set of high–resolution numerical simu-
lations of clusters and a high–resolution simulation of a 'typical' region of the Universe
to analyse the properties of dark matter substructures in haloes of different mass,
and the evolution of the substructure population as a function of redshift. I have
investigated the spatial and mass distribution of dark matter substructures, as well

as their mass and accretion history. In agreement with previous work (Moore et al. 1999a), I find that the shape of the subhalo mass function is almost independent of the mass of the parent halo. Galactic haloes are 'scaled' versions of cluster haloes. The results are robust with respect to numerical resolution, but the halo–to–halo scatter in the simulation set is quite large, thus leaving still room for weak trends with the mass of the parent halo.

Substructures undergo substantial tidal stripping in the dense inner regions of haloes. As a consequence, the radial profile of substructure number density is 'anti-biased' relative to the dark matter profile in the inner regions of haloes. I have investigated in detail the effect of tidal stripping and have shown that, once a sub-halo is accreted by a larger system, tidal stripping is highly effective. The longer a substructure spends in a more massive halo, the larger is the destructive effect. This suggests that substructures are constantly erased in clusters, and are replenished by newly infalling haloes.

One important result of this analysis is the discovery that a significant fraction of the substructures found in present-day clusters, were first accreted at redshifts $z < 1$, implying that tidal truncation of the dark haloes of cluster galaxies happened relatively recently. At $z > 1$, many present-day 'passive' cluster members should still have been central galaxies of their own extended dark haloes. If gas was able to cool in these haloes, these galaxies may have been considerably more active at $z \sim 1$ than at present. Substructures in smaller haloes have histories remarkably similar to those in cluster haloes, suggesting that the efficiency of tidal stripping is largely independent of the mass of the main halo.

In Chapter 3 of this thesis, I have coupled the dark matter numerical simulations with a semi–analytic technique that follows the photometric and chemical enrichment of cluster galaxies in a self–consistent way. The code also follows the chemical enrichment history of the intra–cluster and intergalactic medium.

I have experimented with a number of physically and observationally motivated prescriptions for the feedback process, and I have looked for observational signatures that permit to discriminate between different models. I have shown that, regardless of the adopted prescription, it is possible to adjust the model parameters in order to obtain reasonably good agreement between the model predictions and observational results at low redshift. I have compared model predictions with a number of observational results for galaxies in clusters. The model is successful in reproducing the cluster luminosity function, the slope and zero–point of the Tully–Fisher relation, and a metallicity–mass relation that is in striking agreement with the latest observational results from the SDSS. The good agreement between models and the observational results suggests that my model provides a reasonable description of the circulation of metals between the different baryonic components in the Universe.

In Chapter 4 of this thesis, I have investigated the star formation histories of cluster and field galaxies and I have shown that the hierarchical scenario predicts a quite

strong dependence of these on environment. In agreement with observational data, I find that elliptical galaxies are composed of an old stellar population with most of the stars formed at redshifts larger than 2–3. In my model, the star formation efficiency is higher in massive galaxies, naturally predicting older ages for brighter ellipticals.

I have also investigated the chemical enrichment history of the intra–cluster and intergalactic gas. In particular, I have analysed when the metals in the intra–cluster gas were ejected and which galaxies were mainly responsible for this chemical pollution. I find that the chemical enrichment of the ICM occurs at high redshift: 60–80 per cent of the metals are ejected into the ICM at redshifts larger than 1, 35–60 per cent at redshifts larger than 2 and 20–45 per cent at redshifts larger than 3. About half of the metals are ejected by galaxies with baryonic masses less than $1 \times 10^{10} \, h^{-1} \mathrm{M}_\odot$.

I find that the observed dependence of the baryon fraction on halo virial mass places strong constraints on how exactly galaxies ejected their metals. My results suggest that gas and its associated metals must be ejected very efficiently from galaxies and their associated dark matter haloes. Once the material leaves the halo, it must remain in the diffuse intergalactic medium for a time that is comparable to the age of the Universe. Future studies of the evolution of the metallicity of the intergalactic medium should also be able to clarify the mechanisms by which ejected material is mixed into the environment of galaxies.

In Chapter 5 of this thesis, I have analysed in detail the internal dynamics and the structure of five clusters drawn from the ESO Distant Cluster Survey. I have developed a new method for quantifying the observed amount of substructure in clusters. This method couples the information on the spatial distribution of cluster galaxies projected on the plane of the sky with the information on their velocity distribution. The analysis of the observed sample is complemented by an accurate comparison with a large set of high–resolution numerical simulations. I have built *mock catalogues* from the simulations using selection criteria that resemble as closely as possible the criteria that were used to build the observed sample.

My investigation shows that the amount of substructure found in the simulated clusters is comparable to that found in the observed clusters. The interpretation is, however, complicated by the fact that different selection criteria have been used for the observed and the simulated samples: the simulated clusters are constrained to produce massive virialized systems at redshift zero, while the observed clusters have been selected as virialized systems at redshift ~ 0.5 and ~ 0.8, the epoch when they are observed.

A definitive conclusion is also hampered by the small number of clusters in the observed sample analysed here.

Finally, in Chapter 6 of this thesis I have presented an analysis of the colour–magnitude diagram of a subset of the EDisCS clusters at $z \sim 0.8$. By comparing the results obtained for high redshift clusters with observational data in the Coma cluster, I have shown that high redshift clusters exhibit a deficit of faint red galaxies.

My investigation shows that a large fraction of faint passive galaxies in clusters today must have moved onto the CMR at redshifts lower than 0.8, most likely as a result of the halting of star formation activity in previously star forming galaxies.

My results rule out a single formation scenario in which all red galaxies in clusters have evolved passively after a monolithic collapse at $z \gtrsim 2$–3, indicating that passive galaxies observed in clusters today follow different evolutionary paths, depending on their luminosity. The results are in qualitative agreement with the predictions of hierarchical models. In these models it is assumed that when a galaxy is accreted onto a more massive structure, the gas supply can no longer be replenished by cooling that is suppressed. After the accretion event then, the galaxy evolves passively.

7.2 Future prospects

There are a number of logical extensions of the analysis presented in this thesis. The semi–analytic technique I have developed as a part of this thesis has provided a remarkable agreement with a large body of observational data for galaxies in nearby clusters. I have shown that a good understanding of how the self–regulation between star formation and feedback process works, is necessary to understand the observable properties of cluster galaxies. Observations of the chemical abundance in the intra–cluster and intergalactic medium and of how these evolve as a function of redshift can, in particular, provide important constraints on the mechanisms by which material is ejected and mixed into the environment of galaxies. I plan to further improve the model by taking into account time–dependent yields and by explicitly following the evolution of different elements. This will allow me to address a number of questions related to abundance ratios. In particular I will be able to directly study abundance ratios in the intra–cluster and intergalactic medium. In my model, the star formation is more efficient in large systems, naturally producing a trend towards older ages for more luminous systems. This is contrary to what was predicted before and subsequently cited as a strong failure of the hierarchical scenario (Thomas 1999). However, the results by Thomas were not based on a self–consistent approach (he used the star formation histories predicted by semi–analytic models, but he did not treat the chemical evolution in a consistent way). Only by using the self–consistent approach outlined here, is it possible to accurately compare the data to model predictions.

In Chapter 5 of this thesis I developed a new method to quantify the amount of substructure in clusters by taking into account simultaneously the spatial distribution of galaxies projected on the plane of the sky and their velocity distribution. I have also shown that the state–of–art numerical simulations allow one to carry out a fair and accurate comparison with observed data. As mentioned in the previous section, a definitive conclusion on these results is hampered by the small number of clusters in

the observed sample analysed here and also by the fact that different selection criteria have been used to build the observed and the simulated samples. The simulated clusters correspond to large virialized systems at redshift zero and simulations show that these systems assemble at relatively low redshifts from the mergers of big lumps at large distances. In contrast, the observed sample has been built by selecting large massive systems at high redshift. The simulated sample, therefore, is not *ideal* for this analysis, although the extension to the whole EDisCS dataset could actually improve the match. Ideally, we should use a large cosmological simulation to select a number of massive haloes at epochs corresponding to the redshifts of the observed clusters, and with masses corresponding to those of the observed systems.

The complete EDisCS dataset will provide a large number of clusters at a significant fraction of cosmic time. It will then be possible to carry out an accurate comparison with the large sample of clusters available in the low redshift Universe, and to investigate the effect of substructure on a number of different galaxy properties, such as colour, luminosity, and star formation rate. This kind of comparison will provide important constraints on the evolution of cluster structure as a function of redshift, as well as on the relative importance of different physical mechanisms that drive galaxy evolution in clusters.

Another important result of this thesis is the discovery that high redshift clusters exhibit a deficit of low luminosity red–sequence galaxies. This is in qualitative agreement with the predictions of hierarchical models and rules out a single formation scenario in which all red galaxies in clusters have evolved passively after a monolithic collapse at $z \gtrsim 2$–3. In future, I plan to investigate the constraints that these observations place on the models.

Cosmology has now entered its 'precision era'. Theoretical models that try to reproduce the ever more detailed observational picture of the Universe, will also require ever more complex modelling. Only through a close link between theoretical predictions and observational data, will it be possible to shed light on the physical processes governing galaxy formation and evolution in dense regions. This thesis has demonstrated the importance and the power of such an approach.

7 Concluding remarks

– Invenies aliquid amplium in silvis quam in libris. Ligna et lapides docebunt quod a magistris non audire possis.

St Bernard de Clairvaux

References

Aarseth, S. J., Turner, E. L., Gott, J. R. (1979), *N-body simulations of galaxy clustering. I - Initial conditions and galaxy collapse times*, ApJ, 228, 664

Abadi, M. G., Moore, B., Bower, R. G. (1999), *Ram pressure stripping of spiral galaxies in clusters*, MNRAS, 308, 947

Abell, G. O. (1958), *The Distribution of Rich Clusters of Galaxies.*, ApJS, 3, 211

Adami, C., Mazure, A., Biviano, A., Katgert, P., Rhee, G. (1998), *The ESO nearby Abell cluster survey. IV. The fundamental plane of clusters of galaxies*, A&A, 331, 493

Aguirre, A., Hernquist, L., Schaye, J., Weinberg, D. H., Katz, N., Gardner, J. (2001), *Metal Enrichment of the Intergalactic Medium at z=3 by Galactic Winds*, ApJ, 560, 599

Andreon, S. (2003), *Homogeneity of early-type galaxies across clusters*, A&A, 409, 37

Andreon, S., Ettori, S. (1999), *Is the Butcher-Oemler Effect a Function of the Cluster Redshift?*, ApJ, 516, 647

Aragon-Salamanca, A., Ellis, R. S., Couch, W. J., Carter, D. (1993), *Evidence for systematic evolution in the properties of galaxies in distant clusters*, MNRAS, 262, 764

Arimoto, N., Yoshii, Y. (1987), *Chemical and photometric properties of a galactic wind model for elliptical galaxies*, A&A, 173, 23

Athreya, R. M., Mellier, Y., van Waerbeke, L., Pelló, R., Fort, B., Dantel-Fort, M. (2002), *Weak lensing analysis of MS 1008-1224 with the VLT*, A&A, 384, 743

Böhringer, H., Schuecker, P., Guzzo, L., Collins, C. A., Voges, W., Schindler, S., Neumann, D. M., Cruddace, R. G., De Grandi, S., Chincarini, G., Edge, A. C., MacGillivray, H. T., Shaver, P. (2001), *The ROSAT-ESO flux limited X-ray (REFLEX) galaxy cluster survey. I. The construction of the cluster sample*, A&A, 369, 826

References

Böhringer, H., Voges, W., Huchra, J. P., McLean, B., Giacconi, R., Rosati, P., Burg, R., Mader, J., Schuecker, P., Simiç, D., Komossa, S., Reiprich, T. H., Retzlaff, J., Trümper, J. (2000), *The Northern ROSAT All-Sky (NORAS) Galaxy Cluster Survey. I. X-Ray Properties of Clusters Detected as Extended X-Ray Sources*, ApJS, 129, 435

Balogh, M., Bower, R. G., Smail, I., Ziegler, B. L., Davies, R. L., Gaztelu, A., Fritz, A. (2002), *Galaxy properties in low X-ray luminosity clusters at z=0.25*, MNRAS, 337, 256

Balogh, M. L., Navarro, J. F., Morris, S. L. (2000), *The Origin of Star Formation Gradients in Rich Galaxy Clusters*, ApJ, 540, 113

Bardeen, J. M., Bond, J. R., Kaiser, N., Szalay, A. S. (1986), *The statistics of peaks of Gaussian random fields*, ApJ, 304, 15

Barnes, J., Efstathiou, G. (1987), *Angular momentum from tidal torques*, ApJ, 319, 575

Barnes, J. E. (1992), *Transformations of galaxies. I - Mergers of equal-mass stellar disks*, ApJ, 393, 484

Barnes, J. E. (1999), *Galaxy Interactions*, in *ASP Conf. Ser. 182, Galaxy Dynamics - A Rutgers Symposium*, 463

Barrientos, F., Gladders, M., Yee, H., Ellingson, E., Hall, P., Infante, L. (2003), *The Red-Sequence Cluster Survey*, The Messenger, 112, 40

Bartelmann, M. (1996), *Arcs from a universal dark-matter halo profile.*, A&A, 313, 697

Baugh, C. M., Cole, S., Frenk, C. S. (1996), *Evolution of the Hubble sequence in hierarchical models for galaxy formation*, MNRAS, 283, 1361

Bautz, L. P., Morgan, W. W. (1970), *On the Classification of the Forms of Clusters of Galaxies*, ApJ, 162, L149

Beers, T. C., Flynn, K., Gebhardt, K. (1990), *Measures of location and scale for velocities in clusters of galaxies - A robust approach*, AJ, 100, 32

Bell, E. F., Wolf, C., Meisenheimer, K., Rix, H., Borch, A., Dye, S., Kleinheinrich, M., McIntosh, D. H. (2003), *Over 5000 Distant Early-Type Galaxies in COMBO-17: a Red Sequence and its Evolution since z ∼ 1*, preprint, astro-ph/0303394

194

Benson, A. J., Baugh, C. M., Cole, S., Frenk, C. S., Lacey, C. G. (2000a), *The dependence of velocity and clustering statistics on galaxy properties*, MNRAS, 316, 107

Benson, A. J., Bower, R. G., Frenk, C. S., White, S. D. M. (2000b), *Diffuse X-ray emission from late-type galaxy haloes*, MNRAS, 314, 557

Benson, A. J., Frenk, C. S., Baugh, C. M., Cole, S., Lacey, C. G. (2001), *The clustering evolution of the galaxy distribution*, MNRAS, 327, 1041

Benson, A. J., Frenk, C. S., Lacey, C. G., Baugh, C. M., Cole, S. (2002), *The effects of photoionization on galaxy formation - II. Satellite galaxies in the Local Group*, MNRAS, 333, 177

Bertin, E., Arnouts, S. (1996), *SExtractor: Software for source extraction.*, A&AS, 117, 393

Binney, J., Tremaine, S. (1987), *Galactic dynamics*, Princeton, NJ, Princeton University Press, 1987

Biviano, A. (2000), *From Messier to Abell: 200 Years of Science with Galaxy Clusters*, in *Constructing the Universe with Clusters of Galaxies*

Biviano, A., Katgert, P., Thomas, T., Adami, C. (2002), *The ESO Nearby Abell Cluster Survey. XI. Segregation of cluster galaxies and subclustering*, A&A, 387, 8

Boissier, S., Boselli, A., Prantzos, N., Gavazzi, G. (2001), *Chemo-spectrophotometric evolution of spiral galaxies - IV. Star formation efficiency and effective ages of spirals*, MNRAS, 321, 733

Bolzonella, M., Miralles, J.-M., Pelló, R. (2000), *Photometric redshifts based on standard SED fitting procedures*, A&A, 363, 476

Bond, J. R., Cole, S., Efstathiou, G., Kaiser, N. (1991), *Excursion set mass functions for hierarchical Gaussian fluctuations*, ApJ, 379, 440

Bower, R. G. (1991), *The evolution of groups of galaxies in the Press-Schechter formalism*, MNRAS, 248, 332

Bower, R. G., Balogh, M. L. (2003), *The Difference Between Clusters and Groups: A Journey from Cluster Cores to their Outskirts and Beyond*, preprint, astro-ph/0306342

Bower, R. G., Ellis, R. S., Rose, J. A., Sharples, R. M. (1990), *The stellar populations of early-type galaxies as a function of their environment*, AJ, 99, 530

References

Bower, R. G., Kodama, T., Terlevich, A. (1998), *The colour-magnitude relation as a constraint on the formation of rich cluster galaxies*, MNRAS, 299, 1193

Bower, R. G., Lucey, J. R., Ellis, R. S. (1992), *Precision photometry of early-type galaxies in the Coma and Virgo clusters: A test of the universality of the colour-magnitude relation. I - The data. II. Analysis*, MNRAS, 254, 589

Brunner, R. J., Lubin, L. M. (2000), *A Probabilistic Quantification of Galaxy Cluster Membership*, AJ, 120, 2851

Bruzual , G., Charlot, S. (1993), *Spectral evolution of stellar populations using isochrone synthesis*, ApJ, 405, 538

Bruzual, G., Charlot, S. (2003), *Stellar population synthesis at the resolution of 2003*, MNRAS, 344, 1000

Bullock, J. S., Kravtsov, A. V., Weinberg, D. H. (2000), *Reionization and the Abundance of Galactic Satellites*, ApJ, 539, 517

Buote, D. A., Tsai, J. C. (1996), *Quantifying the Morphologies and Dynamical Evolution of Galaxy Clusters. II. Application to a Sample of ROSAT Clusters*, ApJ, 458, 27

Butcher, H., Oemler, A. (1978), *The evolution of galaxies in clusters. I–ISIT photometry of C10024+1654 and 3C295*, ApJ, 219, 18

Butcher, H., Oemler, A. (1984), *The evolution of galaxies in clusters. V - A study of populations since z approximately equal to 0.5*, ApJ, 285, 426

Cardelli, J. A., Clayton, G. C., Mathis, J. S. (1989), *The relationship between infrared, optical, and ultraviolet extinction*, ApJ, 345, 245

Carlberg, R. G., Yee, H. K. C., Ellingson, E., Abraham, R., Gravel, P., Morris, S., Pritchet, C. J. (1996), *Galaxy Cluster Virial Masses and Omega*, ApJ, 462, 32

Carlstrom, J. E. (2002), *Cosmology with the Sunyaev-Zel'dovich Effect*, APS Meeting Abstracts

Cavaliere, A., Menci, N., Tozzi, P. (1998), *Diffuse Baryons in Groups and Clusters of Galaxies*, ApJ, 501, 493

Charlot, S., Worthey, G., Bressan, A. (1996), *Uncertainties in the Modeling of Old Stellar Populations*, ApJ, 457, 625

Chiba, M. (2002), *Probing Dark Matter Substructure in Lens Galaxies*, ApJ, 565, 17

Chiosi, C., Bressan, A., Portinari, L., Tantalo, R. (1998), *A new scenario of galaxy evolution under a universal Initial Mass Function*, A&A, 339, 355

Cole, S. (1991), *Modeling galaxy formation in evolving dark matter halos*, ApJ, 367, 45

Cole, S., Lacey, C. (1996), *The structure of dark matter haloes in hierarchical clustering models*, MNRAS, 281, 716

Cole, S., Lacey, C. G., Baugh, C. M., Frenk, C. S. (2000), *Hierarchical galaxy formation*, MNRAS, 319, 168

Coleman, G. D., Wu, C.-C., Weedman, D. W. (1980), *Colors and magnitudes predicted for high redshift galaxies*, ApJS, 43, 393

Colín, P., Avila-Reese, V., Valenzuela, O., Firmani, C. (2002), *Structure and Subhalo Population of Halos in a Self-interacting Dark Matter Cosmology*, ApJ, 581, 777

Courteau, S., Rix, H.-W. (1997), *Maximal Disks and the Tully-Fisher Relation*, Bulletin of the American Astronomical Society, 29, 1332

Cowie, L. L., Songaila, A. (1977), *Thermal evaporation of gas within galaxies by a hot intergalactic medium*, Nature, 266, 501

Dahlén, T., Fransson, C., Näslund, M. (2002), *The galaxy population of Cl1601+42 at z=0.54*, MNRAS, 330, 167

Dahle, H., Kaiser, N., Irgens, R. J., Lilje, P. B., Maddox, S. J. (2002), *Weak Gravitational Lensing by a Sample of X-Ray Luminous Clusters of Galaxies. I. The Data Set*, ApJS, 139, 313

Dahlem, M., Weaver, K. A., Heckman, T. M. (1998), *An X-Ray Minisurvey of Nearby Edge-on Starburst Galaxies. I. The Data*, ApJS, 118, 401

Dalal, N., Kochanek, C. S. (2002), *Direct Detection of Cold Dark Matter Substructure*, ApJ, 572, 25

Dalcanton, J. J. (1996), *A Proposal for Finding Clusters of Galaxies at $z \gtrsim 1$*, ApJ, 466, 92

David, L. P., Forman, W., Jones, C. (1991), *Enrichment and heating of the intracluster medium through galactic winds*, ApJ, 380, 39

David, L. P., Jones, C., Forman, W. (1995), *Cosmological implications of ROSAT observations of groups and clusters of galaxies*, ApJ, 445, 578

References

de Bernardis, P., Ade, P. A. R., Bock, J. J., Bond, J. R., Borrill, J., Boscaleri, A., Coble, K., Contaldi, C. R., Crill, B. P., De Troia, G., Farese, P., Ganga, K., Giacometti, M., Hivon, E., Hristov, V. V., Iacoangeli, A., Jaffe, A. H., Jones, W. C., Lange, A. E., Martinis, L., Masi, S., Mason, P., Mauskopf, P. D., Melchiorri, A., Montroy, T., Netterfield, C. B., Pascale, E., Piacentini, F., Pogosyan, D., Polenta, G., Pongetti, F., Prunet, S., Romeo, G., Ruhl, J. E., Scaramuzzi, F. (2002), *Multiple Peaks in the Angular Power Spectrum of the Cosmic Microwave Background: Significance and Consequences for Cosmology*, ApJ, 564, 559

De Grandi, S., Molendi, S. (2001), *Metallicity Gradients in X-Ray Clusters of Galaxies*, ApJ, 551, 153

De Lucia, G., Kauffmann, G., Springel, V., White, S. D. M., Lanzoni, B., Stoehr, F., Tormen, G., Yoshida, N. (2003a), *Substructures in Cold Dark Matter Haloes*, MNRAS in press, preprint astro-ph/0306205

De Lucia, G., Kauffmann, G., White, S. D. M. (2003b), *Chemical enrichment of the intracluster and intergalactic medium in a hierarchical galaxy formation model*, preprint, astro-ph/0310268

de Paolis, F., Ingrosso, G., Strafella, F. (1995), *Dark matter in X-ray-emitting elliptical galaxies*, ApJ, 438, 83

De Propris, R., Colless, M., Driver, S. P., Couch, W., Peacock, J. A., Baldry, I. K., Baugh, C. M., Bland-Hawthorn, J., Bridges, T., Cannon, R., Cole, S., Collins, C., Cross, N., Dalton, G. B., Efstathiou, G., Ellis, R. S., Frenk, C. S., Glazebrook, K., Hawkins, E., Jackson, C., Lahav, O., Lewis, I., Lumsden, S., Maddox, S., Madgwick, D. S., Norberg, P., Percival, W., Peterson, B., Sutherland, W., Taylor, K. (2003a), *The 2dF Galaxy Redshift Survey: the luminosity function of cluster galaxies*, MNRAS, 342, 725

De Propris, R., Stanford, S. A., Eisenhardt, P. R., Dickinson, M. (2003b), *The K-selected Butcher-Oemler Effect*, preprint, astro-ph/0307545

Diaferio, A., Kauffmann, G., Balogh, M. L., White, S. D. M., Schade, D., Ellingson, E. (2001), *The spatial and kinematic distributions of cluster galaxies in a ΛCDM universe: comparison with observations*, MNRAS, 323, 999

Dickinson, M. (1997), *Searches for High Redshift Clusters*, in *The Early Universe with the VLT*, 274

Dressler, A. (1980), *Galaxy morphology in rich clusters - Implications for the formation and evolution of galaxies*, ApJ, 236, 351

Dressler, A., Oemler, A. J., Couch, W. J., Smail, I., Ellis, R. S., Barger, A., Butcher, H., Poggianti, B. M., Sharples, R. M. (1997), *Evolution since z = 0.5 of the Morphology-Density Relation for Clusters of Galaxies*, ApJ, 490, 577

Dressler, A., Shectman, S. A. (1988), *Evidence for substructure in rich clusters of galaxies from radial-velocity measurements*, AJ, 95, 985

Dressler, A., Smail, I., Poggianti, B. M., Butcher, H., Couch, W. J., Ellis, R. S., Oemler, A. J. (1999), *A Spectroscopic Catalog of 10 Distant Rich Clusters of Galaxies*, ApJS, 122, 51

Driver, S. P., Couch, W. J., Phillipps, S., Smith, R. (1998), *Luminosity distributions within rich clusters - II. Demonstration and verification via simulation*, MNRAS, 301, 357

Edge, A. C., Stewart, G. C. (1991), *EXOSAT observations of clusters of galaxies. I - The X-ray data. II - X-ray to optical correlations*, MNRAS, 252, 414

Efstathiou, G. (1992), *Suppressing the formation of dwarf galaxies via photoionization*, MNRAS, 256, 43

Efstathiou, G. (2000), *A model of supernova feedback in galaxy formation*, MNRAS, 317, 697

Escalera, E., Biviano, A., Girardi, M., Giuricin, G., Mardirossian, F., Mazure, A., Mezzetti, M. (1994), *Structures in Galaxy Clusters*, ApJ, 423, 539

Ettori, S., Fabian, A. C., Allen, S. W., Johnstone, R. M. (2002), *Deep inside the core of Abell 1795: the Chandra view*, MNRAS, 331, 635

Evrard, A. E. (1997), *The intracluster gas fraction in X-ray clusters - Constraints on the clustered mass density*, MNRAS, 292, 289

Fairley, B. W., Jones, L. R., Wake, D. A., Collins, C. A., Burke, D. J., Nichol, R. C., Romer, A. K. (2002), *Galaxy colours in high-redshift, X-ray-selected clusters - I. Blue galaxy fractions in eight clusters*, MNRAS, 330, 755

Fall, S. M., Efstathiou, G. (1980), *Formation and rotation of disc galaxies with haloes*, MNRAS, 193, 189

Feretti, L. (2002), *Observational Properties of Diffuse Halos in Clusters*, in *IAU Symposium*, 133

Freeman, K. C. (1970), *On the Disks of Spiral and so Galaxies*, ApJ, 160, 811

References

Fukumoto, J., Ikeuchi, S. (1996), *Thermal and Chemical Evolution of X-Ray Clusters of Galaxies*, PASJ, 48, 1

Garnett, D. R. (2002), *The Luminosity-Metallicity Relation, Effective Yields, and Metal Loss in Spiral and Irregular Galaxies*, ApJ, 581, 1019

Gavazzi, G. (1993), *Colors, Luminosities, and Masses of Disk Galaxies*, ApJ, 419, 469

Geller, M. J., Beers, T. C. (1982), *Substructure within clusters of galaxies*, PASP, 94, 421

Ghigna, S., Moore, B., Governato, F., Lake, G., Quinn, T., Stadel, J. (1998), *Dark matter haloes within clusters*, MNRAS, 300, 146

Ghigna, S., Moore, B., Governato, F., Lake, G., Quinn, T., Stadel, J. (2000), *Density Profiles and Substructure of Dark Matter Halos: Converging Results at Ultra-High Numerical Resolution*, ApJ, 544, 616

Gibson, B. K., Loewenstein, M., Mushotzky, R. F. (1997), *Supernovae Types Ia/II and intracluster medium enrichment*, MNRAS, 290, 623

Gibson, B. K., Matteucci, F. (1997), *On Dwarf Galaxies as the Source of Intracluster Gas*, ApJ, 475, 47

Giovanelli, R., Haynes, M. P., da Costa, L. N., Freudling, W., Salzer, J. J., Wegner, G. (1997), *The Tully-Fisher Relation and H_0*, ApJ, 477, L1

Girardi, M., Borgani, S., Giuricin, G., Mardirossian, F., Mezzetti, M. (2000), *Optical Luminosities and Mass-to-Light Ratios of Nearby Galaxy Clusters*, ApJ, 530, 62

Girardi, M., Manzato, P., Mezzetti, M., Giuricin, G., Limboz, F. (2002), *Observational Mass-to-Light Ratio of Galaxy Systems from Poor Groups to Rich Clusters*, ApJ, 569, 720

Gladders, M. D., Lopez-Cruz, O., Yee, H. K. C., Kodama, T. (1998), *The Slope of the Cluster Elliptical Red Sequence: A Probe of Cluster Evolution*, ApJ, 501, 571

Gnedin, N. Y. (1998), *Metal enrichment of the intergalactic medium*, MNRAS, 294, 407

Gonzalez, A. H., Zaritsky, D., Dalcanton, J. J., Nelson, A. (2001), *The Las Campanas Distant Cluster Survey: The Catalog*, ApJS, 137, 117

Gonzalez, A. H., Zaritsky, D., Simard, L., Clowe, D., White, S. D. M. (2002), *Tests of the Las Campanas Distant Cluster Survey from Confirmation Observations for the ESO Distant Cluster Survey*, ApJ, 579, 577

Gottlöber, S., Klypin, A., Kravtsov, A. (1998), *Tracing Galaxies in High Resolution Cosmological N-body Simulations*, in *Evolution of Large-Scale Structure: From Recombination to Garching,* preprint, astro-ph/9810191

Grevesse, N., Noels, A., Sauval, A. J. (1996), *Standard Abundances*, in *ASP Conf. Ser. 99: Cosmic Abundances*, 117

Gunn, J. E., Gott, J. R. I. (1972), *On the Infall of Matter Into Clusters of Galaxies and Some Effects on Their Evolution*, ApJ, 176, 1

Gursky, H., Kellogg, E., Murray, S., Leong, C., Tananbaum, H., Giacconi, R. (1971), *A Strong X-Ray Source in the Coma Cluster Observed by UHURU*, ApJ, 167, L81

Guth, A. H. (1981), *Inflationary universe: A possible solution to the horizon and flatness problems*, Phys. Rev. D, 23, 347

Heckman, T. M. (2002), *Galactic Superwinds Circa 2001*, in *ASP Conf. Ser. 254: Extragalactic Gas at Low Redshift*, 292

Heckman, T. M., Dahlem, M., Lehnert, M. D., Fabbiano, G., Gilmore, D., Waller, W. H. (1995), *An X-Ray and Optical Study of the Dwarf Galaxy NGC 1569: Evidence for a Starburst-driven Outflow*, ApJ, 448, 98

Heckman, T. M., Lehnert, M. D., Strickland, D. K., Armus, L. (2000), *Absorption-Line Probes of Gas and Dust in Galactic Superwinds*, ApJS, 129, 493

Helly, J. C., Cole, S., Frenk, C. S., Baugh, C. M., Benson, A., Lacey, C., Pearce, F. R. (2003), *A comparison of gas dynamics in smooth particle hydrodynamics and semi-analytic models of galaxy formation*, MNRAS, 338, 913

Helmi, A., White, S. D., Springel, V. (2002), *The phase-space structure of a dark-matter halo: Implications for dark-matter direct detection experiments*, Phys. Rev. D, 66, 63502

Hernandez, X., Ferrara, A. (2001), *Cosmological origin of the lowest metallicity halo stars*, MNRAS, 324, 484

Herschel, W. (1785), *On the Construction of the Heavens*, Philosophical Transactions of the Royal Society of London, 75, 213

Hogg, D. W. (1999), *Distance measures in cosmology*, preprint, astro-ph/9905116

Hut, P., White, S. D. M. (1984), *Can a neutrino-dominated Universe be rejected?*, Nature, 310, 637

References

Jenkins, A., Frenk, C. S., White, S. D. M., Colberg, J. M., Cole, S., Evrard, A. E., Couchman, H. M. P., Yoshida, N. (2001), *The mass function of dark matter haloes*, MNRAS, 321, 372

Jimenez, R., Verde, L., Oh, S. P. (2003), *Dark halo properties from rotation curves*, MNRAS, 339, 243

Jones, C., Forman, W. (1999), *Einstein Observatory Images of Clusters of Galaxies*, ApJ, 511, 65

Kajisawa, M., Yamada, T., Tanaka, I., Maihara, T., Iwamuro, F., Terada, H., Goto, M., Motohara, K., Tanabe, H., Taguchi, T., Hata, R., Iye, M., Imanishi, M., Chikada, Y., Yoshida, M., Simpson, C., Sasaki, T., Kosugi, G., Usuda, T., Sekiguchi, K. (2000), *Color-Magnitude Sequence in the Clusters at $z \sim 1.2$ near the Radio Galaxy 3C 324*, PASJ, 52, 61

Katz, N., Hernquist, L., Weinberg, D. H. (1992), *Galaxies and gas in a cold dark matter universe*, ApJ, 399, L109

Katz, N., Hernquist, L., Weinberg, D. H. (1999), *The Clustering of High-Redshift Galaxies in the Cold Dark Matter Scenario*, ApJ, 523, 463

Katz, N., White, S. D. M. (1993), *Hierarchical galaxy formation - Overmerging and the formation of an X-ray cluster*, ApJ, 412, 455

Kauffmann, G. (1995a), *Hierarchical clustering and the Butcher-Oemler effect*, MNRAS, 274, 153

Kauffmann, G. (1995b), *The observed properties of high-redshift cluster galaxies*, MNRAS, 274, 161

Kauffmann, G., Charlot, S. (1998), *Chemical enrichment and the origin of the colour-magnitude relation of elliptical galaxies in a hierarchical merger model*, MNRAS, 294, 705

Kauffmann, G., Colberg, J. M., Diaferio, A., White, S. D. M. (1999), *Clustering of galaxies in a hierarchical universe - I. Methods and results at z=0*, MNRAS, 303, 188

Kauffmann, G., Haehnelt, M. (2000), *A unified model for the evolution of galaxies and quasars*, MNRAS, 311, 576

Kauffmann, G., Heckman, T. M., White, S. D. M., Charlot, S., Tremonti, C., Peng, E. W., Seibert, M., Brinkmann, J., Nichol, R. C., SubbaRao, M., York, D. (2003), *The dependence of star formation history and internal structure on stellar mass for 10^5 low-redshift galaxies*, MNRAS, 341, 54

Kauffmann, G., Nusser, A., Steinmetz, M. (1997), *Galaxy formation and large-scale bias*, MNRAS, 286, 795

Kauffmann, G., White, S. D. M., Guiderdoni, B. (1993), *The Formation and Evolution of Galaxies Within Merging Dark Matter Haloes*, MNRAS, 264, 201

Kennicutt, R. C. (1998), *The Global Schmidt Law in Star-forming Galaxies*, ApJ, 498, 541

Kent, S. M., Gunn, J. E. (1982), *The dynamics of rich clusters of galaxies. I - The Coma cluster*, AJ, 87, 945

Kinney, A. L., Calzetti, D., Bohlin, R. C., McQuade, K., Storchi-Bergmann, T., Schmitt, H. R. (1996), *Template Ultraviolet to Near-Infrared Spectra of Star-forming Galaxies and Their Application to K-Corrections*, ApJ, 467, 38

Klypin, A., Gottlöber, S., Kravtsov, A. V., Khokhlov, A. M. (1999a), *Galaxies in N-Body Simulations: Overcoming the Overmerging Problem*, ApJ, 516, 530

Klypin, A., Kravtsov, A. V., Valenzuela, O., Prada, F. (1999b), *Where Are the Missing Galactic Satellites?*, ApJ, 522, 82

Kodama, T., Arimoto, N., Barger, A. J., Arag'on-Salamanca, A. (1998), *Evolution of the colour-magnitude relation of early-type galaxies in distant clusters*, A&A, 334, 99

Kodama, T., Bell, E. F., Bower, R. G. (1999), *A Bayesian classifier for photometric redshifts: identification of high-redshift clusters*, MNRAS, 302, 152

Kodama, T., Bower, R. G. (2001), *Reconstructing the history of star formation in rich cluster cores*, MNRAS, 321, 18

Kodama, T., Smail, I., Nakata, F., Okamura, S., Bower, R. G. (2001), *The Transformation of Galaxies within the Large-Scale Structure around a z=0.41 Cluster*, ApJ, 562, L9

Kriessler, J. R., Beers, T. C. (1997), *Substructure in Galaxy Clusters:A Two Dimensional Approach*, AJ, 113, 80

Kroupa, P., Boily, C. M. (2002), *On the mass function of star clusters*, MNRAS, 336, 1188

Kuntz, K. D., Snowden, S. L., Pence, W. D., Mukai, K. (2003), *Diffuse X-Ray Emission from M101*, ApJ, 588, 264

References

Lacey, C., Cole, S. (1993), *Merger rates in hierarchical models of galaxy formation*, MNRAS, 262, 627

Lacey, C., Silk, J. (1991), *Tidally triggered galaxy formation. I - Evolution of the galaxy luminosity function*, ApJ, 381, 14

Lanzoni, B., Ciotti, L., Cappi, A., Tormen, G., Zamorani, G. (2003), *The scaling relations of galaxy clusters and their dark matter halos*, preprint, astro-ph/0307141

Larson, R. B. (1974), *Effects of supernovac on the early evolution of galaxies*, MNRAS, 169, 229

Larson, R. B. (1998), *Early star formation and the evolution of the stellar initial mass function in galaxies*, MNRAS, 301, 569

Larson, R. B., Dinerstein, H. L. (1975), *Gas loss in groups of galaxies*, PASP, 87, 911

Larson, R. B., Tinsley, B. M., Caldwell, C. N. (1980), *The evolution of disk galaxies and the origin of S0 galaxies*, ApJ, 237, 692

Lehnert, M. D., Heckman, T. M. (1996), *Ionized Gas in the Halos of Edge-on Starburst Galaxies: Evidence for Supernova-driven Superwinds*, ApJ, 462, 651

Lin, Y., Mohr, J. J., Stanford, S. A. (2003), *Near-Infrared Properties of Galaxy Clusters: Luminosity as a Binding Mass Predictor and the State of Cluster Baryons*, ApJ, 591, 749

Loewenstein, M. (2000), *Heating of Intergalactic Gas and Cluster Scaling Relations*, ApJ, 532, 17

Loveday, J. (1996), *The APM Bright Galaxy Catalogue*, MNRAS, 278, 1025

Lynden-Bell, D. (1967), *Statistical mechanics of violent relaxation in stellar systems*, MNRAS, 136, 101

Mac Low, M., Ferrara, A. (1999), *Starburst-driven Mass Loss from Dwarf Galaxies: Efficiency and Metal Ejection*, ApJ, 513, 142

Macfarland, T., Couchman, H. M. P., Pearce, F. R., Pichlmeier, J. (1998), *A new parallel P^3M code for very large-scale cosmological simulations*, New Astronomy, 3, 687

Mao, S., Schneider, P. (1998), *Evidence for substructure in lens galaxies?*, MNRAS, 295, 587

Marlowe, A. T., Heckman, T. M., Wyse, R. F. G., Schommer, R. (1995), *Observations of the impact of starbursts on the interstellar medium in dwarf galaxies*, ApJ, 438, 563

Marri, S., White, S. D. M. (2003), *Smoothed particle hydrodynamics for galaxy-formation simulations: improved treatments of multiphase gas, of star formation and of supernovae feedback*, MNRAS, 345, 561

Martin, C. L. (1996), *Kinematic Evidence for Superbubbles in I ZW 18: Constraints on the Star Formation History and Chemical Evolution*, ApJ, 465, 680

Martin, C. L. (1999), *Properties of Galactic Outflows: Measurements of the Feedback from Star Formation*, ApJ, 513, 156

Masset, F. S., Bureau, M. (2003), *On the Spiral Structure of NGC 2915 and Dark Matter*, ApJ, 586, 152

Massey, P. (1998), *The Initial Mass Function of Massive Stars in the Local Group*, in *ASP Conf. Ser. 142: The Stellar Initial Mass Function (38th Herstmonceux Conference)*, 17

Mathis, H., Lemson, G., Springel, V., Kauffmann, G., White, S. D. M., Eldar, A., Dekel, A. (2002), *Simulating the formation of the local galaxy population*, MNRAS, 333, 739

Matsushita, K., Makishima, K., Ikebe, Y., Rokutanda, E., Yamasaki, N., Ohashi, T. (1998), *Largely Extended X-Ray Emission Around the Elliptical Galaxy NGC 4636 Observed with ASCA*, ApJ, 499, L13

Matteucci, F., Gibson, B. K. (1995), *Chemical abundances in clusters of galaxies.*, A&A, 304, 11

Matteucci, F., Vettolani, G. (1988), *Chemical abundances in galaxy clusters - A theoretical approach*, A&A, 202, 21

McKee, C. F., Ostriker, J. P. (1977), *A theory of the interstellar medium - Three components regulated by supernova explosions in an inhomogeneous substrate*, ApJ, 218, 148

Meekins, J. F., Fritz, G., Henry, R. C., Chubb, T. A., Friedman, H. (1971), *Continuous and Pulsed X-ray Emission of the Crab Nebula*, BAAS, 3, 22

Mihos, C. (2003), *Interactions and Mergers of Cluster Galaxies*, preprint, astro-ph/0305512

References

Miller, R. H. (1983), *Numerical experiments on the clustering of galaxies*, ApJ, 270, 390

Mo, H. J., Mao, S., White, S. D. M. (1998), *The formation of galactic discs*, MNRAS, 295, 319

Mobasher, B., Colless, M., Carter, D., Poggianti, B. M., Bridges, T. J., Kranz, K., Komiyama, Y., Kashikawa, N., Yagi, M., Okamura, S. (2003), *A Photometric and Spectroscopic Study of Dwarf and Giant Galaxies in the Coma Cluster. IV. The Luminosity Function*, ApJ, 587, 605

Mohr, J. J., Evrard, A. E., Fabricant, D. G., Geller, M. J. (1995), *Cosmological Constraints from Observed Cluster X-Ray Morphologies*, ApJ, 447, 8

Moore, B. (2000), *Simulating Clusters of Galaxies: A Brief History of "N" and Over-merging*, in *Constructing the Universe with Clusters of Galaxies*

Moore, B., Ghigna, S., Governato, F., Lake, G., Quinn, T., Stadel, J., Tozzi, P. (1999a), *Dark Matter Substructure within Galactic Halos*, ApJ, 524, L19

Moore, B., Katz, N., Lake, G. (1996a), *On the Destruction and Overmerging of Dark Halos in Dissipationless N-Body Simulations*, ApJ, 457, 455

Moore, B., Katz, N., Lake, G., Dressler, A., Oemler, A. (1996b), *Galaxy harassment and the evolution of clusters of galaxies.*, Nature, 379, 613

Moore, B., Quinn, T., Governato, F., Stadel, J., Lake, G. (1999b), *Cold collapse and the core catastrophe*, MNRAS, 310, 1147

Moretti, A., Portinari, L., Chiosi, C. (2003), *Chemical evolution of the intra-cluster medium*, A&A, 408, 431

Mori, M., Burkert, A. (2000), *Gas Stripping of Dwarf Galaxies in Clusters of Galaxies*, ApJ, 538, 559

Moss, C., Whittle, M. (2000), *An Hα survey of eight Abell clusters: the dependence of tidally induced star formation on cluster density*, MNRAS, 317, 667

Mushotzky, R., Loewenstein, M., Arnaud, K. A., Tamura, T., Fukazawa, Y., Matsushita, K., Kikuchi, K., Hatsukade, I. (1996), *Measurement of the Elemental Abundances in Four Rich Clusters of Galaxies. I. Observations*, ApJ, 466, 686

Mushotzky, R. F., Loewenstein, M. (1997), *Lack of Evolution in the Iron Abundance in Clusters of Galaxies and Implications for the Global Star Formation Rate at High Redshift*, ApJ, 481, L63

206

Nakata, F., Kajisawa, M., Yamada, T., Kodama, T., Shimasaku, K., Tanaka, I., Doi, M., Furusawa, H., Hamabe, M., Iye, M., Kimura, M., Komiyama, Y., Miyazaki, S., Okamura, S., Ouchi, M., Sasaki, T., Sekiguchi, M., Yagi, M., Yasuda, N. (2001), *Galaxy Population in a Cluster of Galaxies around the Radio Galaxy 3C 324 at z=1.2*, PASJ, 53, 1139

Navarro, J. F., Frenk, C. S., White, S. D. M. (1995), *The assembly of galaxies in a hierarchically clustering universe*, MNRAS, 275, 56

Navarro, J. F., Frenk, C. S., White, S. D. M. (1997), *A Universal Density Profile from Hierarchical Clustering*, ApJ, 490, 493

Nulsen, P. E. J. (1982), *Transport processes and the stripping of cluster galaxies*, MNRAS, 198, 1007

Oemler, A. J. (1974), *The Systematic Properties of Clusters of Galaxies. Photometry of 15 Clusters*, ApJ, 194, 1

Padmanabhan, N., Seljak, U., Strauss, M. A., Blanton, M. R., Kauffmann, G., Schlegel, D. J., Tremonti, C., Bahcall, N. A., Bernardi, M., Brinkmann, J., Fukugita, M., Ivezic, Z. (2003), *Stellar and Dynamical Masses of Ellipticals in the Sloan Digital Sky Survey*, preprint, astro-ph/0307082

Padmanabhan, T. (1993), *Structure formation in the universe*, Cambridge University Press, 1993

Patton, D. R., Pritchet, C. J., Yee, H. K. C., Ellingson, E., Carlberg, R. G. (1997), *Close Pairs of Field Galaxies in the CNOC1 Redshift Survey*, ApJ, 475, 29

Peacock, J. A. (1999), *Cosmological physics*, Cambridge University Press, 1999

Peebles, P. J. E. (1993), *Principles of physical cosmology*, Princeton University Press, 1993

Peletier, R. F., Davies, R. L., Illingworth, G. D., Davis, L. E., Cawson, M. (1990a), *CCD surface photometry of galaxies with dynamical data. II - UBR photometry of 39 elliptical galaxies*, AJ, 100, 1091

Peletier, R. F., Valentijn, E. A., Jameson, R. F. (1990b), *Near-infrared photometry of bright elliptical galaxies*, A&A, 233, 62

Pen, U. (1999), *Heating of the Intergalactic Medium*, ApJ, 510, L1

Perlmutter, S., Aldering, G., Goldhaber, G., Knop, R. A., Nugent, P., Castro, P. G., Deustua, S., Fabbro, S., Goobar, A., Groom, D. E., Hook, I. M., Kim, A. G.,

References

Kim, M. Y., Lee, J. C., Nunes, N. J., Pain, R., Pennypacker, C. R., Quimby, R., Lidman, C., Ellis, R. S., Irwin, M., McMahon, R. G., Ruiz-Lapuente, P., Walton, N., Schaefer, B., Boyle, B. J., Filippenko, A. V., Matheson, T., Fruchter, A. S., Panagia, N., Newberg, H. J. M., Couch, W. J., The Supernova Cosmology Project (1999), *Measurements of Omega and Lambda from 42 High-Redshift Supernovae*, ApJ, 517, 565

Pettini, M., Shapley, A. E., Steidel, C. C., Cuby, J., Dickinson, M., Moorwood, A. F. M., Adelberger, K. L., Giavalisco, M. (2001), *The Rest-Frame Optical Spectra of Lyman Break Galaxies: Star Formation, Extinction, Abundances, and Kinematics*, ApJ, 554, 981

Pettini, M., Steidel, C. C., Adelberger, K. L., Dickinson, M., Giavalisco, M. (2000), *The Ultraviolet Spectrum of MS 1512-CB58: An Insight into Lyman-Break Galaxies*, ApJ, 528, 96

Pimbblet, K. A., Smail, I., Kodama, T., Couch, W. J., Edge, A. C., Zabludoff, A. I., O'Hely, E. (2002), *The Las Campanas/AAT Rich Cluster Survey - II. The environmental dependence of galaxy colours in clusters at z ∼ 0.1*, MNRAS, 331, 333

Pisani, A. (1993), *A Non-Parametric and Scale-Independent Method for Cluster Analysis - Part One - the Univariate Case*, MNRAS, 265, 706

Pisani, A. (1996), *A non-parametric and scale-independent method for cluster analysis - II. The multivariate case*, MNRAS, 278, 697

Poggianti, B. M. (1997), *K and evolutionary corrections from UV to IR*, A&AS, 122, 399

Poggianti, B. M. (2003), *Color, spectral and morphological transformations of galaxies in clusters*, Ap&SS, 285, 121

Poggianti, B. M., Bridges, T. J., Mobasher, B., Carter, D., Doi, M., Iye, M., Kashikawa, N., Komiyama, Y., Okamura, S., Sekiguchi, M., Shimasaku, K., Yagi, M., Yasuda, N. (2001), *A Photometric and Spectroscopic Study of Dwarf and Giant Galaxies in the Coma Cluster. III. Spectral Ages and Metallicities*, ApJ, 562, 689

Poggianti, B. M., Smail, I., Dressler, A., Couch, W. J., Barger, A. J., Butcher, H., Ellis, R. S., Oemler, A. J. (1999), *The Star Formation Histories of Galaxies in Distant Clusters*, ApJ, 518, 576

Postman, M. (2002), *Multi-wavelength Surveys for Distant Clusters (Invited Speaker)*, in *ASP Conf. Ser. 268: Tracing Cosmic Evolution with Galaxy Clusters*, 3

Postman, M., Lubin, L. M., Gunn, J. E., Oke, J. B., Hoessel, J. G., Schneider, D. P., Christensen, J. A. (1996), *The Palomar Distant Clusters Survey. I. The Cluster Catalog*, AJ, 111, 615

Power, C., Navarro, J. F., Jenkins, A., Frenk, C. S., White, S. D. M., Springel, V., Stadel, J., Quinn, T. (2003), *The inner structure of ΛCDM haloes - I. A numerical convergence study*, MNRAS, 338, 14

Press, W. H., Schechter, P. (1974), *Formation of Galaxies and Clusters of Galaxies by Self-Similar Gravitational Condensation*, ApJ, 187, 425

Press, W. H., Teukolsky, S. A., Vetterling, W. T., Flannery, B. P. (1992), *Numerical recipes in C. The art of scientific computing*, Cambridge: University Press

Quilis, V., Moore, B., Bower, R. (2000), *Gone with the Wind: The Origin of S0 Galaxies in Clusters*, Science, 288, 1617

Rees, M. J., Ostriker, J. P. (1977), *Cooling, dynamics and fragmentation of massive gas clouds - Clues to the masses and radii of galaxies and clusters*, MNRAS, 179, 541

Renzini, A. (1997), *Iron as a Tracer in Galaxy Clusters and Groups*, ApJ, 488, 35

Renzini, A., Ciotti, L., D'Ercole, A., Pellegrini, S. (1993), *Production and Circulation of Iron in Elliptical Galaxies and Clusters of Galaxies*, ApJ, 419, 52

Rhee, G. F. R. N., van Haarlem, M. P., Katgert, P. (1991), *Substructure in Abell clusters*, A&A, 246, 301

Richstone, D., Loeb, A., Turner, E. L. (1992), *A lower limit of the cosmic mean density from the ages of clusters of galaxies*, ApJ, 393, 477

Rocha-Pinto, H. J., Scalo, J., Maciel, W. J., Flynn, C. (2000a), *An Intermittent Star Formation History in a "Normal" Disk Galaxy: The Milky Way*, ApJ, 531, L115

Rocha-Pinto, H. J., Scalo, J., Maciel, W. J., Flynn, C. (2000b), *Chemical enrichment and star formation in the Milky Way disk. II. Star formation history*, A&A, 358, 869

Rood, H. J. (1974), *Empirical Properties of the Mass Discrepancy in Groups and Clusters of Galaxies.*, ApJ, 188, 451

Rood, H. J., Sastry, G. N. (1971), *"Tuning Fork"Classification of Rich Clusters of Galaxies*, PASP, 83, 313

References

Roos, N., Norman, C. A. (1979), *Galaxy collisions and their influence on the dynamics and evolution of groups and clusters of galaxies*, A&A, 76, 75

Rudnick, G., Franx, M., Rix, H., Moorwood, A., Kuijken, K., van Starkenburg, L., van der Werf, P., Röttgering, H., van Dokkum, P., Labbé, I. (2001), *A K-band-Selected Photometric Redshift Catalog in the Hubble Deep Field South: Sampling the Rest-Frame V Band to z =3*, AJ, 122, 2205

Rudnick, G., White, S., Aragón-Salamanca, A., Bender, R., Best, P., Bremer, M., Charlot, S., Clowe, D., Dalcanton, J., Dantel, M., de Lucia, G., Desai, V., Fort, B., Halliday, C., Jablonka, P., Kauffmann, G., Mellier, Y., Milvang-Jensen, B., Pello, R., Poggianti, B., Poirier, S., Róttgering, H., Saglia, R., Schneider, P., Simard, L., Zaritsky, D. (2003), *Studying high redshift galaxy clusters with the ESO Distant Cluster Survey*, The Messenger, 112, 19

Saglia, R. P., Maraston, C., Greggio, L., Bender, R., Ziegler, B. (2000), *The evolution of the color gradients of early-type cluster galaxies*, A&A, 360, 911

Salpeter, E. E. (1955), *The Luminosity Function and Stellar Evolution.*, ApJ, 121, 161

Salucci, P., Walter, F., Borriello, A. (2003), *Lambda CDM and the distribution of dark matter in galaxies: A constant-density halo around DDO 47*, A&A, 409, 53

Sanderson, A. J. R., Ponman, T. J., Finoguenov, A., Lloyd-Davies, E. J., Markevitch, M. (2003), *The Birmingham-CfA cluster scaling project - I. Gas fraction and the M-T_X relation*, MNRAS, 340, 989

Sawicki, M. J., Lin, H., Yee, H. K. C. (1997), *Evolution of the Galaxy Population Based on Photometric Redshifts in the Hubble Deep Field*, AJ, 113, 1

Schaye, J., Aguirre, A., Kim, T., Theuns, T., Rauch, M., Sargent, W. L. W. (2003), *Metallicity of the intergalactic medium using pixel statistics. II. The distribution of metals as traced by C IV*, preprint, astro-ph/0306469

Schechter, P. (1976), *An analytic expression for the luminosity function for galaxies.*, ApJ, 203, 297

Schweizer, F., Seitzer, P. (1992), *Correlations between UBV colors and fine structure in E and S0 galaxies - A first attempt at dating ancient merger events*, AJ, 104, 1039

Scodeggio, M. (2001), *Internal Color Gradients and the Color-Magnitude Relation of Early-Type Galaxies*, AJ, 121, 2413

Seljak, U., Zaldarriaga, M. (1996), *A Line-of-Sight Integration Approach to Cosmic Microwave Background Anisotropies*, ApJ, 469, 437

Sellwood, J. A. (1987), *The art of N-body building*, ARA&A, 25, 151

Shapley, A. E., Steidel, C. C., Adelberger, K. L., Dickinson, M., Giavalisco, M., Pettini, M. (2001), *The Rest-Frame Optical Properties of z∼3 Galaxies*, ApJ, 562, 95

Shectman, S. A. (1973), *Clusters of Galaxies and the Cosmic Light*, ApJ, 179, 681

Sheth, R. K. (2003), *Substructure in dark matter halos: Towards a model of the abundance and spatial distribution of subclumps*, preprint, astro-ph/0304355

Simien, F., de Vaucouleurs, G. (1986), *Systematics of bulge-to-disk ratios*, ApJ, 302, 564

Smail, I., Dressler, A., Couch, W. J., Ellis, R. S., Oemler, A. J., Butcher, H., Sharples, R. M. (1997), *A Catalog of Morphological Types in 10 Distant Rich Clusters of Galaxies*, ApJS, 110, 213

Smail, I., Edge, A. C., Ellis, R. S., Blandford, R. D. (1998), *A statistical analysis of the galaxy populations of distant luminous X-ray clusters*, MNRAS, 293, 124

Smith, S. (1936), *The Mass of the Virgo Cluster*, ApJ, 83, 23

Somerville, R. S. (2002), *Can Photoionization Squelching Resolve the Substructure Crisis?*, ApJ, 572, L23

Somerville, R. S., Primack, J. R. (1999), *Semi-analytic modelling of galaxy formation: the local Universe*, MNRAS, 310, 1087

Somerville, R. S., Primack, J. R., Faber, S. M. (2001), *The nature of high-redshift galaxies*, MNRAS, 320, 504

Spergel, D. N., Verde, L., Peiris, H. V., Komatsu, E., Nolta, M. R., Bennett, C. L., Halpern, M., Hinshaw, G., Jarosik, N., Kogut, A., Limon, M., Meyer, S. S., Page, L., Tucker, G. S., Weiland, J. L., Wollack, E., Wright, E. L. (2003), *First-Year Wilkinson Microwave Anisotropy Probe (WMAP) Observations: Determination of Cosmological Parameters*, ApJS, 148, 175

Springel, V., Hernquist, L. (2003), *Cosmological smoothed particle hydrodynamics simulations: a hybrid multiphase model for star formation*, MNRAS, 339, 289

Springel, V., White, S. D. M., Tormen, G., Kauffmann, G. (2001a), *Populating a cluster of galaxies - I. Results at z=0*, MNRAS, 328, 726

References

Springel, V., Yoshida, N., White, S. D. M. (2001b), *GADGET: a code for collisionless and gasdynamical cosmological simulations*, New Astronomy, 6, 79

Stanford, S. A., Eisenhardt, P. R., Dickinson, M. (1998), *The Evolution of Early-Type Galaxies in Distant Clusters*, ApJ, 492, 461

Stein, P. (1997), *Structure and kinematics of galaxy clusters. II. Substructures and luminosity segregation.*, A&A, 317, 670

Steinmetz, M., Navarro, J. F. (2002), *The hierarchical origin of galaxy morphologies*, New Astronomy, 7, 155

Stoehr, F. (2003), *Simulations of galaxy formation and large scale structure*, Ph.D. Thesis

Stoehr, F., White, S. D. M., Springel, V., Tormen, G., Yoshida, N. (2003), *Dark matter annihilation in the Milky Way's halo*, preprint, astro-ph/0307026

Stoehr, F., White, S. D. M., Tormen, G., Springel, V. (2002), *The satellite population of the Milky Way in a ΛCDM universe*, MNRAS, 335, L84

Summers, F. J., Davis, M., Evrard, A. E. (1995), *Galaxy Tracers and Velocity Bias*, ApJ, 454, 1

Sutherland, R. S., Dopita, M. A. (1993), *Cooling functions for low-density astrophysical plasmas*, ApJS, 88, 253

Tasitsiomi, A. (2002), *The Cold Dark Matter crisis on galactic and subgalactic scales*, preprint, astro-ph/0205464

Terlevich, A. I., Caldwell, N., Bower, R. G. (2001), *The colour-magnitude relation for galaxies in the Coma cluster*, MNRAS, 326, 1547

Thomas, D. (1999), *Abundance ratios in hierarchical galaxy formation*, MNRAS, 306, 655

Thomas, D., Bender, R., Hopp, U., Maraston, C., Greggio, L. (2003), *Kinematics and stellar populations of 17 dwarf early-type galaxies*, Ap&SS, 284, 599

Tormen, G. (1997), *The rise and fall of satellites in galaxy clusters*, MNRAS, 290, 411

Tormen, G., Bouchet, F. R., White, S. D. M. (1997), *The structure and dynamical evolution of dark matter haloes*, MNRAS, 286, 865

Tormen, G., Diaferio, A., Syer, D. (1998), *Survival of substructure within dark matter haloes*, MNRAS, 299, 728

Tozzi, P., Rosati, P., Ettori, S., Borgani, S., Mainieri, V., Norman, C. (2003), *Iron Abundance in the Intracluster Medium at High Redshift*, ApJ, 593, 705

Truemper, J. (1993), *ROSAT - A new look at the X-ray sky*, Science, 260, 1769

van den Bosch, F. C. (2002), *The universal mass accretion history of cold dark matter haloes*, MNRAS, 331, 98

van Dokkum, P. G., Franx, M. (1996), *The fundamental plane in CL0024 at z=0.4: implications for the evolution of the mass-to-light ratio*, MNRAS, 281, 985

van Dokkum, P. G., Franx, M., Fabricant, D., Illingworth, G. D., Kelson, D. D. (2000), *Hubble Space Telescope Photometry and Keck Spectroscopy of the Rich Cluster MS 1054-03: Morphologies, Butcher-Oemler Effect, and the Color-Magnitude Relation at z = 0.83*, ApJ, 541, 95

van Dokkum, P. G., Franx, M., Fabricant, D., Kelson, D. D., Illingworth, G. D. (1999), *A High Merger Fraction in the Rich Cluster MS 1054-03 at z = 0.83: Direct Evidence for Hierarchical Formation of Massive Galaxies*, ApJ, 520, L95

Verde, L., Heavens, A. F. (2001), *On the Trispectrum as a Gaussian Test for Cosmology*, ApJ, 553, 14

Visvanathan, N., Sandage, A. (1977), *The color-absolute magnitude relation for E and S0 galaxies. I - Calibration and tests for universality using Virgo and eight other nearby clusters*, ApJ, 216, 214

Wang, B., Heckman, T. M. (1996), *Internal Absorption and the Luminosity of Disk Galaxies*, ApJ, 457, 645

Warren, B. E., Jerjen, H., Koribalski, B. S. (2003), *HI Rotation Curves of Dwarf Galaxies with High Mhi/lb Ratios*, in *IAU Symposium*

Weinberg, S. (1972), *Gravitation and cosmology: Principles and applications of the general theory of relativity*, New York: Wiley, 1972

White, S. D. M. (1976), *The dynamics of rich clusters of galaxies*, MNRAS, 177, 717

White, S. D. M., Frenk, C. S. (1991), *Galaxy formation through hierarchical clustering*, ApJ, 379, 52

White, S. D. M., Navarro, J. F., Evrard, A. E., Frenk, C. S. (1993), *The Baryon Content of Galaxy Clusters - a Challenge to Cosmological Orthodoxy*, Nature, 366, 429

References

White, S. D. M., Rees, M. J. (1978), *Core condensation in heavy halos - A two-stage theory for galaxy formation and clustering*, MNRAS, 183, 341

Whitmore, B. C., Gilmore, D. M., Jones, C. (1993), *What determines the morphological fractions in clusters of galaxies?*, ApJ, 407, 489

Whitmore, B. C., Miller, B. W., Schweizer, F., Fall, S. M. (1997), *Hubble Space Telescope Observations of Two Dynamically Young Elliptical Galaxies*, AJ, 114, 1797

Wiebe, D. S., Shustov, B. M., Tutukov, A. V. (1999), *Role of disk galaxies in the chemical enrichment of the intracluster medium*, A&A, 345, 93

Wu, K. K. S., Fabian, A. C., Nulsen, P. E. J. (2001), *The soft X-ray background: evidence for widespread disruption of the gas haloes of galaxy groups*, MNRAS, 324, 95

Yee, H. K. C., Ellingson, E., Carlberg, R. G. (1996), *The CNOC Cluster Redshift Survey Catalogs. I. Observational Strategy and Data Reduction Techniques*, ApJS, 102, 269

Yoshida, N., Sheth, R. K., Diaferio, A. (2001), *Non-Gaussian cosmic microwave background temperature fluctuations from peculiar velocities of clusters*, MNRAS, 328, 669

Yoshida, N., Stoehr, F., Springel, V., White, S. D. M. (2002), *Gas cooling in simulations of the formation of the galaxy population*, MNRAS, 335, 762

Young, J. S. (1999), *The Efficiency of Star Formation in Galaxies as a Function of Galaxy Size and Environment*, ApJ, 514, L87

Zabludoff, A. I., Mulchaey, J. S. (1998), *The Properties of Poor Groups of Galaxies. I. Spectroscopic Survey and Results*, ApJ, 496, 39

Zasov, A. V. (1995), *The efficiency of star formation in spiral galaxies*, Astronomy Letters, 21, 652

Zepf, S. E., Silk, J. (1996), *On the Effects of Bursts of Massive Star Formation during the Evolution of Elliptical Galaxies*, ApJ, 466, 114

Zwicky, F. (1937), *On the Masses of Nebulae and of Clusters of Nebulae*, ApJ, 86, 217

Acknowledgements

And now that the thesis is finished I cannot conclude without a thank you to all the people who made this possible.

Very warm thanks go to Simon White & Guinevere Kauffmann, for their invaluable advice and for their continuous encouragement during these three years. I have learned from you much more I could write down in a thesis – many things not related to science at all.

These years here would have been much less special without all the friends I have met. Thanks to Stefano for his friendship and for always tolerating my RADIO3, my technical questions, and me in the last writing weeks. Thanks to Felix, Francesco and Hugues, for many useful (and mostly not–scientific) discussions. Thanks to Christian and Roberto, for sharing many dinners and bottles of wine and for support and friendship. Thanks to Larry for the salsa and for many happy beers. Thanks to Maria, Cornelia and Kate for making life so much easier. Thanks to Volker, for his important advice and help. Thanks to Andrè and Massimo for their friendship and help in many difficult moments. Thanks to Greg for many discussions and for a long, long walk trough Paris. Thanks to Bianca for her support and contagious enthusiasm. Thanks to all the EDisCS team. Thanks to many many others: Hans–Jakob, Elisa & Elisa, Serena, Luigi, Giovanna, Anna, Jarle, Stephane, Sofia, Christy, Benedetta, Claire, Liang, Mara, Kaustuv, Jens, Corina, Christoph, Bjoern, Martin . . . I am surely forgetting a lot of names . . .

I owe special thanks to my *guardian angels* Maurilio & Veronica, for always reminding me the important things and for many, many evenings together. Life was so much easier with you two around! Thanks to my old *crew*. The days I've spent with you will always be unforgettable.

Very special thanks go to my family. Many of the things I've done in my life would have not been possible without your help, support, and encouragement. Grazie per aver sempre sostenuto le mie scelte con fiducia ed incoraggiamento. Questa tesi, che è dedicata a voi, è solo un piccolissimo segno dell'affetto che nutro nei vostri confronti.

And last but not least, special thanks to my 'fidansato' Lorenzo, for just being what you are, for the joy and the serenity you gave me, and for continously trying to teach me how to 'close the office door'. I did not learn that yet, but I'll do. Promised.

Acknowledgements

Curriculum vitae

Personal

Date of birth: 8 March 1976
Nationality: Italian
Marital Status: Single

Education and training

1994   Scientific Lyceum Diploma with 60/60.

1999   Participation in the high–formation school in Naples,"For a critical balance of the physics of the 20th century", held by Prof. Franco Selleri.

2000   Degree in Physics (Astrophysics) *summa cum laude.* Laurea Degree Thesis done at the Osservatorio Astronomico di Capodimonte (Naples). Dissertation: "Evolutionary models for elliptical galaxies at low redshift." (supervisors Prof. M. Capaccioli and Dr. M. Arnaboldi).

2000   Research contract at the Osservatorio Astronomico di Capodimonte for the development of a pipeline for the reduction of WFI 2.2 m images.

2001   Participation in the "XIII Canary Islands winter school of Astrophysics, Cosmochemistry: The Melting Pot of Elements" Tenerife, Canary Islands, Spain

2001–pres. PhD fellowship at Max-Planck-Institut für Astrophysik (Garching bei München, Germany). International Max Planck Research School. Thesis topic: "The evolution of galaxies in clusters". Advisors: S. D. M. White, G. Kauffmann.

Honours and Awards

1989	Winner of an award assigned by the "Consorzio Interprovinciale Alto Calore" for the best composition about "The water and its importance".
1991–1992	Winner of a scholarship from the 'Istituto Nazionale di Previdenza per i Dipendenti dell'Amministrazione Pubblica' (INPDAP) for grades above the average reported during one year of the high school.
1992–1993	Confirmation of the scholarship from the INPDAP.
1993–1994	Confirmation of the scholarship from the INPDAP.
1994–1995	Winner of a scholarship from the INPDAP for grades above the average reported during one academic year at the university.
1995–1996	Confirmation of the scholarship from the INPDAP.
1999	Winner of a scholarship from the 'Istituto Italiano per gli Studi Filosofici' for the participation in the high–formation school "For a critical balance of the physics of the 20th century", held by Prof. Franco Selleri.
2001	Max–Planck–Institute Research fellowship (IMPRS).

Publications on Refereed Journals

1. *The Puzzle of the Polar Structure in NGC 4650A*,
   E. Iodice, M. Arnaboldi, **G. De Lucia**, G. Gallagher, L. Sparke, K. Freeman, AJ, 2002, 123, 195

2. *Substructures in Cold Dark Matter Haloes*,
   G. De Lucia, G. Kauffmann, V. Springel, S. D. M. White, B. Lanzoni, F. Stoehr, G. Tormen, N. Yoshida, MNRAS in press, astro-ph/0306205

3. *Chemical enrichment of the intra–cluster and intergalactic medium in a hierarchical galaxy formation model*,
   G. De Lucia, G. Kauffmann, S. D. M. White, MNRAS in press, astro-ph/0310268

4. *Effects of asphericity and substructure on the determination of cluster mass with weak gravitational lensing*,
   D. Clowe, **G. De Lucia**, L. King, MNRAS in press

5. *The Capodimonte Deep Field: presentation of the Survey and first spectroscopic follow–up,*
J. M. Alcala, M. Pannella, E. Puddu, M. Radovich, R. Silvotti, M. Arnaboldi, M. Capaccioli, M. Dall'Ora, **G. De Lucia**, A. Grado, G. Longo, A. Mercurio, I. Musella, N. Napolitano, M. Pavlov, A. Rifatto, V. Ripepi, submitted to A&A, under revision

6. *Observing the build–up of the colour–magnitude sequence at redshift ~ 0.8,*
G. De Lucia, B. M. Poggianti, et al., in preparation

Other publications

1. *Dating the evolution and the formation scenario of polar-ring galaxy NGC 4650A,*
G. De Lucia, E. Iodice, M. Arnaboldi, 2001, Memorie della SAIt, 72, 789

2. *The Puzzle of the Polar Structure in NGC 4650A,*
E. Iodice, **G. De Lucia**, M. Arnaboldi, J. S Gallagher, L. Sparke, 2001, ASP Conf. Ser., 230, "Galaxy Disks and Disk Galaxies" , 445

3. *Data reduction and astrometry strategies for wide-field images: an application to the Capodimonte Deep Field,*
J. M. Alcalá, M. Radovich, R. Silvotti, M. Pannella, M. Arnaboldi, M. Capaccioli, E. Puddu, A. Rifatto, **G. De Lucia**, A. Mercurio, N. Napolitano, A. Grado, G. Longo, M. Dall'Ora, V. Ripepi, I. Musella, R. Scaramella, 2002, SPIE, 4836, 406

4. *The Capodimonte Deep Field: research projects,*
M. Capaccioli, J. M. Alcalá, M. Radovich, R. Silvotti, M. Pannella, M. Arnaboldi, E. Puddu, A. Rifatto, **G. De Lucia**, A. Mercurio, N. Napolitano, A. Grado, G. Longo, M. Dall'Ora, V. Ripepi, I. Musella, 2003, Memorie della SAIt, 74, 452

5. *The Luminosity Function of EDisCS Cluster Galaxies,*
G. Rudnick, **G. De Lucia**, S. D. M. White, R. Pelló, and the EDisCS collaboration, 2003, Carnegie Observatories Astrophysics Series, Vol. 3: "Clusters of Galaxies: Probes of Cosmological Structure and Galaxy Evolution", ed. J. S. Mulchaey, A. Dressler, and A. Oemler (Pasadena: Carnegie Observatories, http://www.ociw.edu/ociw/symposia/series/symposium3/proceedings.html)

6. *Studying high redshift galaxy clusters with the ESO Distant Cluster Survey*,
   G. Rudnick, S. White, A. Aragón-Salamanca, R. Bender, P. Best, M. Bremer,
   S. Charlot, D. Clowe, J. Dalcanton, M. Dantel, **G. De Lucia**, V. Desai, B.
   Fort, C. Halliday, P. Jablonka, G. Kauffmann, Y. Mellier, B. Milvang-Jensen,
   R. Pelló, B. Poggianti, S. Poirier, H. Róttgering, R. Saglia, P. Schneider, L.
   Simard, D. Zaritsky, 2003, The ESO Messenger, 112, 19

7. *Evolution of galaxies in clusters: semi-analytic models and observations*,
   G. De Lucia, G. Kauffmann, S. D. M. White, 2003, to appear in "Multiwave-
   length Cosmology", Mykonos Conference Proceedings